The University Of Sheffield.

Access to Electronic Thesis

Author:	Gareth Luke Barns
Thesis title:	On Single Well Forced Gradient Tracer Tests: Implications of Aquifer Physical Heterogeneity and Tracer Behaviour
Qualification:	PhD

This electronic thesis is protected by the Copyright, Designs and Patents Act 1988. No reproduction is permitted without consent of the author. It is also protected by the Creative Commons Licence allowing Attributions-Non-commercial-No derivatives.

This thesis was embargoed until December 2012.

If this electronic thesis has been edited by the author it will be indicated as such on the title page and in the text.

On Single Well Forced Gradient Tracer Tests: Implications of Aquifer Physical Heterogeneity and Tracer Behaviour

The University Of Sheffield.

A thesis submitted for the degree of Doctor of Philosophy in the Faculty of Engineering at the University of Sheffield

by

Gareth Luke Barns

(MEarthSci)

Groundwater Protection and Restoration Group

Department of Civil and Structural Engineering

The University of Sheffield

December 2010

Summary

Single well forced gradient tracer tests are a potential cost-effective approach to estimate *in situ* aquifer contaminant fate and transport parameters for use in natural attenuation assessments and remediation schemes. To date dipole flow tracer tests have been used to measure the conservative and hydraulic parameters of an aquifer, while push-pull tests are well characterised for use with biodegrading tracers. The effect of typical aquifer physical heterogeneity on the ability of single well tests to successfully estimate parameters has not yet been characterised. Also, the ability of single well tests to accurately and quickly measure aquifer parameters using tracer mixtures should be analysed.

To investigate the effect of physical heterogeneity on single well tests scaled down ultraviolet imaging experiments were performed in a low profile box. Potential tracers for use in mixtures were investigated through column and batch experiments: Inorganic anions and fluorescein, inorganic cations, acetate and trichlorofluoroethene were considered to measure conservative transport parameters, cation exchange capacity, biodegradation potential and hydrophobic sorption respectively. Numerical modelling was used to simulate reactive tracer signals in single well forced gradient tests.

Results suggest that dipole flow tracer tests are appropriate for measuring conservative transport parameters and the sorption of lowly retarded tracers, but are not highly suitable for biodegrading tracers. Tests could be performed with non-recirculating flow, allowing simpler modelling, if equal injection and extraction flow rates could be ensured. Push-pull tests are suitable for biodegrading tracers and moderate to highly retarded tracers. This limits the potential to use reactive tracer mixtures in these tests. Dipole flow tracer test breakthrough curves are highly susceptible to heterogeneity, and could be used to identify discrete permeability variations in aquifers. The effect of heterogeneity is not significant on push-pull test breakthrough curves, but seriously affects tracer plume migration. Inorganic anions provided the most reliable conservative tracer. Trichlorofluoroethene was found to be a suitable tracer to measure hydrophobic sorption. The biodegradation surrogate chosen for a field test should biodegrade similarly to the contaminant under study.

Acknowledgements

Firstly I would like to thank my supervisors Steve Thornton and Ryan Wilson who have provided invaluable guidance and knowledge during my research. Thanks go also to: Chris Berryman, Ben Eagle, Neil Thomson and Gillian Roos for their work on dipole flow tracer tests; M.Sc. student James North for performing preliminary imaging tests; Undergraduate student Tom Haighton for performing sandbox push-pull tests; Nik Reeves-McLaren from the Department of Materials Science and Engineering for performing XRD analysis on sand samples; Rob McLaren from the University of Waterloo for advice with HydroGeoSphere© modelling and David Parkhurst from USGS for advice with PHREEQC modelling.

I would like to greatly thank Andy Fairburn for being an excellent technician, providing support beyond his remit during my years in the laboratory. Special thanks are also extended to Dick Smith formerly of the Civil and Structural Engineering workshop, who made many things for me often at short notice.

I am extremely grateful to my parents for their support over the years. I would also like to thank everyone in the Kroto Research Institute, that has helped me in the laboratories or office, who are too numerous to mention here. Last but not least, thanks go to all my friends during my time in Sheffield; you have kept me sane over the years.

Table of Contents

Tables and Figures

1. Introduction

1.1. Background

Groundwater pollution is a global problem. Activities related to chemical and pharmaceutical manufacturing, petrochemical production and retail, landfills, and other small-scale activities utilising chemicals have the potential to release large amounts of organic and inorganic contaminants into the environment. Once released, such compounds often find their way into the water cycle. A contaminant is a substance that has entered the groundwater due to human activity [Domenico and Schwartz, 1990]. A substance (natural occurring or anthropogenic) becomes a pollutant when its concentration exceeds a specified threshold, relative to appropriate environmental regulations. Pollutants from a source may percolate through the unsaturated zone to the water table or leach straight into groundwater. Pollutants can exist as non-aqueous phase liquids (NAPLs) or as a dissolved phase in the groundwater. NAPLs form complex source zones, which slowly dissolve into the groundwater. Dissolved pollutants migrate with the groundwater velocity downstream of a source in the saturated zone in pores and fractures. Pollutants can pose health risks and aesthetic problems if they reach receptors such as sources of drinking water and can seriously damage the environment [Ritter et al., 2002].

1.1.1. Aquifer properties

An aquifer is an underground water-bearing layer of rock or unconsolidated deposits that is sufficiently permeable to economically supply water to wells [Domenico and Schwartz, 1990]. Sandstone, unconsolidated sand and other aquifers have natural properties that disperse, retard and reduce dissolved contamination during solute transport. These aquifer properties affect either the bulk flow of the water or the contaminant directly, i.e. its fate and transport. The velocity of flow through intergranular porous media is proportional to the hydraulic gradient present and the

hydraulic conductivity constant (K), defined by Darcy's law. This can be expressed by the equation:

$$Q = -KA\frac{\delta h}{\delta l} \tag{1.1}$$

where Q is the flow rate, A is the area perpendicular to flow and δh /δl is the hydraulic gradient. The minus sign indicates flow is down hydraulic gradient. From Equation 1.1 the groundwater pore or linear velocity can be estimated from:

$$v = -\left(\frac{K}{\Theta}\right)\frac{\delta h}{\delta l} \tag{1.2}$$

where Θ is the porosity. Solute concentrations are also affected by mechanical dispersion and molecular diffusion. Mechanical dispersion primarily relates to mixing processes at the pore scale due to flow velocity gradients in pore spaces, flow path tortuosity and dead-end pore spaces, and at the macroscale due to heterogeneity in hydraulic conductivity distribution (Figure 1-1) [Domenico and Schwartz, 1990]. This is discussed further at the end of this section. Molecular diffusion of solutes also occurs due to concentration gradients, but is normally orders of magnitude lower than mechanical dispersion and can often be considered negligible [Domenico and Schwartz, 1990]. The aquifer dispersivity and diffusion are related by the equation:

$$D^{*} = \alpha v + D \tag{1.3}$$

where α is dispersivity, v is velocity, D* is the combined dispersion coefficient and D is the diffusion coefficient. Usually the effects of molecular diffusion and mechanical dispersion are combined as one term, as they are difficult to separate. Mechanical dispersion induces mixing between contaminated and uncontaminated groundwater in the direction of flow (longitudinal dispersion) and normal to this (transverse dispersion), with corresponding values for α in Equation 1.3. This reduces the contaminant concentration in the aquifer. Longitudinal dispersivity generally exceeds transverse dispersivity by an order of magnitude [Domenico and Schwartz, 1990]. Longitudinal dispersivity has been shown to increase with observation scale, and reach an "asymptotic value" at an observation scale of ~50-500 m [Gelhar et al., 1979; Welty and Gelhar, 1994; Hess et al., 2002]. The hydraulic conductivity and

dispersivity of the aquifer are the main controls on the advection and dispersion of solutes, respectively. Advection and dispersion are combined in the advection-dispersion equation, the one-dimensional form of which is:

$$\frac{\delta C}{\delta t} = \frac{\delta}{\delta x}\left(D^* \frac{\delta C}{\delta x} \right) - \frac{\delta}{\delta x}(vC) \qquad (1.4)$$

The first term on the right hand side describes mass transport by dispersion (and diffusion), assuming constant dispersion by Fick's law, where x is distance, t is time and C is concentration. The second term relates to mass transport by advection. Terms can be added to the equation to describe sorption and biodegradation of contaminants, discussed below.

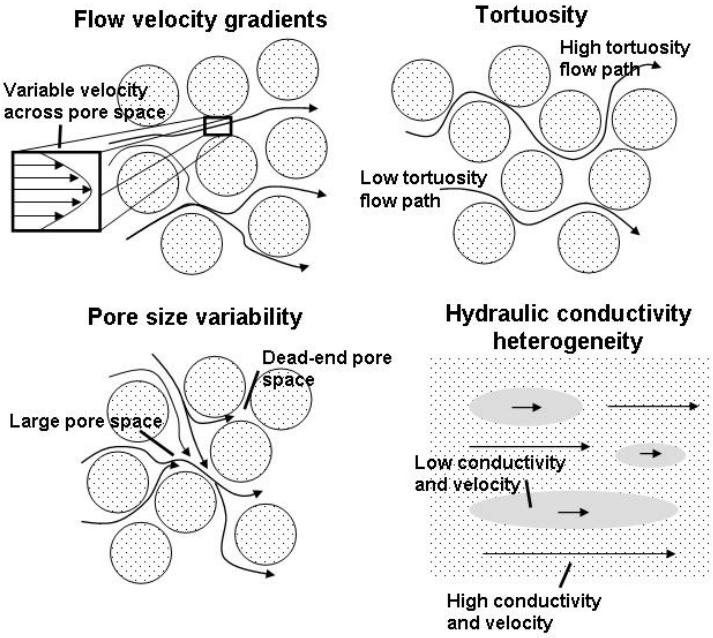

Figure 1-1: Examples of microscale non-idealities that can cause dispersion and an example of flow variability caused by heterogeneity in hydraulic conductivity. Based on Domenico and Schwartz [1990].

Ionic inorganic contaminants can be retarded due to sorption onto aquifer minerals. This is due to interaction of positively charged cations with negatively charged mineral surfaces or negatively charged anions on positively charged mineral surfaces depending on the pH [Yong et al., 1992]. In the typical neutral pH range of aquifers [Banks et al., 1998], sorption of cations onto negatively charged surfaces is most likely. This is as the pH is above the zero point charge of the aquifer minerals (e.g.

metal oxides). The amount of negative charge is known as the cation exchange capacity (CEC) of the aquifer. This is an important property for the attenuation of landfill leachates, acid mine drainage and ammonium pollution [Ceazan, 1989; Christensen et al., 2001]. Sorption onto mineral surfaces, by reversible ion exchange (e.g. NH_4^+) or stronger chemisorption (e.g. metals) can retard the migration of ionic pollutants [Appelo and Postma, 2005]. Under acidic conditions sorption and retardation of anionic contaminants may occur (e.g. Davis et al. [2000]). As the pH is below the zero point charge of aquifer minerals the minerals have positively charged surfaces [Yong et al., 1992]. Organic contaminants can also be retarded by hydrophobic sorption onto organic matter in the aquifer matrix [Karickhoff, 1981; Schwarzenbach, 1993]. The retardation of such organic chemicals is traditionally predicted from the fraction of organic carbon in the sediment and empirical relationships derived for the chemical of interest [Karickhoff, 1981]. Recent research has suggested that the type of carbon present (specifically natural carbon or black carbon) is also an important control in such sorption [Grathwohl, 1990; Allen-King et al., 2002; Accardi-Dey and Gschwend, 2003]. Sorption of organic and inorganic species is typically described by one of three isotherms: Linear, Freunlich and Langmuir (Figure 1-2). Linear isotherms assume that the amount of the solute sorbed (C_{sorb}) increases linearly with the amount in solution (C_{sol}). This relationship best approximates sorption at low concentrations, when sorption sites are not saturated. Freundlich isotherms are empirically derived. They are often used as they allow for surface heterogeneity in sorption site characteristics [Appelo and Postma, 2005]. Both Linear and Freundlich isotherms are limited by not having an upper limit to the amount of solute that can be adsorbed. A Langmuir isotherm assumes a fixed number of sorption sites and hence a maximum amount of a solute that can be adsorbed.

The retardation factor (R) of a species relative to a non-sorbing species is defined by the equation:

$$R = 1 + \frac{p_b}{\Theta} K_d \qquad (1.5)$$

where p_b is the bulk density of the sorbent and K_d is the sorption distribution coefficient. For Linear isotherms K_d is equal to C_{sorb} /$C_{sol.}$ For Freundlich isotherms:

$$K_d = K_F C_{sol}^{n-1} \quad (1.6)$$

where K_F and n are constants. For Langmuir isotherms at low concentrations in the linear part of the curve:

$$K_d = C_{sorb} / C_{sol} = Q^0 / K_L \quad (1.7)$$

where Q^0 is the maximum sorbtive capacity and K_L is a constant. At high concentrations $C_{sorb} = Q^0$ [Appelo and Postma, 2005]. The relationship of K_d to cation exchange capacity and the fraction of organic carbon for the sorption of inorganic and organic species is explained in the relevant chapters.

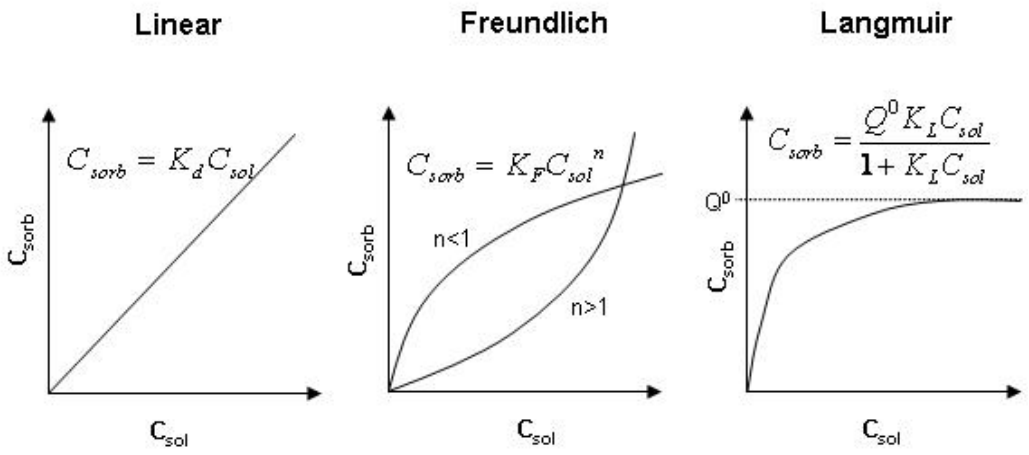

Figure 1-2: Sorption isotherms used to relate the sorbed concentration of a substance (C_{sorb}) to concentration in solution (C_{sol}).

Biodegradation of organic contaminants by microorganisms present in an aquifer occurs using the dissolved organic compound as a carbon source in aerobic respiration, nitrate reduction, metal reduction, sulphate reduction or methanogenesis (see Table 1-1). Biodegradation rates depend on the type of bacteria, amount and type of chemical being consumed and electron acceptor (e.g. O_2, NO_3^- and SO_4^-) concentration [Oya and Valocchi, 1998; Lerner et al., 2000; Antizar-Ladislao and Galil, 2006]. The bioavailability of a compound may also be related to its hydrophobic sorption capacity [Knezovich et al., 1987; Liu et al., 2007], with biodegradation being limited by the desorption rate of a compound. Biodegradation is

often greatest at the plume fringe, where electron acceptor concentrations are high due to mixing of the plume with unpolluted water by dispersion [Lerner et al., 2000; Huang et al., 2003; Tuxen et al., 2006; Elliott et al., 2010]. In the plume centre electron acceptor concentrations are often depleted by anaerobic biodegradation which occurs at a slower rate. Greater dispersion (i.e. higher values of dispersivity, α) will lead to greater mixing and a shorter plume length. It is important to quantify the biodegradation capacity of an aquifer, considering a mass balance between concentrations of electron acceptors, organic contaminants, biodegradation products and alkalinity. Biodegradation rates also need to be estimated [Istok et al., 1997; Haggerty et al., 1998; Hunkeler et al., 1999]. The biodegradation rates of contaminants are typically characterised by Monod kinetics, shown by Lawrence and McCarty [1970] to be:

$$-\frac{dC}{dt} = \frac{kCX}{K_s + C} \tag{1.8}$$

where the left hand side of the equation is the pollutant utilisation rate, k is the maximum specific pollutant utilisation rate, C is the limiting pollutant concentration in the bulk liquid, X is the microbial concentration and K_s is the half saturation coefficient (see Figure 1-3). However these factors are often difficult to determine at the field-scale for plumes, where biodegradation is often simplified to first-order kinetics (e.g Lu et al [1999]). Fate and transport models also commonly assume first-order kinetics for biodegradation [Alvarez and Ilman, 2006]. This assumption is suitable as (a) biodegradation is limited by mass transfer by desorption, dissolution and diffusion, which are commonly first-order processes, and (b) first-order kinetics are favoured at low pollutant concentrations below K_s. Therefore the biodegradation rate can be simplified to:

$$\frac{dC}{dt} = -\lambda C \tag{1.9}$$

where, $\lambda = \frac{kX}{K_s}$ (1.10)

Table 1-1: Typical biological reactions in an aquifer; [CH_2O] represents simple organic matter. [1] General equation from Istok et al. [1997].

Aerobic Respiration	$[CH_2O] + O_2 \rightarrow CO_2 + H_2O$
Denitrification	$5[CH_2O] + 4NO_3^- + 4H^+ \rightarrow 2N_2 + 5CO_2 + 7H_2O$
Sulphate Reduction	$SO_4^{2-} + 2H^+ + 2[CH_2O] \rightarrow 2CO_2 + H_2S + 2H_2O$
Fe (III) reduction	$[CH_2O] + 4FeOOH + 8H^+ \rightarrow 7H_2O + 4Fe^{2+} + CO_2$
Mn (IV) reduction	$[CH_2O] + 2MnO_2 + 4H^+ \rightarrow 2Mn^{2+} + 3H_2O + CO_2$
Methanogenesis	$CO_2 + H_2 \rightarrow CH_4 + H_2O$[1]

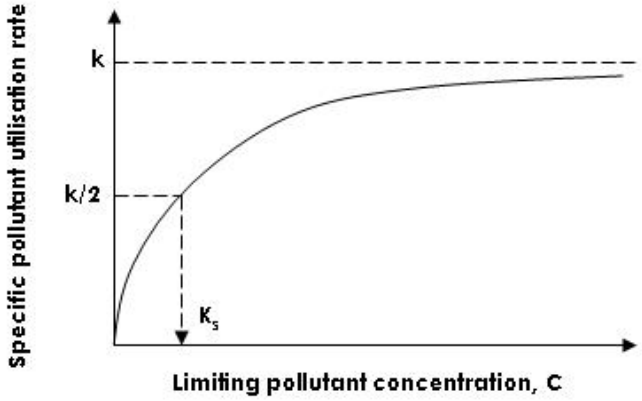

Figure 1-3: Graphical representation of Monod equation for biodegradation, showing derivation of K_s modified from Alvarez and Ilman [2006].

The grain size distributions of aquifers may vary at the scale of small layers and lenses (10^{-1}-10^0 m), leading to variation of hydraulic conductivity by a factor of ~10-100, even in aquifers which appear to be uniform [Sudicky, 1986; Stauffer, 2007]. This causes spatial variation in groundwater velocity, and hence solute migration. Heterogeneity in groundwater flow can be significant for contaminant transport in sand aquifers from the pore scale to metre scale [Freyberg, 1986; Sudicky, 1986; Welty and Gelhar, 1994; Korte et al., 2000]. The presence of mobile and immobile pores spaces, with respect to flow, [Brusseau and Rao, 1989] may affect estimates of biological process, as different microorganisms inhabit different sized pore spaces [Roden and Scheibe, 2005]. Non-equilibrium hydrophobic sorption and ionic sorption can also contribute to dispersion of solutes [Brusseau and Rao, 1989]. On a larger scale, flow heterogeneity can be caused by small zones or layers of different hydraulic conductivity, due to variation in lithology [Gillham et al., 1984]. The effect of hydraulic conductivity distribution on flow heterogeneity has been investigated in longitudinal flow experiments [Danquigny et al., 2004] and two-well convergent field tracer tests [Ptak and Schmid, 1996]. Both experiments were performed with multi-

level samplers at the extraction well. In the studies order of magnitude variations in water velocity with depth were observed. If tracer concentration was measured in these tests at an open long screen well, heterogeneity would result in large dispersion of the breakthrough curve. Heterogeneity in hydraulic conductivity of less than an order of magnitude has also been shown to more than double transverse mixing, through flow focusing [Cirpka et al., 2006; Werth et al., 2006; Rolle et al., 2009]. Spatial variability in groundwater flow (hydraulic conductivity, porosity, dispersivity) and reactive transport (sorption, pollutant biodegradation) properties will result in high and/or low pollutant mass flux paths that may vary by over three orders of magnitude [Devlin et al., 2002; Wilson et al., 2004]. If homogenous

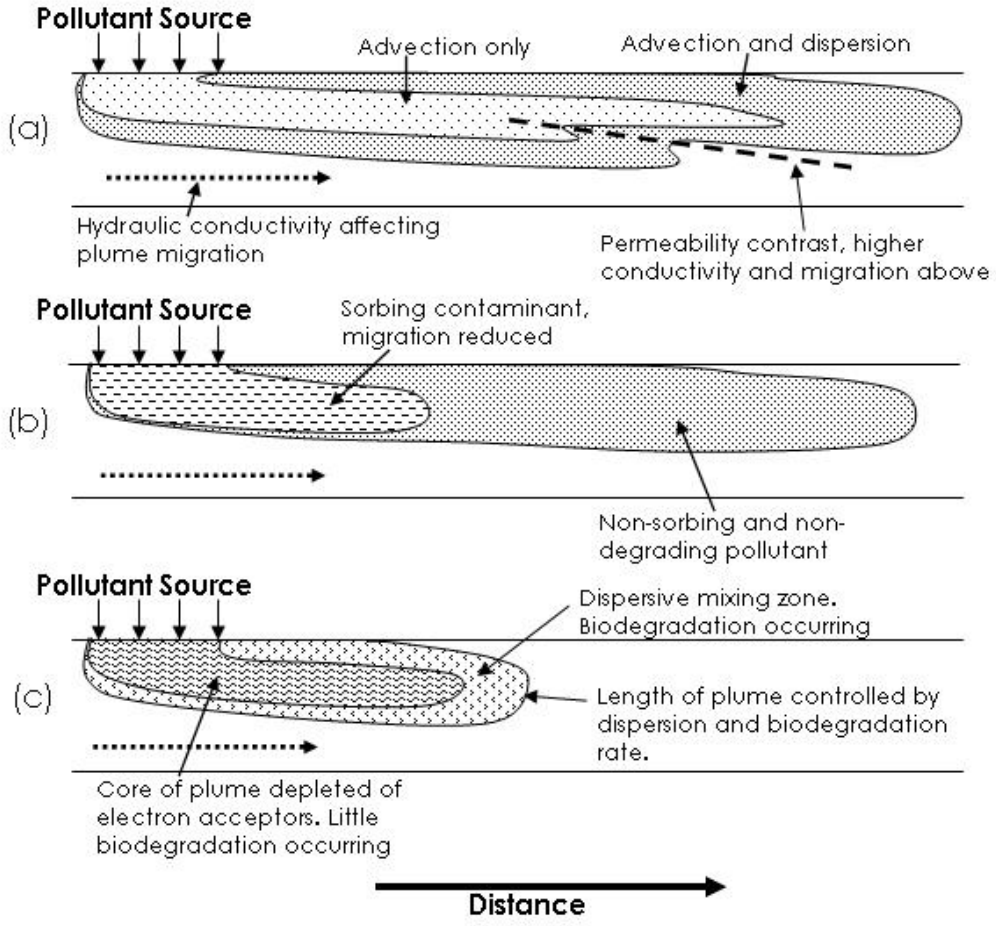

Figure 1-4: Schematic diagram showing the effect of aquifer properties on plume geometry: (a) hydraulic conductivity, dispersivity and heterogeneity; (b) migration of an inorganic or organic sorbing pollutant to a non-sorbing and non-degrading pollutant; (c) migration of a biodegrading pollutant.

conditions are assumed for a heterogeneous aquifer, this could lead to large errors in parameter estimates required for natural attenuation and remediation schemes.

1.1.2. **Natural attenuation and remediation**

Natural attenuation occurs when substance concentrations are dispersed and reduced in an aquifer without any artificial input, due to the natural aquifer properties, as discussed above. Figure 1-8 is a schematic showing how aquifer properties impact pollutant plume migration. Natural attenuation can be predicted through the use of numerical models with prior knowledge of the aquifer properties [Clement et al., 1998], to assess whether substance concentrations will be reduced to a safe and permissible level when a plume reaches a receptor (e.g. drinking water supply well, river, lake). Monitoring the natural attenuation of a pollutant over time (e.g. [Landmeyer et al., 1998; Lu et al., 1999; Devlin et al., 2002; Edward et al., 2009]) assesses whether predictions are correct, and is often more cost-effective than implementing a traditional remediation scheme, such as prolonged extraction of polluted groundwater and treating it *ex situ* (pump and treat) (e.g. Dasch et al. [1997]).

Remediation is required when natural attenuation estimated from measured aquifer parameters is not predicted to reduce substance concentrations to safe levels before reaching a receptor. Many remediation techniques are available, depending on the situation and include air sparging for volatile pollutants close to the water table [Johnston et al., 2002], passive amendment release where specific nutrients are added to an aquifer to stimulate biodegradation [Wilson et al., 1997; Wilson et al., 2002] and permeable reactive barriers which include highly reactive material that adsorbs or degrades the pollutant [Cantrell et al., 1995; Wilkin et al., 2003; Andersson et al., 2004]. Knowledge of mass flux paths is crucial to ensure correct design of many remediation schemes. For example for permeable reactive barriers, if a high mass flux path is not considered the plume may breakthrough the other side of the barrier.

1.1.3. **Tracer tests**

The conservative and reactive properties of an aquifer must be measured accurately at an appropriate scale of resolution, for an aquifer to be considered for monitored natural attenuation (~10^0 to 10^2 m resolution) [Landmeyer et al., 1998; Devlin et al., 2002] or remediation (~10^{-1} to 10^1 m resolution) [Wilson et al., 1997; Wilkin et al., 2003]. Aquifer material can be sampled and analysed for properties which influence both organic and inorganic contaminant attenuation, e.g. cation exchange capacity analysis [Edmeades and Clinton, 1981] or the Walkley Black digestion method to estimate the fraction of organic carbon [van Reeuwijk, 1992]. The sediment can also be used in column or batch studies, with the pollutant(s) of interest (e.g. [Adeel and Luthy, 1995; Hunkeler et al., 1998; Thornton et al., 2000a; Thornton et al., 2000b; Voegelin et al., 2001; Zheng et al., 2002]) This allows specific sorption or biodegradation rates to be obtained, for the pollutant(s). However in these *ex situ* tests, the aquifer material is disturbed and may not be equilibrated with the natural groundwater, or be fully representative of the conditions in an aquifer. This is especially relevant for biodegradation assessments, where there are many potential variables. In addition the relatively small sample may not represent the natural variability of that property in the aquifer. Therefore *in situ* tests are more desirable to effectively sample aquifer properties.

The concentration histories of tracers can be measured using *in situ* tests to estimate aquifer properties [Freyberg, 1986; Wilson, 1998; Hess et al., 2002; Ptak et al., 2004]. These tracers must respond to the same processes affecting the pollutants under investigation (but not necessarily to the same degree), while being suitable and safe for injection into groundwater. Quantifying multiple parameters using individual tracers is time consuming and expensive. The potential to use several tracers in a mixture to simultaneously sample different aquifer properties is highly advantageous. Mixed tracer tests have been performed to investigate multiple cation transport in sandy aquifers [Bjerg and Christensen, 1993; Andersson et al., 2004], reactive

transport of fluorescent dyes and viruses in karst systems [Geyer et al., 2007; Flynn and Sinreich, 2010] and aquifer heterogeneity with multiple DNA tracers [Ptak et al., 2004]. However there is little research on the performance and application of mixed tracer tests to sample multiple aquifer properties in a sand or sandstone aquifer, such as those which are common in the United Kingdom [Kimblin, 1995].

There are many types of aquifer tracer tests. The most basic is a natural gradient tracer test, e.g. [Freyberg, 1986; Sudicky, 1986; Davis et al., 2000], where tracer is released in one or more boreholes and is transported through the aquifer by the natural hydraulic gradient. Tracer concentrations are measured downstream in observation wells and/or multilevel sampler arrays. Hydraulic conductivity is estimated from the peak tracer breakthrough time and the natural hydraulic gradient. This type of test can yield representative aquifer parameters, however the test time scale is weeks to months, during which a large number of samples may be generated. Forced gradient tests can be carried out with multiple boreholes, including divergent and convergent tests and two-well tests (Figure 1-5) [Domenico and Schwartz, 1990]. Flow can be recirculated in the two-well test to form a horizontal dipole. These tests are quicker to perform than natural gradient tests and sample the aquifer between wells. To estimate aquifer hydraulic conductivity the head gradient between the tracer injection and extraction well chambers must be measured, for example using pressure transducers, and an area of flow needs to be assumed. Drilling boreholes for tests may result in large costs for an investigation. The connectivity between boreholes is unknown before the test is performed, so many may be needed to ensure good results. Single well forced gradient tracer tests reduce costs and uncertainty, and sample a volume of aquifer on the scale of 10^0 m^3. A single well forced gradient tracer test suitable for reactive tracers is the push-pull test (PPT) [Istok et al., 1997], although it gives limited information on the hydraulic properties of an aquifer. An alternative test is the dipole flow tracer test (DFTT) [Sutton et al., 2000], which has the potential to measure the hydraulic and reactive properties of an aquifer.

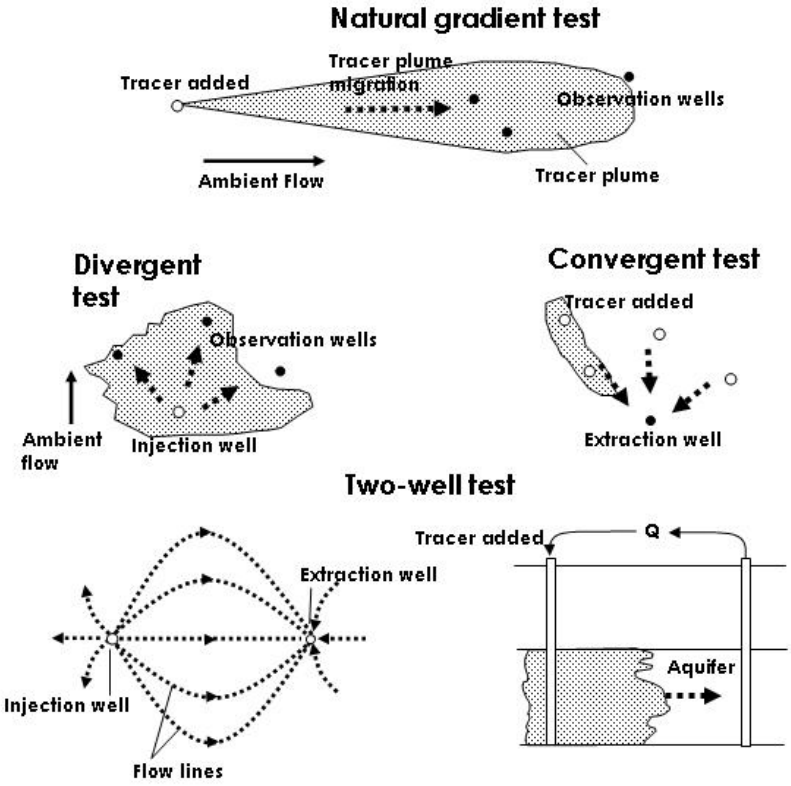

Figure 1-5: Examples of field tracer test, modified from Domenico and Schwartz [1990].

1.1.4. **Dipole flow tracer tests**

Dipole flow, where water is pumped into the well through one chamber and out of another directly above or below has previously been used for the bioremediation of groundwater contaminated with organic chemicals [Stamm, 1995]. The dipole flow test (DFT) as a method to estimate aquifer hydraulic conductivity originates from Kabala [1993], who derived the first analytical solution describing the hydraulic processes occurring when water was pumped from an upper chamber to a lower chamber of equal size in the same well, with both chambers being isolated by inflatable packers (see Figure 1-6). The pumping arrangement imposed dipole flow, with water flowing through the aquifer from the bottom to top chamber. From the draw-down of water in the pumped (top) chamber and draw-up in the injection (bottom) chamber, the analytical solution provides an estimation of horizontal (K_x) and vertical (K_z) hydraulic conductivity and specific storage. Values of K_x and K_z estimated from a DFT will be an average of the permeable media within the aquifer volume sampled by the test. It is useful to know K_z, as aquifers may be strongly

layered. A low K_z may indicate the presence of low permeability layers. If there is a strong component to vertical flow in the aquifer, this could affect long term solute migration. An advantage of a DFT is that there is no net water removed from the well during pumping. Conventional forced-gradient tracer tests produce large volumes of water, which must be disposed of appropriately if contaminated. The sphere of influence of the DFT, in which 90% of the flow occurs, was calculated by Zlotnik and Ledder [1996] to be 4L in the radial direction and 10aL in the vertical direction, where a^2 is the anisotropy ratio (K_x/K_z) and L is the distance from the centre of the central packer to the centre of a chamber, also known as the shoulder length (Figure 1-6).

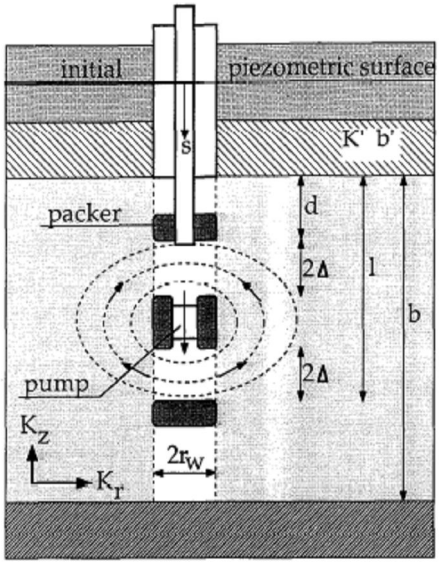

Figure 1-6: Schematic diagram of a dipole flow test [Kabala, 1993], with typical field dimensions of 1 metre for packers, 0.6 metres for chambers (2Δ) and 0.076 metres for well radius (r_w).

There has been good characterisation of DFTs in unconsolidated sand and gravel aquifers, e.g. Zlotnik and Zurburchen, [1998], where hydraulic conductivity was estimated assuming aquifer isotropy. In a later study Zlotnik et al. [2001] found that it was virtually impossible to deduce the anisotropy of an alluvial sand and gravel aquifer from field data due to a large amount of background noise. This led to the assumption of local isotropy in the aquifer in the region of influence of the DFT, thereby allowing the estimation of bulk hydraulic conductivity only. The background noise is likely to relate to a high sensitivity of anisotropy estimates to aquifer

conditions [Xiang and Kabala, 1997]. Steady-state numerical solutions provided a better estimate of anisotropy, when there was a greater distance between chambers (giving a larger averaging area). However, the measured anisotropy was affected significantly when a highly hydraulically conductive "skin zone" was present around the borehole, which could represent a sand pack or a zone disturbed during well installation. A high conductivity in this disturbed zone will lead to an underestimation of anisotropy, as water will travel preferentially in a vertical direction from the injection to extraction chambers. Also if there are large K ratios between layers spanned by the dipole assembly, the test will underestimate the anisotropy [Xiang and Kabala, 1997]. Zlotnik et al. [2001] found good correlation between DFT-obtained K_x values and those from previous pumping tests and laboratory analysis. A subsequent study of a heterogeneous alluvial aquifer in Nebraska provided further correlation of radial hydraulic conductivity (K_r) values with previous tests [Zlotnik and Zurbuchen, 2003]. Through linear regression analysis, a strong correlation was found with the multilevel slug tests and a less strong one with borehole flowmeter tests, due to the absence of a distinct vertical scale in the test. This indicates good consistency of DFT-based K_r estimates, in defining aquifer heterogeneity at a high-resolution. Other DFTs were carried out in an alluvial unconfined aquifer in Denmark [Hvilshoj et al., 2000], using an opposite pumping regime to Kabala [1993] and Zlotnik and Zurburchen [1998]. Estimates of K_z, storativity and anisotropy were not determined to an acceptable accuracy, when calculated from the original analytical solutions of Kabala [1993]. Using sensitivity analysis, only K_x varied by an acceptable factor. Hvilshoj et al. [2000] calculated acceptable K_x and K_z values that were correlated with multi-level slug tests using a nonlinear regression method, data from the dipole assembly and additional peizometers around the borehole.

Evaluation of the original DFT test solution of Kabala [1993] [Hvilshoj et al., 2000] has shown it cannot be used to a reasonable level of acceptability in field tests, thus K_x, K_z, a^2, and storativity cannot all be accurately measured. This may relate to the presence of a skin effect, well-bore storage and/or well losses which were assumed to

be negligible for the analytical solution [Kabala, 1993], or oversimplification of the semi-pervious layer on top of the aquifer. Similarly, theoretical analysis and subsequent testing of Zlotnik et al. [2001] has shown only K_r can be measured and confirmed by other tests. It is possible to calculate a^2 by linear regression, although additional piezometers are needed [Hvilshoj et al., 2000]. This contradicts one of the main benefits of the DFT over other tests outlined by Kabala [1993] (i.e. only 1 borehole needed). The DFT may be able to accurately measure K_x, K_z and anisotropy using tracers.

When applied with a DFT a conservative tracer test provides two crucial functions. Firstly, an extraction chamber breakthrough curve will be produced that demonstrates a dipole flow field has been generated between the two chambers. Secondly, the breakthrough curve can be inverse modelled to estimate the anisotropy in aquifer K. This can be combined with the measurement of draw-down or draw-up of water in the well chambers from the hydraulic part of the test to estimate K_x and K_z. The first DFTTs were performed by Sutton et al. [2000] in unconsolidated deposits. A pulse of Rhodamine Water Tracing dye was injected into the injection chamber over a short time at the start of each test. The dipole flow field was kept constant during the tests. Tracer concentration in the extracted water was measured using a flow-through fluorometer. Tests performed with recirculating water were found to be easier to conduct than non-recirculating tests and did not significantly affect the arrival times of peak tracer concentrations. A summary of the main advantages and disadvantages of recirculating tracer in DFTTs is shown in Table 1-2. If water is recirculated extraction and injection flow rates are known to be always equal, allowing greater confidence in modelling. The recirculation tail of a DFTT breakthrough curve (late time in Figure 1-7) may be useful if investigating biodegradation over long time periods. If water is not recirculated disposal, treatment or re-injection of the extracted water could be possible. However this would increase test preparation and take down time, limiting the amount of DFTTs that could be performed.

Advantages	Disadvantages
1. Extracted water does not have to be disposed of as waste, treated, or reinjected upstream in a polluted zone.	1. If a short circuit is present this signal may obscure a later aquifer signal
2. No effect on estimates of α or a^2	2. Only a short injection period possible
3. Equal extraction and injection flow rates	3. A model incorporating recirculation may be required if investigating biodegradation

Table 1-2: Summary of main advantages and disadvantages of recirculation in DFTTs.

The presence of a skin zone or short-circuiting of the dipole flow around the packers in field tests was shown by a tracer peak ahead of the main aquifer tracer peak. There is uncertainty about possible skin zone effects in DFT tests [Xiang and Kabala, 1997], and therefore the presence or absence of a short-circuit peak is useful to check that a hydraulic dipole field has been properly formed. A streamtube model was used by Sutton et al. [2000] to model such tests, assuming a homogenous anisotropic ($K_r \neq K_z$) aquifer. Initial modelling showed that the t_{peak} (Figure 1-7) at the extraction chamber is linearly related to the anisotropy ratio and also increases with increasing dispersivity. Longitudinal dispersivity was found to be inversely proportional to $t_{arrival}$ (5% peak)/ t_{peak}. Sutton et al. [2000] estimated aquifer parameters in different wells with reasonable precision: K_r varied from 6-9 x 10^{-5} m/s, with low a^2 from 0.5-1.7. This variation may result from aquifer heterogeneity, uncertainty in mean tracer arrival and/or modelling errors. Values of K_r were less than an order of magnitude greater than estimates obtained from flowmeter testing. Differences between values were attributed to different sampling volumes and heterogeneity in the aquifer hydraulic conductivity. DFTTs have also been carried out to identify fracture length, aperture, maximum velocity and matrix dispersivity in fractured rock systems [Sanford et al., 2002]. Although DFTTs have the potential to analyse anisotropy and hydraulic conductivity, a homogenous aquifer is assumed. Anisotropy ratios in DFTs can be significantly affected by background noise and, theoretically, by strongly layered media [Xiang and Kabala, 1997; Zlotnik et al., 2001]. Therefore the effect of discrete variations in aquifer permeability on DFTTs requires investigation to deduce the extent to which this affects tests or can be identified by them. It is also useful to

investigate the potential to use reactive tracers with DFTTs, to obtain data to resolve a full suite of reactive and hydraulic aquifer properties from a single test.

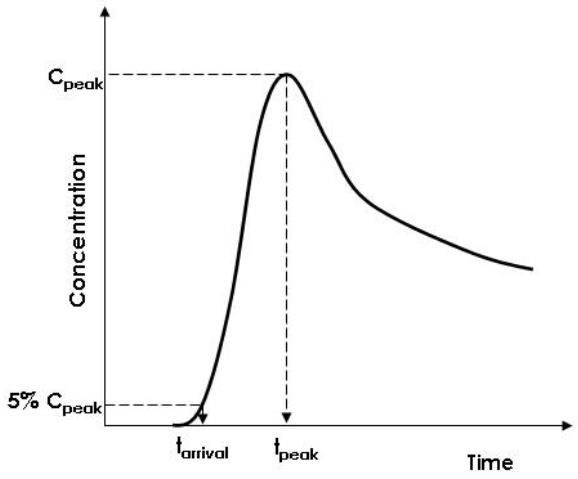

Figure 1-7: Diagram showing derivation of t_{peak} and $t_{arrival}$ from DFTT breakthrough curve

1.1.5. **Push–pull tests**

In a single well pulse test, or PPT, tracer-tagged water is injected from a chamber between two packers at a constant rate and may be followed by clean water for a period to displace the tracer from the near well environment. After a "rest" period to allow biological or chemical reactions to occur (when such tracers are used) water is pumped out at the same rate, and tracer concentration in the extracted water is measured over time (Figure 1-8). These tests do not measure hydraulic conductivity, but dispersivity and chemical parameters can be estimated from the data [Pickens et al., 1981]. Use of these tests to estimate dispersivity has been limited, due to potential problems with scaling and unknown movement of tracer around the well [Domenico and Schwartz, 1990]. However, many experiments have been undertaken to investigate aquifer reactive properties, especially biodegradation. Istok et al. [1997] developed current interest in PPTs with experiments that assessed aerobic degradation, denitrification, sulphate reduction and methanogenesis. Later studies have investigated biostimulation of aerobic bioremediation [Kim et al., 2004; Azizian et al., 2005; Kim et al., 2005; Pitterle et al., 2005; Azizian et al., 2007] and iron and manganese reduction [Kneeshaw et al., 2007; Ko and Ji, 2007; Mailloux et al., 2007]. Biodegradation has been analysed assuming zero- or first-order kinetics, with the

exception of one study, which assumed Monod kinetics [Vandenbohede et al., 2008]. There have also been studies investigating organic sorption [Istok et al., 1999; Hageman et al., 2003], ionic sorption [Pickens et al., 1981; Schroth et al., 2001] and partitioning of non aqueous phase liquids [Schroth et al., 1997; Davis et al., 2002; Istok et al., 2002; Davis et al., 2005]. Although the signal of solutes exhibiting low retardation may be hard to distinguish from conservative tracer signal in sorption experiments [Schroth et al., 2001], the large number of successful studies conducted suggest PPTs are suitable for measuring aquifer reactive properties and investigating the value of tracer mixtures. However, there have been few studies on the flow of water and shape of the tracer plume around the well, despite long-standing concerns about the tests [Domenico and Schwartz, 1990]. Almost all studies assume cylindrical flow. Schroth and Istok [2005] mathematically compared cylindrical and spherical flow solutions. They concluded that when hydraulic conductivity anisotropy is over two and the thickness of the aquifer is small compared with the size of the plume, simulated results are closer to the cylindrical than the spherical flow solution. Conversely, Matthias [2010] considered a tracer plume to form an ellipsoid shape under conditions of anisotropic permeability. However, it was concluded that the effect of realistic heterogeneity on plume radius was unclear. To date direct observation of PPT tracer plume geometry has not been studied. Reasonable data fits have been obtained using literature assumptions [Istok et al., 2002], but complete tracer mass recovery during the extraction phase would be expected. In some studies, mass recovery is as low as 50% for the conservative tracer [Kim et al., 2004; Azizian et al., 2007]. This may be due to loss of tracer from the zone of pumping influence by background hydraulic gradients during rest periods between injection and extraction test phases. These uncertainties must be examined to identify if push-pull tests can reliably measure aquifer reactive properties.

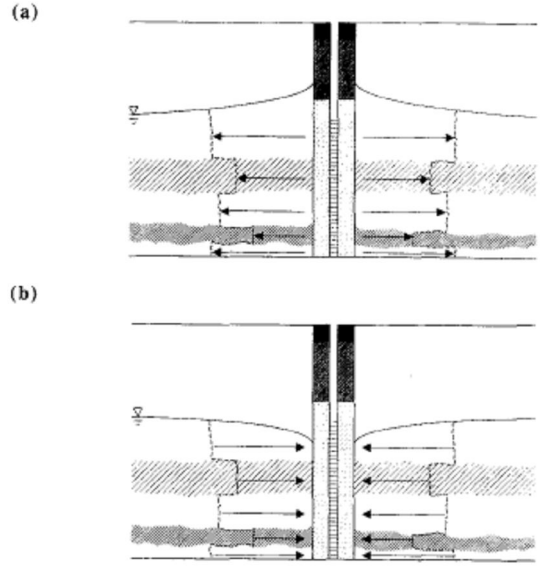

Figure 1-8: Schematic diagram of a push pull test near the water table, taken from Istok et al [1997]; (a) injection phase; (b) extraction phase.

1.2. **Objectives**

The aim of this study was to test the hypothesis that it is possible, using a minimal number of single well forced gradient tracer tests (DFTTs and PPTs), to accurately quantify aquifer parameters that govern contaminant migration, for use in monitored natural attenuation and remediation schemes. The experimental research described was undertaken in a series of laboratory studies, with the following objectives:

1. To investigate the behaviour of conservative tracers in DFTTs and PPTs in an artificial aquifer model, with focus on the area of sampling and tracer pathway during tests.

2. To investigate the effect of mesoscale layered permeability common in aquifers on DFTTs and PPTs: whether this significantly affects the ability of these tests to measure aquifer parameters and if DFTTs and PPTs can be used to identify the presence of this physical heterogeneity.

3. To investigate the performance of different inorganic and organic compounds as potential reactive tracers (separately and in mixtures) for use in single well forced gradient tracer tests to measure aquifer properties at the field-scale

1.3. **Scope of work**

Ultraviolet (UV) imaging tests were undertaken to investigate Objectives 1 and 2. Scaled down single well forced gradient tracer tests were performed in a low profile box filled with glass silica beads. This is understood to be the first time that comprehensive UV imaging of single well forced gradient tracer tests has been performed. This technique allowed the effect of heterogeneity in hydraulic conductivity on the shape and extent of tracer plumes and extraction breakthrough curves to be directly observed. The behaviour of the tracer plumes was also compared with theoretical predictions and assumptions common in the literature. The experimental results were interpreted with HydroGeoSphere© [Therrien et al., 2005], a fate and transport model developed by the University of Waterloo, Canada, in finite difference mode. Model predictions have been shown to correspond well to previous analytical solutions for tracer tests in push-pull and horizontal dipole flow systems [Hoopes and Harleman, 1967; Gelhar and Collins, 1971; Wilson and Miller, 1978; Zheng, 1990].

Objective 3 was investigated using dynamic column and static batch experiments. This allowed the behaviour of tracers to be observed, without the complex flow-field created by the DFTTs or PPTs. These tests were carried out using Permo-Triassic sand, as a model aquifer medium. Tracer performance was investigated individually and in mixtures in column and batch experiments. The signal of reactive tracers in single well forced gradient tests was simulated with HydroGeoSphere© using data derived from the experiments.

A detailed investigation using column tests was conducted with fluorescein and bromide, to compare the suitability of dyes and inorganic anions as conservative tracers. Other anions were also studied to evaluate the most suitable conservative tracer for future tests. Calcium, magnesium and sodium were investigated as potential ionic sorption tracers to investigate cation exchange reactions. These 1-D tests were interpreted using PHREEQC [USGS, 2008] to understand the tracer behaviour in mixtures, and in particular the potential to estimate aquifer CEC using different cations.

Ni-EDTA^{2-} was investigated as a potential anionic tracer for use in acidic and EDTA ($C_{10}H_{16}N_2O_8$)/complex ligand-polluted environments, to predict the migration of Zn, Ca, Co^{2+}, Cu, Pb and other metal cations that form a similar structure with EDTA [Nowack and Sigg, 1996]. EDTA is a highly nucleophilic anthropogenic ligand used in industry (see Figure 1-9). It forms stable complexes with metals, altering their transport behaviour in aquifers. The transport of these metals can be simulated by using EDTA complexed with more stable metals as an anionic tracer. Ni has been shown in previous experiments to form more stable bonds with EDTA than Pb, Zn and Cu [Davis et al., 2000; Hess et al., 2002]. The suitability of this tracer to estimate the retardation of the EDTA complex in neutral pH conditions was investigated.

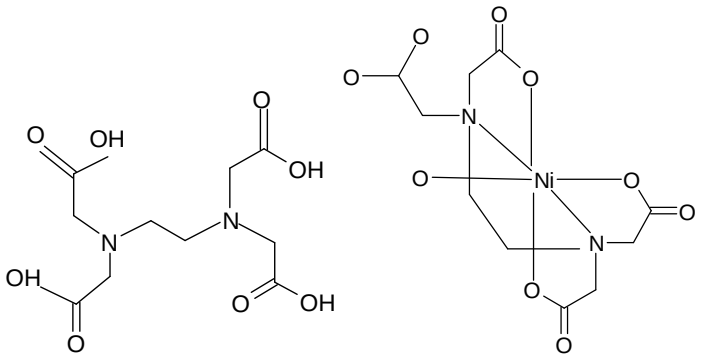

(a) (b)

Figure 1-9: (a) EDTA structure and (b) EDTA complexed with Ni [Nowack and Sigg, 1996]

Acetate ($CH_3CO_2^-$) was chosen as a reactive tracer to assess the biodegradation potential of an aquifer for simple organic compounds. It is readily biodegradable and

is a natural biodegradation product in many contaminant plumes [Thornton et al., 2001; Devlin et al., 2002; Wilson et al., 2004]. It has been used as a carbon source to investigate biodegradation in aerobic, sulphate reducing and fermentation studies in the field and laboratory [Huang and Jih, 1997; Kleikemper et al., 2002; Pombo et al., 2005; Watson et al., 2005; Kneeshaw et al., 2007; Rees et al., 2007]. It has also been shown to biodegrade to inorganic end-products under aerobic conditions [Watson, 2004]. Acetate is not significantly adsorbed to aquifer materials by ionic or hydrophobic reactions, allowing an assessment of biodegradation by comparison with a conservative tracer in a mixture. Therefore study of biodegradation of this compound in the Permo-Triassic sand under forced gradient conditions should highlight effects related to biodegradation and conservative transport. This simplicity also makes acetate suitable for tests in DFTTs, where the effect of biodegradation on the tracer breakthrough is unclear.

Trichlorofluoroethene, TCFE, (Cl_2C_2ClF) is a chlorinated organic compound (see Figure 1-10). It is an uncommon organic molecule in industry and the environment, and has the potential to be used as a tracer to estimate organic sorption and fraction of organic carbon in aquifers, over short time periods. Its structural similarity to trichloroethene (TCE) and tetrachloroethene (PCE), two common groundwater contaminants, means it may be useful to estimate the retardation of these contaminants at polluted sites. The properties of TCFE were investigate to determine whether it was a practical tracer for use in field tests and whether its range of response could be easily measured in forced gradient tracer tests.

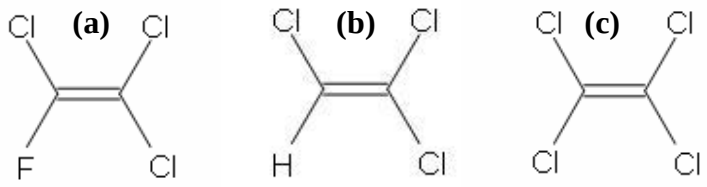

Figure 1-10: (a) TCFE structure; (b) TCE structure; (c) PCE structure

1.4. **Structure of thesis**

This thesis is organised into seven chapters and appendices. This first chapter gives a general introduction to the background and concepts of groundwater tracer techniques, explores the knowledge and methodological gaps in aquifer characterisation, and presents the objectives and scope of this work. The following technical chapters are written as manuscripts intended for submission to peer-review publication. As such, some minor repetition in certain sections is necessarily present. Chapters 2 and 3 cover Objectives 1 and 2, respectively. Chapters 4-6 cover Objective 3, each covering different classes of tracer. Each chapter includes a short literature review. Therefore a comprehensive literature review is not given at the start of this thesis, although some overlap between the introduction background and the individual chapter introductions is expected. The final chapter includes a discussion and synthesis of the results from all chapters, in the context of the thesis objectives, a summary of the main findings and recommended future work. Numerical modelling of reactive tracer single well forced gradient test breakthrough curves is presented, integrating results from the individual research chapters. The appendices contain supplementary information for the thesis; a summary of tests performed in a $4m^3$ artificial aquifer ("sandbox"); a copy of a peer-reviewed conference paper presenting initial findings of UV imaging experiments, which has been accepted for publication in the Groundwater Quality 2010 IAHS Red Book; and DVD-Rs of all experimental data and models.

2. Evaluation of dipole flow tracer tests and push–pull tests in isotropic porous media using UV imaging

Abstract

Vertical dipole flow tracer tests and push–pull tests are single well forced-gradient tracer test methods that can be used to assess aquifer properties for remediation design planning or natural attenuation assessment. The mathematical basis for describing solute transport in tracer plumes resulting from application of these methods is well established, and has generally been validated against observations of dissolved concentration at the laboratory and field scale. However solute transport in such systems has not been directly visualised to compare mathematical theory and breakthrough concentration characteristics to actual solute transport paths. In this work dipole flow tracer and push-pull tracer tests were performed in a low profile box filled with silica glass beads. A fluorescent tracer (fluorescein) was used to deduce the transport paths, which were visualised under ultraviolet light to obtain images. Samples were collected to construct breakthrough concentration histories, which were compared with calibrated tracer concentrations derived from captured images at strategic locations specific to a given test. Datasets were interpreted well by inverse modelling, using HydroGeoSphere©. Tracer cloud migration followed predicted pressure fields and flow lines. Tracer that contributed to peak dipole flow tracer test breakthrough travelled in flow lines close to the well screen, but a significant portion of un-recirculated tracer produced a halo of mass that grew outward from the well over time. Push pull tests were found to sample the porous media further from the well screen than dipole flow tracer tests, but were particularly susceptible to poor mass balance where imperfect packer seals allowed tracer to travel along the well stem during injection. Neither of these phenomena are evident in conventional breakthrough data.

2.1. **Introduction**

Interpretation of forced gradient tracer methods such as dipole flow tracer tests (DFTT) and push-pull tests (PPT) can yield hydraulic and reactive transport properties of an aquifer [Istok et al., 1997; Sutton et al., 2000]. Both tests require only one well, making them more cost-effective at new sites or where previously installed wells may not be suitable for dual-well approaches. A DFTT test involves installing three packers to isolate two sections of well screen. Tracer tagged water followed by tracer-free water is injected in one screen and extracted from the other. The extracted water is then reinjected with periodic sampling to measure the concentration history of the tracer. By recirculating water equal extraction and injection flow rates are guaranteed and there is no effect on estimates of dispersivity (α) or anisotropy. The mathematics of such tests suggest that tracer should move from the injection to extraction chamber following flow lines similar to the magnetic field lines of a bar magnet [Zlotnik and Ledder, 1996; Zlotnik and Zurbuchen, 1998]. In a PPT a volume of tracer tagged water is injected (pushed) into an isolated section of well screen, which may be followed by a slug of tracer free water. Then water is extracted (pulled) from the same screen and sampled to characterise the concentration history of returning tracer. Flow from and to the isolated interval is often conceptualised mathematically as cylindrical in heterogeneous aquifers, with greater migration of tracer in layers with higher hydraulic conductivity [Haggerty et al., 1998; Schroth et al., 2001]. Schroth and Istok [2005] considered the differences between a cylindrical and spherical flow solution, when modelling a simulated tracer breakthrough. Spherical plumes were predicted in isotropic conditions; however they concluded that if there was any significant anisotropy ($a^2 > 2$) in an aquifer flow would be cylindrical. There have been PPT tests conducted in bench-scale physical aquifer models [Istok et al., 2002], but under the assumption that flow was cylindrical, the models were wedge-shaped and consequently represented a highly simplified model of tracer migration in the field.

Interpretation of DFTTs and PPTs (and indeed other tracer test approaches) relies mostly on observations of hydraulic head and tracer concentration at wells. Therefore it is not always obvious when a test produces flawed results, or the reason for this. DFTTs were developed from hydraulic tests where the governing equations [Kabala, 1993; Zlotnik and Ledder, 1996] are solved on the basis of hydraulic head observations in the chambers. However the generation of draw-down in the extraction chamber and draw-up in the injection chamber is not conclusive proof that a vertical dipole flow system has been created. Short-circuiting of flow may be occurring, or the chambers may be hydraulically disconnected due to the presence of fractures or varying permeability zones. A dipole flow can only be conclusively demonstrated by releasing a tracer into the flow-field [Sutton et al., 2000]. If tracer first arrival in tests is quicker than expected this may suggest short circuiting of tracer, along the side of the well screen or between the packers and well screen, with incomplete formation of a dipole flow field. However the remaining tracer breakthrough data may still be representative of the aquifer properties. These imaging experiments seek to provide visual calibration to apparent signals that may manifest in concentration breakthrough data, such as early breakthrough in DFTTs which may indicate short circuiting of tracer as explained above. The design of DFTTs or PPTs benefits from a prior understanding of the expected swept volume and direction of tracer flow under a given pumping rate and duration. Poor mass recovery, low breakthrough curve concentrations and inaccurate or poorly understood transport parameters may arise if this is not understood. Also, knowledge of how tracer migrates close to the well would add reliability to estimates of aquifer dispersivity [Domenico and Schwartz, 1990]. These imaging tests, while not designed to evaluate failure mechanisms, provide a means to visually identify if, when, and how a test deviates from ideal in isotropic conditions.

It was decided to use ultraviolet (UV) fluorescent imaging to capture tracer migration in tests. Fluorescent imaging is less susceptible to background noise than visible light imaging [Huang et al., 2002]. There are several fluorescent tracers (e.g. rhodamine

WT, sulforhodamine B, pyranine, and fluorescein) that have been evaluated for a range of tracing objectives [Smart and Laidlaw, 1977; Sabatini and Al Austin, 1991; Kasnavia et al., 1999; Ghanem et al., 2003]. For this work, fluorescein was selected due to its large dynamic detection range, low expected sorption to silica beads (as used in this study), low volatility, high solubility, conservative transport nature, strong colour contrast under UV light and ease of quantification [Kasnavia et al., 1999]. UV imaging has previously been used in very small-scale transport experiments to evaluate dispersion in porous media [Gaganis et al., 2005], pore-scale heterogeneity [Corapcioglu and Fedirchuk, 1999], non-aqueous phase liquid partitioning [Jones and Smith, 2005] and biodegradation processes [Huang et al., 2003; Rees et al., 2007]. Larger scale experiments have been used to investigate transverse dispersion [Chiogna et al., 2010] and converging tracer tests [Chao et al., 2000b].

2.2. **Methods**

2.2.1. **Imaging box construction**

A 2-D aquifer box model was constructed from 8 mm thick acrylic, with internal dimensions of 150 cm length x 75 cm height x 2.6 cm depth. Holes were drilled and tapped on the exterior, near the top and bottom of each end wall, to accept brass fittings and polymer tubes, which provided water overflow and hydraulic head control. At each end wall, an open chamber (i.e. separated from the porous media) was created to allow rapid hydraulic control. The chambers consisted of a 2.5 cm diameter slotted pipe wrapped in 100 µm stainless steel mesh. A fully penetrating custom-made well screen was inserted midway between the end chambers, and spanned the full depth of the box. Blank uPVC 1 inch well screens were obtained from Marton Geotechnical Services and slotted manually with a thin kerf saw to give 0.27 mm approx. wide slots with an open area of around 7 % in the slotted segments. This is similar to the open area in larger, commercially available slotted well screens. Slots were cut to leave two strips of uncut material that, when inserted into the box, were adjacent to the front and back acrylic walls. The non-slotted sides of the well

screen were filed down flat to maximise contact with the box walls. Once all fittings and well screen were installed, the box was wet packed with 300–355 μm silica glass beads (Potters Ballotini Ltd.) to a total depth of 72 cm, after washing with dilute nitric acid and multiple deionised water rinses to remove any soda residue. The water level was raised to produce 1 cm of standing water above the bead pack. The porosity of the beads was estimated as 0.37, by measuring the mass difference between dry and saturated beads. The box was held stable in a tubular steel frame (Figure 2-1), which rested on a stable laboratory bench in direct connection with a concrete floor. This minimised vibration and other mechanical disturbances.

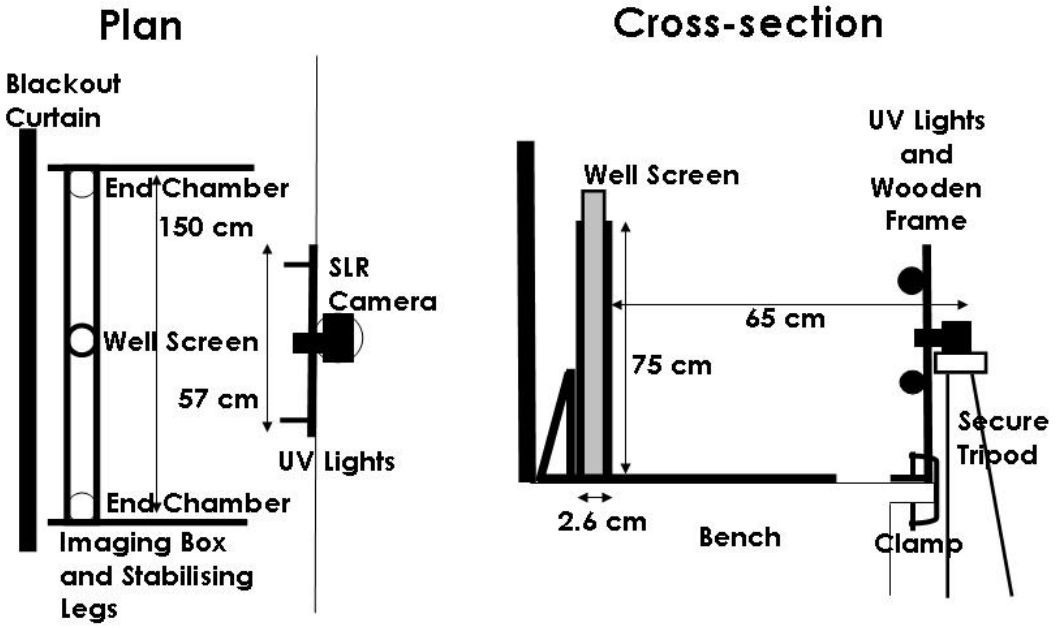

Figure 2-1: Schematic of imaging set-up for experiments. Not to scale

The in-well apparatus was made from alternating uPVC and silica discs mounted on a threaded stainless steel rod. Packers were formed from tightened groupings of the discs, with the silica forming a friction seal against the well screen. This flexible design allows for a range of packer and chamber lengths. 0.3 cm diameter silica tubing was passed through holes in the discs allowing flow of solution. For the PPT the chamber was 3.7 cm and packers 6.7 cm. For DFTTs the chambers were 3.7 cm, middle packer 6.7 cm and end packers 3.0 cm. The apparatus was positioned centrally in the well screen.

2.2.2. **Imaging configuration and calibration**

A Canon EOS 450D digital SLR was used to capture the images. This was placed on a stable tripod focused on the centre of the box, with the back of the camera 65 cm away from the front face of the box (Figure 2-1). This gave a field of view approximately 65 cm x 40 cm. 350 nm UV black lights (57 cm long) were placed horizontally above and below camera (just behind the lens), secured to the bench via a custom-made wooden frame. A black out curtain was placed behind the box to optimise contrast. Experiments were performed in darkness apart from the UV light. The laboratory used had no windows and a blacked out door.

The imaging experiments were designed to observe tracer transport and quantify concentrations in various regions of the flow system. Therefore images needed to be calibrated to aqueous concentration to permit comparison between images and temporal concentration histories. A calibration box 25 cm x 25 cm x 2.6 cm was constructed from the same acrylic used for the box model. Fluorescein solutions were evenly distributed in the box. To make up stock solutions a 1 litre volume of 100 mg/l fluorescein was prepared using ultra high quality (UHQ) water. Sodium hydroxide (NaOH) was added to aid dissolution, and the solution was titrated to neutral pH. It was intended to keep the experiments neutral as fluorescein fluorescence varies with pH [Sabatini and Al Austin, 1991]. Calibration standards of 2.5, 5, 10, 20 and 40 mg/l were prepared from the stock solution. Each standard was introduced into the bead-filled calibration box such that the concentration was evenly distributed. Despite repeated washing of the glass silica beads, the pH of water in contact with the glass beads drifted to pH 10. However, since both calibration and experiments were conducted using the same beads any pH rise and increase in fluorescence in images is accounted for by the calibration. Good correspondence was observed in initial tests between image concentrations and predicted values and concentrations did not exceed the expected maximum value.

Nineteen different camera configurations were tested to obtain the best calibration for images (see Appendix A). This range of calibrations and imaging procedure was based upon previous work by Bridge [2007] and North [2008]. The camera settings that provided the best calibration are shown in Table 2-1**,** with the calibration for this set-up shown in Figure 2-2. New calibrations were performed for each stock solution made. Also, because incident UV lighting was used, it was possible that image intensity might vary within the area captured by the camera (greater between the two UV light reflections than outside them, different again where the light bars reflected), see Figure 2-3. To account for this, image intensity was calculated separately for different parts of the picture. Some calibration standards were exposed to UV light for extended periods, to determine if degradation of fluorescence might occur during the experiments: none was observed. Images were processed for green light intensity on Image J, a public domain programme (http://rsbweb.nih.gov/ij/). From the second test onwards the images were normalised by the green light intensity of a constant reflector.

Table 2-1: Parameters and settings of SLR camera used in experiments

Parameters	Camera Settings
Angle	24mm
Flash	Off
White Balance	Custom
Focal Length	f8
Shutter Speed	1.3 seconds
ISO	100

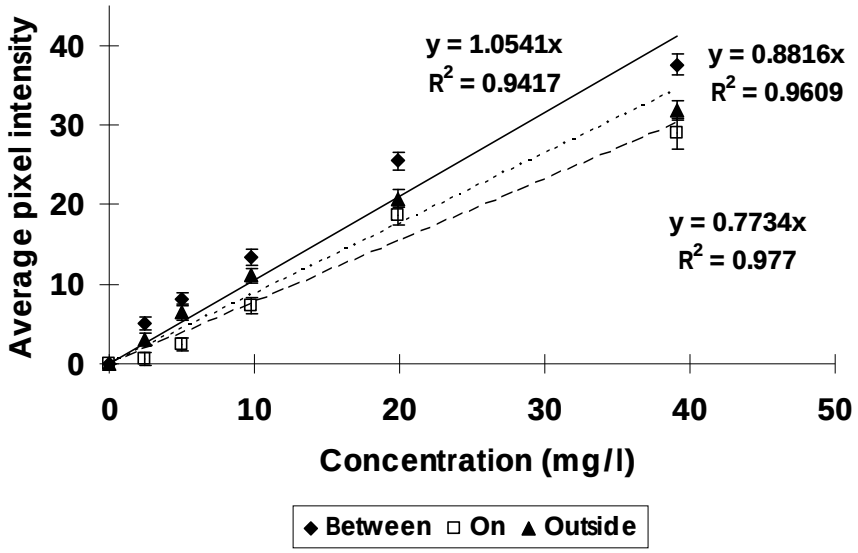

Figure 2-2: Initial image calibration plot for different places in the calibration box for the camera settings in Table 2-1. Between, On and Outside refer to the position of the sampled pixels relative to the light reflections of the two UV lights.

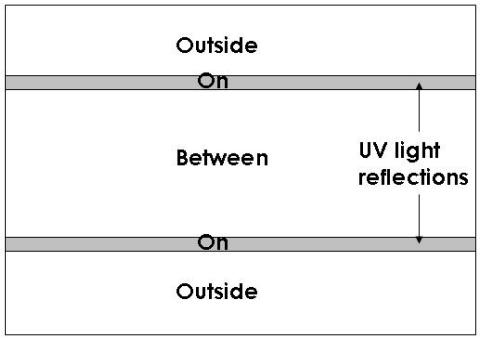

Figure 2-3: Regions on an image taken by digital SLR in the experimental set-up position (Figure 2-1) relative to UV light reflections. The relationship between green light intensity and tracer concentration in these regions has been calibrated separately (see Figure 2-2).

Due to the pH rise in solutions in contact with the beads, fluorescein fluorescence was greater after the tracer had passed through the box than before. Therefore the fluorescein stock solutions could not be used to calibrate tracer breakthrough curve concentrations in aqueous samples. It was decided to use Br/Cl as a co-tracer to determine breakthrough curve concentrations as values should not be affected by changes in pH.

UV light intensity is reduced due to quenching by the water, beads and acrylic. This affects light as it travels from the UV lights to the fluorescein molecule. The UV light that is emitted by the fluorescing molecule is also quenched as it travels back to the

camera. This quenching causes the imaging to have an effective imaging penetration depth, which was estimated using the Beer-Lambert law (see Appendix A). The absorbance of UV light of the fluorescein stock solutions was measured on a Biochrom® S2100 diode array spectrophotometer. The quenching effect of the acrylic and beads could not be estimated using the instrument. For the beads this may have been due to them having a high refractance, while a small sample size excluded measurement of the acrylic. At 2.5 mg/l fluorescein the mean imaging depth was estimated to be 7 mm. This decreases for higher concentrations so that for 40 mg/l all imaging is estimated to be from the closest mm. However experimental results suggest a greater effective imaging depth. A test was performed where 40mg/l fluorescein was pumped into the centre of the calibration box, saturated with water at a slow rate (see Appendix A). Images were taken and it was assumed that the plume formed was spherical. The intensity of the captured images suggested that the effective penetration depth of imaging was approximately 7 mm. Therefore if tracer is concentrated beyond this depth then fluorescein concentrations may be underestimated. Conversely, if tracer is predominantly towards the front 7 mm of the box then fluorescein concentrations may be overestimated. Light is seen at the back of the box during tests, indicating that the beads do not adsorb all light. The imaging depth was considered suitable as the box could not be made thinner, good image calibrations were obtained and modelling could be performed in three dimensions.

2.2.3. **Test set – up**

DFTTs and PPTs were carried out in the box, as shown in Figure 2-4. Before the first test, and between each subsequent one, the box was flushed until there was no fluorescence in images taken. Stock solutions were made up to 40 mg/l fluorescein. For the first test the stock solution was made up to approximately 80 mg/l Cl, but for future tests this was changed to approximately 300 mg/l Br to ensure more reliable breakthrough curve concentrations. During tests the box was topped up with deionised water and water was released through the overflows to ensure a constant water table.

For DFTTs the flow system was first established by pumping deionised water, using an Istmatec ISM832A pump and 1.42 mm bore solvent resistant PVC tubing, into the injection chamber and out of the extraction chamber at approximately 5.4 ml/min for at least 10 minutes. The first test (DFTT1) was performed with injection into the bottom chamber and extraction from the top chamber. In the second test (DFTT2) the chambers were reversed. The DFTTs were performed in recirculating mode to ensure equal injection and extraction flow rates. For conservative tracers whether the tracer is recirculated or not has no effect on parameters obtained [Sutton et al., 2000]. The plumbing system was designed as a closed circuit, which had to be broken during tracer injection (see Figure 2-4). During tracer injection water was pumped into the injection chamber at 5.4 ml/min and out of the extraction chamber at 6 ml/min for 15 minutes. During this time flow was not allowed to recirculate back to the reservoir because tracer-free returning water would dilute the tracer stock (valve A closed, valves B and C open). Rather, tracer was drawn from the stock reservoir and extracted water was directed to the extraction reservoir. After tracer injection, the closed circuit was reinstated (valve A open, valves B and C closed). The difference between injection and extraction rates in non-recirculating mode may be due to small differences in hydraulic head between the chambers, or slight variation in the bore of the pump tubing. To collect samples valve A was temporarily closed and valves B and C opened for approximately 1 minute. The sample was collected in a vial over 30 seconds after 15 seconds of purging. Solution collected in the extraction reservoir during tracer injection and purging before sample collection was injected into the box during this period to minimise mass loss caused by sample collection. Images and aqueous samples were taken more rapidly at the start of the test to capture breakthrough, every 3 or 5 minutes. This was reduced to 10 minutes after 90 minutes and to 20 minutes after 160 minutes.

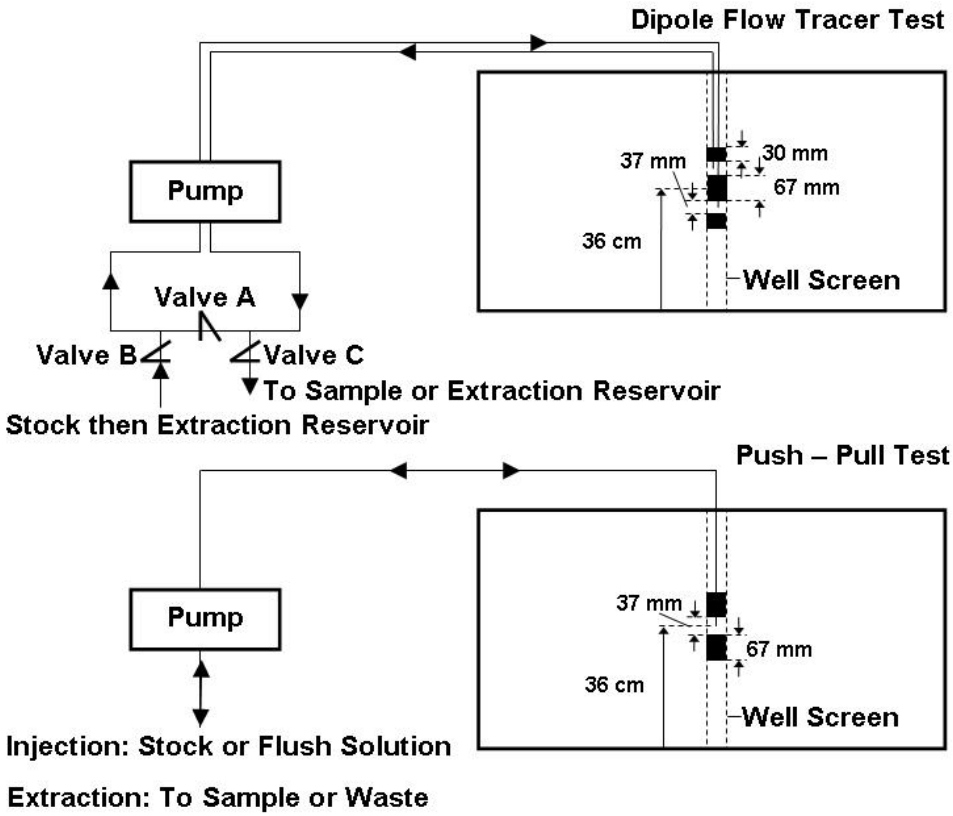

Figure 2-4: Diagram of test set-up. The position of packers (filled areas) and chambers (open areas between packers) in the well screen is shown. The DFTT shown is set up for injection in the bottom chamber and extraction in the top chamber.

For the PPT tracer was injected at 3 ml/min for 80 minutes. Then deionised water was injected at the same rate for 40 minutes as a flush solution, so the tracer migrated away from the well chamber. Images were taken every 5 minutes during the injection phase. During the extraction phase water was pumped out at 3 ml/min for 4 hours. Aqueous samples and images were collected every 5 minutes, reducing to 10 minutes after 2 hours and to 20 minutes after 3 hours.

Br and Cl were analysed on a Dionex DX-120 Ion Chromatograph. A RFIC™ Ionpac® A514A 4 x 250 mm analytical column was used for anion analysis with an eluent of 8 mM Na_2CO_3 and 1mM $NaHCO_3$. Samples were diluted to the calibration range of the instrument. The lower reliable detection limit with a 10 µl sample loop was 0.6 mg/l

for Br and 0.4 mg/l for Cl. Analytical error was ± 2 % for anions. Samples were stored in a -10 ºC refrigerator until analysed.

2.3. **Results**

2.3.1. **Dipole flow tracer tests**

2.3.1.1. **Breakthrough curves**

For the DFTTs time was normalised to the characteristic time (t_c) of tracer breakthrough, after Sutton et al [2000]. This is the time of travel between the closest edges of the injection and extraction chamber, assuming characteristic pore scale velocity on a chamber face, i.e. when flow is only along the side of the well screen, not through the bead pack. For these tests t_c was modified to assume 2-D radial flow from the well, rather than 3-D, given the configuration of the aquifer box model, using:

$$t_c = \frac{16\theta r_w \Delta(L-\Delta)}{Q} \tag{2.1}$$

$$t_d = \frac{t}{t_c} \tag{2.2}$$

where Q is the pump flow rate, θ is the effective porosity of the bead pack, r_w is the well radius, Δ is half the chamber length, L is the distance between the centre of the central packer and the centre of the chambers (also known as the shoulder length) and t is time. A test where a peak occurs around 1 or 2 t_d suggests short circuiting of flow around the central packer, with tracer taking the shortest route between chambers along the side of the well screen [Sutton et al., 2000]. Concentration was normalised to stock concentrations for the tests (C/C_0).

Two isotropic medium tracer tests were performed: one with injection in the top chamber and one with injection in the bottom chamber. The tracer breakthrough was consistent for these tests, in terms of main peak position and intensity (Figure 2-5). This suggests that for relatively short chamber spacing (e.g. when DFTTs are used to

gather high resolution information), the chamber tracer is injected into is not important. For longer chamber spacing, the difference in elevation head may affect the performance of a peristaltic pump configured in recirculating mode.

When tracer was injected into the bottom chamber (DFTT1), initial breakthrough is after 2.1 t_d, with a peak concentration at approximately 5.2 t_d. There was one clear peak after a delay. These results demonstrate two things: 1) there was a hydraulic connection between the injection and extraction chamber and 2) there were no significant short circuits between the chambers, either around the packers or in the bead pack near the well. The rise in concentration after 10 t_d indicates recirculation of the main peak, which is expected when tests are conducted in the recirculating mode. For DFTT2, where tracer was injected into the top chamber with extraction from the bottom, a short circuit is evident in the form of a small breakthrough peak at 2.1 t_d. The main tracer peak arrived at 5.2 t_d. This twin peak phenomenon was noted by Sutton et al. [2000], and may indicate leakage around the packers, or the development of a preferred pathway in the bead pack surrounding the well. The short circuit peak may contribute mass to the second peak, and thus may be why the main peak was higher in DFTT2 (C/C_0 = 0.209) than in DFTT1 (C/C_0 = 0.169). If tracer was not recirculated the peaks of both tests would be expected to be similar. The difficulty in deducing a mechanism that explains premature tracer breakthrough was a key reason prompting the development of this imaging method.

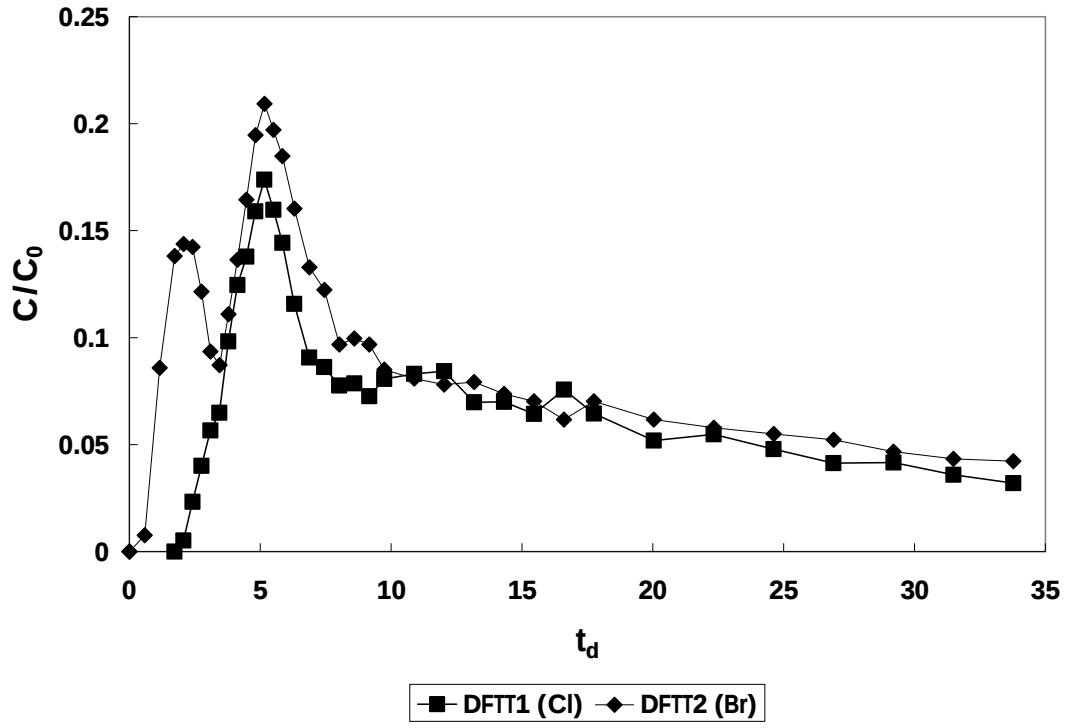

Figure 2-5: DFTT breakthrough curves. Concentration normalised against stock concentration is plotted against dimensionless time. Note the similar time and concentration of the main peaks.

2.3.1.2. **Imaging**

The injected tracer formed a plume according to the hydraulic head field and tracer flow lines (Figure 2-6). The plume centred on the injection chamber, as shown by image mosaics in Figure 2-7 and Figure 2-8. All images are presented in false colour. Concentration increases with the colour sequence black/ dark blue/ light blue/ green/ yellow/ orange/ red/ white. Red and white represents concentrations close to input concentration. At early times the plume formed in both DFTT1 and DFTT2 develops evenly in all directions. The halo-shaped plume formed from non-recirculated tracer becomes more elliptical towards the top well chamber, in response to the lower hydraulic head induced by extraction from this chamber. Initial tracer breakthrough is conveyed along the shorter flow lines close to the well, which are then recirculated and form the secondary fainter and wider tracer halo most clearly evident in the third picture in Figure 2-7, with a clear gap between it and the outer tracer halo. The outer halo always represents the non-recirculated tracer fraction and is the main contributor to the primary breakthrough peak at the extraction chamber (Figure 2-5). In the tail of

the breakthrough curve most of the concentration is contributed by recirculated tracer mass. As more mass is recirculated the faint recirculating halos merge to form a low concentration centre of the plume, evident in the last three images in each mosaic.

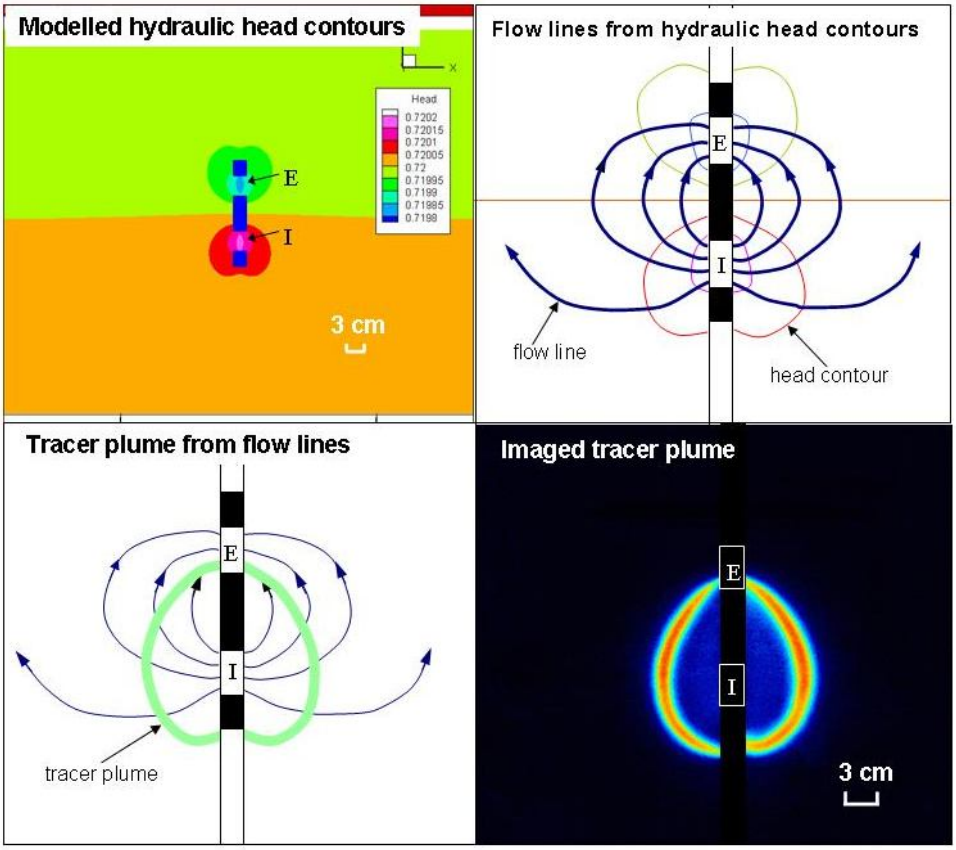

Figure 2-6: Diagram showing relationship between hydraulic head contours, tracer flow lines and tracer plume in a DFTT. The diagram is for a t_d of 5.79. I = injection chamber, E = extraction chamber. Hydraulic head contours estimated with HydroGeoSphere© (see modelling section).

The asymmetry in the DFTT1 tracer plume at later time may be due to a very small head gradient that was present across the box, with flow from left to right, induced by the overflow ports on either end of the box being at slightly different levels. This asymmetry was not observed in DFTT2, which suggests that it was not caused by heterogeneity in the bead pack. It is also noteworthy that the short circuit peak observed in the DFTT2 concentration history was not detected in any images. This suggests that the short circuit peak was due to flow from leakage around the packers and/or very near the well.

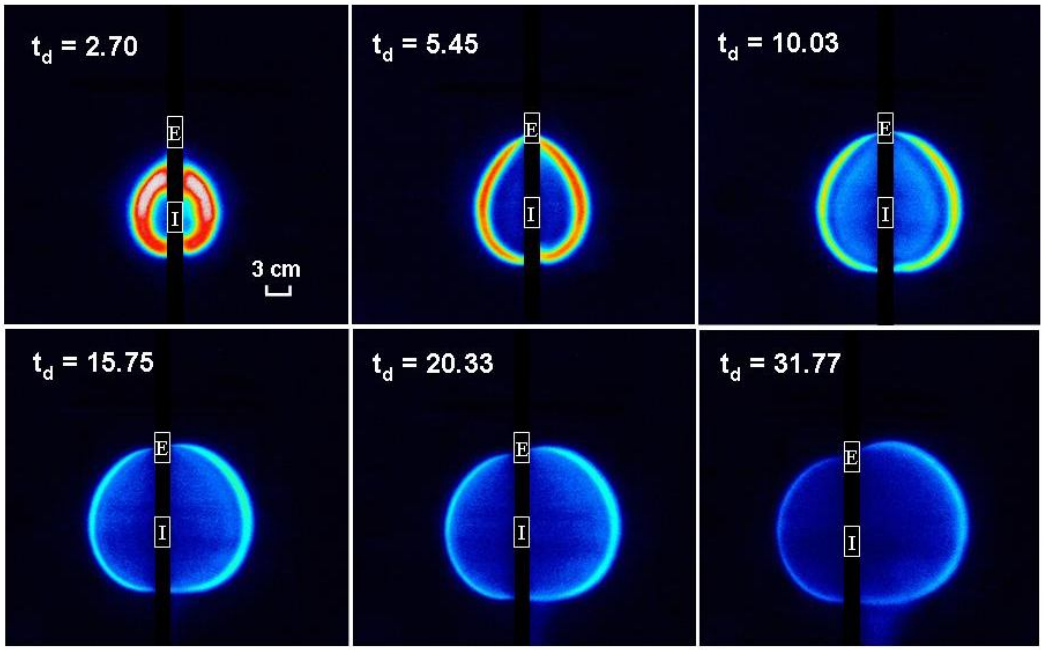

Figure 2-7: Image mosaic of selected times from DFTT1. I = injection chamber, E= extraction chamber. See text for further discussion. A vertical black bar is added to the images to improve clarity and show the position of the well screen.

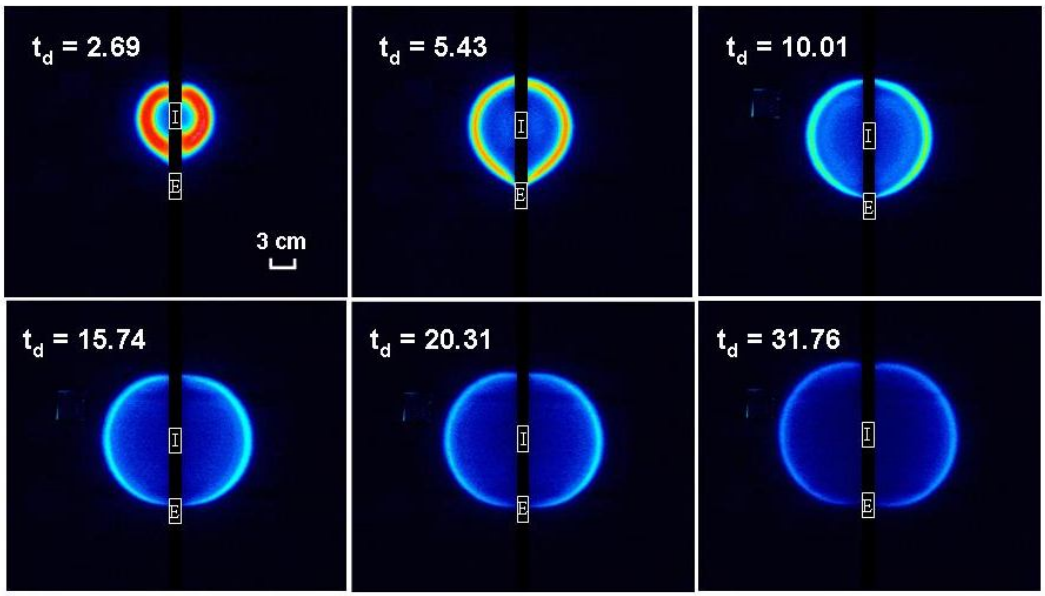

Figure 2-8: Image mosaic of selected times from DFTT3. I = injection chamber, E= extraction chamber. See text for further discussion

Image intensities at points of interest were measured over an area of approximately 2000 pixels (equal to dimensions of 0.9 cm x 0.9 cm), centred on the point of interest. To investigate tracer injection a point was chosen 2 cm from the well screen at the centre of the injection chamber (point A in Figure 2-9). This point avoided any near well variation and allowed a 2000 pixel sample without sampling the well screen.

Tracer concentration was measured to the left and right of the well to test repeatability. The results were similar, suggesting symmetrical injection of tracer (Figure 2-10). Smooth peaks are evident at 2.3 t_d in each test. The standard deviation was up to a half the measured value on the falling and rising limbs in places. This is due to the steep rise in tracer concentration over the short distance covered by the area of interest, suggesting a low dispersivity. Secondary peaks occur at 8.84 and 7.55 t_d in DFTT1 and DFTT2, respectively. These represent the recirculation of the main extraction peak. Average concentrations do not exceed a C/C_0 of 1. This shows that tracer calibrations are valid and account for increases in fluorescein fluorescence due to pH change. To analyse extraction concentrations imaging points B, C and D were chosen (see Figure 2-9). This helped identify which flow paths contribute to the tracer breakthrough curve at a given time. It was found that little or no tracer reached point D (results not shown). A point was also chosen at E (Figure 2-9) to investigate the contribution to the breakthrough curve of tracer that travelled close to the well. The localised image processing analysis focussed on the extraction well during DFTT1 showed that peaks had lower intensity and arrived later on the left hand side of the well compared with the right. This correlates with the image mosaic of DFTT1 (Figure 2-7), where the plume increases in size faster on the right hand side. In contrast there is good symmetry in DFTT2 (not shown), with only a slight bias of tracer flow towards the right hand side of the box at late times. This test was done in the same position in the well as DFTT1. For both tests imaging point E had a similar peak breakthrough time to the extraction well breakthrough curve and has the highest peak concentration of the imaged points. This suggests movement of tracer close to the well screen. Peaks for imaging points B and C were consecutively later, suggesting movement of tracer on longer flow lines, further out from the well screen. These flow lines contribute to the tail in the extraction well breakthrough curve. Tails to the imaging point peaks are long suggesting contribution from recirculated mass.

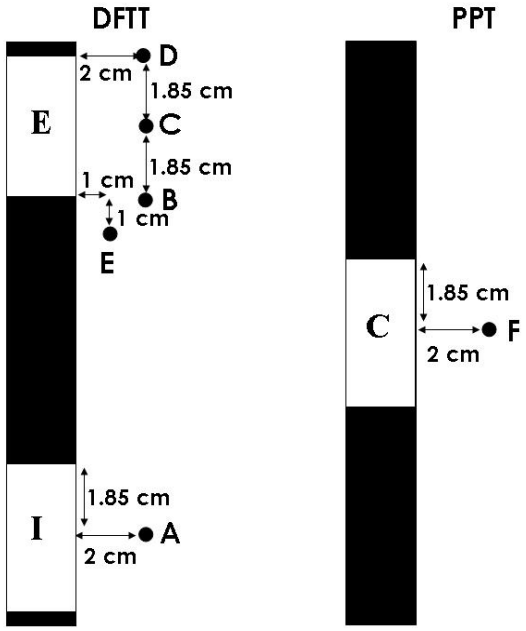

Figure 2-9: Imaging point locations for tests analysed relative to the well chamber. Points are analysed on the left and right hand side of the well screen. For the DFTT with injection in the top chamber the imaging point locations are flipped around the centre of the middle packer.

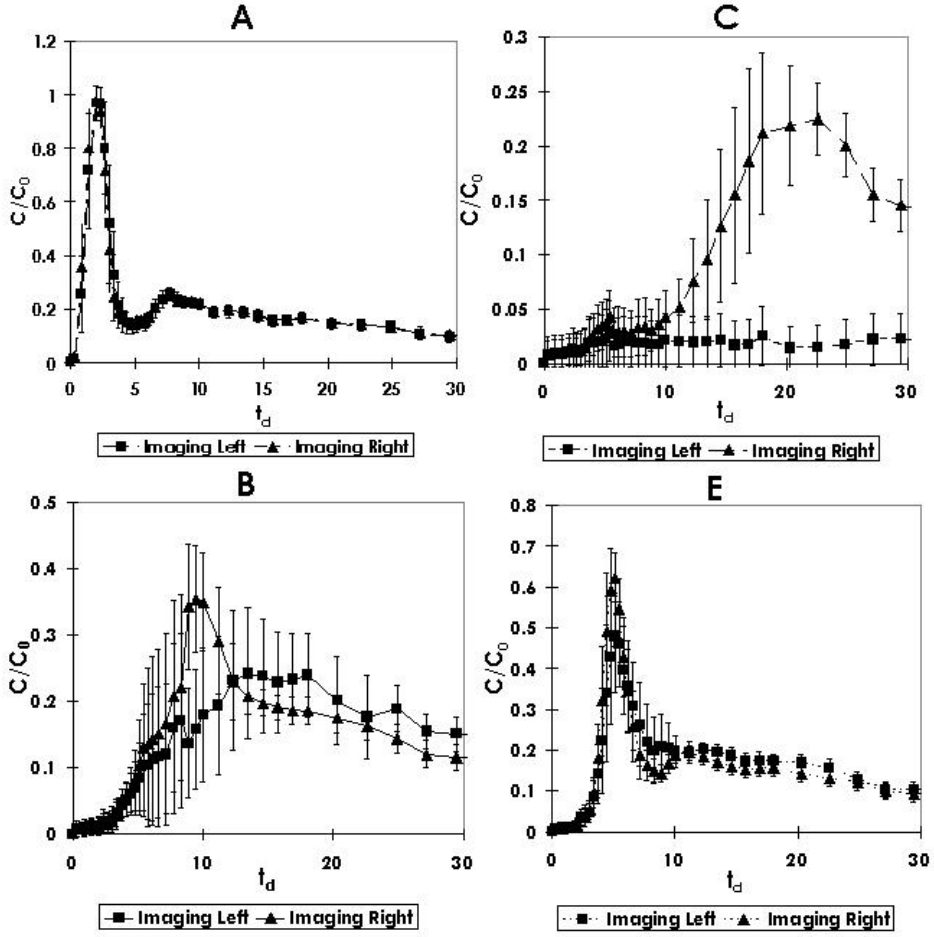

Figure 2-10: Imaging point breakthrough curves for DFTT1. See Figure 2-9 for location of the points. Large error bars reflect sharp concentration gradients.

The peak concentration at the imaging points is higher than that observed in the extraction well breakthrough curves (Figure 2-5). This is because the imaging points directly measure the high concentration tracer halo, while the concentration at the extraction chamber is an average of all extracted water. Lower peak concentrations indicate that tracer has travelled further in the beads, assuming constant dispersion.

2.3.1.3. **Tracer mass**

A comparison was made between tracer mass history calculated from aqueous samples and that obtained from imaging analysis. Tracer mass was normalised to the known total injected mass to directly compare the mass of fluorescein and Br or Cl. Mass loss from sampling was estimated from aqueous concentrations of Br or Cl, assuming that each sample took 30 seconds to collect. Mass in the box was calculated by measuring the intensity over an area covering the tracer plume and estimating the volume of water in the field of view. The entire image was not used to calculate mass as signal in the background noise led to an overestimation. There is good correspondence between the mass calculated using the aqueous samples and imaging for DFTT1 and 2 (Figure 2-11). This suggests that the tracer concentration in the front 0.7 cm of the box, where the imaging is biased towards, is representative of the concentration across the box. The small mass loss due to the aqueous sampling is not apparent in the mass estimated with the images, suggesting that the decrease in mass due to this process is less than the error in measurement. Also, the absence of a significant decrease in mass in the images shows that most mass is present in the bead pack within the area captured by images.

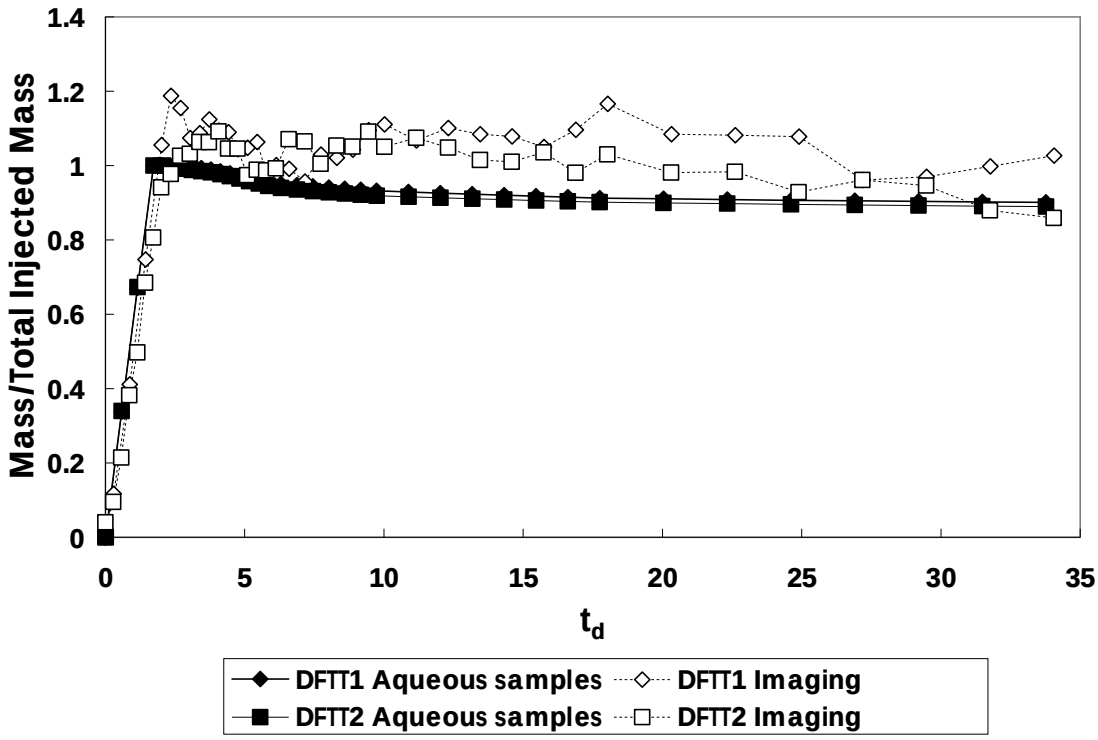

Figure 2-11: Total mass of fluorescein tracer in the box versus dimensionless time. Mass was calculated separately from aqueous samples and imaging analysis

2.3.2. **Push-pull test**

2.3.2.1. **Breakthrough curve**

Time was normalised in the PPT injection phase by dividing the water volume injected up to the observed time (V) by the total volume injected over the entire phase (V_i). This assumes a constant flow rate. Time was normalised for the PPT extraction phase by dividing the total volume extracted at the observed time (V_e) by V_i. The peak of the extraction breakthrough was seen at 0.6 V_e/V_i and the majority of mass had been extracted by 1.5 V_e/V_i. The breakthrough peak from 0.4 to 0.7 V_e/V_i has a broad apex close to a C/C_0 of 1 and steep rising and falling limbs suggesting low dispersion of the tracer.

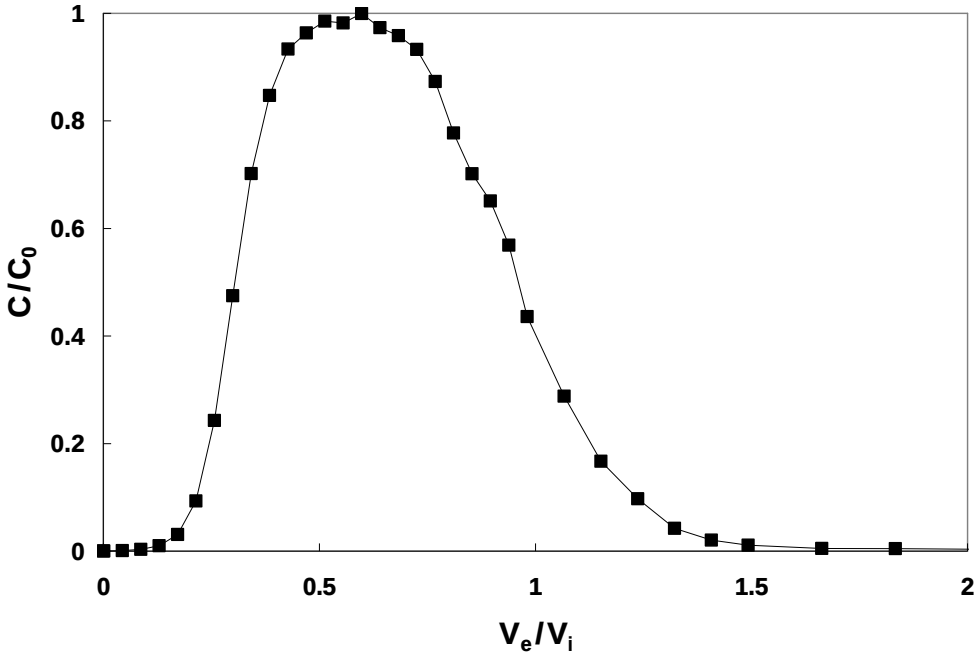

Figure 2-12: Tracer breakthrough curve of Br concentration for PPT

2.3.2.2. **Imaging**

The tracer plume formed in the PPT was consistent with the hydraulic head field and flow lines (see Figure 2-13). Tracer moved out from the chamber during the injection period equally in all directions so that by the end of the period a thick, near circular halo, was evident (Figure 2-14). This shows that water flow was equal in all directions, away from the area of high pressure induced by injection. The halo was

slightly thicker towards the top. This may be an artefact of the test boundary conditions, as the base of the box is a no flow boundary, while water is extracted by overflows at the top.

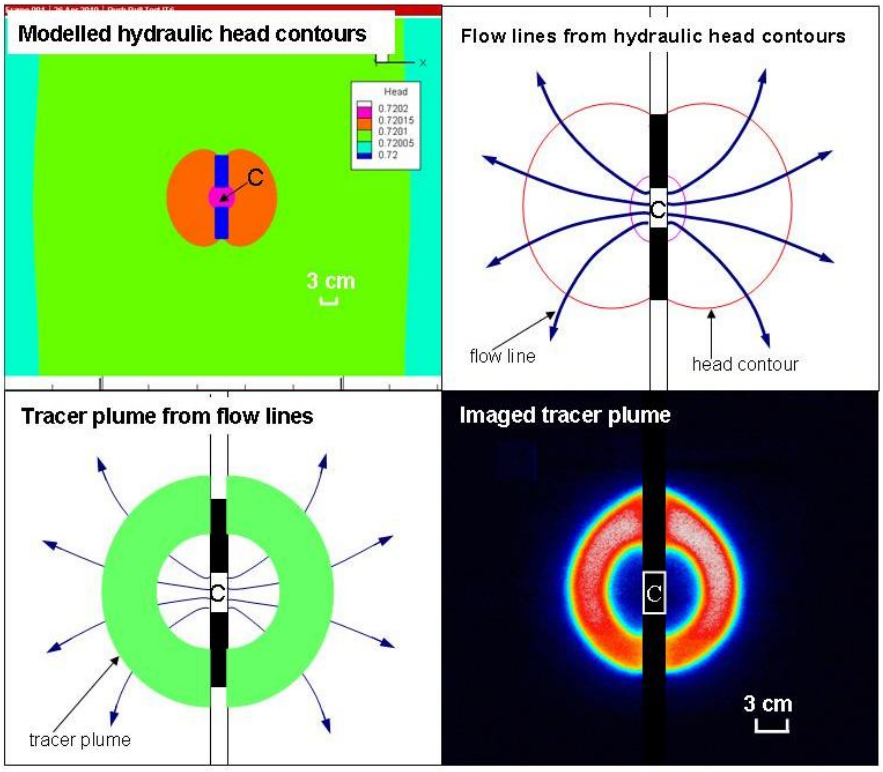

Figure 2-13: Diagram showing relationship between hydraulic head contours, tracer flow lines and tracer plume for a PPT. The diagram illustrates the end of the injection period. C = well chamber. Hydraulic head contours estimated with HydroGeoSphere© (see modelling section).

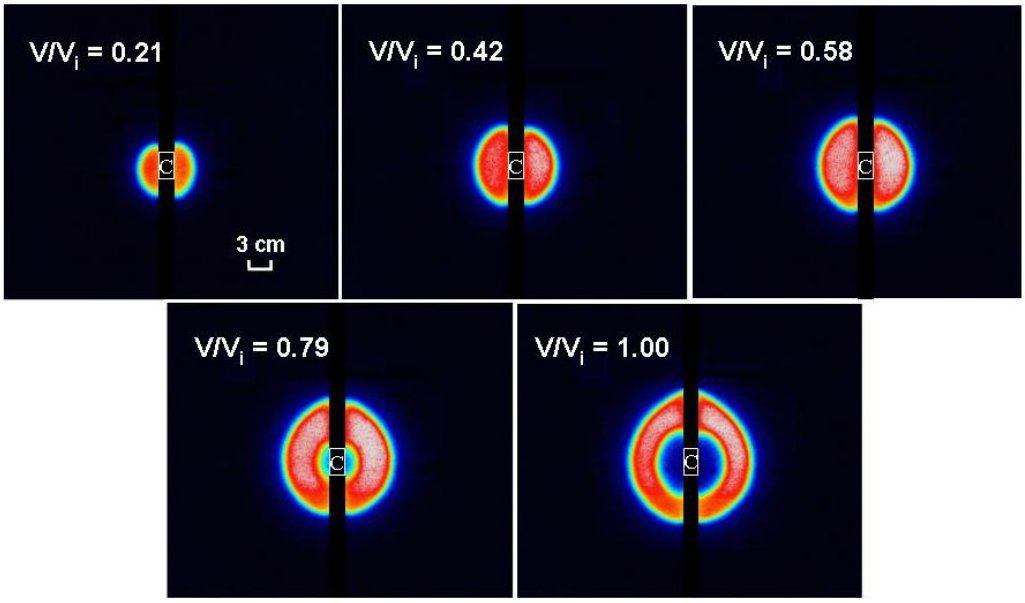

Figure 2-14: Image mosaic of selected times from the injection phase of the PPT. C = chamber, for further discussion see text.

Tracer was removed evenly from all directions, during most of the extraction phase (see Figure 2-15). At 0.77 and 1.07 V_e/V_i more tracer is left on the right side of the box, due possibly to small variations in porosity or a slight head gradient (as discussed earlier for DFTT1). At 1.24 V_e/V_i most tracer mass has been removed apart from a small amount visible as faint vertical tendrils near the well. A very small amount of tracer may have migrated to the open well segments or stagnant zones around the packers during the injection period, which is then slowly pumped back. Leakage around packers would increase this phenomenon and cause a poor mass balance.

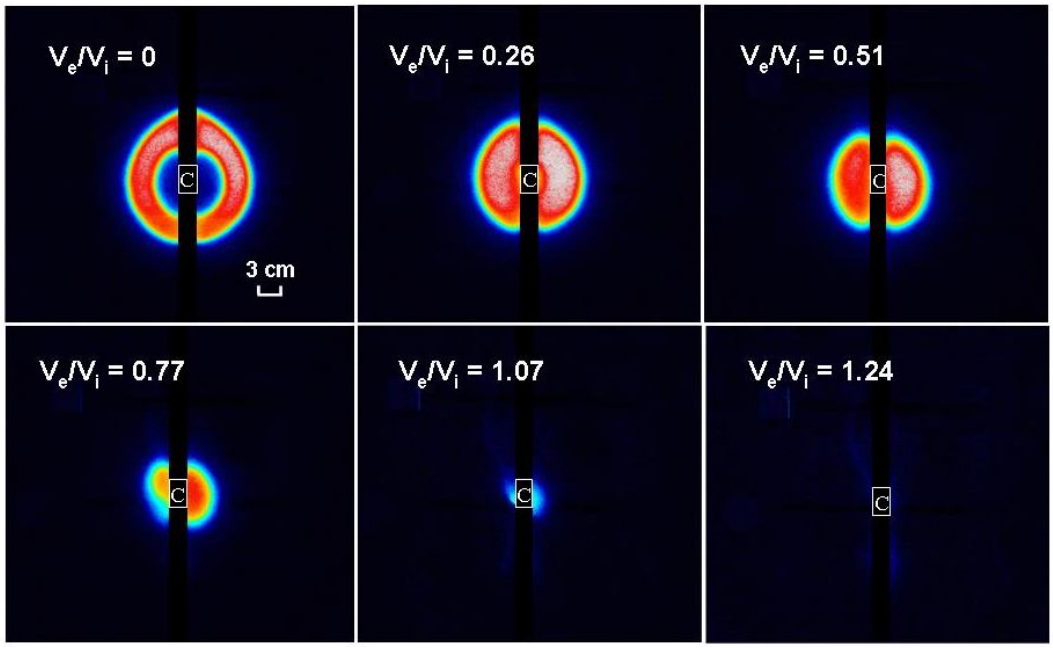

Figure 2-15: Image mosaic of selected times from the extraction phase of the PPT. C = chamber, image intensity at V_e/V_i = 1.07 and 1.24 is exaggerated compared with the other images. See text for further discussion.

As with the DFTTs, imaging points were chosen 2 cm out from the well screen, parallel to the centre of the chamber on the left and right side. This allowed tracer injection and extraction to be analysed close to the well. The position of point F chosen for analysis is shown in Figure 2-9. Further points were analysed, but due to the uniform nature of tracer flow in the test did not provide useful data on this and are not discussed here. Tracer breakthrough during the injection phase was slightly earlier

on the right side, while during the extraction phase breakthrough was earlier on the left hand side and there is greater offset between the left and right hand tracer histories. This may relate to the slight head gradient across the box from left to right (observed in DFTT1 results), which would bias injection of tracer to the right and extraction from the left, and lead to an increase in offset over time. This head gradient did not seriously affect these isotropic tests, but could present problems in a heterogeneous media. Low dispersion of the tracer is suggested by flat tops to the image concentration histories at point F close to a C/C_0 of 1 and steep rising and falling limbs.

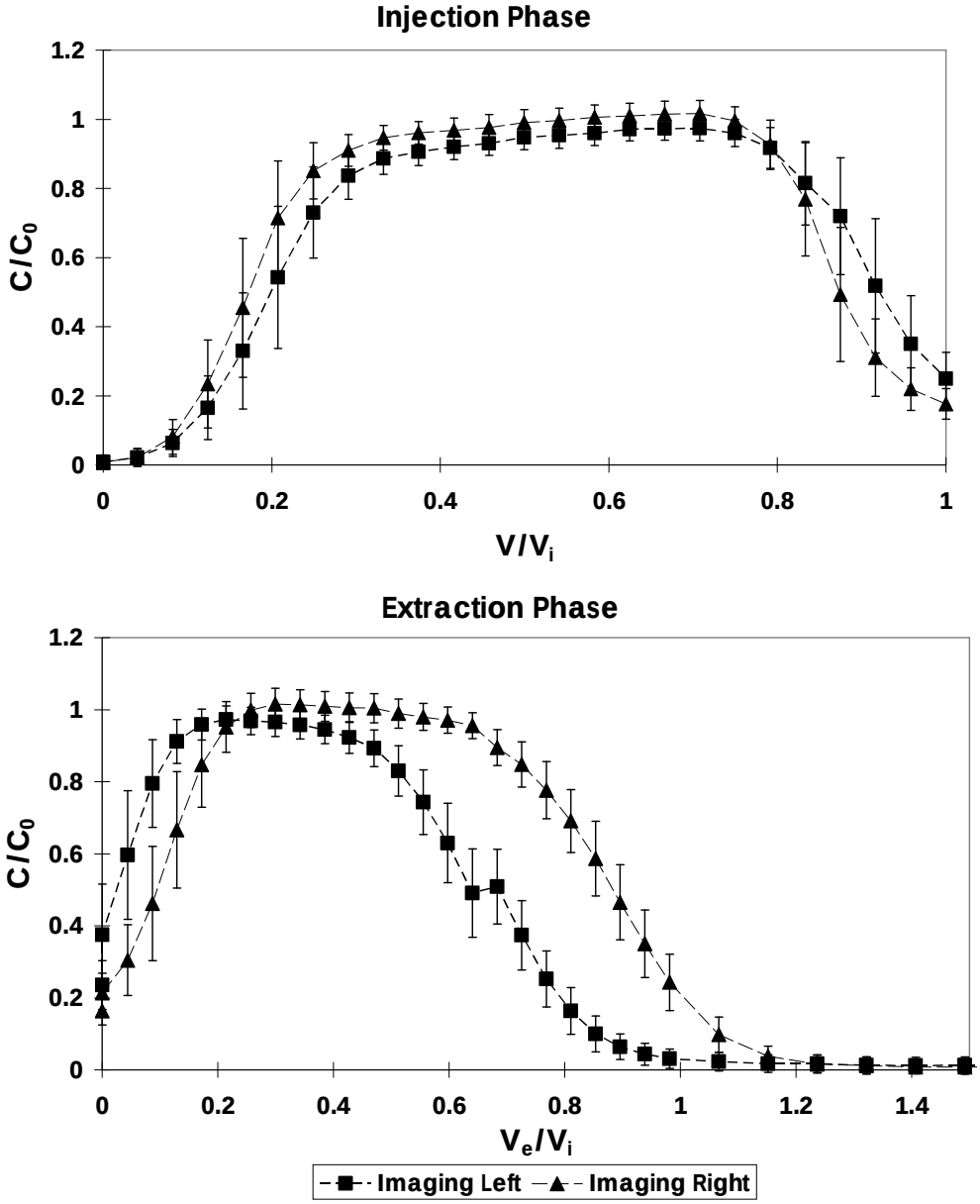

Figure 2-16: Imaging point breakthrough history for point F (see Figure 2-9) during PPT.

The area of influence and measurement of a PPT is the volume which the tracer and flush fills at the end of injection assuming 100 % recovery of tracer mass. The maximum radial extent of tracer can be estimated from imaging: an average value of 7.34 cm was measured. This value was slightly larger at the top of the plume and slightly lower at the base. The plume is expected to be larger towards the centre of the box (midway between the front and back sides of the aquifer box), due to injection from a circular well in a 2-D domain. Therefore, as the image penetration depth at best was estimated to be 7 mm the estimate of maximum radial extent of the tracer plume is likely to be a slight underestimation.

2.3.2.3. **Tracer mass**

There was generally good agreement between the tracer mass predicted from aqueous concentrations and imaging during the injection and extraction period (Figure 2-17). During injection it was assumed that tracer was injected at a constant rate and concentration. Tracer mass calculated from imaging was slightly less than that calculated from the aqueous concentration. This suggests that the tracer concentration towards the front of the beads is less than the average concentration across the shortest internal dimension of the box. It also suggests that the peak of tracer mass is in the centre of the box, as explained above. The tailing of mass during the extraction period is longer when calculated by the image than from well breakthrough concentrations. This may reflect a contribution from background noise to values obtained by imaging. Mass recovery of tracer was calculated from breakthrough curve concentrations at 104.4 % at the end of the test. This is likely due to any analytical errors in the measurement process being compounded by integration of results. However, it was noted that there was still tracer visible in the images at late time, suggesting that mass balance should have been less than 100 %.

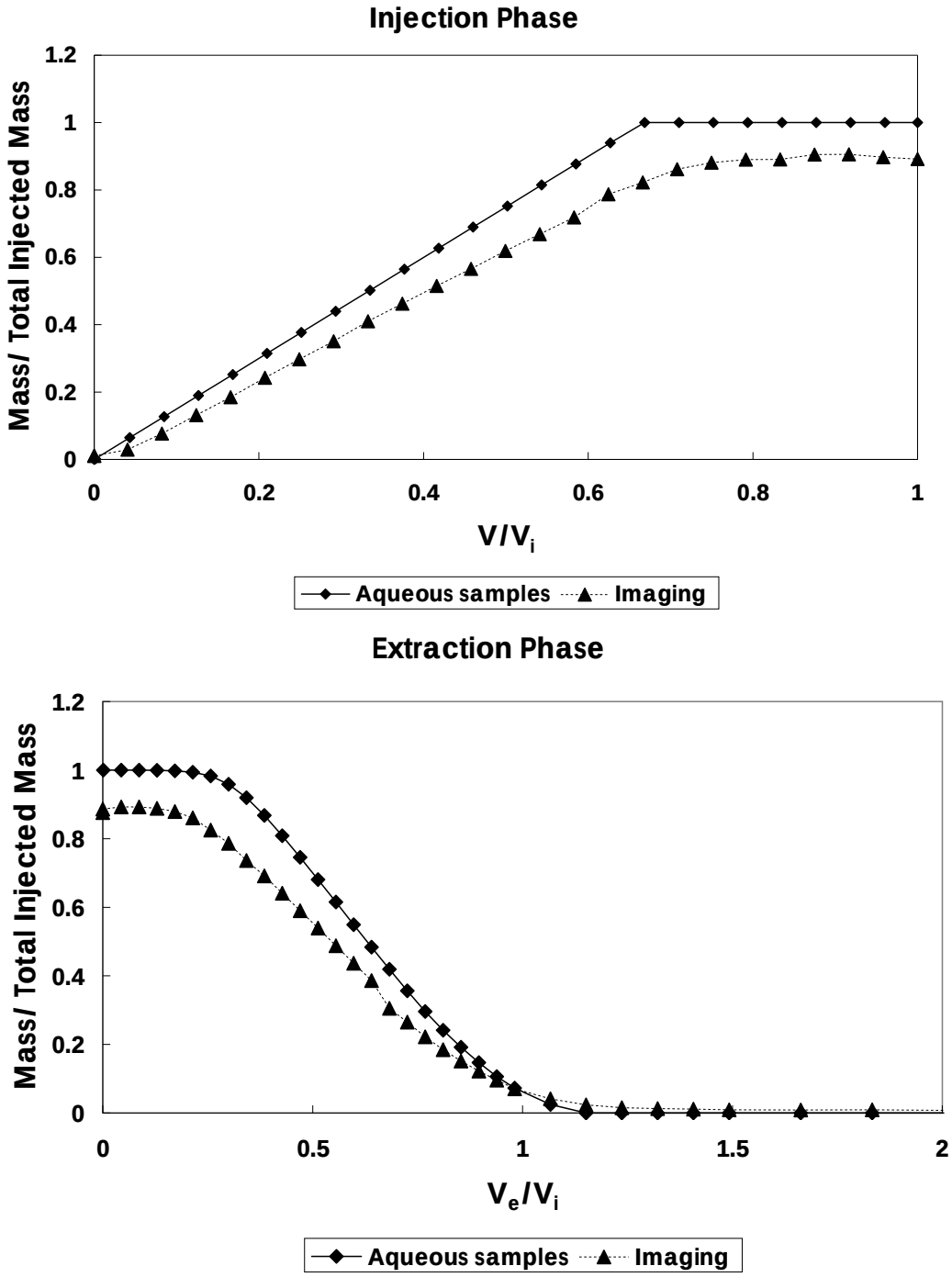

Figure 2-17: Total mass of fluorescein tracer in the box for both phases of the PPT. Mass was calculated separately from aqueous stock and breakthrough curve samples and from images taken during experiments.

2.4. **Modelling**

2.4.1. **Dipole flow tracer tests**

2.4.1.1. **Breakthrough curves**

Modelling was performed for tests in HydroGeoSphere© (HGS), a fate and transport model, supported by the University of Waterloo [Therrien et al., 2005], in finite difference mode. HGS predictions have been shown by Therrien et al. [2005] to correspond well to the analytical solution of a tracer test in a push-pull system [Gelhar and Collins, 1971], and analytical solutions of solute transport in a horizontal non-recirculating dipole flow system in isotropic and heterogeneous conditions [Hoopes and Harleman, 1967; Wilson and Miller, 1978; Zheng, 1990]. Aquifer properties (e.g. porosity, dispersivity, hydraulic conductivity) can be applied in discrete zones and reactive tracer transport can be modelled.

HGS was chosen as it has been shown to correspond to the analytical solutions of complex flow systems (see above) and can be finely discretised. HGS does not incorporate mass recirculation, so DFTT extraction well concentration histories and imaging-derived tracer histories could only be modelled until the end of the non-recirculated tracer peak breakthrough and start of the concentration tail. The conservative parameters (hydraulic conductivity anisotropy and dispersivity) which can be obtained from the DFTT breakthrough curve only depend on the initial breakthrough and tracer peak, which have been shown not to vary between non-recirculating and recirculating conditions [Sutton et al., 2000]. Therefore estimation of conservative parameters from modelling should not be affected by HGS not recirculating mass. The tracer tail in DFTTs is important for the study of biodegrading tracers. The imaging box was assumed to be dominated by 2-D flow and transport, but the model domain was discretised in 3-D. This was done as some 3-D variability was expected due to the well screen being curved, which was expected to cause some minor radial flow. HGS can overestimate diffusion if the grid discretisation is too

large [Therrien et al., 2005]. To limit this 2 mm, 3.25 mm, 2 mm (x, y, z) grid discretisation was used near the well screen. Using a smaller grid discretisation did not significantly vary the modelled breakthrough curves. The hydraulic conductivity of the beads was estimated to be 7.15×10^{-3} m/s, based on bead size and porosity using the equations of Corapciolglu and Fedirchuk [1999] and the Kozeny Carman Equation [Bear, 1972]. Packers were defined as immobile zones and the aquifer model walls were automatically defined as no-flow boundaries. Four millimetres of bulging each side of the well screen in the centre of the box was considered by defining the dimension through the bead pack as 3.4 cm. The directly measured porosity was assumed to be true and kept constant for all models.

A better fit to the breakthrough curve main peaks for DFTT1 and DFTT2 was obtained using the measured experimental injection rate of 5.4 ml/min rather than the 6.2 ml/min extraction rate. These flow rates could only be measured when the dipole test was in non-recirculating mode. Since the prevailing pumping rate during recirculation could not be measured, it was assumed that the injection and extraction pumping rates were limited to the lower pump rate of 5.4 ml/min. This may be a function of the suction-based pumping action, with the injected water travelling up head gradient and extracted water down head gradient. There may also be a contribution from pressure head, particularly when tracer was injected into the bottom chamber: the lower injection flow rate reflects the pressure needed to push water into the pores where pressure head was slightly higher compared with the upper chamber.

The dispersivity of the beads was considered to be isotropic in all dimensions at this small scale of observation. Longitudinal and transverse dispersivity cannot be defined in the x, y, z dimensions of a finite volume model for DFTTs and PPTs, as flow is complex not linear. Also, the mathematics associated with dipole flow and push-pull methods commonly assume homogeneity. The route mean square error [*Berthouex and Brown*, 2002] between observed and modelled concentrations was lowest for a dispersivity of 0.005 m for DFTT1 and 0.001m for DFTT2 (Figure 2-19). However

for DFTT1 a dispersivity of 0.001 m produced a best estimated peak concentration and shape. Therefore a dispersivity of 0.001 m was chosen for future modelling. With this dispersivity a good approximation of peak height and position and slope of initial breakthrough was obtained for DFTT1 and DFTT2, with model fit efficiencies [Bolster and Hornberger, 2007] of 94.3 % and 72.6 % respectively. There is also a good estimation of initial breakthrough for DFTT1. The lower model efficiency of DFTT2 is likely due to the presence of the short circuit peak. The initial breakthrough is obscured by the short-circuit peak, and the latter also contributes mass to the main peak. In this case the main peak can still be easily delineated and does not seem to be greatly affected by the smaller peak.

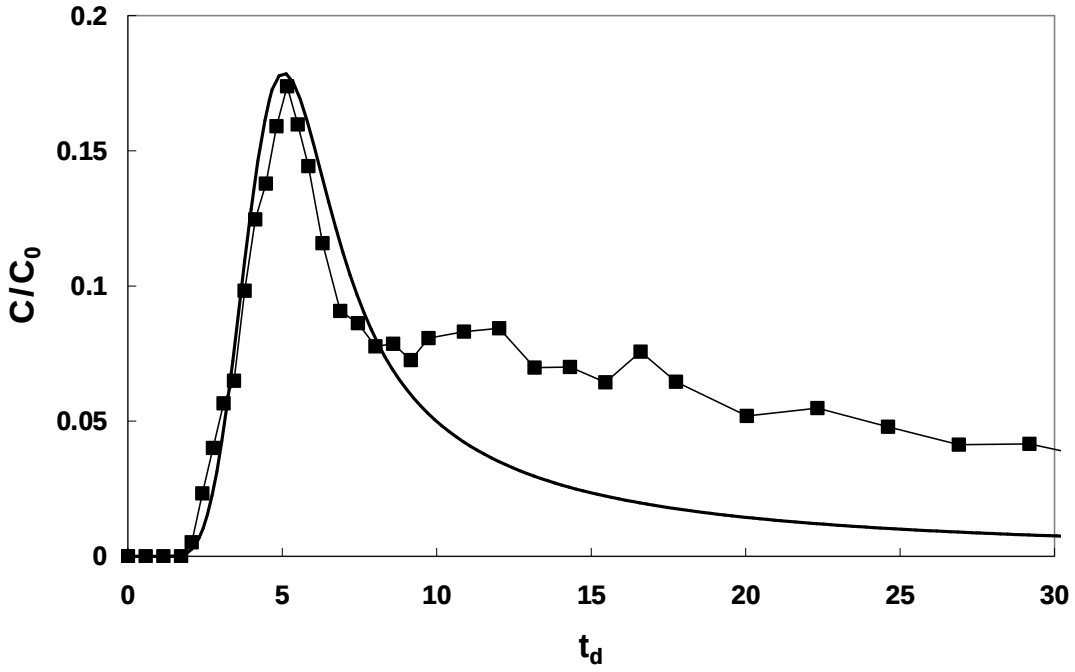

Figure 2-18: Extraction well Cl breakthrough curve for DFTT and fitted model. Modelled curve for DFTT2 not shown. The first recirculation peak is expected at 10.4 t_d.

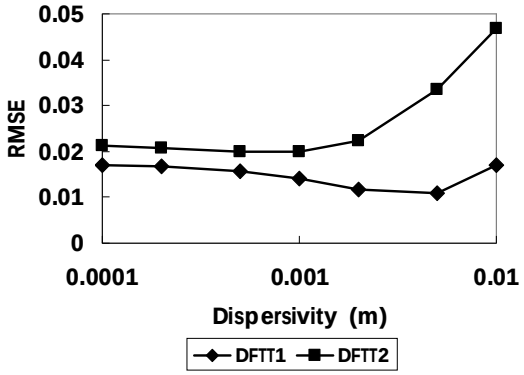

Figure 2-19: Route mean square error of model fits to DFTT breakthrough curves, with varying dispersivity

2.4.1.2. **Imaging**

The main aim of modelling the imaging experiments was to fit the extraction chamber breakthrough using the measured experiment operational parameters and aquifer model boundary conditions. Therefore, where a good fit between model and imaging data is obtained, it is assumed that this indicates that the bead pack functioned according to the properties and boundary conditions defined in the model to fit the breakthrough curve. For the imaging concentrations at imaging point A (Figure 2-9) there is good agreement between observed and modelled peak concentrations, with a model efficiency of 91.8% for DFTT1 (Figure 2-20). However, the modelled breakthrough curve is slightly later than observed values. A reason for this may be that the bulging near the injection chamber was slightly less than observed at the top of the box. Alternatively, tracer breakthrough could be focused on the front (imaged side) of the box rather than in the centre or back.

For imaging points around the extraction chamber (imaging points B, C and E), the model predicted DFTT1 and DFTT2 peak concentrations reasonably well (Figure 2-20), but earlier breakthrough than observed. Peak concentration breakthrough time estimated by HGS for imaging points agreed with observed peak concentration time at points 1 cm to half a chamber width further away from the centre of the dipole. For imaging point C HGS accurately estimated peak time of imaging point B and for imaging point B it accurately estimated peak time of imaging point E. The predicted

tracer concentration around the extraction chamber did not vary with distance into the bead pack. This suggests the plume is spread evenly over the shortest dimension of the box and that differences between the model and data are not due to inaccuracy in the distance into the bead pack modelled. Overall, this difference between HGS predicted and actual peak times suggests that the locus of extraction is closer to the centre of the dipole apparatus than expected. It probably relates to the packed beads not acting like a perfectly homogenous media as modelled, perhaps due to variations in packing density. Care was needed during packing near the well to avoid damaging or disturbing the well screen, which may create localised variation in packing of bulk density. A slight inflexion of ~1 cm of the tracer towards the extraction chamber was evident very close to the well screen in tests, which may support this hypothesis.

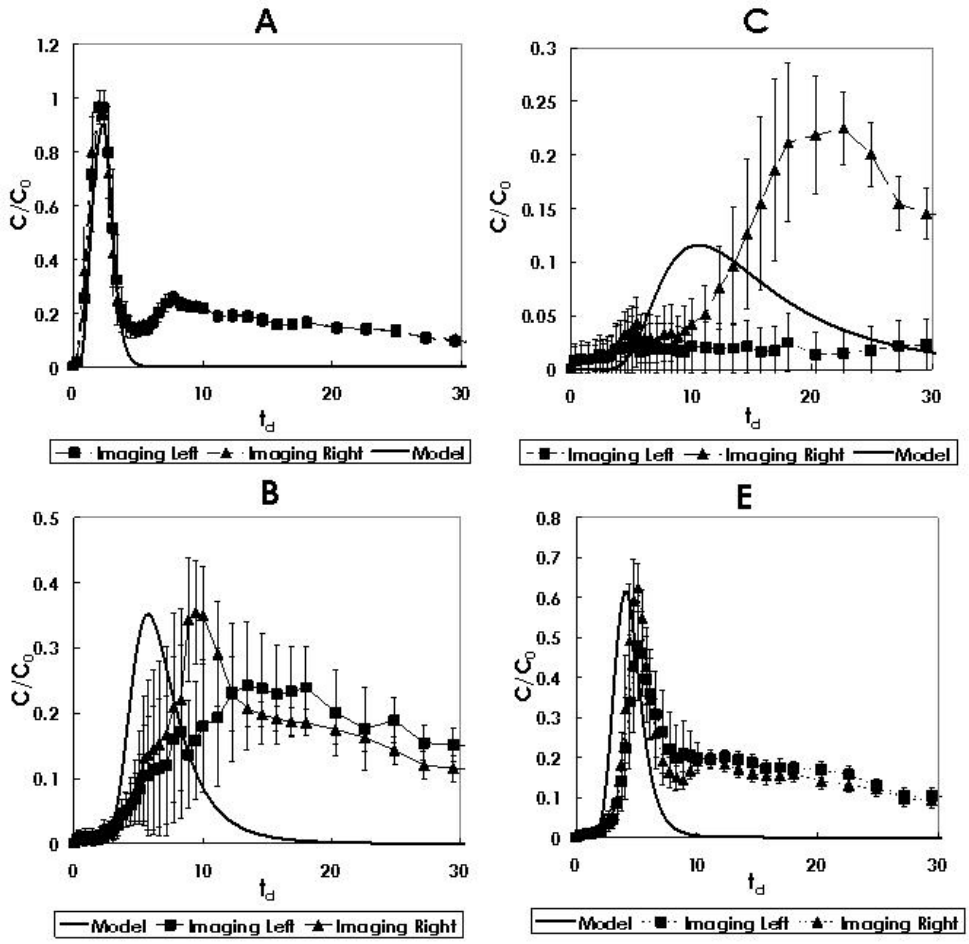

Figure 2-20: Tracer concentrations measured by imaging and model predictions for imaging points (Figure 2-9) in DFTT1. Notice peak height is well modelled, but peak time is better predicted by a point further away from the centre of the dipole apparatus. Similar results were seen for DFTT2 (not shown).

The growth of the tracer plumes in each test, and similarity between them, can be observed by measuring the horizontal distance away from the well screen of maximum tracer concentration at the depth corresponding to the centre of the dipole apparatus. If flow is assumed to be symmetrical around a horizontal line running through the middle of the central packer (as theory predicts), this value represents the maximum horizontal distance away from the well screen (d_x) that a given flow line (f_x), and part of the concentration halo will be (see Figure 2-21). Therefore the maximum radial extent of the flow lines that contribute to the breakthrough curve can be estimated, from which the area of sampling of the test can be predicted. At the time of maximum breakthrough in both tests (5.16 td) d_x was 0.017 m. Therefore the flow lines that contribute to the tracer peak all occurred within this distance of the well screen. The point of measurement is half way between the extraction and injection chamber on the flow line and the water velocity along the flow line is constant [*Sutton et al.*, 2000]. Therefore breakthrough time of the flow line is twice the time of measurement of d_x. At approximately 20 t_d the d_x for DFTT1 and DFTT2 is 0.072 and

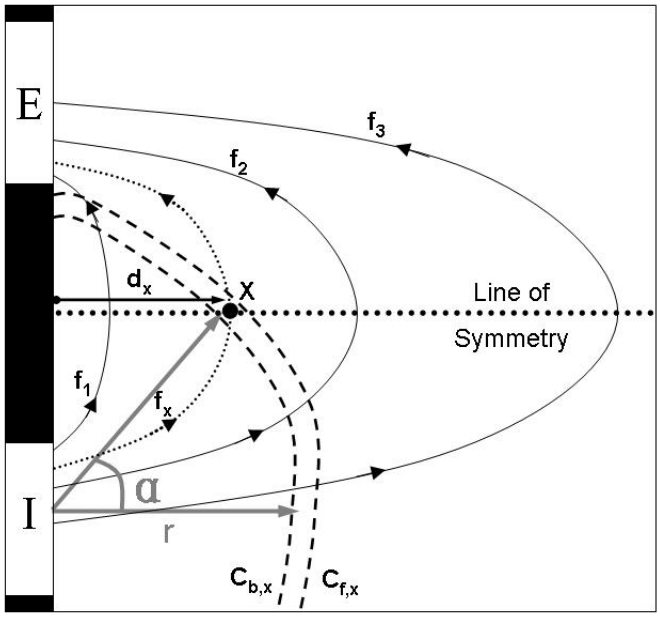

Figure 2-21: Diagram to explain measurement of d_x and relationship to flow lines and concentration. I = injection chamber, E = extraction chamber, f_x = flow line at time x, $C_{b,x}$ = back of high concentration halo at time x, $C_{f,x}$ = front of high concentration halo at time x, X = intersection of high concentration halo line symmetry at time x, d_x = distance out to X at time x, r = radius of tracer plume, *α* is defined in Eq 2.4. See text for further explanation.

0.080 m respectively. This suggests that around 40 t_d, over which the tests were performed, flow lines that contributed to the extraction chamber breakthrough curve all occurred within 0.08 m of the well screen.

From further analysis of this dynamic point (x) relationships between d_x, time and the maximum concentration are evident. Time is linearly correlated to d_x^2 (Figure 2-22). The R^2 correlation coefficients of average values, left and right of the well screen, for DFTT1 and DFTT2 are 0.95 and 0.96, respectively. There is greater variation between left and right values in DFTT1, where more asymmetry was also evident in the images. Very low values in early times are partly due to some tracer travelling in the bulge around the well screen. If ideal 2-D conditions existed this correlation is expected to improve. The slopes are similar for both graphs showing good precision in the test. The relationship of distance and time probably relates to injected water spreading out in an approximate thin vertical disc from the injection chamber. The radius squared of the disc is directly correlated to volume, which in turn depends on the flow rate and time elapsed. Therefore, from consideration of two terms of the injected volume, the time elapsed is correlated to the square of the disc radius.

$$r^2 = A \cdot \frac{Qt}{\pi b \theta} \tag{2.3}$$

The disc thickness is b, which corresponds to the shortest internal dimension of the box, θ is porosity, Q is flow rate and t is time. "A" is an empirical constant which takes into account water from the disc that is recirculated and reinjected, which therefore does not add to its volume. This assumes that the plume is a circle and d_x is related to r by the following equation derived from trigonometric relationships in Figure 2-21, where the angle α is a function of time and tends to zero as the plume grows and d_x and r values become similar.

$$d_x = r \cdot \cos\alpha \tag{2.4}$$

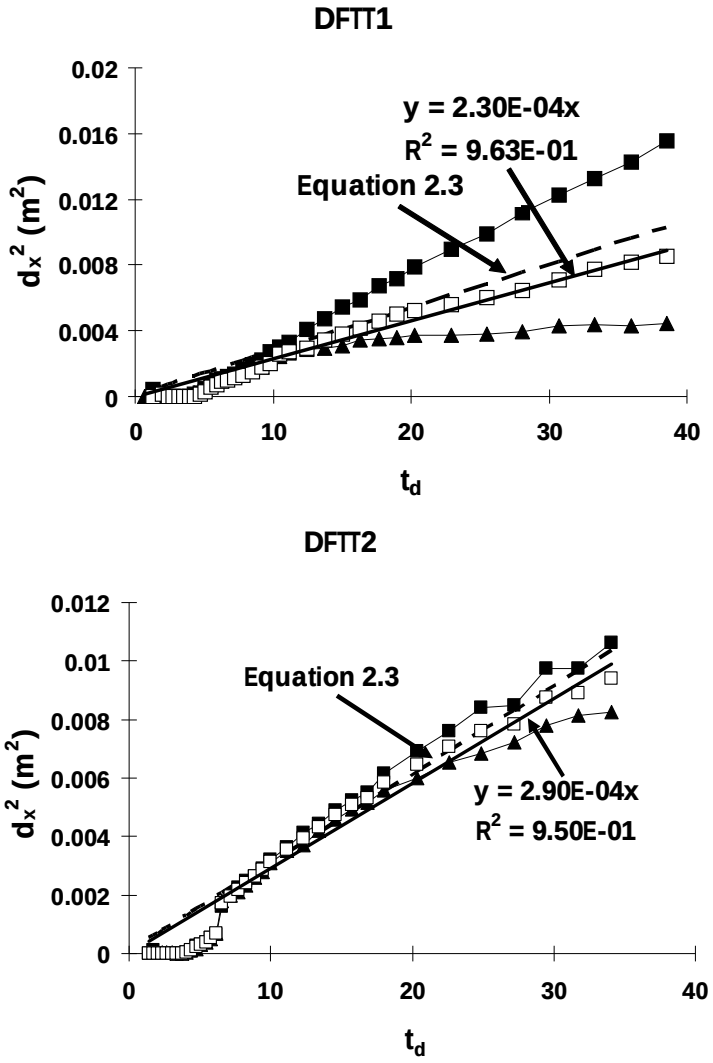

Figure 2-22: d_x^2 plotted against dimensionless time. Black squares = right side of the well screen, black triangles = left side of the well screen, open squares = average. A linear fit to the average (solid line) and estimate using Equation 2.3 assuming α is 0 and an "A" of 0.25 (dashed line) is also shown.

At early time during the test the simplifying assumption that the plume is circular is less accurate. This is shown in Figure 2-7 and Figure 2-8, where the plume is ovoid early in the experiment. Also at early time α would be expected to be large, resulting in a small d_x. Therefore the results would not be expected to follow a linear relationship as observed in Figure 2-22. At later time α is close to zero and does not vary greatly, and therefore a linear trend is seen. If the test was performed in 3-D, time would be expected to be linearly correlated to d_x^3. A good fit to experimental data for both tests is found for Equation 2.3, assuming α is 0, for an "A" of 0.25. This value of the constant A suggests ~ 75 % of injected water is quickly extracted and

recirculated. Good model efficiencies (88.6 and 98.3 % for DFTT1 and DFTT2 respectively) are obtained using the Equation after ~ 6.5 t_d.

Data from DFTTs show a clear inverse linear correlation between the maximum concentration parallel to the centre of the dipole apparatus (i.e. at x) and d_x (Figure 2-23). Early time points where α was large have been discounted. The R^2 correlation coefficients of average values, left and right of the well screen, for DFTT1 and DFTT2 are 0.99 and 0.98 respectively. The correlation represents dilution of the tracer halo as it travels further into the bead pack, showing dispersion and dilution over time. The inverse correlation is also probably due to the model being 2-D. The concentration halo can be approximated to a thin crust on the outside rim of a thin disc and therefore is linearly related to its radius. As the surface area increases the concentration decreases. If the thickness of the halo is assumed to be small then tracer concentration at x can be related to d_x by the following equation:

$$C_x = \frac{M \cos\alpha}{2\pi d_x \theta b c} \qquad (2.5)$$

The thickness of the halo is represented by c and M is the mass of tracer in the halo. This assumes that tracer mass is distributed evenly in the halo. As the part of the halo measured at x is non–recirculated tracer, M can be considered constant. Therefore the inverse correlation between tracer concentration and d_x is as expected. For DFTTs performed in 3-D maximum tracer concentration would be expected to have an inverse correlation with d_x^2. Reasonable fits to the data is obtained for Equation 2.5 after ~6.5 t_d, assuming α is 0 and using the d_x calculated from Equation 2.4, with model efficiencies of 45.5 and 56.4 % for DFTT1 and DFTT2 respectively. The thickness of the halo was taken to be the average radius of the tracer plume at the end of the injection phase, which was measured at 0.031 m.

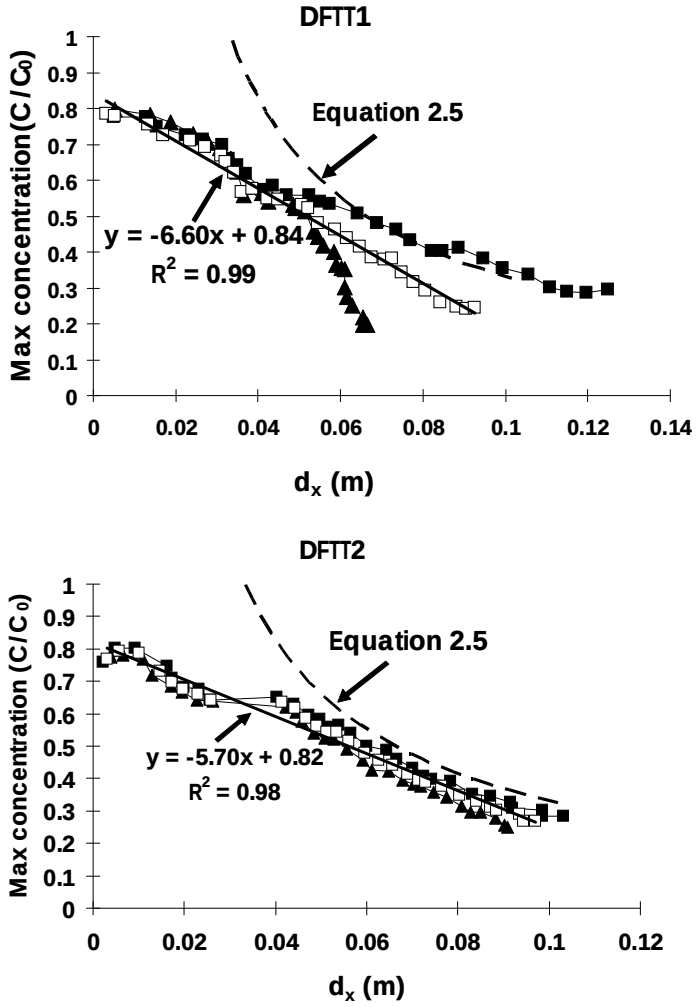

Figure 2-23: Maximum concentration parallel to centre of dipole apparatus plotted against d_x^2. Black squares = right side of the well screen, black diamonds = left side of the well screen, open squares = average. A linear fit to the average (solid line) and estimate using Equation 2.5 assuming α is 0 (dashed line) is also shown.

Using 3-D modified versions of the equations described above it should be possible to estimate the area sampled by DFTTs in the field and the decrease in tracer concentration with distance for isotropic conditions. Good estimations are achieved even though A is assumed to be constant and angle α assumed to be 0. Both are expected to vary with the flow field formed, which depends on the set-up parameters of a DFTT. The angle α also significantly varies with time early in an experiment, but above ~6.5 t_d good accuracy can be obtained assuming α is 0. The 3-D version (i.e. sphere instead of disc) of Equation 2.3 is:

$$d_x^{\,3} = A\frac{Qt}{4\pi\theta} \qquad (2.6)$$

Assuming the constant A is 0.25 and α is 0, at a flow rate of 1 l/min it would take 24 hrs for tracer in a DFTT to sample ~ 0.34 m out into the aquifer and arrive back at the extraction chamber. Over the same period a test run at 10 l/min will sample ~ 0.73 m out into the aquifer. The 3-D version of Equation 2.5 is:

$$C_x = \frac{3M \cos\alpha}{4\pi r^2 \theta c} \qquad (2.7)$$

If tracer is injected for 15 minutes from the equation it can be calculated that for both scenarios (d_x is ~ 0.34 m and Q = 1 l/min, and d_x is ~ 0.73 m and Q = 10 C_x) C_x is 0.57 C/C_0. If tracer was injected for 1 minute C_x would be 0.20 C/C_0. Assuming constant dilution due to dispersion along the flow lines, concentrations would be half these values when the flow lines reach the extraction chamber. Here the tracer will be further diluted by extracted clean water.

2.4.1.3. **Tracer mass**

As HGS cannot account for recirculated mass, the value measured by aqueous samples and imaging could not be modelled. However modelling provides a prediction of mass recovery to compare with breakthrough of un-recirculated tracer. During DFTT1 68.1% of tracer was predicted to arrive at the extraction well. A large proportion of tracer mass is estimated to breakthrough early on, with 50% of mass arriving after 11.3 t_d. This suggests the tracer mass predominantly travels in the faster flow lines close to the well screen (as shown in the imaging analysis and theory predicts). This suggests that the simplifying assumption for Equation 2.5 that mass is spread evenly in the halo, is not completely accurate. However it is still useful for estimating tracer concentration. Good mass recovery would be achieved for a prolonged non–recirculating test.

2.4.2. **Push–pull test**

2.4.2.1. **Breakthrough Curve**

The breakthrough curve (Figure 2-24) was fitted with a dispersivity of $1x10^{-5}$ m. The route mean square error between the data and model is reduced for a lower dispersivity of $1x10^{-6}$ m (Figure 2-25), but the reduction was less than 0.001 (dimensionless) and was not considered significant. As for the DFTT modelling, the aquifer box was assumed to be 3.4 cm thick to account for 0.4 cm of bulging on each side of the box. The DFTTs and PPTs were modelled with the same grid discretisation and numerical oscillation was not significant, so any model limitations should affect both types of test. Measured concentrations are larger than modelled in the centre of the breakthrough curve and slightly lower in the limbs, with an overall model efficiency of 98.3%.

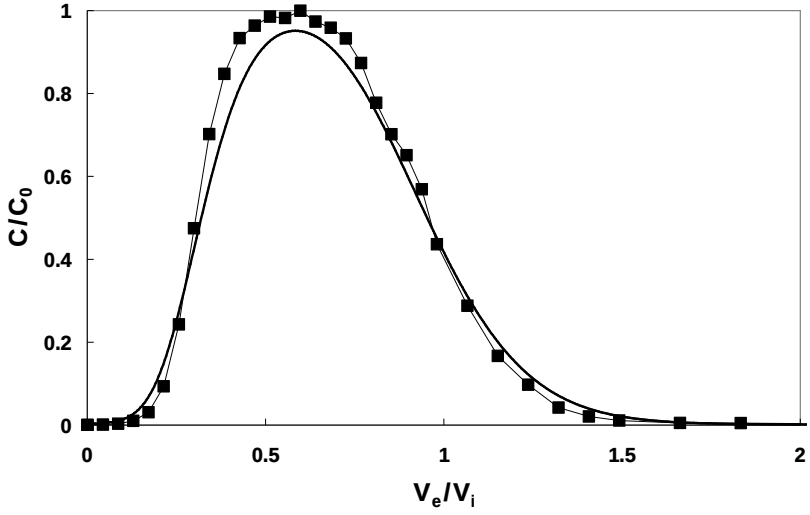

Figure 2-24: Extraction phase well chamber Br breakthrough curve concentrations from PPT and fitted model curve.

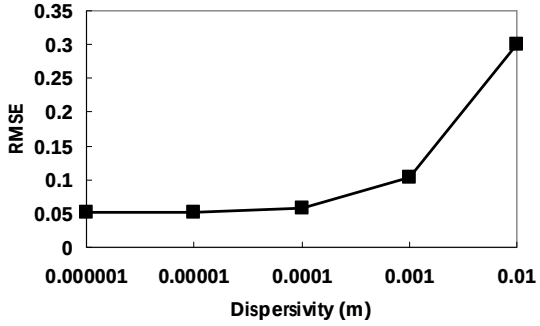

Figure 2-25: Route mean square error of model fits to PPT breakthrough curve with varying dispersivity.

2.4.2.2. **Tracer imaging**

The small upwards bias of tracer seen in images was taken into account by modelling the overflow in HGS as a weak extraction well in the open well section above the top packer. Equal overflow from each side of the box was approximated by a single extraction node in the centre. This produced a similar concentration plot at the end of the test as that seen in imaging (not shown). This suggests that injected tracer mass may migrate into the water above (or below) the packers during injection, where it is likely to only respond slowly to extraction. To minimise this effect, longer packers could be used.

Greater variability in concentrations along the short axis of the box was found for PPTs than DFTTs. This may be due to more simple flow out and into the well chamber in a PPT than a DFTT, with greater mass where the well screen protrudes furthest into the beads. This was suggested in the assessment of total mass from the images during the test. The PPT may have also been more affected by the bulging seen in the tests than the DFTT.

Fitting of injection phase imaging concentrations of imaging point F (Figure 2-9) with HGS suggests that tracer concentrations during initial breakthrough can be simulated well with model nodes that correspond with positions 0 mm and 4 mm into the beads (Figure 2-26). These values correspond with the low penetration depths estimated by separate testing and the Beer-Lambert law. Root mean square analysis supports this interpretation, with the lowest error occurring between the average (left and right side of the well screen) image concentration and model for the 0mm bead depth (Figure 2-27). However the 4mm depth has only slightly higher error and provides a better visual fit to the initial breakthrough. The fit for extraction phase imaging concentrations is less good, as any deviation from the data at the end of the injection phase is carried through to the start of the extraction phase. Still, the modelling and statistical analysis show that points closer to the edge of the box provide a better fit than points in the centre of the bead pack.

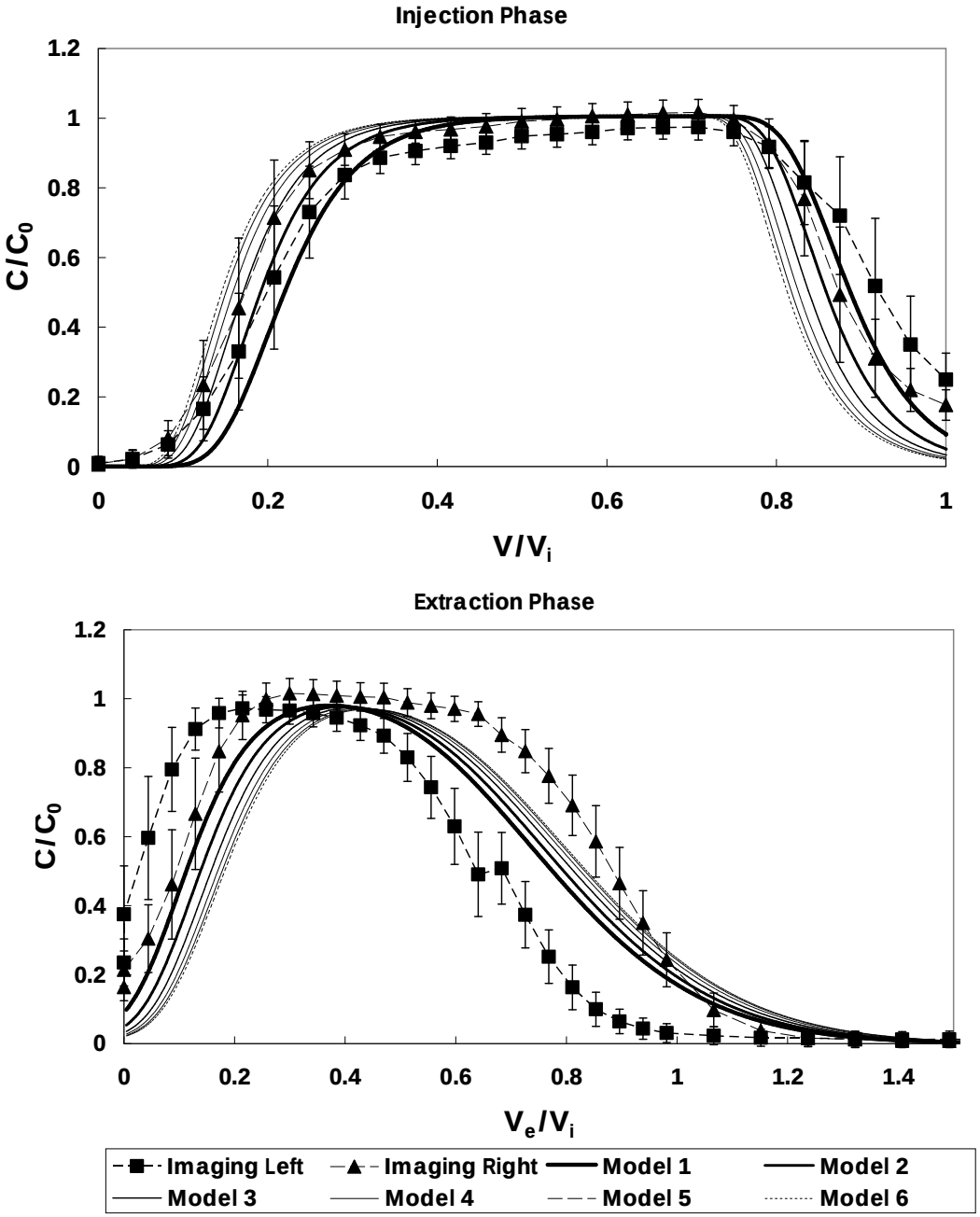

Figure 2-26: Concentrations calculated from imaging data at point F, see figure 2-9. They are plotted against model predictions for points at various depths into the bead pack (Model 1 – no distance into beads, Model 2 – 4 mm into beads, HGS 3 – 7.25 mm into beads, HGS 4 – 10.5 mm into beads, HGS 5 – 13.75 mm into the beads and HGS 6 – 17 mm into the beads).

2.4.2.3. **Tracer mass**

Overall there is more mass in the measured than modelled breakthrough, which is presumed to result from slight overestimation of Br concentrations during analysis (see results). The mass recovery predicted by the model is 99.2 % over the test, compared with 104.4 % predicted by tracer breakthrough concentration. The model

indicates a long tail of mass in the tests that was also evident in the images (Figure 2-28), and may relate to the small amount of mass that migrated to the open well segments during the experiment.

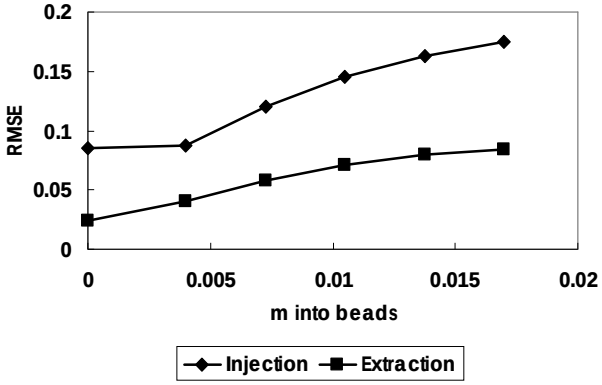

Figure 2-27: Route mean square error between model fits and average imaging data for imaging point F, with varying model depth into the beads.

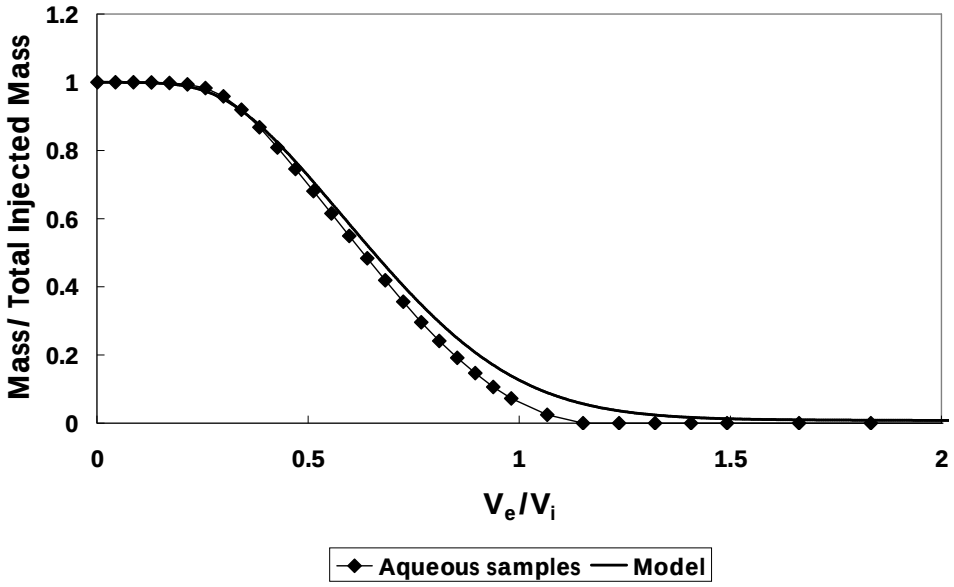

Figure 2-28: Total fluorescein mass in the box in the extraction phase of the PPT, calculated from aqueous samples and predicted by modelling.

2.5. **Discussion**

2.5.1. **Effectiveness of imaging technique**

The good simulation of imaging data by HGS and estimation of mass recovery indicates that UV imaging is an effective tool to explore forced gradient tracer tests. The results have suggested that imaging only penetrates ~ 4 mm into the bead pack. Although imaging does not cover the entire depth of the box, experiments can still be

effectively modelled if the model is discretised in three dimensions. Imaging and modelling results of DFTTs suggest that the tracer concentration is evenly distributed across the box, while in the PPT this distribution is variable. This variation may be due to the slight curvature of the well screen used and the fundamental differences in the respective flow systems.

Previous imaging experiments in the literature have been performed with box thicknesses between 1.248 mm and 1.91 cm and bead sizes between 212 μm and 1.248 mm [Corapcioglu and Fedirchuk, 1999; Huang et al., 2002; Oates et al., 2005; Rees et al., 2007]. In these tests the highest longitudinal dispersivity calculated was $2.9x10^{-3}$ m for the 1.91 cm thick box and 0.71-1.19 mm beads [Oates et al., 2005], and the lowest was $4x10^{-4}$ m for a 5 mm thick box and 213-300 μm beads [Rees et al., 2007]. The dispersivity measured for DFTTs in the box was 10^{-3} m and is similar to this range of estimates. Dispersivity measured in the PPT was $1x10^{-5}$ m, much lower than the range of estimates in the literature. This suggests that the value probably does not accurately represent the silica bead media. However the value provided a good fit for imaging concentrations and extraction phase breakthrough curve profile. A dispersivity estimate obtained from Equation 13 of Cassiani et al. [2005] and experimental parameters from this study is within an order of magnitude of the value obtained from HGS modelling of the PPT. This suggests that the low dispersivity value is not due to modelling inaccuracies. Work from Tiedeman and Hsieh [2004] suggested that convergent radial flow tests produced lower dispersivity estimates than two-well dipole tests. This was explained by a significantly lower area of sampling and less local aquifer heterogeneity. However both these factors were similar between DFTTs and PPTs in these experiments. Also there was much greater variation in dispersivity between radial and dipole flow experiments in this study, than between radial and uniform flow studies in the literature. Dispersivity has been shown to reach asymptotic values far from the source [Freyberg, 1986], therefore greater variability in dispersivity in the near well environment should be expected. It is possible that the near well environment sampled in the imaging experiments is below the

representative elementary volume of the bead pack and a constant dispersivity value for the media is not appropriate at the scale of the tests. Differences may result from the flow regimes of the different tests, which has been seen at a large scale [Neuweiler et al., 2001]. For PPTs tracer travel times along different flow lines should be near equal, whereas for DFTTs travel times and flow line length increases away from the well. Therefore when tracer breakthrough from different flow lines is summed a larger dispersivity would be expected for DFTTs, i.e. a large ensemble dispersivity. Overall, the results suggest that accurate parameters can be obtained from imaging experiments at this scale. However there may be greater uncertainty in dispersivity compared with previous tracer sweep experiments [Corapcioglu and Fedirchuk, 1999; Huang et al., 2002; Oates et al., 2005; Rees et al., 2007].

Dispersivity measured with the PPT was much lower than expected from literature values. Also PPTs do not measure hydraulic conductivity, while for DFTTs this can be obtained by measuring the draw-down and draw-up in the well chambers [Kabala, 1993]. Therefore DFTTs are the more suitable test to obtain aquifer conservative transport parameters *in situ*, when isotropic conditions are present.

Due to the weight of the beads and water there was bulging towards the centre of the box. This was taken into account within the modelling. A practical solution is to add a vertical restraint across the top of the well screen to minimise any effect on imaging and provide physical support. Multiple restraints were considered originally, but there was concern that it would limit the range of imaging possible.

2.5.2. **Dipole flow tracer tests**

There was good agreement between observed tracer plumes in the experiment with hydraulic head and tracer concentration fields predicted by the model. There was no significant difference between the DFTTs, regardless of injection / extraction chamber assignment. This suggests that tracer transport was not affected by density effects and that the impermeable bottom and end walls did not affect flow (an impermeable

boundary may be expected to deflect tracer away from it [Zlotnik and Ledder, 1996]). The similarity between the up-flow and down-flow DFTTs is evident in the breakthrough curves, which could be modelled with the same input parameters. In addition, both image sequences and model results showed similar variation of d_x with time and maximum plume concentration. There were good model fits to image-derived tracer concentrations at points next to the injection well, but measured tracer breakthrough occurred later than predicted around the extraction well. Deviation of predict tracer breakthrough from the observed results is attributed partly to the bulging of the box in tests, which certainly resulted in an uneven bead thickness. The observed delays in image point breakthrough (relative to predictions) may have been caused by variations in bulk density close to the well screen. These variations would lead to a slight bias in water extraction and hence tracer migration close to the well, rather than a less hydraulically favourable route through the bead pack and measured points. An inflexion of the tracer plume of ~1 cm was apparent towards the extraction chamber close to the wells screen, showing this preferential migration. Breakthrough times at the extraction chamber were modelled accurately by HGS. This shows that slight preferential migration of tracer close to the well screen did not significantly affect the length of tracer flow lines. Porosity and hydraulic conductivity may be slightly larger here due to variable packing around the circular well. This effect may be reduced if larger beads were used, allowing more uniform packing and bulk density. Results suggest that if there is relatively high hydraulic conductivity and variable bulk density around the well in the field, this effect might be observed or accentuated to cause short circuiting of tracer. It is possible to test this hypothesis by conducting a test at a higher flow rate to amplify the effects of preferential flow paths.

The flow lines that contribute to the main peak breakthrough do not deviate far from the central well. In DFTT1 at maximum breakthrough (t_d = 5.16) d_x was 0.017 m. This means that tracer that comprised the extraction well peak breakthrough was entirely confined to this zone. This distance also likely represents the maximum radial extent of the streamtube that breaks through at 10.22 t_d. Sutton et al [2000] calculated

that at 11 t_d.,10% of model stream tubes had broken through, with these stream tubes making up the main breakthrough peak. This corresponded with a maximum radial distance value of these stream tubes, normalised by anisotropy and multiplied by shoulder length, (r/aL) of 0.4. This agrees well with the finding from this study that the majority of flow that contributes to the breakthrough curve does not travel far out into the beads. Radial distance values obtained in these experiments were larger than those predicted by Sutton et al [2000]: at 11.12 t_d a r/aL value of 0.97 was calculated for DFTT1. However, this is probably due to the 2-D constraints in these experiments, forcing a given volume of tracer to travel further from the well screen than in a 3-D domain. Overall the analysis shows that the tracer seen in DFTT breakthrough curves only samples an area reasonably close to the well. Modelling of mass recovery of a non–recirculating system suggests that the tracer does not spread out evenly from the injection well with the majority of tracer travelling in the shorter flow lines closer to the well. Therefore the assumption in Equation 2.5 that mass is spread out evenly in the plume is likely an oversimplification. At time t of a 3-D test t is linearly related to the cube of the maximum radial distance from the well of the flow lines that make up the breakthrough curve, up to 2t. Therefore a long test would be required to sample a significant portion of the aquifer in a field tracer test. Using Equation 2.6 it was calculated that in 3-D field conditions at a flow rate of 1 l/min it would take 24 hrs for tracer in a DFTT to sample ~ 0.34 m out into the aquifer and arrive back at the extraction chamber. Over the same period a test run at 10 l/min will sample ~ 0.73 m out into the aquifer. If a short central packer is used data from this interval into a DFTT is likely to be lost in the tail of the breakthrough curve. Therefore a long central packer should be used, at least twice the length as the distance out into the aquifer that must be sampled, to obtain a later breakthrough peak. A test needs to be run for at least twice as long as the peak breakthrough time, to ensure a full breakthrough curve history. Therefore, DFTTs may need to be run over multiple days to sample the required distance into an aquifer. Equation 2.6 does not take into account the dipole set-up parameters and borehole size. There is great scope to define the influence of these factors computationally with some experimentation, so that DFTTs can always

be effectively designed. Constant A and the variation with time of angle α also need to be defined to give accurate results. Angle α can be assumed to be 0 for middle to late times. The maximum tracer concentration present in the outer tracer halo will decrease with distance away from the well. In tests concentration showed a negative linear correlation with d_x, therefore in 3-D it is expected that the concentration is negatively linearly correlated to d_x^2. If sampling a large volume of the aquifer a tracer with a broad analytical detection range would be needed, as significant dilution will occur in the aquifer and at the extraction well. Therefore, both time and tracer concentration limits the sampling area in DFTTs

In contrast, the maximum extent of a tracer plume is much larger with 90 % [Zlotnik and Ledder, 1996] of flow expected at an r/aL of 10 and 100 % over a much larger distance. This was shown in tests with the high concentration halo becoming more dilute and larger over time. The halo seen in images represents tracer that has not been recirculated. The longer flow lines travel further out from the injection chamber in all directions the larger the plume becomes. As the flow lines deviate from each other tracer concentrations in the halo become more dilute. The tracer plumes did not seem to be affected by the bottom impermeable boundary of the model, suggesting the flow field is not significantly affected by the box boundaries [*Kabala*, 1993]. The size of the large flow field that is produced by dipole flow is equivalent to the maximum extent of the tracer plume (r/al of 10). It is much greater than the extent of the tracer plume at peak extraction chamber breakthrough (r/al of 0.26). The flow field creates draw-down and draw-up in the chambers, which can be measured in the field to estimate hydraulic conductivity, while through modelling the breakthrough peak of the tracer plume, anisotropy and dispersivity can be determined. Therefore for a DFTT, a value of hydraulic conductivity would be measured over a larger area than parameters obtained by tracers. When applying estimates obtained from tests the area sampled should be kept in mind.

2.5.3. **Push-pull tests**

The PPT images formed a thick circle at the end of the injection phase. The average radial extent was measured at 0.073 m, therefore the tracer plume filled an area comparable with that of DFTTs which took a similar amount of time to perform. However the PPT extraction breakthrough curve for a lower flow rate sampled significantly further into the aquifer than the DFTT breakthrough curve peak. A PPT run at 1 l/min with 12 hour injection phase and 24 hr extraction phase will sample ~ 0.54 m out into the aquifer, assuming spherical flow. At 10 l/min this is ~ 1.16 m. With these set-up parameters a PPT samples further out than a DFTT run for a similar time (see above). Also unlike DFTTs tracer sampling this distance should make up the breakthrough peak, irrespective of packer size.

As the tracer plume in this 2-D study formed a circle, it is presumed that in 3-D a PPT in isotropic conditions will form a spherical plume. This agrees with the theory of Schroth and Istok [2005]. The spherical nature of PPTs should be considered in field tests. Tracer will travel in equal amounts up and down the well, and therefore if long injection periods are used there is a risk of losing tracer to the well, depending on the length of packers used. This will lead to long tailing of tracer concentrations and a low mass recovery during the extraction phase, perhaps seen in the tests of Kim et al. [2004], that makes the estimation of aquifer parameters using numerical models difficult. Tracer loss may be enhanced by leaks around the packers or a significant skin zone around the well. Results from this study suggest that the more isotropic the aquifer, the closer tracer mass will remain to the well. Therefore, parameter estimates may be dominated by the conditions near the well, primarily physical disturbance induced by well installation. However, as PPTs sample further out into the aquifer than DFTTs, they represent the most reliable method to estimate reactive transport parameters of aquifers *in situ*, under isotropic conditions.

2.6. **Conclusions**

This study has shown that UV imaging tests of scaled down forced gradient tests can be performed without being seriously affected by boundary conditions or the observation scale. This allows the further investigation of forced gradient tests using this approach, to evaluate more complicated scenarios.

Tracer breakthrough curve peaks for DFTTs and PPTs were accurately modelled using HGS. The tracer appeared to be less dispersed in PPTs by two orders of magnitude. This may have been due to a much greater variability in travel times of flow lines in DFTTs compared with PPTs. The dispersivity estimated in DFTTs corresponds with that obtained in similar scale imaging tests. Therefore DFTTs are recommended over PPTs for the *in situ* measurement of aquifer conservative transport parameters. Tracer migration observed in images was consistent with that expected from head gradients and predicted flow lines. However tracer concentrations around the extraction chamber in DFTTs could not be simulated by HGS. This may relate to preferential tracer migration close to the circular well screen, due to variable packing.

For DFTTs the maximum radial distance of flow lines and their extraction chamber breakthrough times can be estimated from image analysis. Tests must be carefully designed to ensure a suitable aquifer volume is sampled and tracer is detectable across a wide concentration range at the extraction well. Simple equations are proposed to help with this process. If long injection periods are used for PPTs in isotropic conditions there is a significant risk of tracer migrating to the open well segments, a poor mass recovery being obtained during extraction and parameter estimates being biased by the near well aquifer conditions. In isotropic conditions the tracer that makes up the breakthrough peak travels less distance from the well in DFTTs than PPTs. This implies PPTs may be a more reliable test for obtaining aquifer reactive transport parameters *in situ.*

3. Evaluation of the effects of layered heterogeneity on single well forced gradient tracer tests using UV imaging

3.1. Abstract

In porous media it is important to characterise mesoscale heterogeneity, such as discrete layers with variable permeability, to understand the fate and transport of contaminants in aquifers. This heterogeneity is often not considered when modelling tracer tests in the field, which can result in averaged solute transport parameters that may fail to identify high flux paths critical to the design of remediation systems. This is especially true for single well forced gradient tracer tests, which can be used to quickly measure aquifer properties for natural attenuation and remediation assessments. Whether these tests can detect discrete layering, or if their performance is compromised by the presence of it, has not been examined in detail. Dipole flow and push–pull fluorescent dye tracer tests were undertaken in a pseudo 2–D tank to compare actual transport behaviour to that apparent in tracer concentration histories, with the aim of linking breakthrough curve shape to layered heterogeneity. A 3-layer model aquifer was created with different sized silica glass beads, and tests were conducted with the tracer injection located at different depths relative to the permeability contrast. The tracer migration, photographed under ultraviolet light, was compared with conventional tracer breakthrough histories. Modelling showed that dipole flow tracer test tracer breakthrough curves could be reproduced by the inclusion of discrete layers, but such tests may also be adversely affected by strong anisotropy. In push-pull tests breakthrough curves did not differ from those observed in non-layered systems, but the aquifer sampled by the tracer cloud varied greatly depending on the position of the permeability contrast. Challenges in modelling some breakthrough curves also suggested that near-well effects (not accounted for by most numerical models) may increase the uncertainty of parameters estimated from modelling tests that only sample a small volume of the aquifer.

3.2. **Introduction**

It is well recognised that aquifers rarely have homogeneous and isotropic flow fields. Heterogeneity can significantly affect contaminant flow at the centimetre to metre scale [Freyberg, 1986; Sudicky, 1986; Korte et al., 2000; Stauffer, 2007], and even pore scale [Welty and Gelhar, 1994]. In a modelling experiment, [Stauffer, 2007] showed that mesoscale heterogeneity, in the form of sedimentary layers or lenses of varying permeability, can significantly affect solute transport. An important objective in polluted aquifer assessments should be to quantify hydraulic and reactive transport properties at a scale necessary to reduce uncertainty in natural attenuation assessments or remediation system design. Spatial variability in groundwater flow (hydraulic conductivity, porosity, dispersivity) and reactive transport (sorption, contaminant decay) properties results in high and/or low mass flux paths [Devlin et al., 2002; Wilson et al., 2004]. Failure to identify these could severely affect the performance of treatment schemes or predictions of natural attenuation. Recent studies have shown that natural attenuation in aquifers is sensitive to transverse horizontal dispersivity [Lerner et al., 2000; Ham et al., 2004; Cirpka et al., 2006; Maier and Grathwohl, 2006; Werth et al., 2006]. It follows that accurate measurement of dispersivity will also benefit remediation design. Natural gradient tracer tests have been used to estimate longitudinal and transverse dispersivity by spatial interpretation of an injected tracer plume in a heterogeneous flow environment (e.g. [Freyberg, 1986; LeBlanc et al., 1991]). However tests take a long time to perform and may require a large amount of samples to be analysed. Therefore they are impractical for efficient determination of aquifer properties.

Forced gradient tracer tests involve injecting tracer in an imposed flow system to estimate aquifer transport parameters. This minimises the test time and the number of samples required for analysis [Fetter, 1994]. Two well convergent tests, where the injection rate is less than extraction rate, have been tested in the field to assess variability in vertical flow paths [Ptak and Schmid, 1996]. By sampling injected tracer

using a multilevel sampler in the extraction well, a vertical profile of velocity and dispersivity was resolved, although these values were an average along the flow path between injection and extraction. Single well forced gradient tests (dipole flow tracer tests and push-pull tests) have the operational flexibility to quantify parameters at sub-meter scale using a packer assembly in a single long-screened well (provided it is appropriately designed) and can be performed in less than a day, making them a cost effective test alternative. A description of how these tests are conducted is given in Chapter 1. The dipole flow test was initially developed by Kabala [1993] to characterise the hydraulic properties of an aquifer. The method was extended by [Sutton et al., 2000] to include a groundwater tracer component to improve reliability and estimate transport properties: herein referred to as dipole flow tracer tests (DFTTs). These tests also have the potential to measure reactive transport properties. Istok [1997] initiated current interest in the single-well pulse or push-pull test (PPT) to estimate biodegradation. Tests have also been used to measure inorganic and organic sorption (e.g. [Pickens et al., 1981; Hageman et al., 2003]). However they provide little information on hydraulic parameters and may not be suitable to accurately estimate dispersivity [Domenico and Schwartz, 1990].

Modelling of laboratory or field data is typically performed to estimate the desired aquifer parameters. For such modelling hydraulic conductivity (K) is often assumed to be homogenous, but for DFTTs this assumption can be used to predict the K anisotropy of an aquifer [Sutton et al., 2000]. For PPTs and single well injection tracer test models the flow-field is often assumed to be spherical [Bauer et al., 2001; Huang and Goltz, 2006], as seen in isotropic conditions in Chapter 2. When there is significant layered anisotropy or a confining layer Schroth and Istok [2005] predicted cylindrical flow of tracer. Mathias [2010] considered a plume to form an ellipsoid shape under homogenous anisotropic permeability conditions. However he concluded the effect of realistic heterogeneity on plume radius was unclear. While anisotropy is factored into the equations describing both DFTTs and PPTs [Sutton et al., 2000; Schroth and Istok, 2005], neither can directly quantify the properties of discrete media

layering within the tested aquifer volume. At the local scale sampled by dipole and push-pull tests (e.g. 0.5 -1m around a small diameter well), the assumption of homogeneity may introduce significant uncertainty to the estimated aquifer parameters, if discrete layers with different permeability were present within the tested zone. Xiang and Kabala [1997] found discrete layering to significantly affect hydraulic dipole flow tests and therefore it is also likely to affect DFTTs. Such heterogeneity will almost certainly bias the estimation of reactive transport parameters, due to, for example, the complicated flow system, poor tracer mass recovery and compound dispersion effects.

In this study, the effects of strong permeability/K contrast layering on the tracer signal obtained from dipole and push-pull tracer testing were evaluated using a bench-scale pseudo 2-D aquifer model. Others have used smaller artificial aquifer models to assess the effect of heterogeneity on longitudinal and vertical transverse dispersion [Chao et al., 2000a; Danquigny et al., 2004; Olsson and Grathwohl, 2007; Rolle et al., 2009] under uniform horizontal flow conditions. Some studies have employed visible light imaging to characterise tracer plumes without the disturbance induced by removal of water samples [Jaeger et al., 2009]. For the experiments described in this study, ultraviolet (UV) fluorescent imaging was used as it is less sensitive to background noise than visible light imaging [Huang et al., 2002]. UV imaging has previously been used to study dispersion [Gaganis et al., 2005], pore-scale heterogeneity [Corapcioglu and Fedirchuk, 1999] and biodegradation [Huang et al., 2003; Rees et al., 2007]. Fluorescein was used as a tracer because it exhibits negligible hydrophobic sorption to silica beads [Kasnavia et al., 1999]. The experiments in this study are at a larger scale of observation that the studies mentioned above to accommodate the desired scale of permeability layering.

3.3. **Method**

3.3.1. **Imaging box set-up**

An acrylic box with internal dimension of 150 cm x 75 cm x 2.6 cm and a wall thickness of 0.8 cm was constructed. End–chambers consisted of a slotted pipe, surrounded by a 0.1 mm mesh. 1 inch well screens were obtained from Marton Geotechnical Services and slotted manually with a thin kerf saw to give approximate 0.27 mm wide slots with an open area of around 7 % in the slotted segments. This is similar to the open area in larger, commercially available, slotted well screens. The non-slotted sides of the well screen were filed down to fit tightly in the centre of the box. A steel restraining bar was placed either side of the box, directly over the well screen, and was pinned together at each end. This reduced the amount of bulging occurring in the centre of the box due to the large weight of beads and water when packed. The position of the bar meant there was little effect on imaging. 300–355 μm (small) and 600-800 μm (large) glass silica beads were obtained from Potters Ballotini Ltd, to represent media with different hydraulic conductivities when packed. All beads were washed with dilute nitric acid and rinsed to remove any soda residue. All beads were wet packed in the box to a depth of 72 cm, with 1 cm of standing water on top. To represent simple physical heterogeneity in the box, 3 cm thick layers of the different bead type to the bulk material was placed at a height of 36 cm in the box. To represent a high-K layer in a lower K background the large beads formed the layer, with the small beads filling the rest of the box. The opposite was true when forming the low-K layer. The porosity of both types of beads was estimated to be ~0.37, by measuring the mass difference between dry and saturated beads. The hydraulic conductivity of the beads was calculated to be 7.15×10^{-3} m/s for the small beads and 3.26×10^{-2} m/s for the large beads, based on their porosity and median grain size [Bear, 1972; Corapcioglu and Fedirchuk, 1999]. These values were used for modelling the experimental results. This represents a K contrast of 4.55, which is within the range of variability of presumed homogenous sand aquifers, e.g. the CFB Borden aquifer in Canada has a K which varies by a factor of 30 [Sudicky, 1986]. The

layer was positioned centrally in the box to allow the well apparatus to be moved up and down to perform tests in different positions, without being affected by boundary conditions.

3.3.2. **Imaging configuration and calibration**

This is a concise form of the tracer calibration procedure; a fuller account is given in Chapter 2. A Canon EOS 450D digital SLR was used to capture the images. This was placed on a stable tripod focused on the centre of the box, with the back of the camera 65 cm away from the front face of the box. 350 nm UV black lights were placed above and below camera, secured to the table on a frame (see Figure 3-1). A black out curtain was placed behind the box. Experiments were performed in darkness apart from the UV light. Calibration tests were performed for the glass beads in a calibration box for fluorescein concentrations up to 40 mg/l. Solutions were evenly distributed in the box. Nineteen different camera configurations were tested to obtain the best calibration for images (see Appendix A). This range of calibrations and imaging procedure was based upon previous work by Bridge [2007] and North [2008]. The camera settings that provided the best calibration are shown in Table 3-1, with the first calibration for this set-up for both bead sizes shown in Figure 3-2. To account for variation in stock strength a new calibration was performed for each solution made. Also it was expected that image intensity would be greater in the centre of the image between the two light reflections than outside or on them. To account for this image intensity was calculated separately for different parts of the picture (between, on and out side the two light reflections). The calibration in Figure 3-2 is for the area of image between the two light reflections. No fluorescence degradation was seen under UV light, with no significant variation in fluorescence measured on a luminescence spectrometer for fluorescein solutions left in front of the UV lights for a similar period to tests performed. Br was used as a tracer to determine breakthrough curve concentrations in aqueous samples. Images were processed for green light intensity on Image J, a public domain programme (http://rsbweb.nih.gov/ij/). Images were normalised by the green light intensity of a

constant reflector. A test that analysed the growth of a spherical plume, Beer Lambert law calculations and isotropic tests (see Appendix A and Chapter 2), suggested that the maximum mean penetration depth of imaging was approximately 4-7mm into the beads. The imaging depth was considered suitable as the box could not be made thinner, good image calibrations were obtained and modelling could be performed in three dimensions.

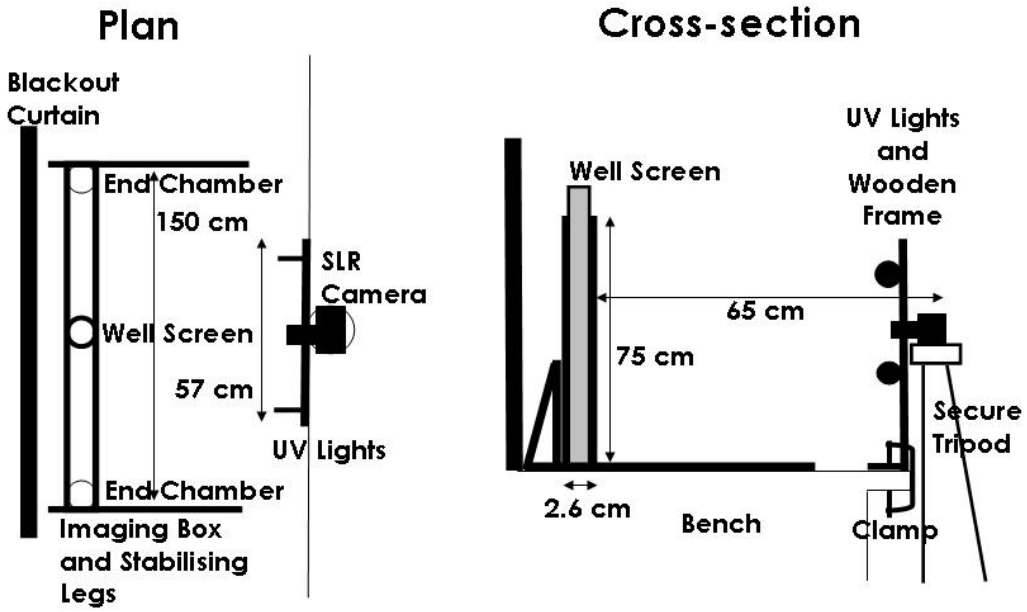

Figure 3-1: Schematic of imaging set-up for experiments. Not to scale

Table 3-1: Parameters and settings of SLR camera used in experiments

Parameters	Camera Settings
Angle	24mm
Flash	Off
White Balance	Custom
Focal Length	f8
Shutter Speed	1.3 seconds
ISO	100

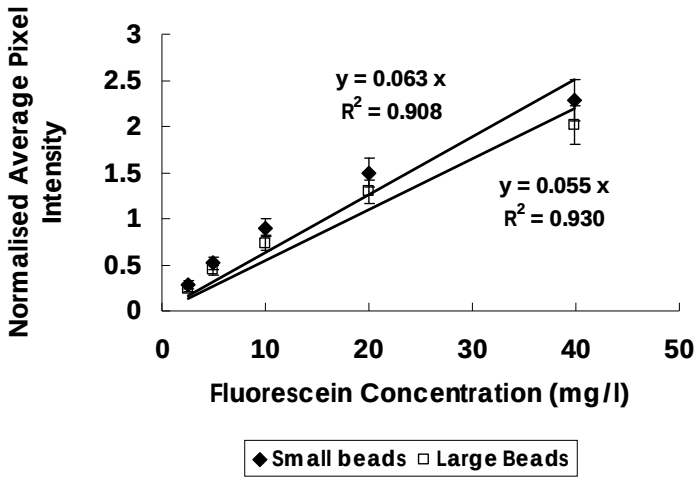

Figure 3-2: Initial image calibration plot for the different bead sizes in the calibration box for the camera settings in Table 3-1. Pixel intensity is measured in between the UV light reflections.

3.3.3. **Test set-up**

Before the first and between each subsequent test the box was flushed until there was no fluorescence in images. Stock solutions were made up to 40 mg/l fluorescein and ~320 mg/l Br. The water table in the box was kept constant by adding or removing water with a syringe during tests.

The in-well apparatus was made from alternating uPVC and silica disks mounted on a threaded stainless steel rod. Packers were formed from tightened groupings of the discs, with the silica forming a friction seal against the well screen. A length of 3 mm outer diameter silica tubing was passed through holes in the discs to allow flow of solution. For DFTTs the chambers were 3.7 cm, middle packer 6.7 cm and end packers 3 cm. For PPTs the chamber was 3.7 cm and packers 6.7 cm. In the tests the apparatus was adjusted so that the layer of different permeability/K was positioned where it would have a large impact and also represent an end member scenario. For DFTTs the tests were performed with the layer bisecting the injection chamber, extraction chamber and the middle packer. For PPTs the tests were performed with the layer bisecting the well chamber or displaced 3 cm below the centre of the well chamber. A 3 cm displacement was chosen as the layer is in a clearly different position to the chamber while still likely to affect tracer flow.

For all DFTTs tracer was pumped into the injection (top) chamber and from the extraction (bottom) chamber at ~5.6 ml/min, using an Istmatec ISM832A pump. The DFTTs were performed in recirculating mode to ensure equal injection and extraction flow rates. For conservative tracers whether the tracer is recirculated or not has no effect on parameters obtained [Sutton et al., 2000]. Before the start of tracer injection deionised water was pumped through the system at the same flow rate for approximately 10 minutes. This allowed the dipole flow field to reach hydraulic equilibrium. Tracer injection lasted 15 minutes. During this time flow was not recirculated back to the injection reservoir because tracer-free returning water would dilute the tracer stock (valve A closed, valves B and C open, see Figure 3-3). Rather, tracer was drawn from the stock reservoir and extracted water was directed to the extraction reservoir. After tracer injection, the closed circuit was reinstated and hence flow was recirculated for the rest of each test (valve A open, valves B and C closed). To collect samples valve A was temporarily closed and valves B and C opened for approximately 1 minute. The sample was collected in a vial over 30 seconds after 15 seconds of purging. Solution collected in the extraction reservoir during tracer injection and purging was injected into the box during these periods to minimise mass loss caused by sample collection. Images and aqueous samples were taken more rapidly at the start of the test (every 5 or 3 minutes) to capture breakthrough. This reduced after 90 minutes to 10 minutes and after 160 minutes to 20 minutes.

For all PPTs tracer was injected at 3 ml/min for 80 minutes. Then deionised water was injected at the same rate for 40 minutes as a flush solution, so the tracer migrated away from the well chamber. Images were taken throughout the injection phase every 5 minutes. During the extraction phase water was pumped out at 3 ml/min for 4 hours. Aqueous samples and images were collected regularly every 5 minutes during peak breakthrough, reducing after 2 hours to 10 minutes and after 3 hours to 20 minutes.

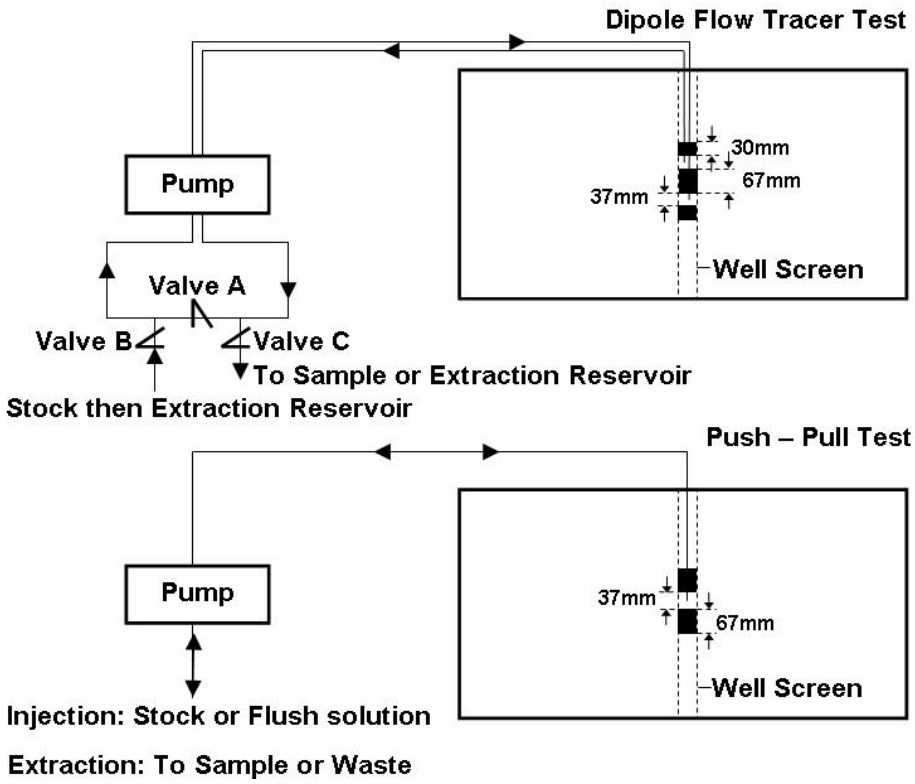

Figure 3-3: Diagram of test set-ups. The position of packers (filled areas) and chambers (open areas between packers) in the well screen varied with test performed. For the DFTT the injection chamber is the bottom chamber

Br was analysed on a Dionex DX-120 Ion Chromatograph. A RFIC™ Ionpac® A514A 4 x 250 mm Analytical Column was used for anion analysis with an eluent of 8 mM Na_2CO_3 and 1mM $NaHCO_3$ .Samples were diluted to the range of calibration on the instrument. The lower limit of reliable detection with a 10 µl sample loop was 0.6 mg/l. Analytical error was ± 2 %. Samples were stored in a -10 ºC refrigerator, prior to analysis.

3.4. **Results**

3.4.1. **Dipole flow tracer tests**

3.4.1.1. **Tracer breakthrough curves**

For DFTTs time was normalised to the characteristic time, t_c, of tracer breakthrough after Sutton et al [2000], to account for slight variations in flow rate between tests. This is the travel time between the closest edges of the injection and extraction

chamber, assuming flow along the well screen sides (see Figure 3-3). For these tests t_c was modified to assume 2-D radial flow from the well rather than 3D.

$$t_c = \frac{16\theta r_w \Delta(L-\Delta)}{Q} \tag{3.1}$$

$$t_d = \frac{t}{t_c} \tag{3.2}$$

Q is the pump flow rate, θ is the effective porosity of the packed beads, r_w is the well radius, Δ is half the chamber length, L is the distance between the centre of the central packer and centre of the chambers (also known as the shoulder length) and t is time. A test where a peak occurs around 1 or 2 t_d suggests short circuiting of flow around the central packer, with tracer taking the shortest route between chambers along the side of the well screen [Sutton et al., 2000]. Concentration was normalised to stock concentrations for all tests.

In all 6 tests, one single peak was observed at initial tracer breakthrough, which did not occur until well after 2 t_d. This suggests that no short circuiting around the well screen or a disturbed zone around the well occurred during the test and therefore the tracer has travelled through the bead pack. Breakthrough curves for the high-K layer experiments are shown in Figure 3-4. When the layer bisected the central packer the peak concentration was 0.28 C/C_0 after 4.14 t_d. When the layer bisected either the injection or extraction chamber the peak concentration arrived at approximately 5.65 t_d. There is only minor difference in the shape of these two curves: tracer breakthrough where the layer bisected the extraction chamber has slightly higher peak and tail concentrations. In all three curves, a second breakthrough peak occurs at ~10 t_d. This represents tracer that has recirculated through the closed injection/extraction plumbing and the fastest flow paths in the imposed dipole field. Similar recirculation peaks were noted by Sutton [2000] in field tests. The results show that the tracer breakthrough curve profile depends on the location of the high-K layer relative to the packer assembly.

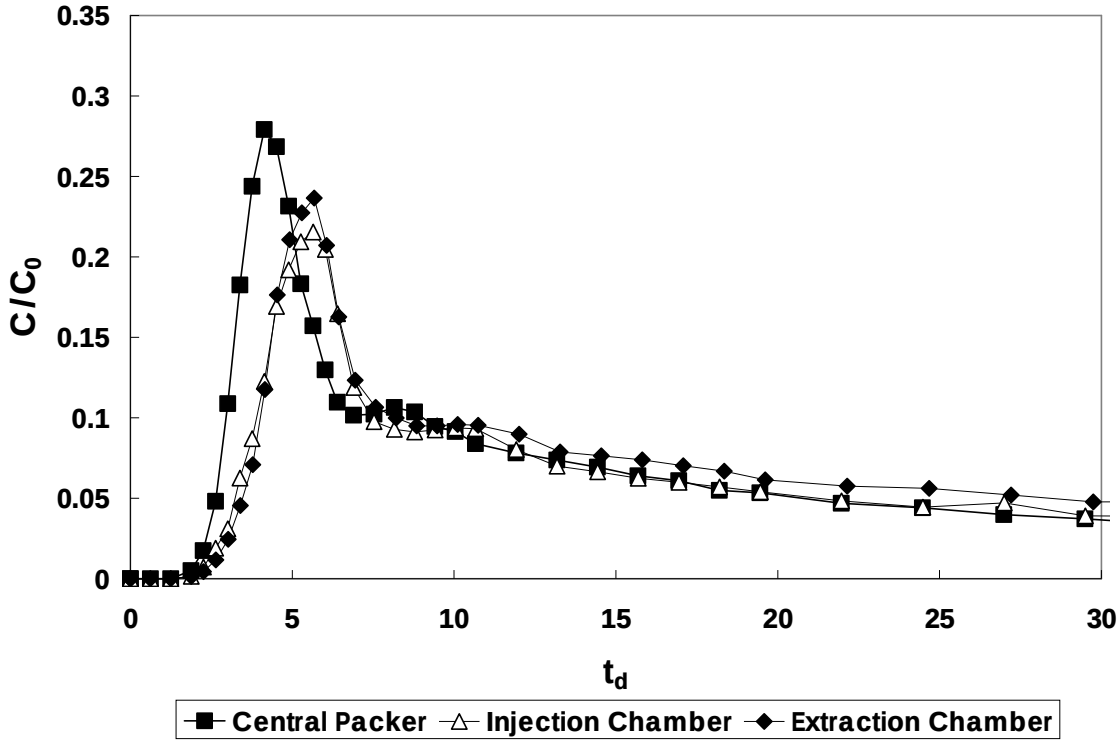

Figure 3-4: Breakthrough curves for DFTTs with a high-K layer present. The key refers to where the high-K layer bisects the in-well apparatus

Tracer breakthrough curves for the low-K layer experiments are shown in Figure 3-5. Again variation of breakthrough profile is seen when the layer is in different positions relative to the dipole apparatus. When the layer bisected either well chamber, the curves were of similar magnitude, shape, and peak concentration breakthrough time (approximately 4.15 t_d). There was a slight difference when the layer bisected the injection chamber: slightly lower peak concentration and earlier initial breakthrough. When the low-K layer was located in the middle of the central packer, tracer breakthrough occurred later (5.48 t_d) and was of lower magnitude (0.19 C/C_0). The breakthrough curve tail also has a lower concentration, indicating less tracer mass reaches the extraction chamber in this experiment, than the other low-K layer experiments.

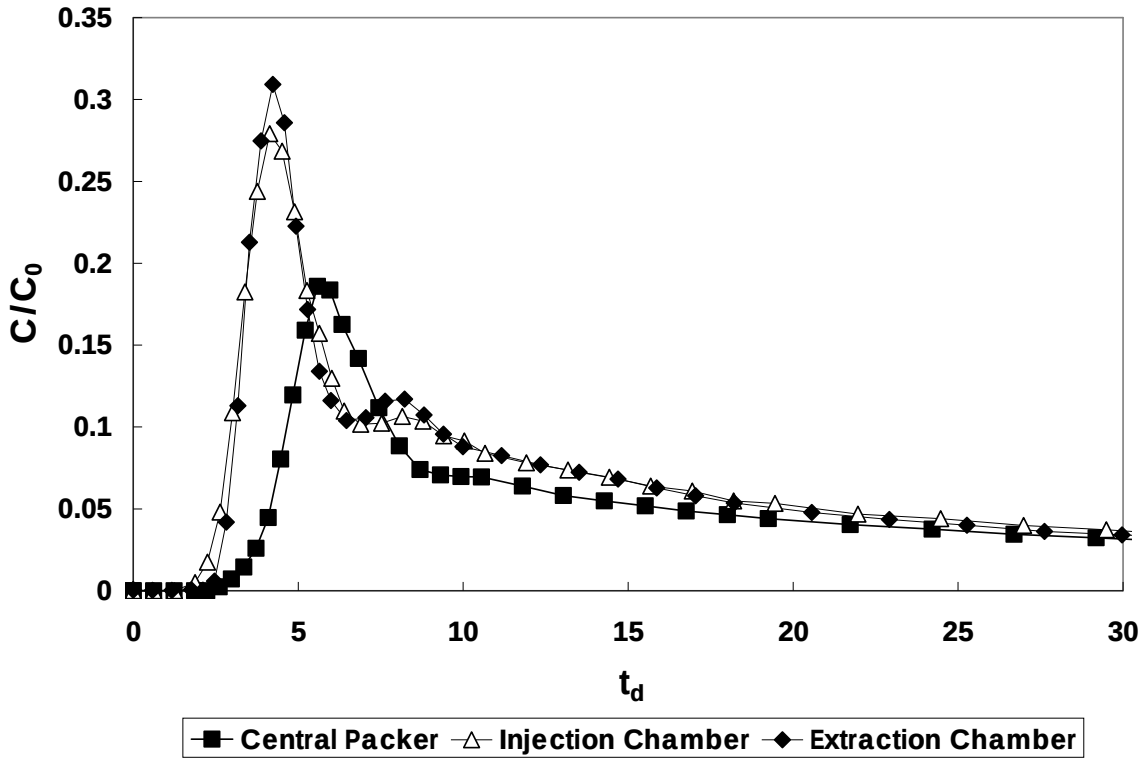

Figure 3-5: Breakthrough curves for DFTTs with a low-K layer present. The key refers to where the low-K layer bisects the in-well apparatus

3.4.1.2. **Imaging**

Green light intensity images for the DFTTs are shown in Figure 3-6 to Figure 3-11. All images are presented in false colour. Concentration increases with the sequence black/ dark blue/ light blue/ green/ yellow/ orange/ red/ white. Red and white represent concentrations close to input concentration. The contrast of the images was increased to show the plume geometry clearly at various times, as a priority. Consequently the image intensities do not all show the same relationship to concentration. The un-recirculated tracer forms a high contrast halo-shaped plume in all images. A fainter secondary halo representing recirculated tracer can be seen in all tests. For the tests with earlier extraction chamber breakthrough times this secondary halo occurs after 5 t_d, while for tests with a later breakthrough it occurs after 10 t_d. The time for the recirculation halo to be seen corresponds to the first arrival time of tracer at the extraction chamber, plus the time for it to travel through the plumbing back to the injection chamber. By the end of the test, this recirculation halo merges with other recirculated mass to form a central low concentration tracer cloud

surrounded by the halo of un-recirculated tracer that has migrated out along the slowest flow paths. In most tests, a small plume can be seen below the injection chamber after 30 t_d. This represents a small amount of tracer that has travelled down below the lower packer and probably into the open well screen below. It has then been slowly drawn out of the well under the background hydraulic gradient field. Image processing to show the main plume geometry has exaggerated the intensity of the lower plume.

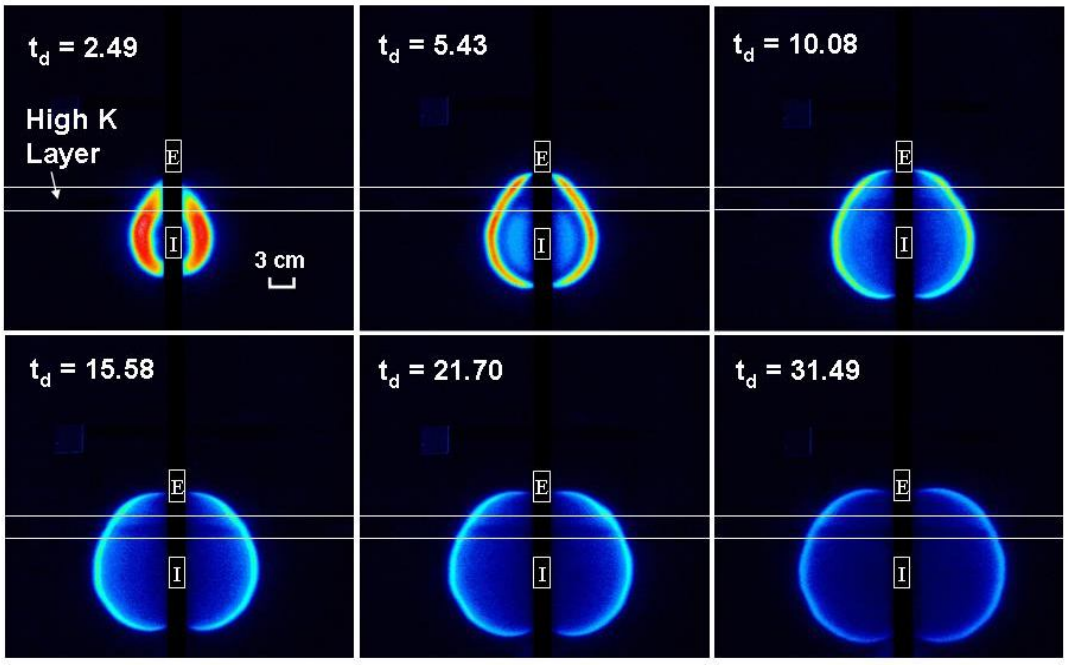

Figure 3-6: Green light intensity images during DFTT with a high-K layer bisecting the central packer. K = hydraulic conductivity.

When a high-K layer bisects the central packer (Figure 3-6), the early time tracer plume is elongated in the vertical direction, as mass rapidly migrates through that layer. Advection and longitudinal dispersion will both occur in the vertically upward direction. This should lead to early and slightly sharpened breakthrough, which is confirmed in Figure 3-4. The plume becomes more circular in shape over time as mass moves outward from the well along the more horizontal flow lines before bending upwards and back towards the extraction chamber. Along these outer dipole flow paths, the fraction of total travel distance that occurred in the high-K layer is

very small (<10%). There is good symmetry between the left and right side of the plume, implying that there is no ambient flow field present.

The presence of a high-K layer bisecting the injection chamber (Figure 3-7) allowed tracer to move horizontally outwards along that layer before turning towards the extraction chamber. This means there are proportionately more long flow paths compared to when the high-K layer was between the injection and extraction chambers. Thus tracer breakthrough is delayed and more dispersed (Figure 3-4). Over time, the plume shape becomes an asymmetrical ellipsoid, with a larger diameter half above the high-K layer (extraction side) and smaller bottom half. The asymmetry effect is amplified over time as an increasing proportion of recirculated tracer travels in the upper, long flow paths.

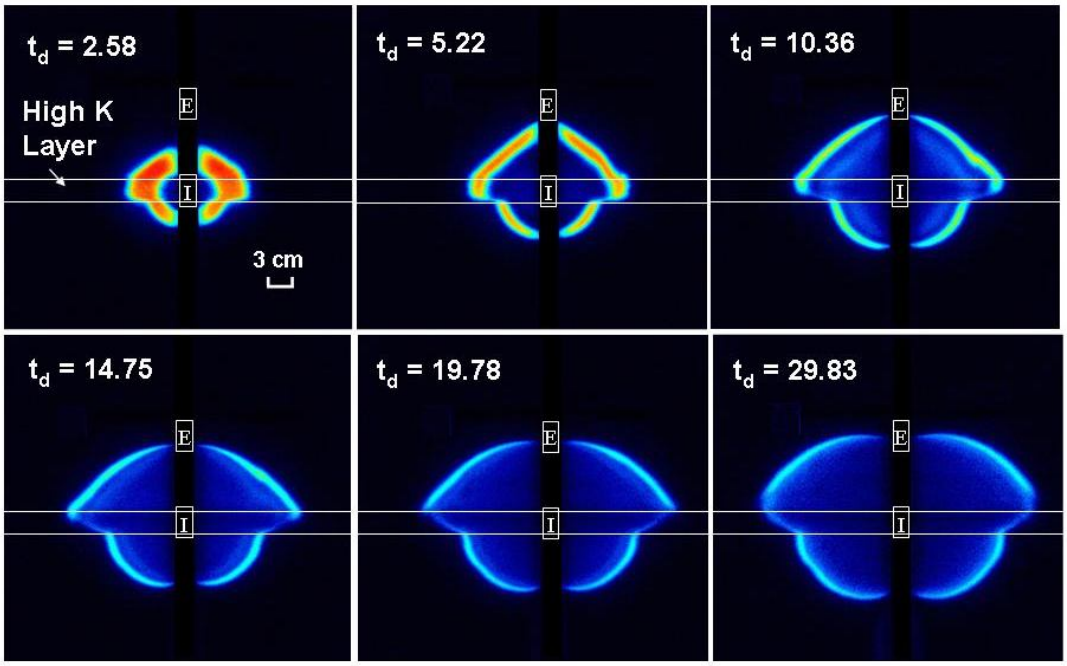

Figure 3-7: Green light intensity images during DFTT with a high-K layer bisecting the injection chamber.

When the high-K layer bisected the extraction chamber, it had very little effect on the tracer plume at early times (Figure 3-8). Proportionately more water is extracted from that layer than the surrounding lower K media, meaning that velocity in the dipole flow system near the well is reduced and tracer breakthrough is later and weaker than when the high-K layer is absent. The effect on the plume at later time is to flatten the

top, as flow entering the layer is refracted, and cause more tailing of tracer concentration (Figure 3-4).

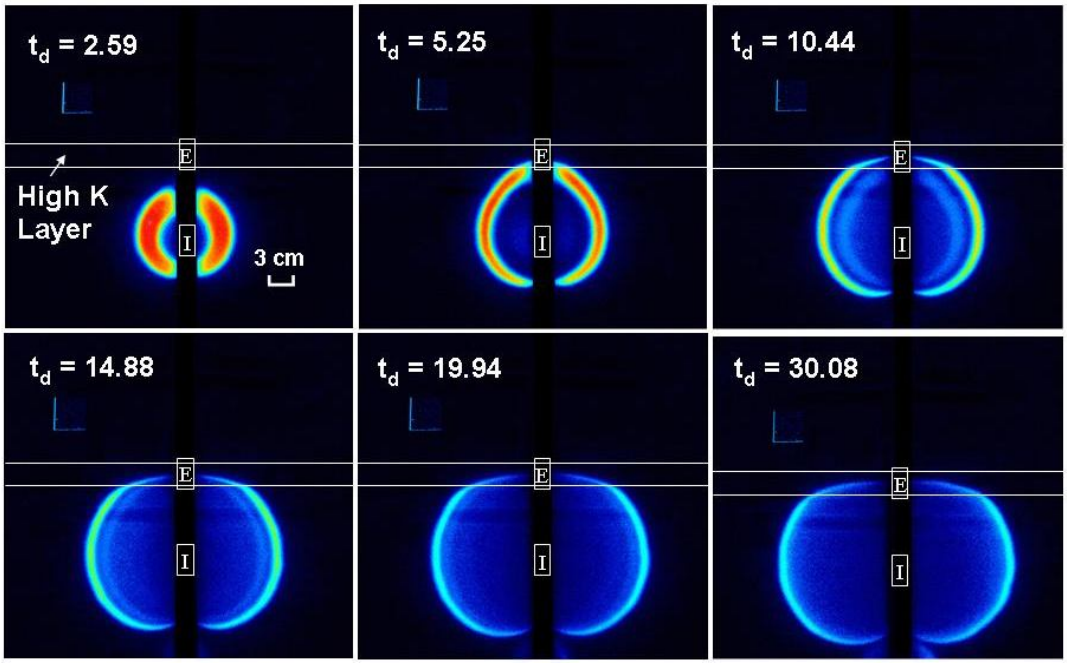

Figure 3-8: Green light intensity images during DFTT with a high-K layer bisecting the extraction chamber.

When a low-K layer bisects the central packer, the resulting tracer plume appears wider than when no layer is present (Figure 3-9), with the maximum lateral extent just below the layer. Since the flow lines are predominantly vertical midway between the chambers (where the low-K layer was located), there is no pronounced asymmetry in the plume either side of the layer. However, since tracer must travel longer paths as time passes, breakthrough is delayed. In this experiment, the tracer plume became increasingly asymmetrical, either side of the well screen at later time. This may have been caused by air being accidentally injected for a short period due to a plumbing failure. As the event occurred after the main peak, it was not considered to have significantly affected results. The box was repacked after this experiment to remove the problem.

When the low-K layer was positioned such that it bisected the injection chamber (Figure 3-10), initial horizontal migration of tracer was reduced and vertical migration

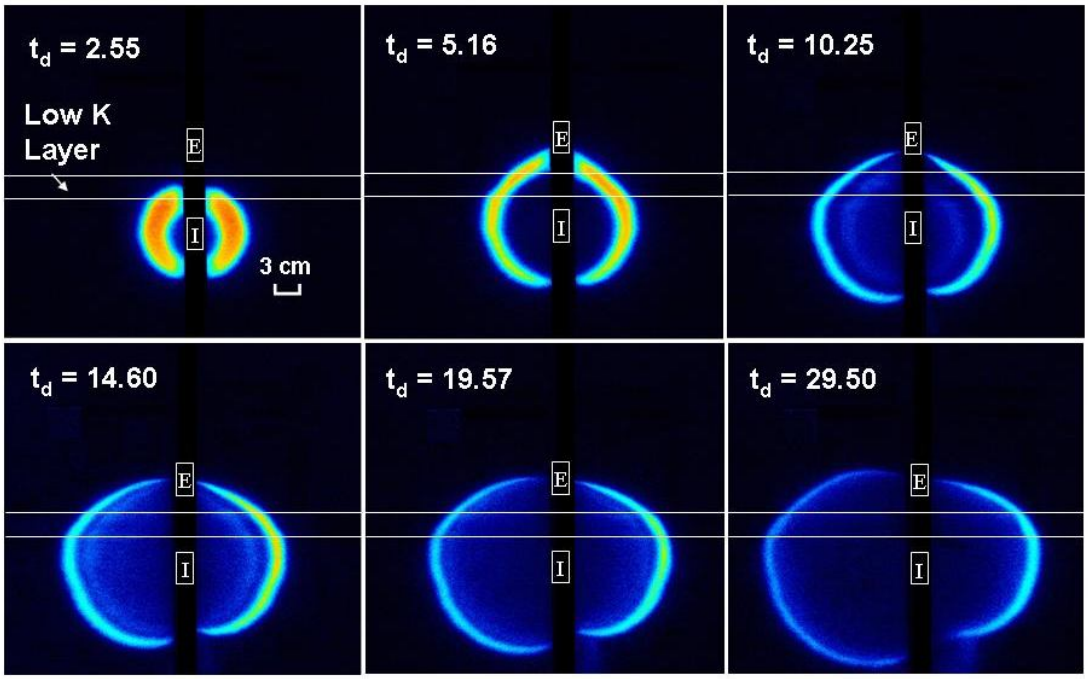

Figure 3-9: Green light intensity images during DFTT with a low-K layer bisecting the central packer.

between the chambers was proportionately higher. The overall result is quicker first arrival and less dispersed tracer breakthrough (Figure 3-5). The half of the plume below the layer is larger than the half above it, due to upwards flow of the tracer injected into the bottom high-K zone being impeded by the presence of the low K layer. Therefore the extraction chamber tracer breakthrough curve is expected to be dominated by the upper half of the tracer plume.

When the low-K layer bisected the extraction chamber (Figure 3-11), initial vertical migration of the tracer plume seems to be slightly increased. Enhanced vertical migration may indicate that the extraction drew water preferentially, and at a higher velocity, from the higher K beads just above and below the low-K layer. The result was early breakthrough compared with that resulting from a centrally located low-K layer (Figure 3-5) or no layer at all. At later time the top of the plume becomes more convex, suggesting migration of tracer along slower, more curved, flow lines through the layer.

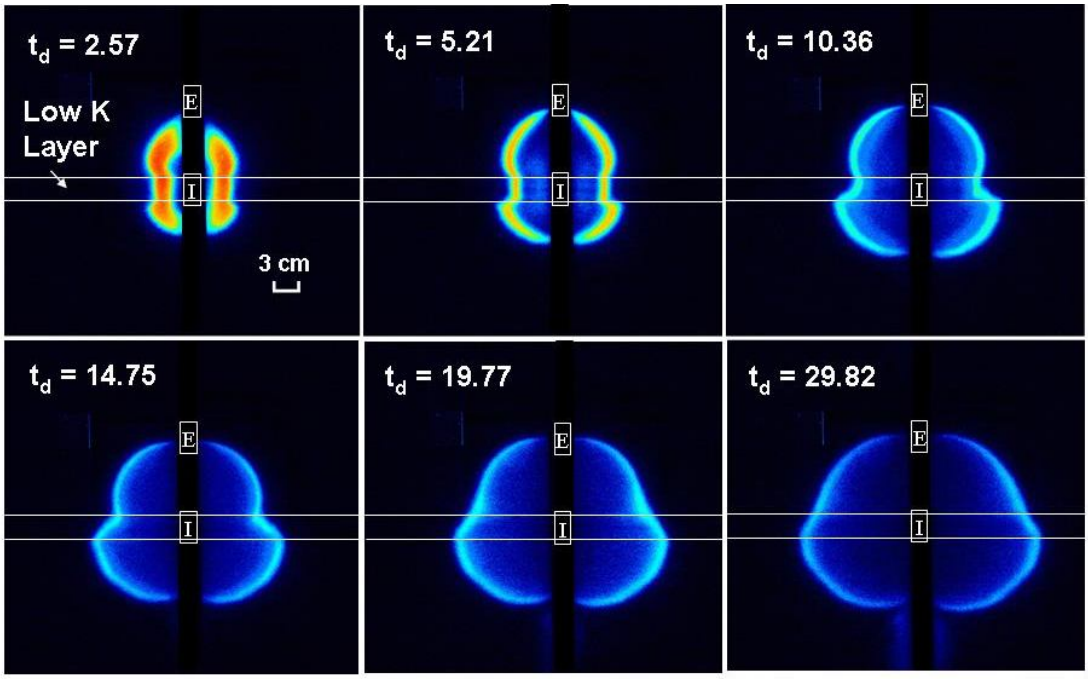

Figure 3-10: Green light intensity images during DFTT with a low-K layer bisecting the injection chamber.

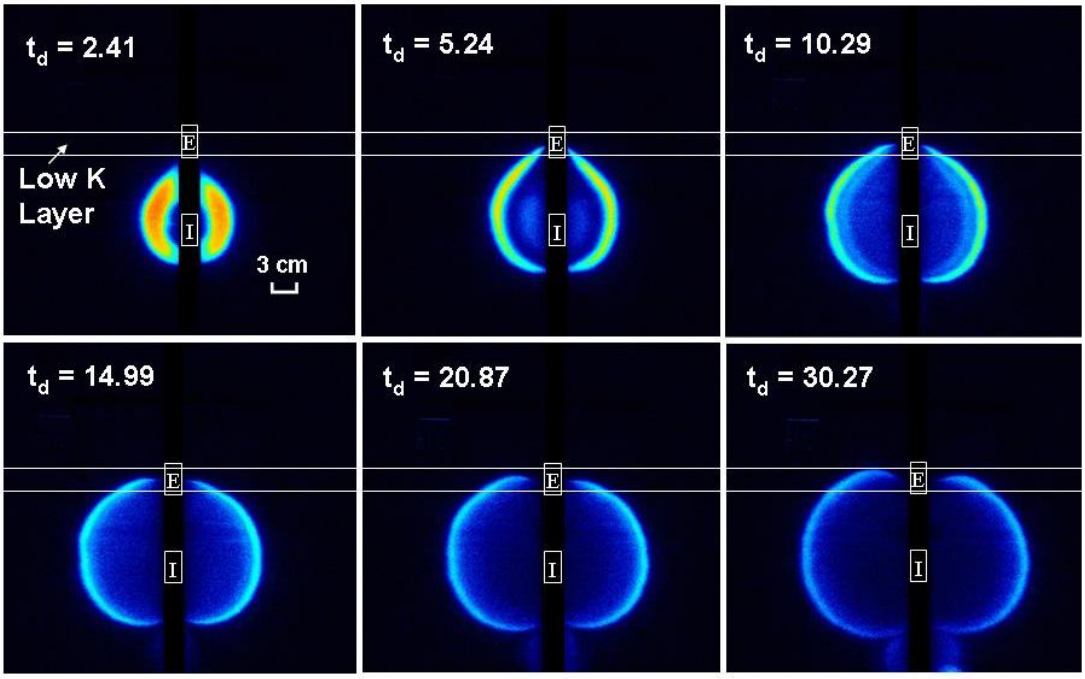

Figure 3-11: Green light intensity images during DFTT with a low-K layer bisecting the extraction chamber.

To analyse the effect of the layer on tracer migration further a point B (Figure 3-12) was chosen to measure image intensity for all images. This was 2 cm out from the

side of the well screen, parallel to the bottom of the extraction chamber on both sides. This observation point was chosen as it represents the flow lines close to the well screen that dominate contributions to the breakthrough curve (see Chapter 2). Also, as this location is close to the end of the tracer pathway (regardless of layer configuration), tracer was likely to have been affected by the high or low hydraulic conductivity layer present. The 2 cm step-out from the well screen should avoid any near-well transport effects, while allowing a reasonable pixel sample (~2000 pixels/ 0.9 cm x 0.9 cm) to be measured.

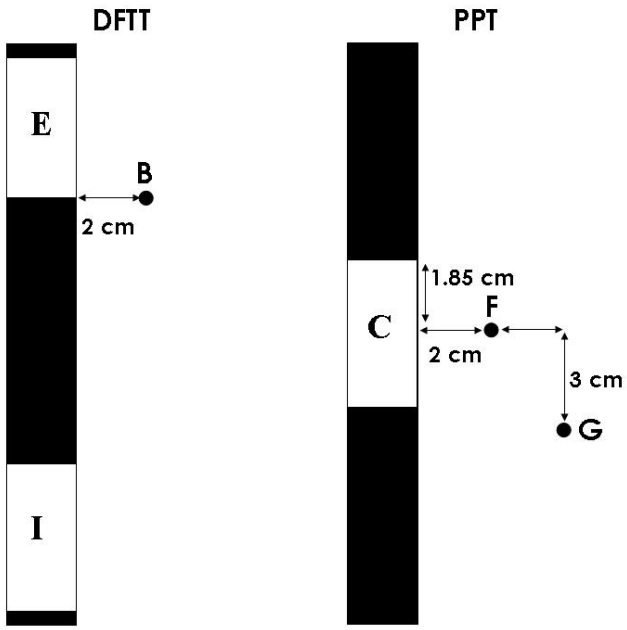

Figure 3-12: Position of imaging points used for analysis of tests. Images are analysed on both sides of the well.

The arrival of the tracer cloud at the observation point when the high-K layer was located across the central packer showed some asymmetry between the left and right sides of the well (Figure 3-13). This may be due to slight variation in porosity, bulk density, thickness and/or elevation of the layer. The average arrival time was approximately 7.5 t_d, which is later than that observed in the extraction chamber concentration history (~4 t_d). The higher conductivity in that layer may have deflected flow lines in towards the well annulus, drawing tracer in. As such, the observation point did not sample the higher concentration paths. This suggests that this case is more sensitive to slight variations in layer thickness, which may cause asymmetry.

The peak concentration is ~2 times higher than the extraction breakthrough curve peak. This indicates that the imaging evidently sampled a relatively high fluorescence intensity path, while the extraction samples are an integration of all paths.

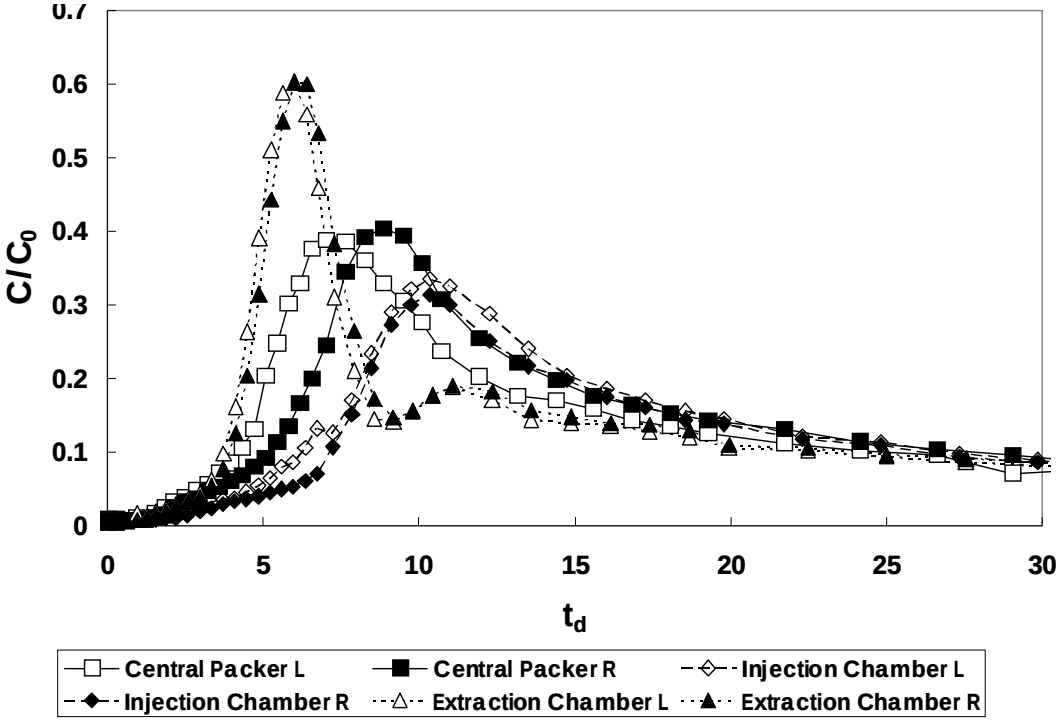

Figure 3-13: Fluorescein concentrations for imaging point B, in DFTT experiments with a high-K layer present. Results are shown for data taken to the left and right side of the well screen. The key refers to where the high-K layer bisects the in-well apparatus

When the high-K layer bisected the injection chamber, the tracer peak arrived at ~10 t_d, which is about 4.5 t_d later than observed in extraction data, and of a similar relative concentration magnitude (Figure 3-13). As noted previously, tracer preferentially migrated along the high-K layer away from the well, and therefore had to travel further overall. This caused the arrival at the observation point to be later than at the extraction chamber, suggesting it did not sample the primary tracer migration paths. The reduced peak concentration relative to when the layer bisected the central packer indicates that the tracer has travelled further to reach the imaging point, assuming constant dispersion.

A normalised tracer peak concentration of ~0.6 arrived at the observation point at approximately 5.5 t_d when the high-K layer bisected the extraction chamber (Figure

3-13). This arrival time is similar to that obtained from extraction samples, but the relative concentration is ~3 times higher. This suggests that extraction chamber concentrations are heavily diluted due to preferential extraction of water in the high-K layer. Preferential extraction would also quicken the breakthrough of flow lines further out, that travel a greater distance in the layer and slow the flow of closer flow lines, leading to later extraction chamber breakthrough (Figure 3-4).

The low-K layer produced the opposite behaviour to the high-K layer cases. When the low-K layer was placed across the central packer, peak tracer arrival at the left and right side of the well was similar to that of the high-K layer located in the same place (Figure 3-14). This indicates that layers between the hydraulic chambers do not significantly change tracer flow line geometry close to the well, but may affect arrival at the extraction chamber, commensurate with its thickness and permeability.

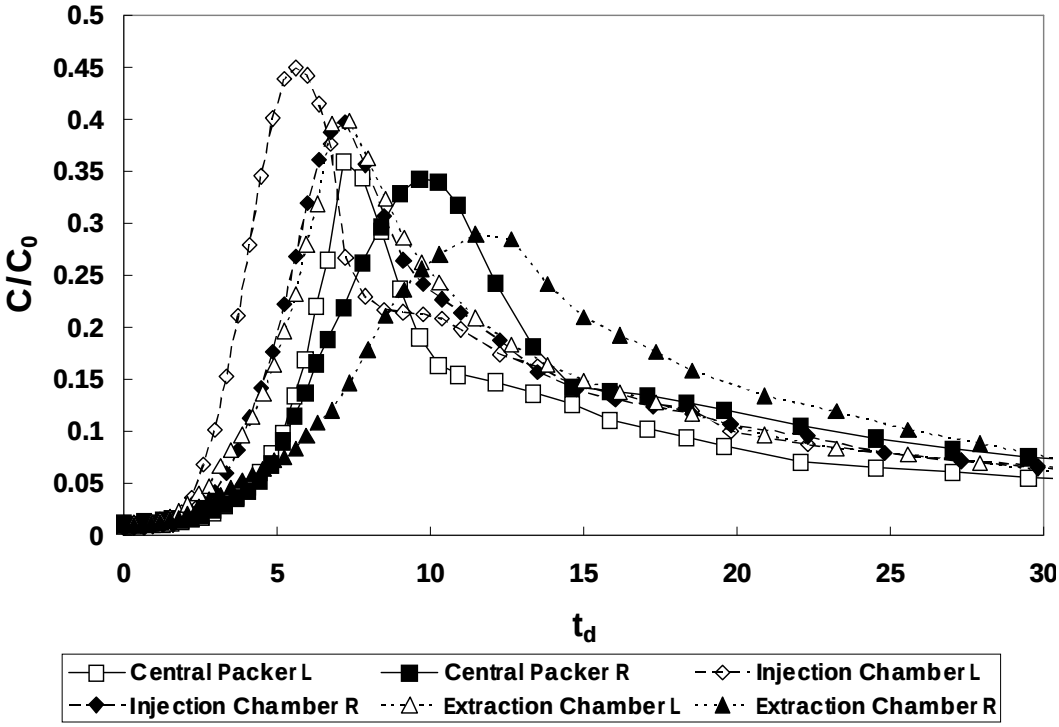

Figure 3-14: Fluorescein concentrations for imaging point B, for DFTT experiments with a low-K layer pre sent. Results are shown for data taken to the left and right side of the well screen. The key refers to where the low hydraulic conductivity layer bisects the in-well apparatus.

When a low-K layer was placed across the injection chamber, mass was preferentially introduced into the higher K beads above and below the layer. Figure 3-10 clearly

shows asymmetrical tracer distribution caused by that preferential injection. The tracer above the layer is drawn to the extraction chamber and therefore the tracer halo does not grow outwards over time. The quick flow lines are shown by the image point peak breakthrough at ~6 t_d earlier than the other low K experiments (Figure 3-14). The overall rapid arrival is also mirrored in the extraction chamber breakthrough curve (Figure 3-5).

With the low-K layer was located across the extraction chamber, preferential extraction occurred from the higher K beads above and below the layer. Overall tracer breakthrough was similar to when the layer was across the injection chamber (Figure 3-5), but tracer arrival at the observation points was later (Figure 3-14). This perhaps reflects that primary tracer pathways did not pass in the vicinity of the imaging points. In all low-K layer tests, there was much more variability in left and right side tracer distributions, suggesting that differences in bulk density, thickness and/or elevation of the layer might cause asymmetrical flow. The right side was always delayed relative to the left, supporting the hypothesis of a hydrogeological bias. This had a profound effect on the concentrations estimated at the observation point. The greatest left/right asymmetry occurred when the low-K layer was across the extraction chamber. If the layer was thinner on the left side, more high K beads would have been in hydraulic connection with the well, resulting in preferential extraction and therefore quicker tracer arrival than on the right side. This effect would be obscured in the extraction well data, which homogenised all the flow lines into an integrated breakthrough.

3.4.1.3. **Tracer mass**

Tracer mass in the system was compared between that calculated from aqueous samples and that obtained from imaging analysis. Mass was normalised to the known total injected mass so that the mass of fluorescein and Br could be directly compared. Mass from aqueous samples was calculated from Br concentrations assuming that each sample took half a minute to collect. The rate of water injection/extraction, and therefore the injected tracer concentration, was assumed to be constant during tracer

injection. From the images, mass in the box was calculated by measuring the fluorescent light intensity in a 2-D field containing the tracer plume, and calculating the volume of water from the field dimensions, box depth and measured bead porosity. The entire image was not used to calculate mass as signal in the background noise led to an overestimation. Slight increases in image-estimated mass in Figure 3-15 and Figure 3-16 are due to different image sample sizes, leading to a slight increase in background noise. At early times, mass is slightly underestimated from the images, compared to that obtained from dissolved concentrations. This may suggest that the box is not fully mixed across the depth of view. Due to the curvature of the central well tracer may preferentially migrate nearer the middle of the bead pack, which lies on the limits of the average imaging penetration depth. Alternatively the image calibration used (Figure 3-2) may have underestimated tracer concentrations at high values. For the difference between mass estimates to be due to analytical error in measurement of Br^-, breakthrough concentrations would have to be underestimated by ~ 50 %. This is unlikely as the analytical precision was good.

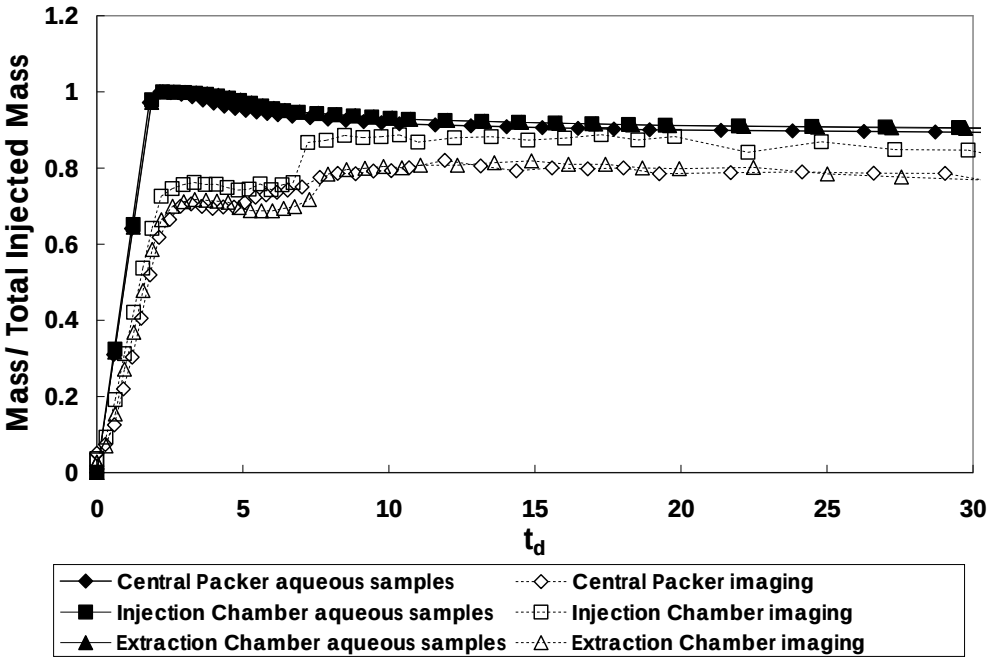

Figure 3-15: Fluorescein mass estimated from aqueous samples and imaging for DFTTs performed with a high hydraulic conductivity layer. The key refers to where the high hydraulic conductivity layer bisects the in-well apparatus.

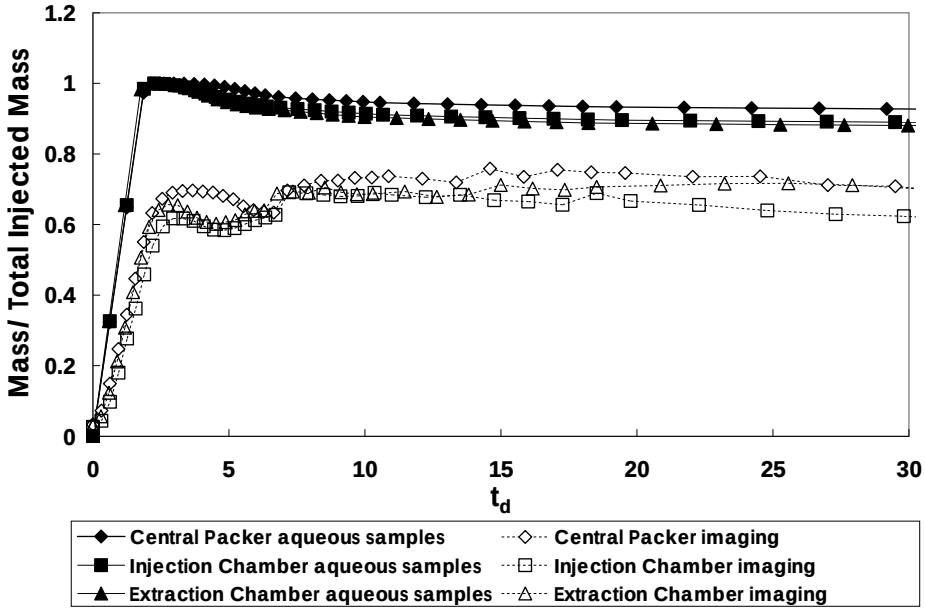

Figure 3-16: Fluorescein mass estimated from aqueous samples and imaging for DFTTs performed with a low-K layer. The key refers to where the low K-layer bisects the in-well apparatus.

3.4.2. **Push-pull tests**

3.4.2.1. **Tracer breakthrough curves**

Time was normalised in the PPT injection phase by dividing volume injected at a point (V) by the total volume injected over the entire phase (V_i). This assumed a constant flow rate. Time was normalised for the PPT extraction phase by dividing the total volume extracted at a certain point (V_e) by V_i. There is no significant difference in breakthrough curves for these tests (Figure 3-17). This is not unexpected as the normalised PPT extraction phase breakthrough curve mean arrival time (V_e/V_i) is largely independent of tracer velocity. The breakthrough peak is broad and with a similar concentration for all tests. Rising and falling limbs also have similar geometry. This implies that dispersion is comparable in all tests. The falling limb breakthrough curve has a slightly higher dispersion and tail concentration for the experiments with a low-K layer present. This may indicate some tracer being retained in the low-K layer for a short time. The earlier breakthrough when a high-K layer bisects the chamber, compared with the other experiments, may partly reflect under measuring of extraction flow rate.

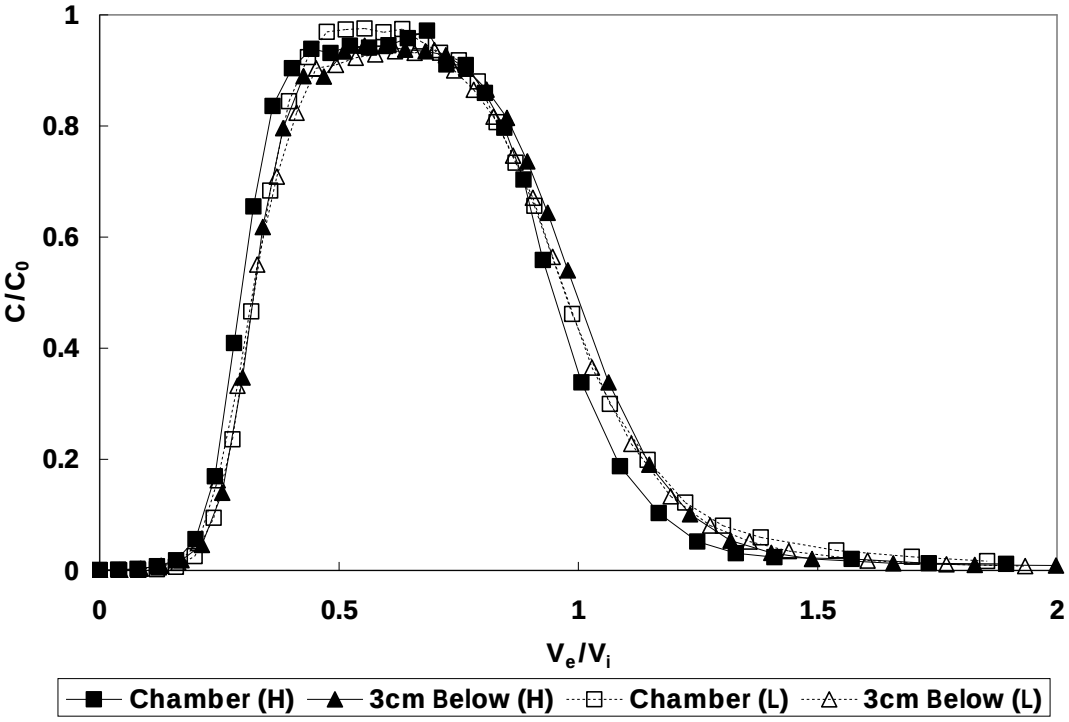

Figure 3-17: Well chamber extraction phase breakthrough curves for Br during PPTs performed. The key refers to the position of the high (H) or low (L) K layer.

3.4.2.2. **Imaging**

Image mosaics of the tracer cloud geometry during PPTs are shown in Figure 3-18 to Figure 3-21. There is good symmetry between the left and right side for all experiments, indicating a consistent layer thickness and permeability on either side of the box, and lack of an ambient hydraulic head gradient. In each test, late time extraction images show two near vertical tendrils of fluorescence above the screen. These are small amounts of tracer that reached the open well screen above the upper packer during the injection phase, which is drawn back down during extraction. Fluorescence intensity of these features is exaggerated in the later extraction phase images due to the processing procedure and the amount of tracer in these tendrils is insignificant compared with the total mass injected in each experiment. Close inspection of the images suggests that the extraction phase tracer cloud has rougher boundaries than the injection phase, particularly near the boundary between bead layers. This probably reflects flow refraction between the two layers.

The presence of a high-K layer bisecting the chamber (Figure 3-18) enhanced initial horizontal migration of tracer mass and also reduced vertical migration. Overall the tracer cloud forms a flattened diamond shape after injection, as tracer reaches twice the distance from the well in the high-K layer compared with the host media. The high-K layer also enhances the rate of tracer extraction. During extraction (especially at 0.81 V_e/V_i), there is higher fluorescence intensity near the interface between bead types. This indicates a velocity gradient across the media interface, where higher velocity is found in the centre of the high-K layer.

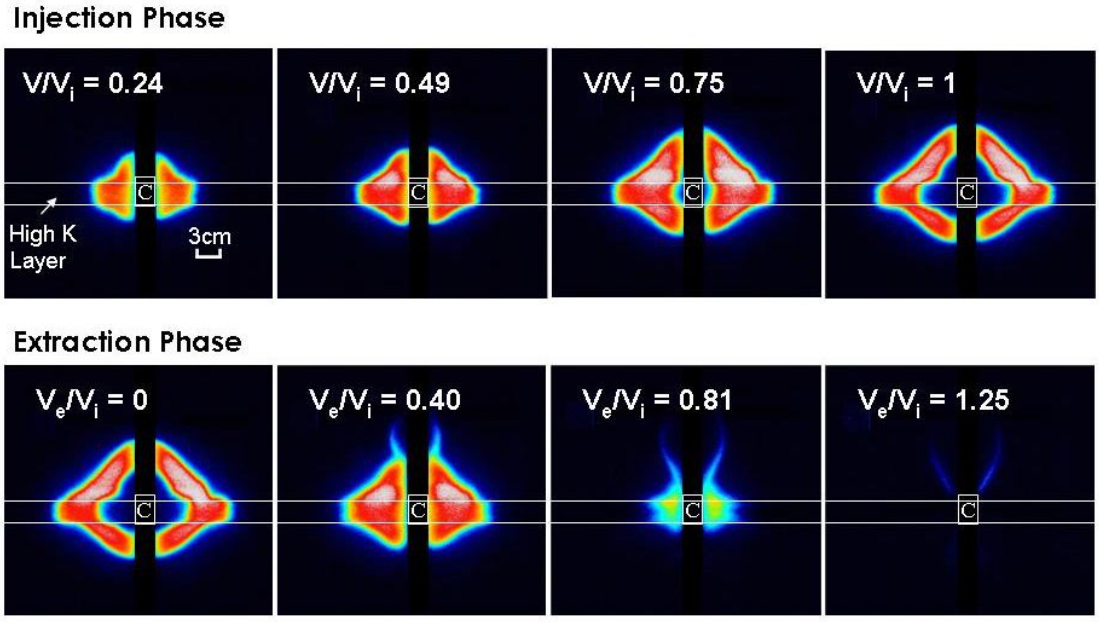

Figure 3-18: Green light intensity images during PPT with a high-K layer bisecting the well chamber. K = hydraulic conductivity

The effect of the layer is also evident when it is located 3 cm below the centre of the well chamber (Figure 3-19). During injection, tracer has migrated down and along the high-K layer, and also below the injection screen a greater distance than above it (facilitated by the layer). This suggests that if there is a more conductive layer near the injection screen, tracer will follow the resulting hydraulic perturbation. The presence of the layer below the chamber decreases tracer loss to the open screen above the upper packer, while slightly increases loss to the open screen below the lower packer.

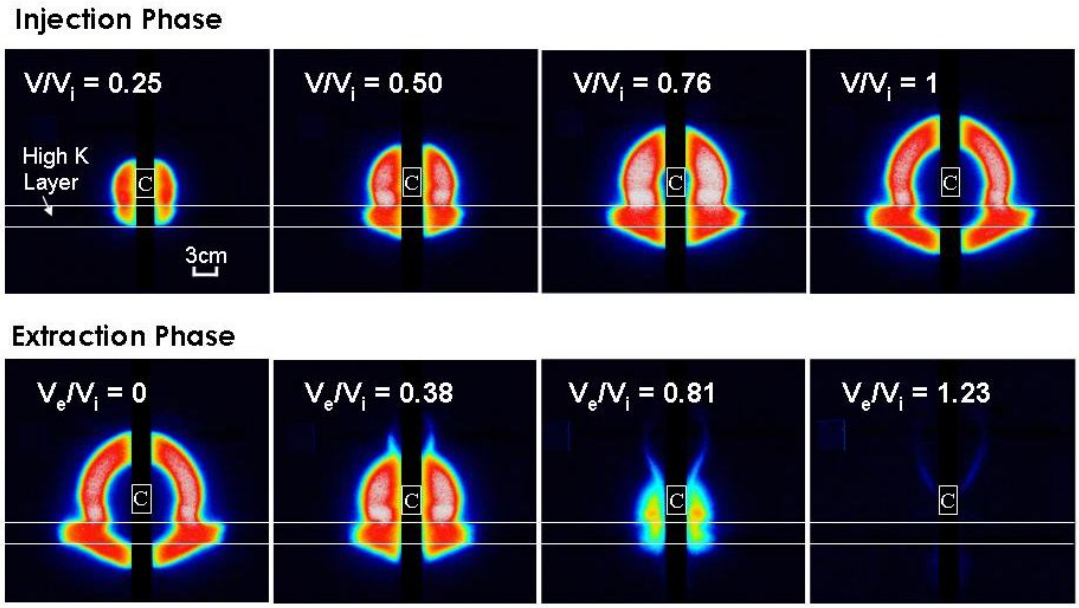

Figure 3-19: Green light intensity images during PPT with a high-K layer 3 cm below the centre of the well chamber.

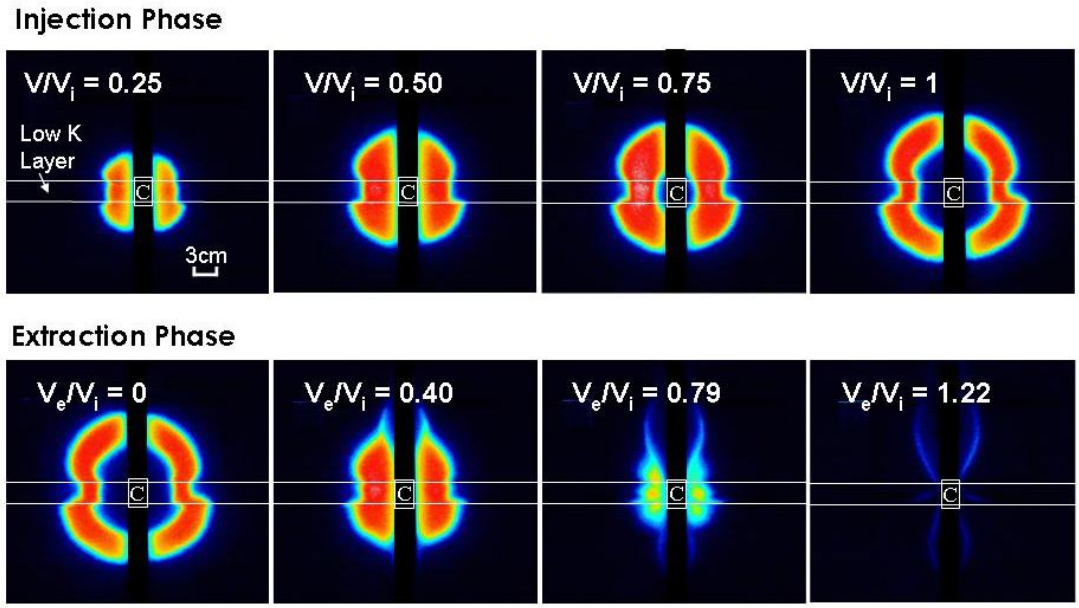

Figure 3-20: Green light intensity images during PPT with a low-K layer bisecting the well chamber.

When a low-K layer bisects the well chamber (Figure 3-20) horizontal migration of the tracer is decreased but vertical migration increased. The greater vertical migration increases the loss of tracer to both open well segments, shown by the tendrils in the later extraction phase images. A small amount of mass is retained in the low-K layer at 1.22 V_e/V_i and highlights the impact that the location of this layer has on tracer tailing.

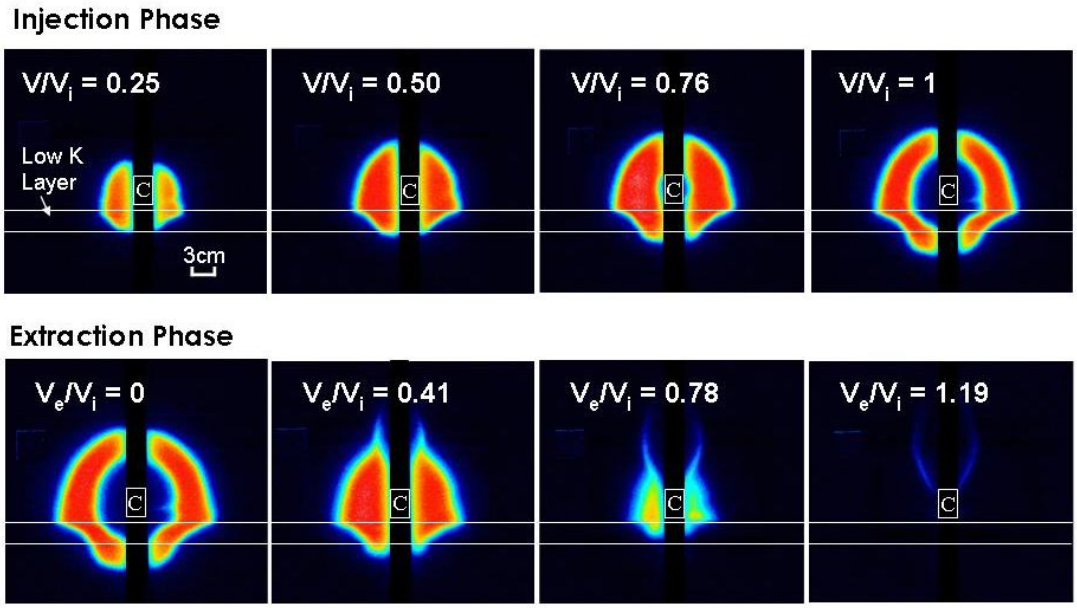

Figure 3-21: Green light intensity images during PPT with a low-K layer 3 cm below the centre of the well chamber.

When the low-K layer was positioned 3 cm below the chamber, it caused a similar reduction in horizontal flow (Figure 3-21). Most of the tracer cloud is above the layer, with only a small amount below it at the end of the injection phase. During the extraction phase tracer does not seem to be retained for a long period in the low-K layer, as opposed to when the low-K layer bisects the well chamber. The difference may be due to small variations in permeability, or tracer could have been retained in the layer outside the imaging penetration depth.

3.4.2.3. **Tracer mass**

Tracer mass in the system, calculated from aqueous samples and imaging, is shown for PPTs in Figure 3-22 and Figure 3-23. The variation is similar between imaging and aqueous sample results. There is a slight step increase two thirds of the way through the image-derived injection phase cumulative mass curve for the case where the high-K layer bisected the chamber. This is probably due to an increase in pixel sample size, which incorporated a patch of high background noise. Estimated mass from imaging for most experiments is a quarter to one third less than that estimated from aqueous samples. This suggests that the centre of mass in the experiments is towards the middle of the bead pack, outside of the mean imaging penetration depth

or the image calibration used may have underestimated tracer concentrations at high values, as was hypothesised for DFTTs. Mass balances from aqueous samples suggest that all fluorescein has been removed by 1.5 V_i/V_e into the extraction phase. However Br is still evident in the breakthrough curve at this time and mass is still estimated from the images. Concentrations of Br may have been slightly overestimated during chemical analysis, even though the analytical precision was good. Higher mass in the imaging estimates at late extraction phase time may partly reflect background noise interference, but some is also due to tracer still present in the box. The imaging data tail which had the greatest mass at extraction phase late time was when the well chamber was bisected by a low-K layer. This corresponds to breakthrough curve data, as this test showed the greatest dispersion on the falling limb.

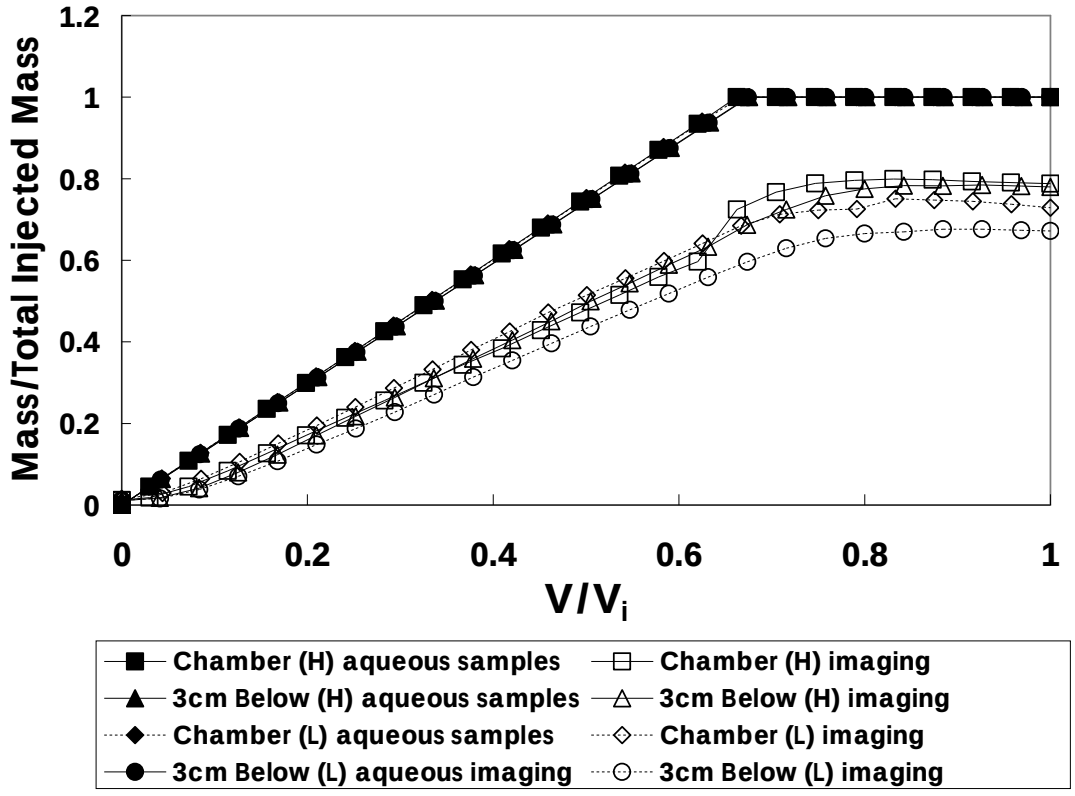

Figure 3-22: Fluorescein mass estimated from aqueous samples and imaging during the injection phase for PPTs. The key refers to the position of the high (H) or low (L) K layer.

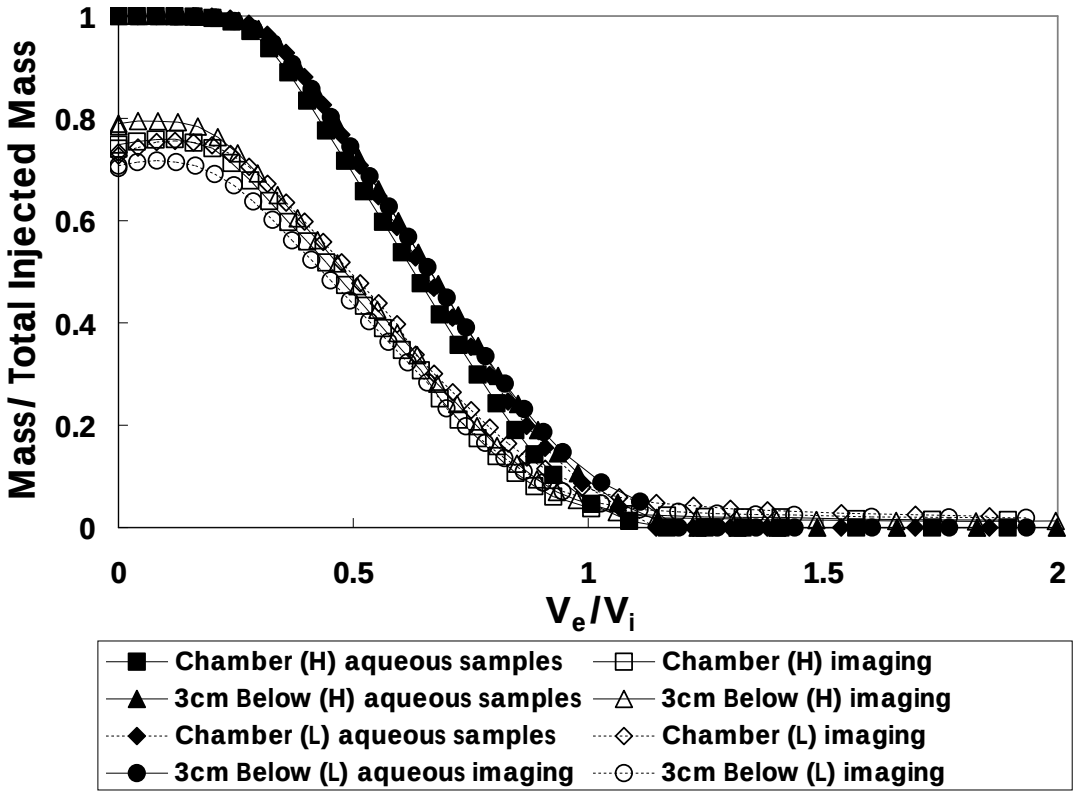

Figure 3-23: Fluorescein mass estimated from aqueous samples and imaging during the extraction phase for PPTs. The key refers to the position of the high (H) or low (L) K layer.

3.5. **Modelling**

3.5.1. **Dipole flow tracer tests**

3.5.1.1. **Tracer breakthrough curves**

HydroGeoSphere© (HGS) is a fate and transport model, supported by the University of Waterloo [Therrien et al., 2005]. HGS predictions have been shown to correspond well to the analytical solution of a tracer test in a push-pull system [Gelhar and Collins, 1971], and analytical solutions of solute transport in a horizontal non-recirculating dipole flow system in isotropic and heterogeneous conditions [Hoopes and Harleman, 1967; Wilson and Miller, 1978; Zheng, 1990]. Aquifer properties (e.g. porosity, dispersivity, hydraulic conductivity) can be applied in discrete zones and reactive tracer transport can be modelled.

HGS was chosen as it has been shown to correspond to the analytical solutions of complex flow systems (see above) and can be finely discretised. HGS does not incorporate mass recirculation, so DFTT extraction well concentration histories and imaging-derived tracer histories could only be modelled until the end of the non-recirculated tracer peak breakthrough and start of the concentration tail. The conservative parameters (hydraulic conductivity anisotropy and dispersivity) which can be obtained from the DFTT breakthrough curve only depend on the initial breakthrough and tracer peak, which have been shown not to vary between non-recirculating and recirculating conditions [Sutton et al., 2000]. Therefore estimation of conservative parameters from modelling should not be affected by HGS not recirculating mass. The tracer tail in DFTTs is important for the study of biodegrading tracers. The imaging box was assumed to be dominated by 2-D flow and transport, but the model domain was discretised in 3-D. This was done as some 3-D variability was expected due to the well screen being curved, which was expected to cause some minor radial flow. HGS can overestimate diffusion if the grid discretisation is too large [Therrien et al., 2005]. To limit this 2 mm, 3.25 mm, 2 mm (x, y, z) grid discretisation was used near the well screen. Using a smaller grid discretisation did not significantly vary the modelled breakthrough curves. Packers were defined as immobile zones and the aquifer model walls were automatically defined as no-flow boundaries. A dispersivity of 0.001m was used in the models, as this provided the best fit to data in isotropic tests (see Chapter 2).

Tracer breakthrough curve data was compared with model predictions for the discrete bead layer configuration tested and isotropic conditions (Figure 3-24). There are slight differences between the layered and isotropic simulations, and the experimental data is simulated better using the layered model. When a high-K layer bisects the central packer, peak tracer breakthrough occurs earlier and at higher magnitude than when no layer is present. However, when it bisects either chamber tracer breakthrough is slightly later (given the small scale of these experiments, the differences are significant). When a low-K layer bisects the central packer peak tracer breakthrough

is later with decreased concentration compared with isotropic conditions. However, when it bisects either chamber simulated peak tracer breakthrough is earlier with increased concentration. Two similar signals may represent different aquifer conditions. For example a high-K layer bisecting the central packer would look similar to a low-K layer bisecting either well chamber.

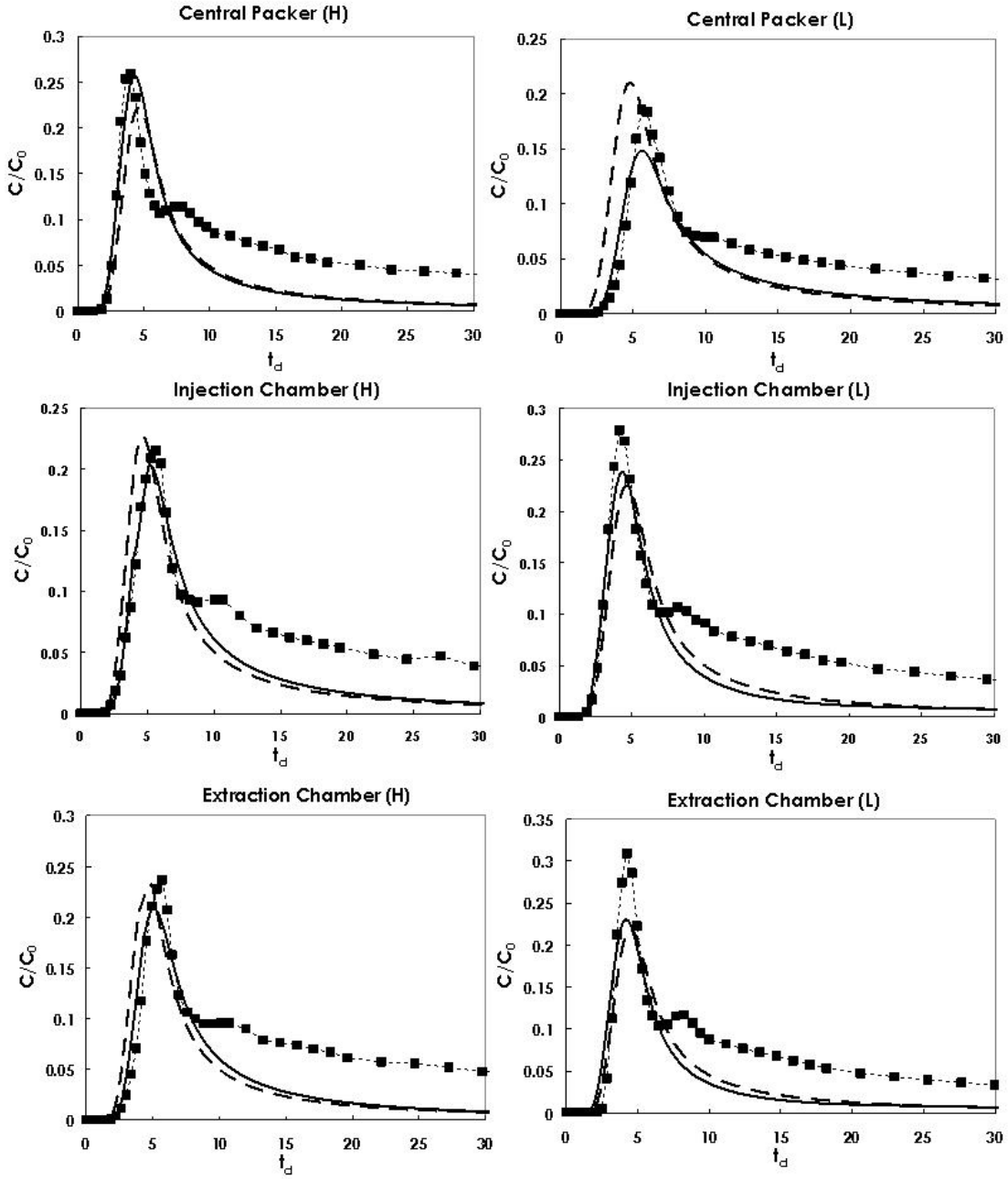

Figure 3-24: Simulated DFTT breakthrough curve data. The solid line is the predicted breakthrough under test conditions and the dashed line under isotropic conditions. Each test is labelled by the position of the high (H) or low (L) K layer.

Table 3-2: Estimated model fit parameters for DFTTs. Model efficiency applies to the fitting of the main breakthrough peak, but not the tail.

Test	Peak Time Model/Data	Peak Concentration Model/Data	First Arrival Time Model/Data	Model Efficiency (%)
Central Packer (H)	1.07	1.00	0.90	85.50
Injection Chamber (H)	0.91	0.94	1.12	98.03
Extraction Chamber (H)	0.91	0.88	0.91	93.06
Central Packer (L)	1.00	0.80	0.99	92.65
Injection Chamber(L)	1.06	0.86	1.07	96.53
Extraction Chamber (L)	0.97	0.75	0.76	89.43

The model fit to experimental data was analysed by comparing test condition predictions with actual peak times and concentrations, and first arrival time. The model efficiency [Berthouex and Brown, 2002; Bolster and Hornberger, 2007] of predicted tracer breakthrough fitted to the main breakthrough peaks was also estimated (Table 3-2). These parameters only concern the breakthrough peak and are therefore not affected by the absence of tracer recirculation in the HGS model (see above). Peak time in DFTTs is linearly related to the bulk K anisotropy ratio, if modelling a homogenous media, and longitudinal dispersivity is inversely proportional to $t_{arrival}$ (5% peak)/t_{peak} [Sutton et al., 2000]. A good fit to peak time and concentration would also enable the retardation of a sorbing tracer relative to a conservative tracer to be calculated. Model efficiency is a good way to evaluate the overall fit of the model. This would be an important parameter if the biodegradation rate of a biodegrading tracer was being calculated, relative to a conservative tracer, as greater confidence would be given to biodegradation rates estimated from fitted curves. Model peak times are all within 10% of actual peak times. This is a very good fit as tracer breakthrough curves were not sampled continuously, therefore the highest concentration time may be slightly displaced from the actual peak. Peak concentration is accurately predicted by the model when a high-K layer bisects the central packer, but is underestimated in all other cases, particularly in the low-K layer scenario. This may have been caused by the low-K layer being thinner than 3 cm at certain points: defining a layer 2 cm thick resulted in better model fits to peak concentration (but not

peak time). However, the layer in all tests was close to 3 cm, and may vary by less than 0.1-0.2 cm. Peak height estimates were also not significantly improved by decreasing the dispersivity. There may have been a greater mass of tracer passing along the dominant flow lines, making the breakthrough peak higher than that predicted by the model. In the low-K layer case these flow lines may have represented the quickest migration path through the layer. Preferential tracer flow in zones close to the well screen, due to slight variations in bulk density caused by packing variability, may also have led to the increase in peak height. First arrival time was defined as the closest time point to 0.01 C/C_0. Model data was within 10 % of actual data for four of the six tests. It was slightly overestimated when a high-K layer bisected the injection chamber and underestimated when a low-K layer bisected the extraction chamber. Therefore in some cases layered heterogeneity may lead to inaccurate estimates of aquifer dispersivity. Model efficiency was > 85 % in all cases and > 90 % in four tests. For the two scenarios under 90%, biodegradation rates calculated if a biodegrading tracer was also used would have greater uncertainty. It is noteworthy that these deviations from the model are for a simplistic case with a low-K contrast, which in the field is likely to be more complicated and could be assumed to be isotropic or homogenous for modelling purposes. This could lead to much greater uncertainty in parameters obtained.

3.5.1.2. **Imaging and hydraulic head field**

A simulated breakthrough curve does not confirm if the heterogeneity present has affected the tracer similarly in the model and experiment. Different scenarios can produce similar tracer breakthrough curves. Images were compared to model predictions at ~10 t_d (Figure 3-25 and Figure 3-26) and predicted hydraulic head fields (Figure 3-27). At this time, any hydraulic effect caused by the presence of a layer of contrasting K will be evident. As HGS does not recirculated mass the model images do not show the recirculated tracer halo. All modelled tracer plumes have the same shape as the images, validating the modelling approach and confirming that variations in tracer flow between tests are predominantly due to the presence of the horizontal

layers. Maximum predicted concentrations in the tracer halo are similar across all tests, suggesting concentration is time-dominant rather than scenario-dominant. Test tracer halos reach to the middle of the extraction chamber in the model, but only the bottom half during experiments. This suggests slight preferential movement of tracer close to the bottom of the extraction chamber during the experiments, which was also seen in isotropic tests (see Chapter 2). This difference between the model and tests did not create any significant difference between predicted and actual extraction well breakthrough curve concentration. However, it means that modelling analysis of imaging points around the extraction well would not provide any further insights. The hydraulic head field has a larger range of values when the majority of the beads are low-K and the layer is high-K (Figure 3-27). Greater draw-down or draw-up is expected in the well chambers under lower K conditions.

The hydraulic head field when a high-K layer bisects the central packer shows a shallow gradient across the layer (Figure 3-27). This implies that the layer is aiding flow between the chambers, leading to a quick breakthrough as seen in Figure 3-4. When a high-K layer bisects the injection chamber the most tracer mass is above the injection chamber (Figure 3-25). As tracer concentrations are not significantly depleted in this zone it suggests the tracer is travelling along long flow paths to the extraction well, leading to later peak concentration times. This is matched by the hydraulic head field which shows that the high-K layer aids horizontal movement of tracer during injection, leading to longer flow paths. When the high-K layer bisects the extraction chamber it represents a sink for the negative pressure generated by extraction. This leads to preferential extraction of tracer in the layer.

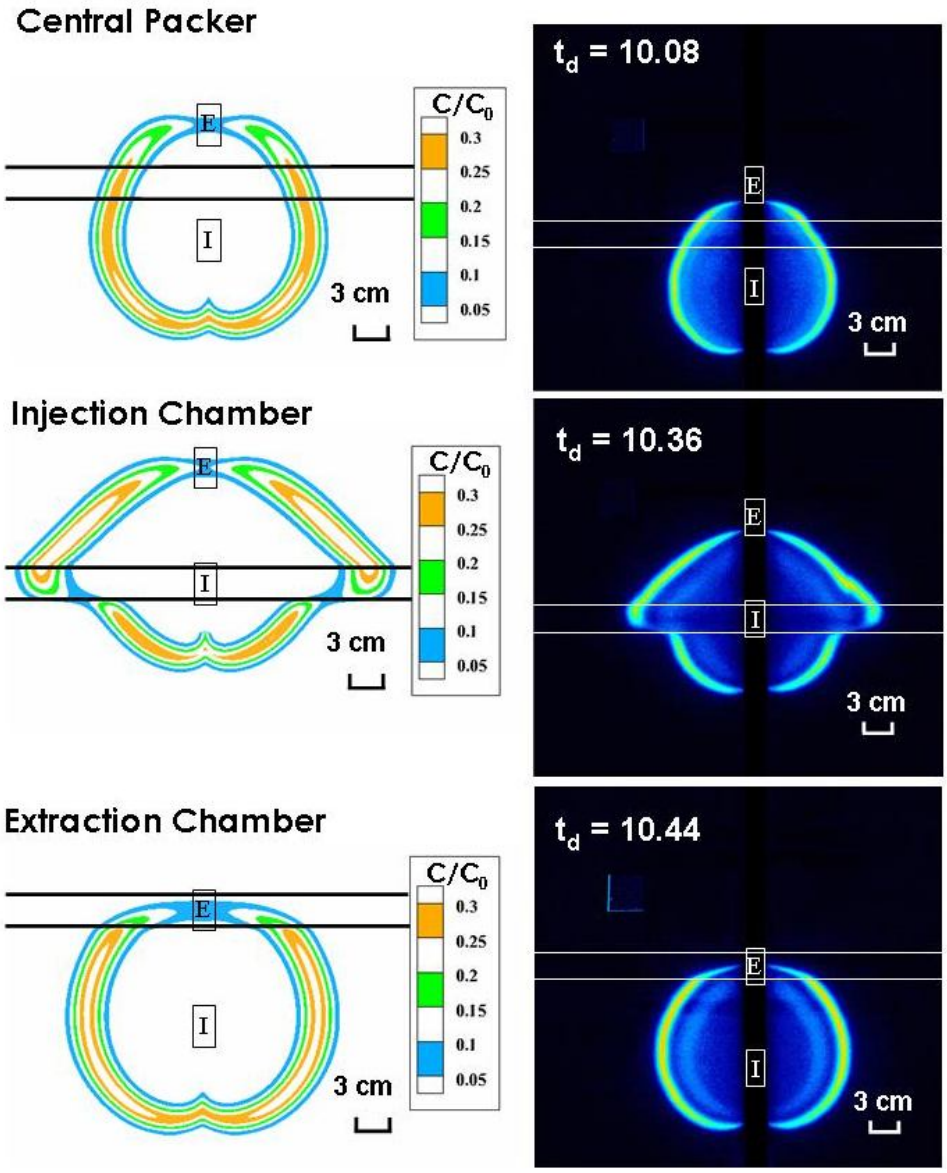

Figure 3-25: Images and model predictions for approximately 10 t_d into DFTTs with a high-K layer present. Each test is labelled by the position of the layer. Concentration in the model predictions is normalised to input concentration.

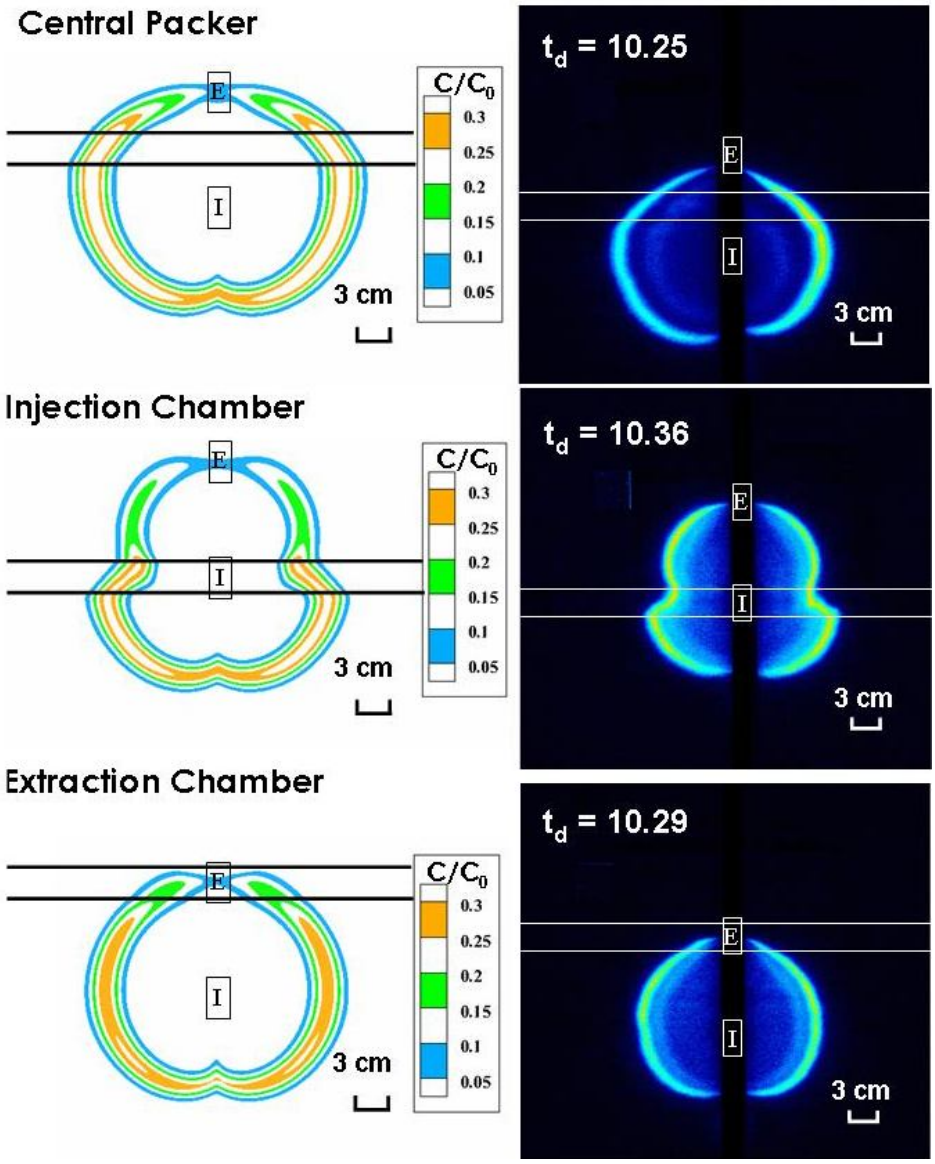

Figure 3-26: Images and model predictions for approximately 10 t_d into DFTTs with a low-K layer present. Each test is labelled by the position of the layer. Concentration in the model predictions is normalised to input concentration.

The hydraulic head field shows a steep hydraulic gradient across the low-K layer when it bisects the central chamber (Figure 3-27). This shows that the layer is impeding tracer flow between chambers, leading to greater horizontal flow and the wide tracer plume profile seen in the model and images (Figure 3-26). When a low-K layer bisects the injection chamber tracer concentrations in the model are much lower in the top half of the plume than the bottom half. This implies tracer is slowly being released from the low-K layer, but is then quickly travelling along fast flow lines to the extraction chamber. The hydraulic head field shows that tracer migration is

reduced in the low-K layer and increased in the high-K beads either side, aiding the early breakthrough seen at the extraction chamber (Figure 3-5). The lower half of the tracer cloud is larger as the negative pressure of the extraction chamber is partially negated by the presence of the low-K layer. When the low-K layer bisects the extraction chamber the hydraulic field implies that water is preferentially extracted from the high-K beads just above and below the layer. Preferential extraction from below the layer would causes quick breakthrough at the extraction chamber (Figure 3-5).

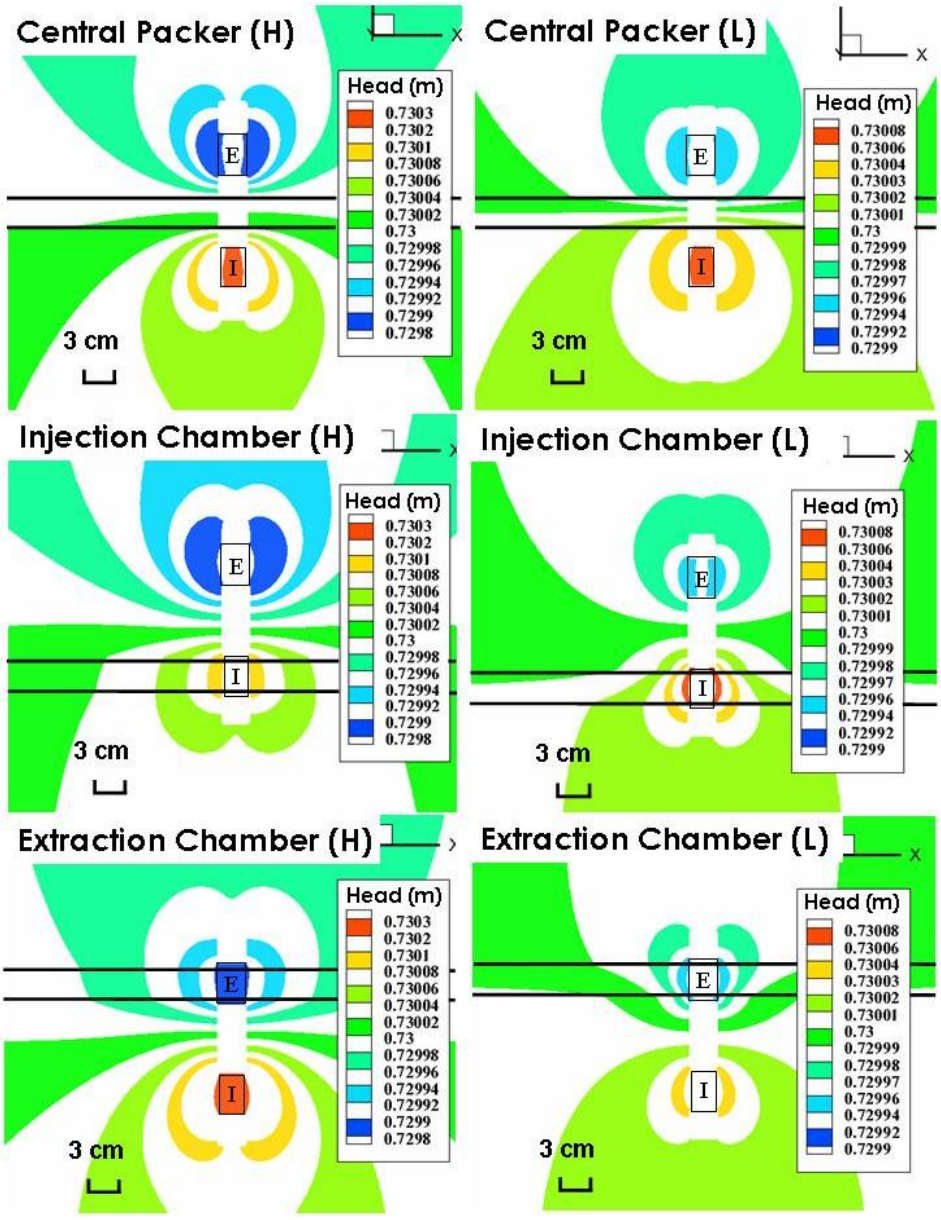

Figure 3-27: Hydraulic head fields estimated by HGS for DFTTs conducted. Each test is labelled by the position of the high (H) or low (L) K layer.

3.5.1.3. **Tracer mass**

HGS can be used to predict the non-recirculated mass that has reached the extraction chamber over time (see Figure 3-28). This helps to quantify the effect of heterogeneity on the entire tracer cloud, not just the tracer peak. The contribution of non-recirculated tracer to the breakthrough peak can be assessed by comparing when 50 % of the tracer mass has reached the extraction chamber. For most tests 50 % mass breakthrough is around 10 t_d. This implies that a large portion of mass in the test travels along the fastest flow lines close to the well, making up the main peak breakthrough. After this point breakthrough of non-recirculated tracer is much slower, with recirculated tracer mass dominating the extraction well breakthrough curves. The time of 50 % mass breakthrough is most significantly affected when the layer bisects the central packer, with the time for the low-K layer case (18.98 t_d), more than twice that in the high-K layer case (8.17 t_d). This is much larger than the difference in peak concentration time between the tests and suggests a larger portion of the non-recirculated mass makes up the tracer peak in the high-K layer scenario. Compared with isotropic conditions, a larger proportion of the total injected mass contributes to the extraction chamber breakthrough curve over the entire test period when a high-K layer is present and less when a low-K layer is present. Significantly this suggests that the breakthrough curve signal for the low-K layer scenario is dominated by a small portion of the total non-recirculated and recirculated tracer travelling close to the well screen. The difference between all tests where a layer bisects a well chamber is less than 1 t_d. Although cases with a low-K layer have earlier 50 % mass breakthrough times, less overall non-recirculated mass is seen over the total test time.

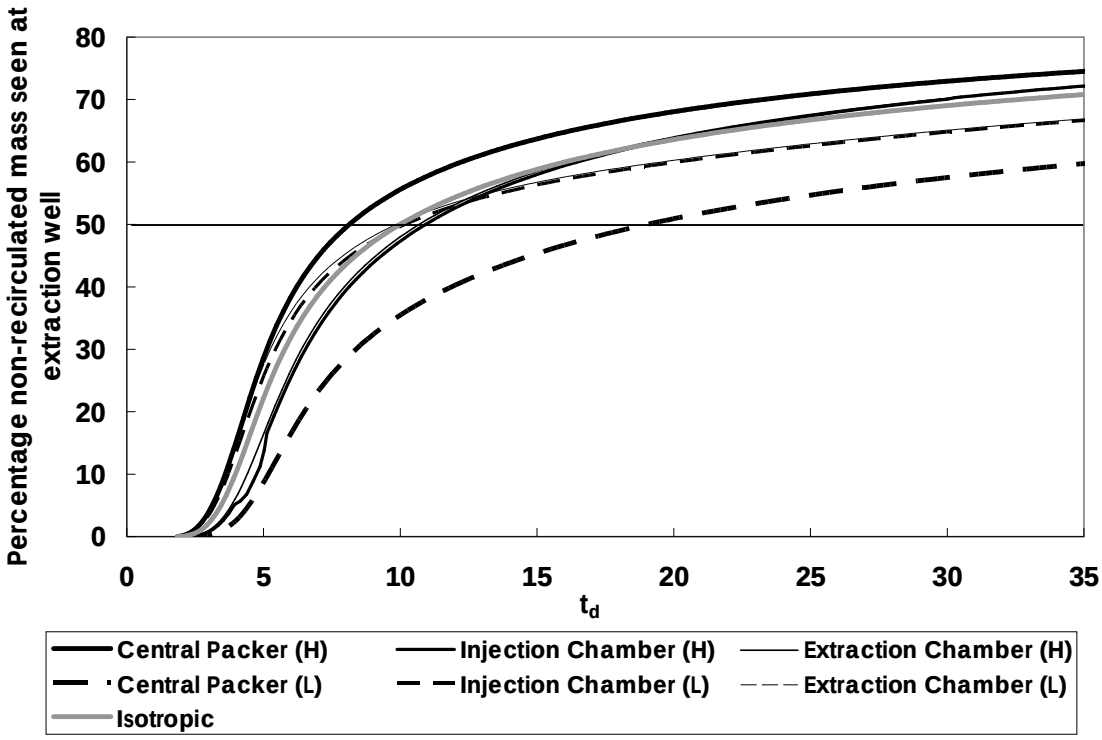

Figure 3-28: Amount of non-recirculated tracer mass estimated from modelling that has reached the extraction chamber during DFTTs performed in isotropic conditions. Each test is labelled by the position of the high (H) or low (L) K layer.

3.5.2. **Push-pull tests**

3.5.2.1. **Tracer breakthrough curves**

HGS was used to interpret the PPT. Dispersivity was assumed to be $1x10^{-5}$ m, as this provided the best fit for the isotropic test (see Chapter 2). Simulated tracer breakthrough curves are not significantly better if they are modelled in layered heterogeneous or isotropic conditions (Figure 3-29 and Table 3-3), with slightly better fits for the isotropic models in three of the tests. This implies that the presence of layered heterogeneity has little affect on breakthrough curves. The downward limbs of the low-K layer tests seem to be better modelled; however this may be due to a slight underestimation of flow rate in tests.

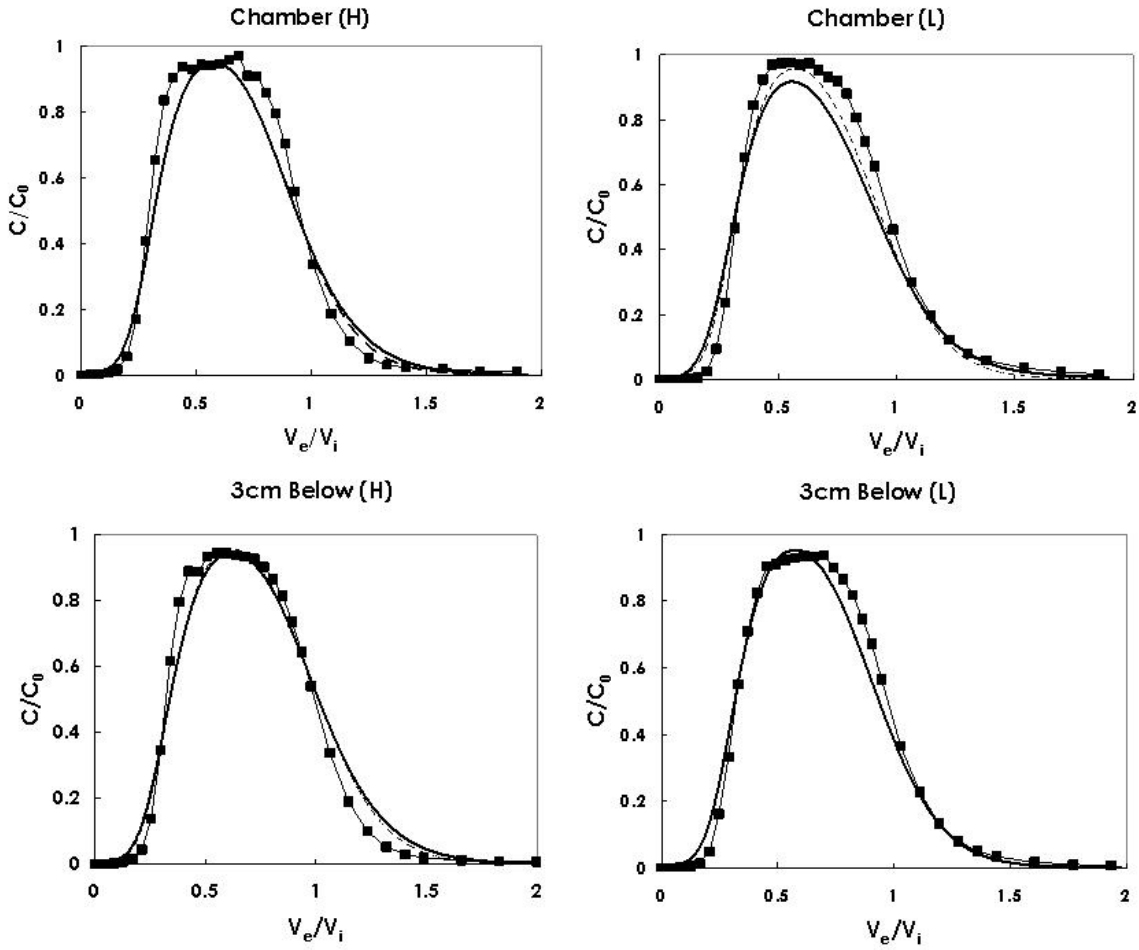

Figure 3-29: Simulated PPT extraction phase breakthrough curves. The solid line and dashed line are the predicted breakthrough curves under test conditions under isotropic conditions, respectively. Each test is labelled by the position of the high (H) or low (L) K layer.

Table 3-3: Model efficiencies and mass recovery for PPTs.

	Model Efficiency (%)		Mass Recovery (%)	
	Isotropic	With Layer	Test	Model
Chamber (H)	96.42	98.06	103.72	98.56
3cm Below (H)	98.14	97.80	103.41	98.51
Chamber (L)	97.73	95.62	105.58	96.63
3cm Below (L)	98.39	98.38	101.29	98.83

3.5.2.2. **Imaging and hydraulic head field**

Heterogeneity affects the tracer plume geometry more than the extraction well breakthrough curves. The model and image was compared at the end of the injection phase to show the maximum effect of the layered heterogeneity (Figure 3-31). Images

were also compared with the hydraulic head field predicted by HGS at the end of the injection phase (Figure 3-30). The model suggests tracer should migrate further when a high-K layer is located across or below the injection chamber, than was observed in the experiment. Also, when a low-K layer bisects the chamber, the model predicts less horizontal migration of tracer than was observed. This may be due to the K of the two bead sizes being more similar than estimated by the equations used. However the tracer plume geometry and breakthrough curves of DFTTs were reproduced well with the calculated K values, suggesting they are correct. The low imaging penetration depth may cause a slight underestimation in migration; however the modelling in Chapter 2 shows that it should not be this extreme. Near-well preferential flow paths, cause by variations in bulk density (so called “skin effects”) which are not included in the model may dampen lateral tracer movement. The model predicts greater dispersion of the tracer plume in the high-K layer and lower dispersion in the low-K layer, reflecting the lower water velocity in the latter.

The hydraulic head around the injection chamber is greater when the 3 cm layer has a higher K than the host media (Figure 3-30). A higher pressure would be expected in the chamber in areas of lower K. This suggests that the host media not the layer is responsible for the magnitude of the hydraulic head. When a high-K layer is present across the extraction chamber, the hydraulic field is elongated horizontally along the layer, as it partially alleviates the hydraulic pressure. This suggests that the tracer flow should be elongated horizontally along the high-K layer, as observed in the experiment.

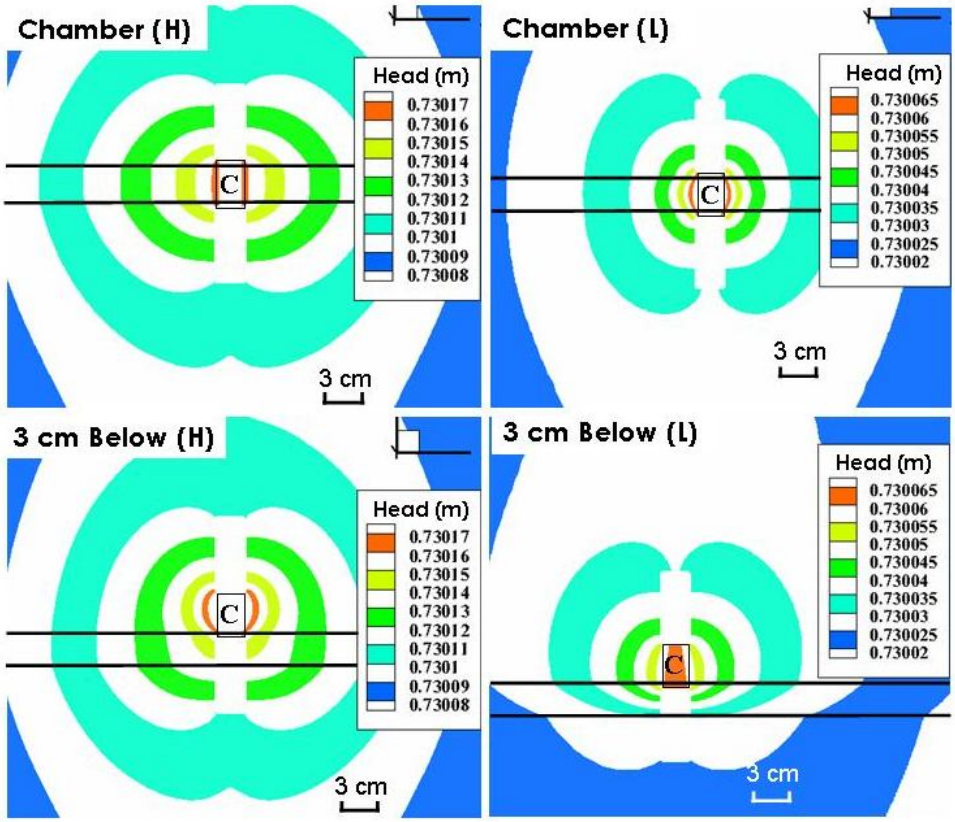

Figure 3-30: Injection phase hydraulic head fields estimated by HGS for PPTs conducted. The minimum hydraulic head is 0.73 m for all models. Each test is labelled by the position of the high (H) or low (L) K layer.

When the high-K layer is offset 3 cm below the centre of the chamber the hydraulic head field is also elongated horizontally along the layer. This also suggests maximum horizontal migration of tracer along this layer, as shown in images. When a low-K layer is present across the chamber the hydraulic head field is shortened horizontally and expanded vertically. The low-K layer reduces the water flow, but the hydraulic pressure is alleviated by the high-K media above and below the layer. This leads to greater vertical tracer migration and less horizontal migration, as seen in the images, and may also greater tracer mass migration to the open well segments. When a low-K layer is present 3 cm below the centre of the chamber the hydraulic head field is elongated upwards and shortened below, implying that the low-K layer restricts water flow. Greater upwards tracer movement and increased migration to the top open wells segment would be expected, as observed in images.

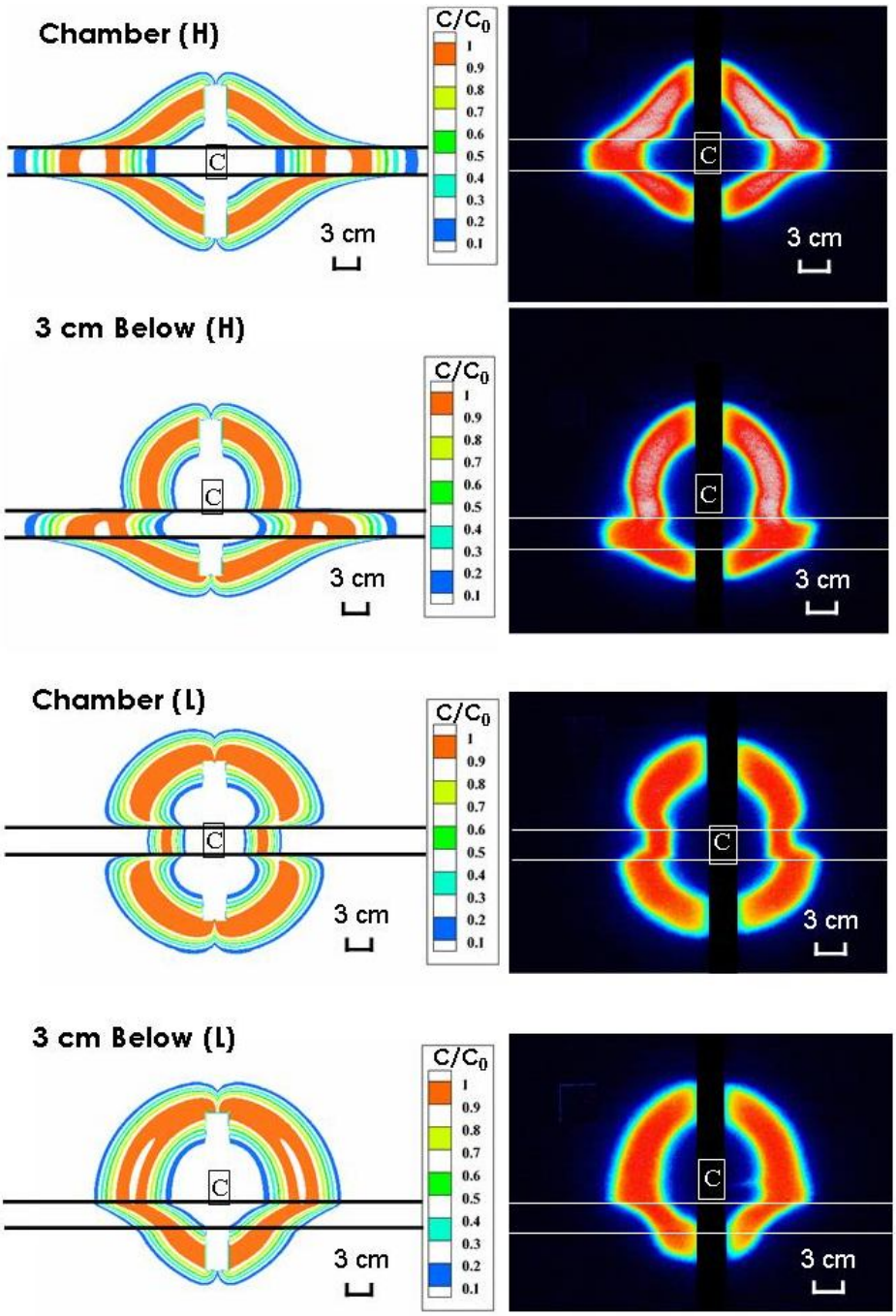

Figure 3-31: Images at the end of PPT injection phases compared with model predictions. Predicted concentration is normalised to input concentration. Each test is labelled by the position of the high (H) or low (L) K layer.

Tracer migration along the layers can be further investigated by measuring concentrations at strategic points on images and comparing these with model predictions. Results were also compared for predictions under isotropic conditions to assess if the layer significantly affected tracer migration. Imaging point F (Figure 3-12) was chosen for tests when the layer bisected the chamber. When the layer was 3

cm down imaging point G (Figure 3-12) was chosen, which is further out than imaging point F to allow time for tracer to migrate downwards to the layer, providing greater deviation from isotropic conditions. Results are shown in Figure 3-32. The images confirm that when the layer bisects the chamber, outward lateral migration is quicker when a high-K layer is present relative to a low-K layer. However, the difference is much less than predicted by the model and both are quicker than predicted for isotropic breakthrough. The difference is most evident where a low-K layer was present: mean breakthrough predicted by the model was 0.1 V/V_i units later than observed in the experiment. This may be due to an area of lower bulk density close to the well screen, as seen in other experiments (Chapter 2), that reduces the difference between the layers. Figure 3-32 also shows that image-derived normalised concentrations on the curve plateau slightly exceed 1.0. Measurement error contributes to approximately half this difference. There may also be slight differences between the calibration and test conditions (e.g. position of box, lighting and camera and/or area sampled). Error for imaging point F may lead to slight underestimation in breakthrough time, but is ~10 % at most and unlikely to seriously affect results.

For the case where a high-K layer is displaced 3 cm below the centre of the chamber the imaging point G tracer concentration profile is reproduced best by isotropic conditions, showing that tracer migration along this path is less than predicted by the model. This may have been caused by the zone of low bulk density close to the well screen aiding vertical transport of tracer and dampening the effect of the layer. In the low-K case, there is a good match between the image and the model, even though there is some variation between the left and right sides of the image.

Overall there is good similarity between the modelled tracer cloud and images. However, it was possible that tracer migration in the experiments was attenuated due to near-well flow effects that cannot be included in the model. Such effects may have been caused by variation in layer thickness (especially near the well), positioning of the layer, heterogeneous porosity, or lower bulk density near the well. The latter is

likely, given the care needed when filling the box with glass beads to avoid damaging or moving the well.

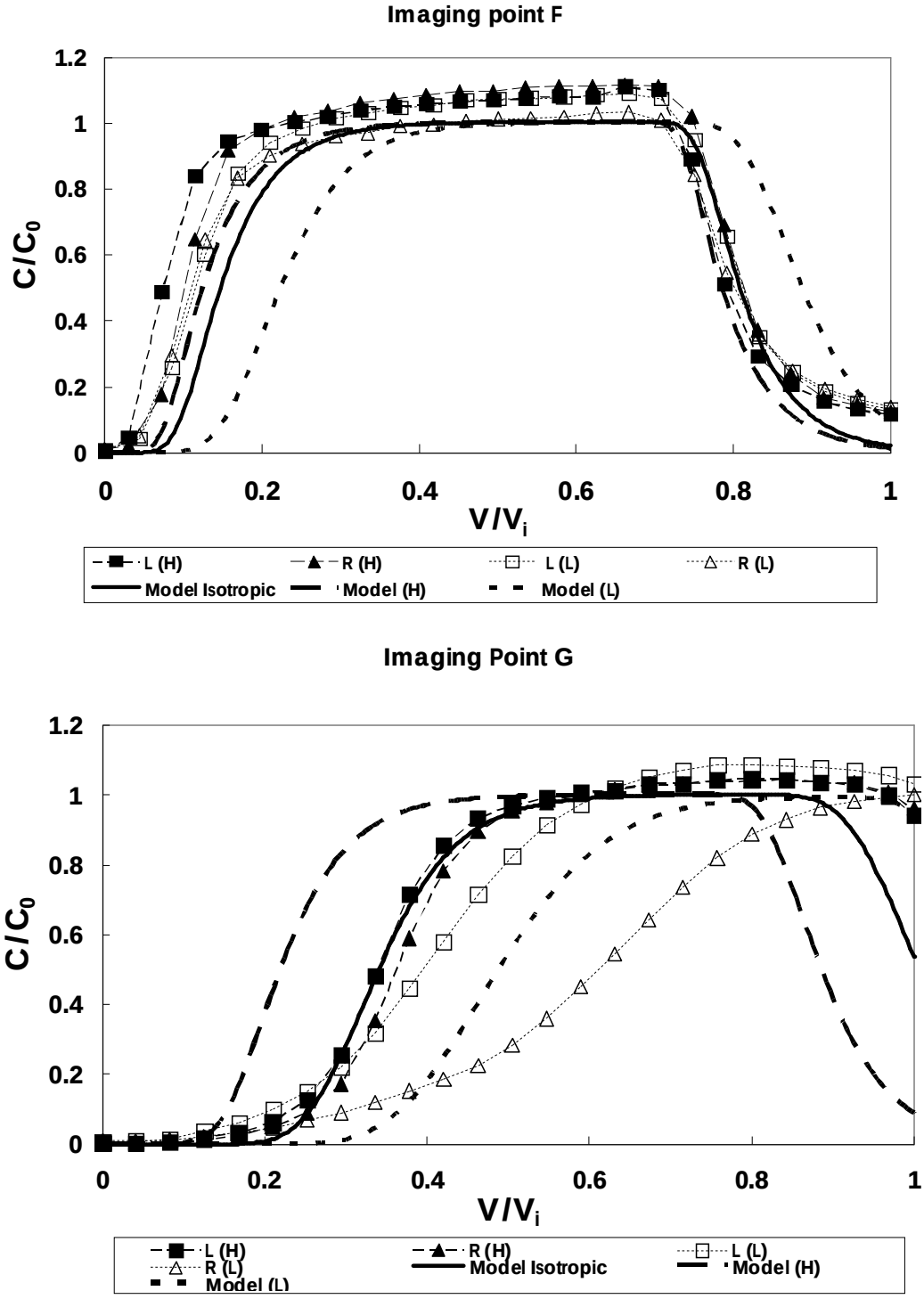

Figure 3-32: Selected imaging point (see figure 3-12) breakthrough concentrations and model predictions during PPT injection phases. L = left, R = right, (L) = low-K layer, (H) = high-K layer.

3.5.2.3. **Tracer mass**

Mass recovery estimated from breakthrough concentrations was over 100 % for all tests (Table 3-3). This is probably due to analytical error in the tracer measurements, which has been compounded by integration of results. The accuracy of Br analysis was ± 2 %. The aqueous sample based mass balance exceeded 100 % by a maximum of 6 % but this was not considered to be a significant error. There was still tracer visible in the images at late time, suggesting that the mass balance should have been less than 100 %. Mass recoveries calculated from the model simulations were between 96.63 and 98.5 %, which is probably a more representative estimate. Some mass balance shortfall could be expected due to a small amount of tracer migrating to the open well segments, which was seen in the model and tests. Also, the images in the low-K layer test showed a small amount of tracer was retained in a low flow zone in the low permeability zone (Figure 3-20). Therefore, mass recovery in field scale tests may not achieve 100 % unless the test has a long extraction phase and analytical detection is low enough to resolve the low tailing in tracer concentration.

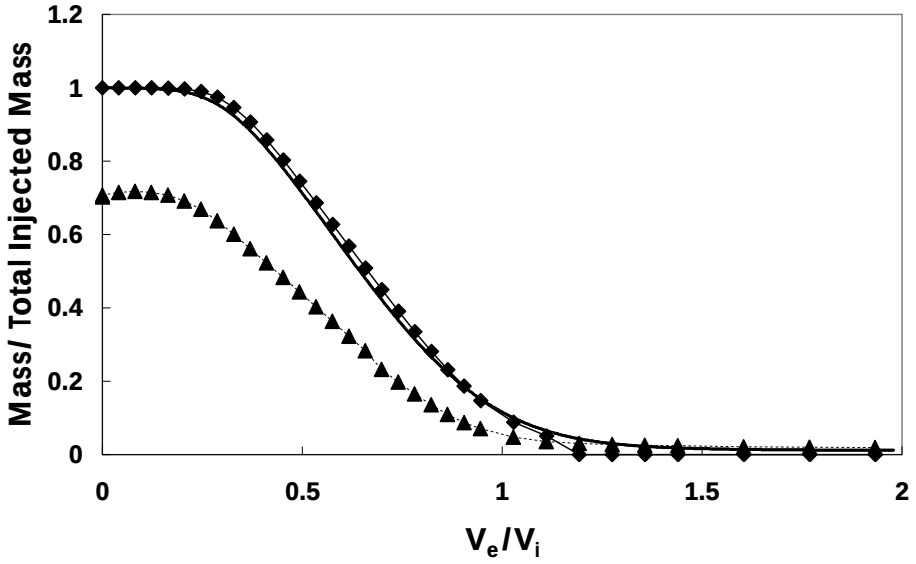

Figure 3-33: Fluorescein mass calculated from breakthrough curve samples and model simulation for extraction phase of PPT with low-K layer 3 cm below well chamber.

3.6. **Discussion**

3.6.1. **Effect of layer heterogeneity on tracer tests**

The presence and position of layered heterogeneity significantly affected the extraction chamber breakthrough curves and plume geometry for DFTTs. For example, when a high-K layer bisected the central packer the plume at early time was vertically elongated (Figure 3-6), as the large beads aided tracer migration on the shorter vertical flow lines close to the well screen, leading to early breakthrough (Figure 3-4). However when a high-K layer bisected the injection chamber, tracer travelled far out along the layer (Figure 3-7), increasing the proportion of longer flow paths and delaying breakthrough (Figure 3-24). DFTTs are likely to be sensitive to the position of a layer of different K, due to the strong curvature of their flow lines. Therefore in different places a permeability contrast will aid or hinder flow in different directions. Thus, tracer plume geometry and breakthrough curve parameters are scenario-dependant. The sensitivity of dipole flow to heterogeneity has previously been observed in hydraulic tests [Xiang and Kabala, 1997].

The presence of layered heterogeneity does not significantly change the PPT breakthrough curve (Figure 3-17), but does significantly affect tracer plume geometry. Horizontal migration of tracer in images is greatest in the high-K bead media (Figure 3-18). When a low-K layer is present net vertical migration of tracer viewed in images is increased (Figure 3-20). This leads to more tracer migrating to open well screen sections in the injection phase, resulting in the appearance of vertical tendrils in extraction phase images. The effect of layers is significant, even when offset from the chamber (Figure 3-19 and Figure 3-21). Tracer flow lines for PPTs have low curvature and the velocity along a flow line during the injection phase is opposite to that during the extraction phase (as shown in images where a high-K layer aided injection and extraction and a low-K layer restricted both). Therefore, there will be little difference in the extraction phase breakthrough curve of different scenarios. This conforms with previous modelling (using analytical solutions) that has shown that

spherical and radial flow (the two end-member scenarios of possible flow in PPTs) breakthrough curves for PPTs do not vary significantly [*Schroth and Istok*, 2005].

Tracer mass estimated from images was slightly less than mass estimated from aqueous concentrations for both DFTTs and PPTs (e.g. Figure 3-15 and Figure 3-23). This was due to underestimation of mass in images at high tracer concentration, due to calibration error, and/or the tracer concentration at the imaging penetration depth being less than the average across the whole box, as tracer was injected from a circular well screen into a 2-D domain. The second issue did not affect modelling interpretation, as the model was discretised in three dimensions. Estimates of mass present did not vary significantly with scenario for both types of test. This reflects the small amount of tracer mass that was removed by sampling in DFTTs and the similarity of breakthrough curves in PPTs.

3.6.2. **Modelling evaluation**

HGS, in finite difference mode, was used to interpret single well tracer tests with layered heterogeneities present. Good simulations of the breakthrough curves for DFTTs and PPTs (Figure 3-24 and Figure 3-29), were obtained when the model incorporated discrete layering. DFTT breakthrough curves differed significantly from isotropic conditions, but PPTs did not. DFTT breakthrough curve peaks were well modelled, even though HGS does not incorporate recirculation. Also plume geometries were well matched by HGS for DFTTs (e.g. Figure 3-25). This indicates that HGS is suitable for modelling DFTT experiments and also that the interpretation of plume geometry in the modelling section and estimates of non-recirculated mass observed at the extraction chamber (Figure 3-28) are valid. However HGS over-predicted the effect of layers for PPTs (Figure 3-31) and imaging point breakthroughs were not well predicted (e.g. Figure 3-32). HGS has been verified against analytical solutions for horizontal dipole flow and PPTs [Hoopes and Harleman, 1967; Gelhar and Collins, 1971], therefore would be expected to model DFTT and PPT results accurately under ideal conditions. In Chapter 2 it was observed that variation in bulk

density close to the well screen, due to variable packing, caused slight preferential water flow close to the extraction chamber. This led to differences between simulated and actual imaging point breakthrough curves for DFTTs. If this also occurs in these experiments, it may aid initial vertical movement of tracer, reduce the effect of the layers and/or cause inconsistent flow close to the chambers during PPTs. Preferential flow may also have caused the slight underestimation of peak breakthrough concentration for DFTTs. However, this effect does not always occur, as imaging point breakthrough for the PPT in isotropic conditions in Chapter 2 was simulated well. Variations of bulk density affect breakthrough and plume geometry of DFTT and PPTs in different ways, probably relating to the different flow regimes in the tests. Therefore the success of HGS modelling may vary between test types. Small variations in the thickness and depth of the layer between the modelled and tested scenarios may have also caused some differences. This would explain why, when no layer was present, the PPT imaging point in Chapter 2 was simulated well. However, is not sufficient to explain differences between predicted and actual imaging point concentrations and DFTT peak concentrations in this study. Imaging concentrations over 1.0 C/C_0 suggest some measurement error and tracer concentrations may vary with depth into the bead pack. However these experimental uncertainties are small compared with the difference between the modelled PPT and actual plume geometry. The HGS model used assumed zones with consistent properties and it was not considered suitable to incorporate detail into the model that could not be separately verified. Overall, the modelling showed that the variation in breakthrough curves and plume geometries were predominantly due to changes in the flow field caused by layers with different K.

3.6.3. **Implications and field-scale applications**

DFTT tracer breakthrough curve profiles when layered heterogeneity is present are clearly different to predicted isotropic profiles. Therefore, it may be possible to use inverse modelling of field-derived DFTT test data to delineate the position of layers in the field. However, as observed in Figure 3-24, the similarity of breakthrough curves

for a scenario when a low-K layer bisected the injection or extraction chamber of the dipole apparatus, fits to a breakthrough curve may be non-unique. Both curves indicate nearly identical first arrival, peak concentration and a recirculation tail with a second peak at the same time, despite the obvious differences in flow path taken by tracer visible in the images. These two curves are markedly different to the case where a low-K layer bisects the central packer. It is clear that forcing an isotropic model onto a layered heterogeneous scenario will lead to inaccurate parameterisation. Homogenous but anisotropic conditions could be assumed [Sutton et al., 2000], but the tests described here suggest that the position of a heterogeneous layer is as crucial as its properties in determining its effect on the tracer cloud. By performing at least two DFTTs in a well, a distance equivalent to the dipole shoulder length apart, it should be possible to detect a discrete layer, or deduce if a breakthrough curve signal represents the aquifer or the position of the dipole apparatus relative to a layer of different K in the aquifer. The depth and thickness of a layer could be resolved by systematically lowering the dipole and repeating tests. The resolution of thin layers will only be possible with a short dipole shoulder length. In these tests, this length was 5.2 cm, which is not practical for field testing. The link between layer thickness and dipole shoulder lengths is the subject of future modelling.

Even in these controlled laboratory box model tests, it was found that tracer migration in a dipole flow field is sensitive to skin effects near the well screen. As such, wells installed with an engineered sand pack, or without but using a hollow-stem auger, are not suitable for DFTTs. Wells must be constructed to minimise disturbance near the well annulus. Testing should perhaps be limited to aquifers where it is possible to install wells using direct-push methods. This sensitivity to variation in hydraulic conductivity has previously been observed in simulated dipole flow tests (no tracer)[Xiang and Kabala, 1997]. An original strength of DFTTs was to determine anisotropy [Sutton et al., 2000]. However, significantly less non-recirculated mass is predicted to reach the extraction chamber over reasonable time scales, relative to isotropic conditions, when a layer ~1/5th the K of the surrounding media bisects the

central packer (Figure 3-28). To put this in perspective, the well-studied sandy aquifer at CFB Borden, Canada [Sudicky et al., 1983; Freyberg, 1986; Mackay et al., 1986; Sudicky, 1986], generally considered to be relatively homogeneous, has a K contrast on the order of 30. Using this value in the HGS model suggests ~33% of the non-recirculated mass will be seen after 35 t_d and less than 10% of the total mass will contribute to the breakthrough peak. These are probably overestimates, as the model boundary conditions may force tracer through the low permeability layer. In such cases in the field a small amount of the injected tracer could make up the majority of the breakthrough curve, or none of the injected tracer could breakthrough. In principle, low mass recovery should still allow estimation of aquifer properties by inverse modelling, if sufficiently high tracer concentrations are recorded. However, if a biodegrading tracer is introduced with a conservative tracer, and the aquifer heterogeneity causes weak breakthrough of the latter, the biodegrading tracer may not be detected. It may be possible to improve non-recirculated mass recovery, by conducting asymmetrical dipole tests: extracting at a higher rate than injecting. However, higher extraction will probably compress flow lines towards the well, shortening travel distances and thus sampling less of the aquifer (as in convergent two well tests [Ptak and Schmid, 1996; Chao et al., 2000a]). Also, as asymmetrical tests do not allow for full recirculation, some of the extracted water (if contaminated) would require treatment and disposal. Higher flow rates may also reduce the effect of layered heterogeneity on tracer breakthrough curves and increase near-well effects.

There was little variation between PPT extraction phase breakthrough curves for the different scenarios, where three out of four could be simulated using the model for isotropic conditions. This suggests for simple biodegradation modelling spherical flow could be assumed for low anisotropy conditions, with little detriment to modelled parameters. This justifies the simplified modelling approach of Schroth and Istok [2005]. However, poor understanding of variability in aquifer K means that the path taken by a tracer during a test remains unknown. This study shows that even small contrasts in hydraulic conductivity significantly affect the tracer cloud

geometry. Additional information could be gathered from multilevel samplers near the test well, but the samplers and possible disturbed zone around them would likely affect tracer migration. Also, the added sampling instrumentation would make testing more time consuming and expensive.

The effect of layered heterogeneity on tracer cloud geometry was less than predicted by modelling for PPTs. In the field this would manifest as a greater than predicted spherical flow component. Assuming cylindrical flow in layered anisotropic conditions [Schroth et al., 2001] may lead to poor prediction of where mass has migrated. The ease in which mass can migrate to more highly conductive layers offset from an injection chamber makes modelling breakthrough curves assuming homogenous anisotropic conditions unsuitable, as a regular ellipsoid shape is predicted [Mathias, 2010]. An inaccurate prediction of the radial extent of flow can lead to errors in estimated solute retardation and hence sorption coefficients of sorbing tracers, if used in analytical solutions [Schroth et al., 2001]. The greater than predicted vertical migration of tracer during tests is most likely due to highly conductive zones near the well screen. In the field this could be much greater due to well disturbed zones or installed sand packs, while in these experiments beads have been hand packed around the well screen. The quality of the packer seal against the well screen may also be an issue. Vertical migration could lead to tracer reaching open well segments, leading to strong tailing in mass recovery. Low-K zones close to the well chamber are likely to increase this migration. A high-K layer may also decrease mass recovery if there is a large hydraulic gradient or long rest period between extraction and injection phases. If the tracer migrates far from the well it may leave the test area of influence and not return to the well during the extraction phase. In preliminary testing (not shown) a head gradient of ~0.001, which is lower than estimates for the Borden aquifer [Sudicky, 1986], led to loss of tracer from the area of influence. Although test flow rates used were over an order of magnitude less than in field tests (e.g. [Istok et al., 1997]). Field tests would be expected to have a larger area of influence and be less affected by the presence of a background head gradient. To a

lesser extent tracer was retained in low flow zones in the low-K layer and slowly leached out, which may be more prominent in clay-rich strata, with the effect increased for sorbing tracers. The tests suggest that PPTs should have at least a conservative tracer mass recovery of 95%, considering analytical error, to be successful. Values less than this suggest that the factors discussed above have contributed to lower mass recovery, sometimes seen in field tests [Kim et al., 2004; Azizian et al., 2007].

In conclusion, the high sensitivity of DFTTs to aquifer heterogeneity makes them well-suited to quantifying layer properties in low anisotropy aquifers. Suitable inverse modelling, which considers the possible presence and properties of discrete layers, would provide greater confidence in estimated transport parameters. The effect of horizontal layered heterogeneity in tests is less than predicted for PPTs, perhaps due to vertical migration of tracer near the well. This could lead to poor mass recovery during test extraction phases. Localised zones of preferential flow close to chambers were present for all tests despite the care taken to pack the beads around the well. The effects were small in these tests, but are likely to be more extreme in the field where disturbed zones and well sand packs represent a more significant fraction of the well diameter.

4. Evaluation of inorganic ions, fluorescein and Ni-EDTA as tracers in single well forced gradient tests

4.1. Abstract

Accurate assessment of aquifer solute transport parameters is important for the evaluation of pollutant natural attenuation. Tracer tests were carried out in columns filled with a Permo-Triassic sand. An assessment was made of the suitability of different inorganic compounds, fluorescein and Ni-EDTA as tracers in mixtures to estimate aquifer properties in single well forced gradient tracer tests, dipole flow tracer tests, and push-pull tests. Fluorescein and inorganic anions were investigated as conservative tracers. Sodium, magnesium and potassium were investigated as tracers to estimate the cation exchange capacity of the sand. Ni-EDTA was also investigated as a tracer to estimate the transport of heavy metals when attached to complex ligands. Inorganic anions were found to be more reliable conservative tracers than fluorescein. Sodium with magnesium or potassium was found to be the most suitable combination of cations for use as dual tracer when performing a blind assessment of the cation exchange capacity of an aquifer. Retardation of Ni-EDTA was found to be low under neutral pH conditions and when sorbed this complex may lead to an underestimation of cation exchange capacity

4.2. Introduction

4.2.1. Review of non-reactive tracers

Non-reactive (or conservative) tracer tests are often used to characterise the hydrogeological properties of aquifers [Freyberg, 1986; Ptak and Schmid, 1996; Sutton et al., 2000]. The term “conservative” relates to the quantitative mass recovery of the injected tracer and “non-reactive” is used to describe the absence of reaction or chemical interaction between the tracer and aquifer material. Therefore, the

breakthrough curve (BTC) of a conservative tracer can be used to estimate the hydraulic conductivity, dispersivity, dilution and solute residence time in the aquifer.

Inorganic anions such as Br^-, Cl^-, I^- and F^- are often used for conservative tracer tests. Although negatively charged species, they do not commonly react with the aquifer matrix. This is because typical mineral surfaces in aquifers have a zero point charge at low pH, therefore at the near-neutral pH of most groundwaters [Banks et al., 1998; Thornton et al., 2000b], they have a net negative charge [Yong et al., 1992]. These anions can be affected by anion exclusion in clay-rich strata, where negatively charged surfaces of the aquifer matrix repel the anion. This effectively enhances the tracer migration. Also Br^- and Cl^- are highly nucleophilic, which could lead to dissolution/precipitation reactions within the aquifer [Davis, 1985; Wilson, 1998]. These effects are commonly assumed to be negligible, as aquifers where tracer tests are conducted do not have a large surface charge [Christensen et al., 2001] and therefore are not favourable for nucleophilic reactions. Anionic salt tracers do not decompose, are inexpensive and easy to use. Their dissolved concentration and resultant breakthrough behaviour can be estimated in the field using ion electrodes. If the input concentration is too high density affects may occur which would affect results. Br^- commonly has a low background concentration in groundwater and is more easy to use in tracer tests than Cl^- and NO_3^-, which have higher natural concentrations [Davis, 1985].

Fluorescent organic dyes are also used as conservative tracers as they are inexpensive and easy to measure at low concentrations by spectroscopic analysis, giving high sensitivity. However, in some conditions, as described below, they are reactive and are therefore restricted in use. Adsorption of fluorescent organic dyes onto mineral and organic surfaces can lower their fluorescence and cause a relative retardation [Smart and Laidlaw, 1977; Sabatini and Al Austin, 1991]. The fluorescence of these tracers typically varies with temperature, $CaCO_3$ content, decreases with decreasing pH and decreases with increasing salinity [Reznek et al., 1979; Davis, 1985]. Some

fluorescent dyes may also biodegrade [Bottrell et al., 2010]. These factors can modify tracer concentrations in tests and lead to different fluorescent dyes having different BTCs [Brown, 1971]. Fluorescein, the most commonly used dye, is green and is usually complexed with K^+, Na^+ or available as a pure compound. In tests of karst hydrology systems it was found to be the most retarded and dispersed dye [Brown, 1971]. However other studies have shown that it has low reactivity [Smart and Laidlaw, 1977; Sabatini and Al Austin, 1991].

Rhodamine is a fluorescent xanthene dye used as a conservative tracer for aquifer characterisation [Sutton et al., 2000], or a surrogate sorbing tracer for contaminant transport studies, depending on which isomer is used. It can be easily measured by fluorimetry at low concentration (e.g. 0.1 ppb) and is non-toxic [Vasudevan et al., 2001]. Care needs to be taken during interpretation if using Rhodamine water tracing dye (RWT), a mixture of sorbing and conservative isomers. If not treated as two separate compounds the double breakthrough signal caused by the conservative and sorbing isomer may be misinterpreted [Sabatini and Al Austin, 1991].

The light noble gases (helium, argon and neon) and sulphur hexafluoride, SF_6, are also used as conservative tracers. The gases are limited to use in the saturated zone, as they would otherwise strongly partition into the gas phase retarding them. This also means care is needed to minimise losses of these tracers from injection to analysis. Their main advantage compared with anionic tracers is a much lower detection limit (e.g. ppt) [Wilson, 1998]. SF_6 has been shown to behave identically to Br^- in laboratory sand columns [Wilson and Mackay, 1993]. It is non-toxic and not affected by degradation or ionic adsorption. It should not be used as a conservative tracer if organic material is present, as it has a slight hydrophobic tendency. Gas tracers are injected into the aquifer in tagged bubbles by sparging or diffusion through a water impermeable emitter [Wilson, 1998]. This makes gas tracers unsuitable for use alongside tracers pumped into the aquifer in aqueous solutions and therefore also in forced gradient tests.

Fluorobenzoate isomers may also be useful at non-acidic pH conditions, if other tracers are not suitable [Dahan and Ronen, 2001]. Most behave similarly to Br^- in soils with an organic carbon content up to 3.5 % [Bowman and Gibbens, 1992] and may be more useful than Br^- if there is a high clay content that leads to anionic exclusion [Jaynes, 1994]. They are measured using HPLC analysis.

Stable isotope tracers such as ^{18}O and D can potentially be used, although they are relatively expensive. Such isotope tracers can be used to assess the contribution of groundwater from different sources. Katz et al. [2004] used the $^{15}N/^{14}N$ ratio in NO_3 to access nitrate contamination and ground water age.

In this study, fluorescein was chosen as a conservative tracer, due to ease of measurement and giving a visual aid. This was compared with Br^-, SO_4^- and Cl^- to evaluate behaviour in mixtures and identify which compound provided the most consistent estimates of relevant aquifer parameters, with the lowest uncertainty in values. These tracers can all be measured by ion chromatography. SO_4^- may not be suitable if biodegradation by sulphate reduction is being evaluated in a test. F^- was not considered, as it has a detection peak close to that of acetate (used in Chapter 5) when analysing by ion chromatography.

4.2.2. **Review of inorganic sorbing tracers**

Inorganic cation species typically sorb onto negatively charged surfaces of aquifer and soil particles, retarding their migration, by the process of ion exchange. Adsorption is considered to be reversible as cations equilibrate with background competing cations. Therefore quantitative tracer recovery would be expected over time. Adsorption of these tracers may lead to desorption of native cations on the sorbent surface. The increase of the desorbed species in the groundwater can also be measured during breakthrough of the sorbed (added) tracer.

Sorption of an inorganic cation is related to the cation exchange capacity (CEC) of the sorbent, which is a measure of its negative surface charge [Appelo and Postma, 2005]. The CEC can be estimated from the BTC of the tracer and displaced cations and aquifer properties. From the tracer retardation factor, R, the distribution coefficient, K_d (ratio of tracer sorbed / tracer in solution), can be calculated:

$$K_d = \frac{\Theta}{p_b}(R-1) \tag{4.1}$$

where p_b is bulk density of the sorbent and Θ is the sorbent porosity. From concentrations of the tracer cation, A^{n+}, and displaced cation, B^{m+}, the selectivity coefficient, $K_{A/B}$ can be calculated from the exchange reaction equation:

$$^1/_n\ B\text{-}X_n + {}^1/_m\ A^{m+} \leftrightarrow {}^1/_m\ A\text{-}X_m + {}^1/_n B^{n+} \tag{4.2}$$

from,

$$K_{A/B} = \frac{[A-X_m]^{1/m}[B^{n+}]^{1/n}}{[B-X_n]^{1/n}[A^{m+}]^{1/m}} \tag{4.3}$$

Square brackets in the equation denote activities and –X denotes that the cation is attached to an exchange site. The constants m and n denote the positive charge of cations A and B respectively. Equation 4.2 conforms to the *Gaines-Thomas* convention [Appelo and Postma, 2005]. Selectivity coefficients can be used in geochemical calculations to assess sorption in multi-component systems, while the simpler K_d concept does not account for interaction between the injected cation tracer and native cations on the aquifer matrix. From K_d and $K_{A/B}$, at low tracer concentrations as expanded by [Wilson, 1998], CEC can be calculated:

$$CEC = \frac{K_d[B]}{K_{A/B}} \tag{4.4}$$

Alternatively, CEC can be estimated with numerical reactive transport codes, using a BTC curve-fitting approach [Thornton et al., 1996]. The CEC can be used to estimate the natural attenuation of landfill leachate plumes, which may have concentrations on the order of 1 g/l of Na^+, K^+, Fe, Mn, NH_4^+, Ca^{2+} and Mg^{2+} [Thornton et al., 2000b; Christensen et al., 2001].

Na^+. K^+ and Mg^{2+} salts are typically used as sorbing tracers with conservative anions, which allow a conservative and sorbing tracer test to be simultaneously conducted to estimate different aquifer properties. Mixtures of cation tracers can be used to evaluate the retardation of each cation [Bjerg and Christensen, 1993; Andersson et al., 2004]. However at high concentration, or with specific cations (e.g. K^+), preferential and competitive effects may occur [Valocchi et al., 1981; Sposito, 1983]. At Cl^- concentrations of 0.05 M or above (which may be typical for a tracer test) Sposito [1983] found that Ca^{2+} was sorbed preferentially to clay over Mg^{2+}, due to the formation of thermodynamically favourable $CaCl^+$ complexes. This may lead to an underestimation of CEC if Mg is used as a tracer. The effect is also possibly seen in the results of Valocchi et al [1981], where the Ca^{2+} breakthrough is less than the injected water concentration and the Mg^{2+} breakthrough is higher. Alternatively the high concentrations used may have caused $CaCO_3$ to precipitate if solubility was exceeded. This suggests that tracer concentrations should be kept below 0.05 M, a sensible limit being 0.01 M. Preferential sorption effects may also occur at low concentrations. K^+ may be preferentially sorbed relative to Ca at low concentration; the effect being significant below ~0.5 mM K [Bjerg et al., 1993]. It was suggested that this non-ideal exchange behaviour may have been caused by specific sorption of K^+ in clay lattices. If the ionic strength of a tracer solution is significantly reduced during a test, perhaps due to dilution from relatively fresh groundwater, the more highly charged cations can be preferentially sorbed [Appelo and Postma, 2005].

In this study, the CEC of the sand was measured using NaBr, NaCl, $MgSO_4$ and KBr salts. The cations in these salts have all been used in field tracer tests [Valocchi et al., 1981; Dance, 1983; Ceazan, 1989; Bjerg and Christensen, 1993]. The performance of cations as tracers on their own and in pairs was investigated. If a cation with "low" sorption potential, such as Na^+, is mixed with a cation with "high" sorption potential, such as K^+, then this arrangement should allow measurement of the CEC from one of the BTCs, if Na^+ is only slightly retarded, or K^+ is highly retarded with an unclear breakthrough peak [Bjerg and Christensen, 1993]. Using a range of cations therefore

improves the reliability of aquifer CEC estimates from a tracer test. Since the sensitivity of a dipole flow tracer test (DFTT) in the estimation of CEC is so far unknown and the retardation factor in push-pull tests (PPTs) can only be delineated from variations in breakthrough curve slope relative to a conservative tracer, it is useful in this context. Calcium was not considered suitable as a tracer cation, as it is a dominant background cation in groundwater in many aquifers and is directly influenced by chemical precipitation/dissolution reactions (e.g. $CaCO_3$), particularly in calcareous aquifers. The behaviour of the injected cation (if Ca^{2+}) may be masked by the response of the background Ca^{2+}. Also, as discussed, calcium may be preferentially adsorbed over other cations if chloride concentrations are high.

4.2.3. **Ni-EDTA**

EDTA ($C_{10}H_{16}N_2O_8$) is a highly nucleophilic anthropogenic ligand used in industry. It forms stable complexes with various metals (e.g. U^{6+} [Davis et al., 2000] and heavy metals (e.g. Cd, Pb and Hg) [Nowack and Sigg, 1996]), altering their transport behaviour in aquifers. The transport of these metals complexed with EDTA can be simulated by using EDTA complexed with more stable metals as an anionic tracer. Ni-EDTA was investigated as a potential anionic tracer, for use in acidic and EDTA / complex ligand-polluted environments. It can be used to evaluate the migration of Zn, Ca, Co, Cu and Pb with EDTA. EDTA forms strong complexes with these metals in a quinquedente structure in the pH range of 4-8 (Figure 4-1), and forms inner sphere sorption complexes [Nowack and Sigg, 1996].

The sorption properties of metal-EDTA complexes depend strongly on their structure [Nowack and Sigg, 1997], and therefore Ni-EDTA cannot be used to predict the migration of all metals complexed with EDTA. Multi-species tracer tests have been undertaken in Cape Cod, Massachusetts to identify the most appropriate metal to complex EDTA with [Davis et al., 2000; Hess et al., 2002]. Natural gradient tracer tests were undertaken in an acidic sewage-contaminated aquifer. EDTA was

complexed with Ni, Pb, Cu and Zn, forming predominantly Me-EDTA^{2-} anionic

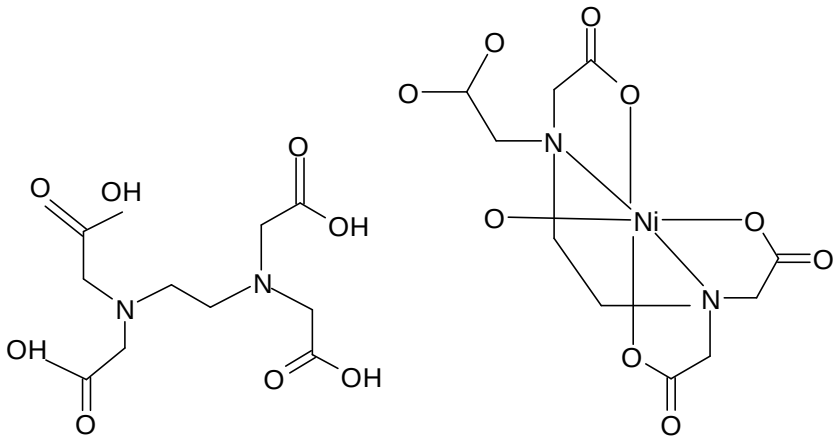

(a) (b)

Figure 4-1 : (a) EDTA structure, (b) EDTA complexed with Ni [*Nowack and Sigg*, 1996].

complexes. Adsorption of the Me-EDTA^{2-} complexes was expected to increase with decreasing pH (as aquifer mineral surface charge became more positive) and compete with the adsorption of phosphate, sulphate and other anions. The loss of injected metals over time was Pb$\geqslant$ Zn> Cu> Ni. The recovered mass of Ni was relatively constant and had a retardation factor of 1.2, relative to the conservative tracer used (Br^-). Metals were attenuated due to non-reversible adsorption onto Fe- and Al-oxyhydroxides or exchange with Fe^{3+}, after dissolution of ferric oxide by the EDTA. A decrease in removal of injected metals over time was correlated with a decrease in dissolution rate of ferric hydroxides with complexed EDTA [Nowack and Sigg, 1997], suggesting that the latter mechanism is most likely. Complexed Ni only starts to exchange with Fe^{3+} at very low concentration, where Fe exchange is thermodynamically more stable [Kent et al., 2002]. This makes the Ni-EDTA complex quite stable under most aquifer conditions. The centre of Ni-EDTA^{2-} adsorption edges (i.e. 50 % Ni-EDTA^{2-} adsorbed) varies from pH 6.5 to 8.35 on typical adsorbent oxides at 1 µM concentration [Nowack et al., 1996]. This is in the pH range of most aquifers [Banks et al., 1998; Thornton et al., 2000b]. Therefore Ni-EDTA^{2-} retardation may vary significantly in aquifers. This potentially makes Ni-EDTA^{2-} an effective tracer to evaluate anion exchange, when investigating metal

migration in EDTA complexes. EDTA is resistant to biodegradation and so should not affect acetate migration in mixed tracer tests.

4.3. **Methodology**

4.3.1. **Development of column design**

Initial experiments used clear acrylic columns, 0.75 m long with an internal diameter of 0.05 m. Fourteen sample ports were spaced evenly along the column and consisted of 18 gauge 3.8 cm needles fixed with Swagelock® fittings. Two ml syringes were attached to the needle to extract samples. Plates were attached to the ends of the column with 8 bolts and wing nuts, and a seal was made with a rubber o-ring to stop leakage. These sampling ports provide finer resolution of solute BTC and a small purge volume. The size of the columns was suitable for conducting forced gradient tracer tests in 1-day experiments with the pumps available. A pore volume residence time in the column of 4 hours would equate to a velocity of 0.187 m/hr. This is similar to flow rates used in field forced gradient tests [Ptak and Schmid, 1996; Istok et al., 1997].

Apart from initial experiments to assess the CEC of the sand and behaviour of conservative tracers, these columns were not used in the later tests (Table 4-1). This was for a number of reasons. The acrylic was liable to stress fractures if screws were over tightened, leading to leaks that could not be satisfactorily repaired. Tensol cement and silicon sealant was required to prevent leakage in joints round the end plates, but some leaks could not be completely fixed. The sample ports also often became blocked with fine sand, which was difficult to clear.

Table 4-1: Summary of column design and tests performed for the two different styles of column

	Acrylic Columns	uPVC Columns
Length	0.75 m	0.75 m
Internal diameter	0.05 m	0.053 m
Sample ports	15	3
Test performed	Hydraulic and CEC calibration tests	Hydraulic and CEC calibration tests Ionic tracer mixture tests Ni-EDTA tests

The column design was therefore simplified to overcome these problems. New columns of similar dimension were constructed from opaque uPVC pipe with end caps attached using silicon sealant. These columns were 0.75 m long with an internal diameter of 0.053 m. This size was considered suitable after PHREEQC (a numerical geochemical and transport model supported by the United States Geological Survey [USGS, 2008]) simulation of experiments run with different column dimensions. Three sample ports were spaced evenly along the column, which was considered a sufficient number to allow good resolution of solute BTC. For the samples ports a BSPP nipple adaptor 1/4 inch x 1/4 inch was screwed into the side of the column. This was attached to a standard lever 1/4 inch BSP ball valve. A seal was obtained to the column using Teflon tape, fibre washers and silicon sealant. A 6 mm tubing adaptor was connected to the other end of the ball valve for sampling using a syringe. A small disk of 100 micron mesh was placed between the nipple adaptor and the ball valve to prevent sediment loss. These sample ports had a larger dead volume to purge than those in the acrylic columns, but minimised blockage and leakage.

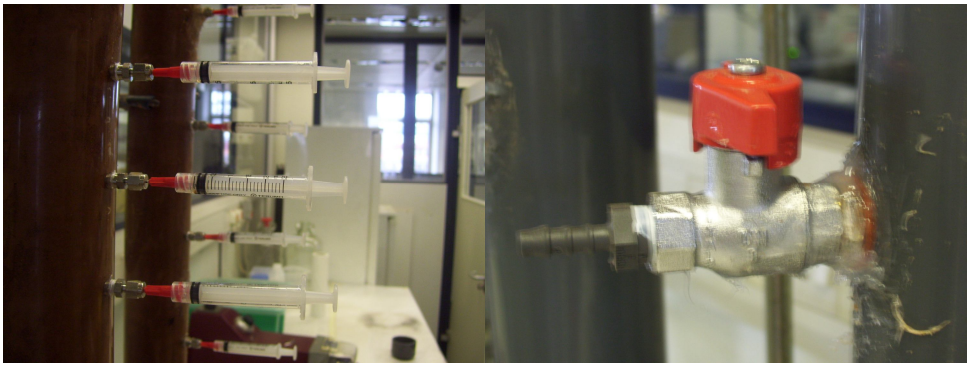

Figure 4-2: Sample ports for the acrylic columns in the left picture and uPVC column in the right picture.

The end fittings on the columns were a Swagelock® fitting with an o-ring face seal. Fibre washers and silicon sealant were used on the uPVC columns to provide an airtight seal. These connected the column to rigid 6 mm outer diameter PTFE tubing. Push-fitting t-connectors were used when flow was to be split. Swagelock® toggle valves were used for the sample ports at the ends of each column. These provided quick sampling during tests with a low purge volume.

A Watson Marlow 501U pump was used to inject the tracer solution through the columns from the base up, with a different line for each column. This ensured that flow in the columns was independent of any variation in hydraulic conductivity and that tracer breakthrough times could be accurately predicted.

Figure 4-3: Picture of the new (left) and old style (right) columns in the vertical position.

4.3.2. **Experimental design**

The columns were filled with the same Permo-Triassic sand that was used in the acetate column experiments (Chapter 5).This was supplied from the Builders Centre Ltd, Sheffield, S2 1TA, taken from Carlton Forest Quarry, Worksop. The sand was chosen to represent a typical red sandstone aquifer in the U.K. [Kimblin, 1995]. The >1.18 mm size fraction was removed by sifting to reduce packing heterogeneity. The column was dry packed in 5-10 cm intervals before being slowly saturated with a

synthetic groundwater composition based on unpolluted sandstone aquifer concentrations at the Site for Innovative Research on Natural Attenuation (SiREN) in Carrington [unpublished Shell data]. The synthetic groundwater was made using inorganic salts added to deionised water, to represent the cation concentrations in the aquifer. However, the high Na concentration ($4.74x10^{-3}$ M) in the aquifer was reduced for the synthetic groundwater. Alkalinity was kept low to identify any small variation during the tests.

The experiments were performed in up-flow mode and most samples were taken at the end of the columns. Intermediate samples could be also taken at sample ports (locations shown in Figure 4-3). The columns were equilibrated with synthetic groundwater before the start of the experiments for at least 10 pore volumes. Modelling with PHREEQC showed that this was sufficient for each column to reach chemical equilibrium. A pore volume is the volume of water present in the saturated column.

Table 4-2: Inorganic ion concentration (M) of SiREN site groundwater and salts added to deionised water to produce synthetic groundwater.

Ion	SiREN site	Synthetic Groundwater
Ca^{2+}	1.54×10^{-3}	1.54×10^{-3}
K^{+}	5.14×10^{-4}	5.14×10^{-4}
Mg^{2+}	4.94×10^{-4}	4.94×10^{-4}
Na^{+}	4.74×10^{-3}	1.00×10^{-3}
Cl^{-}	1.01×10^{-3}	4.58×10^{-3}
SO_4^{2-}	3.86×10^{-4}	4.94×10^{-4}

A summary of the column tests performed is shown in Table 4-3. Tracer in initial calibration tests was injected at two different flow rates to identify any effect of velocity on solute dispersion. The fluorescein and Br^{-} BTC provided estimates of porosity and longitudinal dispersivity, as well as confirming the quality of the column packing. The Na^{+} BTC and background ion concentrations helped to give an estimate

of the sand CEC. The fluorescein was used as the reference conservative tracer and a visual aid to estimate when breakthrough occurred. Inorganic conservative ions compared were Cl^-, Br^- and SO_4^{2-}, these anions commonly complexed in salts with Na^+, Mg^{2+} and K^+ and can be quantified simply by ion chromatography. Injection concentrations allowed good accuracy in analysis and sensitivity to column parameters, while not being masked by the background ion signal. After the experiments, columns were flushed until the output fluorescence reduced to pre-test levels. This required approximately 12 pore volumes of flushing.

Ni-EDTA concentrations used were similar to previous field tests [*Davis et al.*, 2000]. The Na^+ concentration was also increased by the Ni-EDTA stock, which was made with di-sodium EDTA and Ni nitrate, boiling the solution for 1 hour to ensure formation of the complex [Nowack et al., 1996]. Retardation of Ni-EDTA was expected to be low due to the pH of the columns (pH7), which is in the middle of the expected sorption edge of Ni-EDTA onto iron oxides [Nowack and Sigg, 1996].Therefore, 2 pore volumes was considered a suitable volume of tracer to pass through the columns.

4.3.3. **Chemical analysis**

All samples were filtered through a 0.2 µm polyethersulfone membrane. A 100 µl aliquot of 0.1 M HCl was added to 2.5 ml of sample to minimise sorption onto the sample container. Samples were stored frozen in a -10˚C refrigerator. Fluorescein concentration was measured by proxy of fluorescence on a Perkin Elmer Luminescence Spectrometer LS30. The excitation wavelength was 474 nm and the emission wavelength was 514 nm. Fresh calibration solutions were used for each analysis. Ni was measured on a Perkin Elmer AAnalyst 200 Atomic Adsorption Spectrometer, at a wavelength of 232 nm and slit width of 1.8 nm. It was assumed that EDTA remained complexed with Ni throughout the experiments and this was not measured separately. The limit of detection for Ni was 0.01 mg/l.

All other inorganic ions were analysed on a Dionex DX-120 Ion Chromatograph. A RFIC™ Ionpac® A514A 4 x 250 mm Analytical Column was used for anion analysis, with an eluent of 8mM Na_2CO_3 and 1 mM $NaHCO_3$ and a RFIC™ Ionpac® C512A 4 x 250 mm Analytical Column was used for cation analysis, with an eluent of 20 mM methane sulphonic acid. The samples were diluted to the calibration range of the instrument. The lower limits of detection were below 1 mg/l except for PO_4^{3-}. Exact values are given in Appendix B. The analytical precision, based on replicate analysis, was ± 2 % for anions and ± 4 % cations, respectively.

Alkalinity (as mg/L $CaCO_3$) was measured on 20 ml samples during the experiments using a Hach® test kit and digital titrator. Standardised sulphuric acid (0.16 N) was used and values were measured to an accuracy of ± 3.82 mg/l (~3.8×10^{-5} M) $CaCO_3$. This allowed measurements to be made quickly after sampling. Sample pH was measured directly in the centrifuge tube after collection and before alkalinity analysis. The probe was recalibrated each day with fresh standards.

Table 4-3: Summary of column tests performed. Fl = fluorescein. Tracers solutions were made up in synthetic groundwater (Table 4-2). All tests were performed under constant injection conditions for approximately 8 hours.

Tests	Tracers and concentration	Flow rate (ml/min)	Test time (Pore Volumes)	Objectives
Fast and slow calibration tests for each column	Fl (10^{-4} M)/NaBr (10^{-2} M)	Slow tests~3.2 Fast tests ~5	Slow tests ~2 Fast tests ~4	Compare Fl and Br as conservative tracers. Obtain column hydraulic parameters and CEC Identify any effect of velocity on dispersion
Ionic tracer comparisons and mixtures	$MgSO_4$/Fl, KBr/Fl, $MgSO_4$/KBr/Fl, KBr/NaCl/Fl, $MgSO_4$/NaBr/Fl and $MgSO_4$/NaCl/Fl (Fl (10^{-4} M)/ Ionic tracers (10^{-2} M))	All tests ~5	~8 (Samples taken from intermediate ports)	Compare anions as conservative tracers. Investigate performance of cations on own and in mixtures. Assess potential of using two cations together to measure CEC
Ni-EDTA tests	Ni-EDTA (10^{-3}M)/ NaBr ($5x10^{-3}$M) Ni-EDTA (10^{-3}M) /NaBr (10^{-3}M) Ni-EDTA (10^{-4}M) /NaBr ($5x10^{-3}$M) Ni-EDTA (10^{-4}M) /NaBr (10^{-3}M)	5..0 3.1 5.1 3.0	~2	Investigate Ni-EDTA retardation at neutral pH and whether its presence affects estimation of CEC

4.4. **Assessment of sand used in tests**

4.4.1. **Grain size analysis**

The grain size distribution of the Permo-Triassic sand was measured by mechanically shaking. The sand is medium grained and very poorly sorted. The grain size distribution is leptokurtic (Figure 1-4). The inclusive graphic skewness suggests a slight skew towards fine grain sizes, but a comparison of the mode, median and mean suggests a slight skew towards coarse grain sizes. Inconsistency between the two methods was likely caused by an unsmooth grain size distribution. Overall this implies that the grain size distribution is near symmetrical. Approximately 60% was <300 μm in diameter. This fine material is likely to contribute to the high CEC of the sand (see below), but at high flow rates may be mobilised.

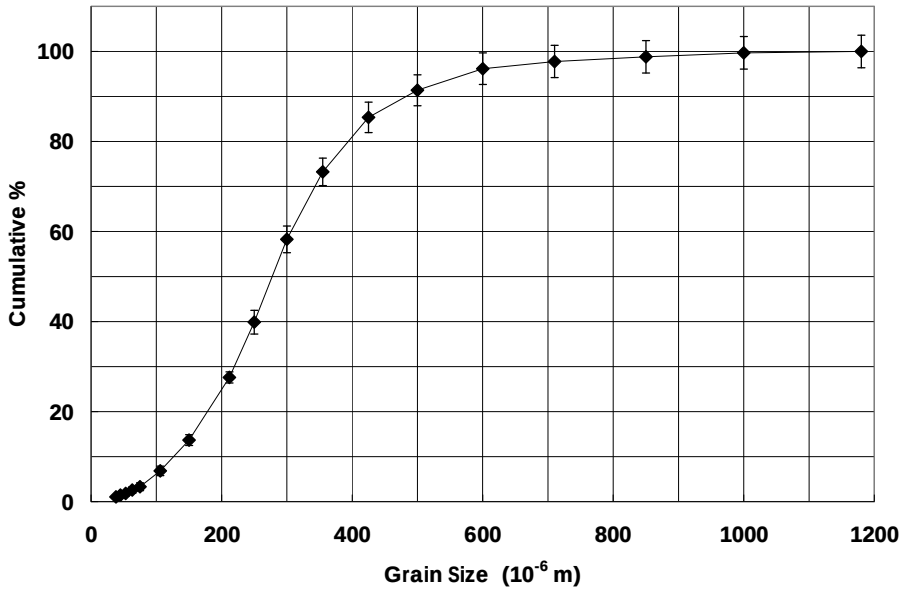

Figure 4-4: Cumulative grain size plot of Permo-Triassic sand. Leptokurtic grain size distribution is indicated by the graphs steep slope.

4.4.2. **CEC analysis**

The CEC of the sand was measured using the method of Edmeades and Clinton [1981], with corrections for total alkalinity. The chemical analysis was performed by the Sheffield Assay Office. The CEC was estimated as 1.59 meq/100g, with a

standard deviation of 0.25 meq/100g for particles up to 1.18 mm in diameter. The CEC is mostly contributed to by smaller particles separated off during sieving, with particles below 150μm having a CEC of 2.96 meq/100g (standard deviation of 0.33 meq/100g). The 1.18 mm-150 μm size fraction had a CEC of 1.54 meq/100g (standard deviation of 0.12 meq/100g). These estimates are similar to the value of 1.4 meq/100g estimated by Eagle [2006].

4.4.3. **Measurement of hydraulic conductivity**

The hydraulic conductivity of the sand columns was estimated using a simple application of Darcy's Law. As the length and cross-sectional area of a column and the change of head are known, the hydraulic conductivity of the column can be estimated by measuring the flow rate, for a constant pump speed. This measurement was performed after all experiments had been completed in a column, prior to repacking for other tests. This ensured that high flow rates which may occur during these measurements (possibly mobilising fine sand fractions), would not affect the experiments. The flow rates were measured in triplicate for each column, with values for individual columns varying by 3.00 ± 2.08 %, showing good consistency. As seen in Table 4-4 the estimated hydraulic conductivity is quite consistent for the columns, suggesting that the packing procedure was reproducible.

4.4.4. **Mineralogy of sand**

XRD analysis showed that the sand is mainly quartz with some calcite and aluminium oxides. A small amount of fine-grained clay minerals is probably present, but it was not considered necessary to fully characterise this fraction for these specific experiments. Iron oxide coatings are clearly visible on the sand grains. The $CaCO_3$ content of the sand was 3.8 wt% [Smalley, 2004].

Table 4-4: Hydraulic conductivity measurements for columns. Each line represents a different time a column was packed

Δh (m)	Q (ml/min)	K (m/s)
0.42	2.43	3.28E-05
0.42	3.93	5.30E-05
0.42	5.67	7.64E-05
0.40	2.43	3.93E-05
0.40	2.86	4.63E-05
0.40	3.53	5.00E-05
0.40	2.63	3.73E-05
0.40	5.73	8.12E-05
0.40	2.26	3.21E-05
0.40	3.63	5.15E-05
0.40	2.06	2.93E-05
0.37	3.20	4.90E-05
0.37	1.90	2.91E-05
Average		**4.67E-05**
Standard Deviation		***1.66E-05***

4.5. **Results and Modelling**

4.5.1. **PHREEQC and STANMOD modelling**

PHREEQC was used for forward modelling to evaluate the experiment design: column dimensions, ionic tracer concentrations, pore volumes to run in an experiment (and consequently flow rate) and column flushing time.

Inorganic anions and fluorescein were assumed to act conservatively and were modelled with the 1-D transport modelling programme STANMOD [Simunek et al., 1999], to obtain estimates of the longitudinal coefficient of hydrodynamic dispersion (D) and pore water velocity. The velocity and longitudinal dispersivity (D/ velocity) obtained were used to model ion transport with PHREEQC. The retardation factor of Ni-EDTA breakthrough was estimated using STANMOD assuming the pore water velocity estimated from the conservative tracer to be true.

PHREEQC was used to estimate CEC and sorption coefficient values for the ion data in the column experiments. In PHREEQC cation exchange is defined by half reactions

according to the *Gaines-Thomas* convention [Appelo and Postma, 2005] where the sorption coefficient (K_A) is the equilibrium constant of the equation:

$$A^n + nX^- = AnX \quad (4.5)$$

where A is the cation, X is a sorption site and n is the cation charge. An example input file is given with full explanation in Appendix B. Estimates of CEC in the calibration tests were obtained with each cation having a different K_A value, which was the same for all columns. In the ion tracer comparison and mixture experiments cation profiles were first fitted by keeping the CEC value fixed and varying each cation K_A. If a good fit could not be obtained this way the CEC value was varied within error of the laboratory measurement.

4.5.2. **Column hydraulic and CEC calibration tests**

Estimates of CEC, longitudinal dispersivity and effective porosity were all obtained from these column experiments. The experiments also allowed the performance of Br^- and fluorescein as conservative tracers to be compared. Breakthrough curves of fluorescein and Br^- were first modelled with STANMOD which gave the velocity of the tracer through the column and the longitudinal coefficient of hydrodynamic dispersion, D, (longitudinal dispersivity (α_L) x average water velocity). Estimates of velocity and α_L for Br^- were then used in PHREEQC to interpret the cation BTC. The pore fluid velocities were approximately 0.23 m/hr in the slower tests and 0.45 m/hr for the faster tests. Columns labelled with a lower case letter in graphs and tables are the acrylic columns and columns labelled with a higher case letter are the uPVC style columns. STANMOD fits of Br^- and fluorescein were good for all tests with high model efficiencies obtained from route mean square error analysis [Berthouex and Brown, 2002; Bolster and Hornberger, 2007], see Table 4-5. However model efficiencies are lower in the fast fluorescein tests, with a higher standard deviation, showing greater deviation of data from smooth breakthrough.

Table 4-5: Average model efficiency of STANMOD model fits to Br and fluorescein data during column calibration tests. Fl stands for fluorescein.

	Average (%)	SD (%)
Fl Slow Test	99.53	0.35
Br^- Slow Test	99.40	0.41
Fl Fast Test	97.83	1.17
Br^- Fast Test	99.79	0.21

4.5.2.1. **Effective porosity**

The effective porosity of each column was estimated from the pore volume flushing time of fluorescein or Br^-, calculated by STANMOD, the column dimensions and average flow rate during the test, which was measured three times from the end sample port location. The estimates obtained are shown in Table 4-6. These show good reproducibility between tests and between values obtained using fluorescein and Br^-, with low standard deviation.

Table 4-6: Effective porosities obtained from column calibration experiments. Lower case columns are the acrylic design and upper case the uPVC design.

	Column							
Porosity Estimate	a	b	A	B	C	D	E	F
Fl Slow Test	36.07%	36.67%	34.33%	39.63%	35.88%	36.11%	38.20%	41.73%
Br^- Slow Test	36.26%	35.74%	33.80%	39.81%	35.38%	35.20%	38.35%	42.16%
Fl Fast Test	36.52%	35.58%	34.06%	40.55%	36.71%	34.12%	37.64%	41.43%
Br^- Fast Test	38.73%	35.79%	35.21%	40.71%	37.77%	34.38%	38.61%	43.60%
Average	**36.89%**	**35.94%**	**34.35%**	**40.18%**	**36.43%**	**34.95%**	**38.20%**	**42.23%**
Standard Deviation	*1.24%*	*0.49%*	*0.61%*	*0.53%*	*1.04%*	*0.90%*	*0.41%*	*0.96%*

Statistical tests (analysis of variance and paired students' t-test) were performed with a significance level of 0.05. The null hypothesis was that the mean porosities from the different data sets analysed (Fluorescein slow test, Br^- slow test, fluorescein fast test, Br^- fast test) are equal. If the p value obtained is higher that the level of significance the null hypothesis is accepted and vice versa (see Table 4-7). An analysis of variance test of all porosity values gave a very high p value, suggesting good overall reproducibility in the estimates of column porosity.

Table 4-7: P-values obtained from statistical tests relating to estimates porosity and longitudinal coefficient of hydrodynamic dispersion values. The level of significance used for tests was 0.05. If the p-value is below the level of significance the null hypothesis (see text) is rejected.

	P-value	
	Porosity	D
Analysis of variance test	0.95	0.12
Students' t test pairs		
Fl slow and Br^- slow	0.25	0.58
Fl fast and Br^- fast	0.0098	0.0006
Fl slow and Fl fast	0.49	0.43
Br^- slow and Br^- fast	0.042	0.046

Individual paired students' t-tests were used to test the similarity between pairs of data sets. The null hypothesis is that there is no difference in variance between the two data sets analysed. The hypothesis was not rejected for the fluorescein and Br^- slow test pair and was rejected for the fluorescein and Br^- fast test pair. This shows the greater disparity between Br and fluorescein values seen at the higher flow rates. This may be due to the problems encountered with normalisation of the fluorescein concentration, explained in the next section. The null hypothesis was not rejected for fluorescein slow and fast test pair but was for Br^- slow and fast test pair. The null hypothesis would not be rejected for the Br pair if a slightly lower level of significance was used. The data suggests good consistent performance of fluorescein at different flow rates and reasonable consistency for Br^-. Columns a, b, A, C and D have a porosity of 34.9% to 36.9%. The porosity of the other columns is a little higher, but the low dispersion in BTCs (Figure 4-5 and Figure 4-6) suggests that these columns are well packed.

4.5.2.2. **Longitudinal coefficient of hydrodynamic dispersion**

The estimates of D are more variable than porosity, with a standard deviation over one third of the average value in some cases (Table 4-8). There may be inaccuracy in estimates using the fluorescein BTC. The fluorescence BTC were normalised to an average of the last 5 readings at the end of the experiment, when the tracer concentration had stabilised at a peak. It was not normalised to the input fluorescence, as the pH (7-8) at the end of the column was higher than that of the stock solution (5-

6). Separate testing showed that the stock solution fluorescence depended on pH (Appendix B). Therefore the fluorescence of a specific concentration was larger at the end of the column than the stock solution. In some tests the fluorescence decreased slightly towards the end of the test, most likely due to a small decrease in pH seen. This led to some peaks (Figure 4-6) of around 1.2 x maximum fluorescence. This in turn leads to shortening of the modelled tracer rising limb and under-estimation of D. This is clearly seen in the fast flow rate tests, where the fluorescein estimated D is less than that predicted by Br^-, which was normalised to its input concentration. This effect may also have caused the lower model efficiency of STANMOD fits to fluorescein data in fast tests. This shows that Br^- is a more reliable conservative tracer than fluorescein in this situation. However fluorescein is still useful, allowing quick analysis and identification of when tracer breakthrough starts. The estimates of the average coefficient vary from 2.26×10^{-5} to 4.93×10^{-5} m^2/min, which shows good similarity between the columns. Statistical tests were performed on the data the same as on the porosity values, with similar conclusions (see Table 4-7). The analysis of variance tests showed good reproducibility between values of D in all tests. Values for the faster tests are not twice as large as the slower tests, as would be expected, if α_L of the columns was constant. Results are similar for the paired data sets. This suggests that velocity does not significantly affect the dispersion seen in the column experiments.

Table 4-8: Longitudinal coefficients of hydrodynamic dispersion (D) obtained from column calibration tests. Lower case columns are the acrylic design and upper case are the uPVC design. All values x10^{-5}.

D estimate	Column							
(m^2/min)	a	b	A	B	C	D	E	F
Fl Slow Test	2.08	2.00	4.54	2.56	3.19	4.55	2.11	2.14
Br^- Slow Test	3.42	1.51	4.43	2.65	2.60	3.37	3.46	3.34
Fl Fast Test	2.44	2.60	4.50	1.71	2.67	1.42	1.51	3.24
Br^- Fast Test	4.12	2.91	6.25	2.76	4.52	3.48	2.65	6.10
Average	**3.01**	**2.26**	**4.93**	**2.42**	**3.24**	**3.21**	**2.43**	**3.70**
Standard Deviation	*0.93*	*0.62*	*0.88*	*0.47*	*0.89*	*1.31*	*8.29*	*1.69*

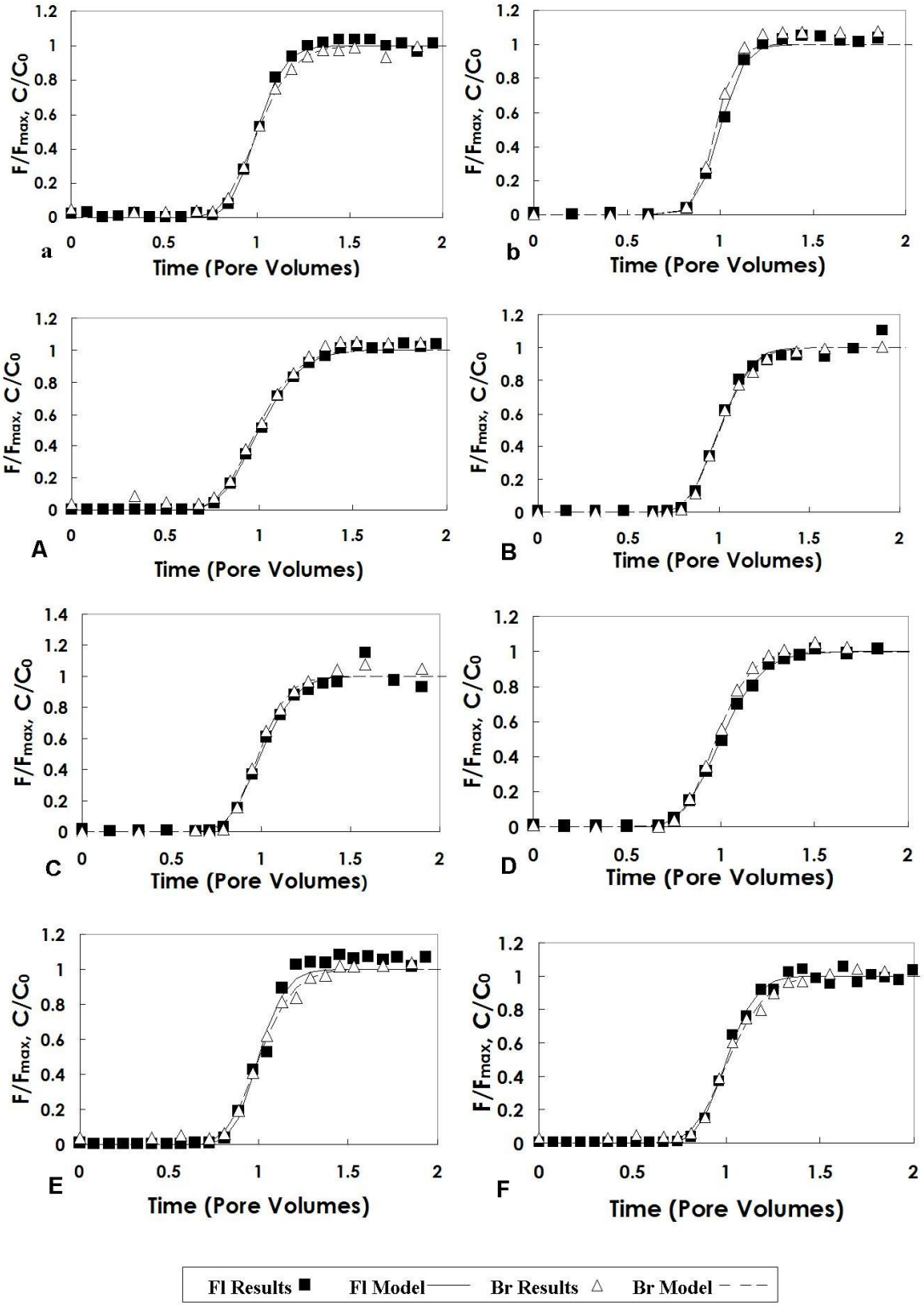

Figure 4-5: Comparison of fluorescein and Br^- BTCs during slow flow rate calibration tests for all columns. Br^- concentration and fluorescein fluorescence are normalised to input and maximum values respectively.

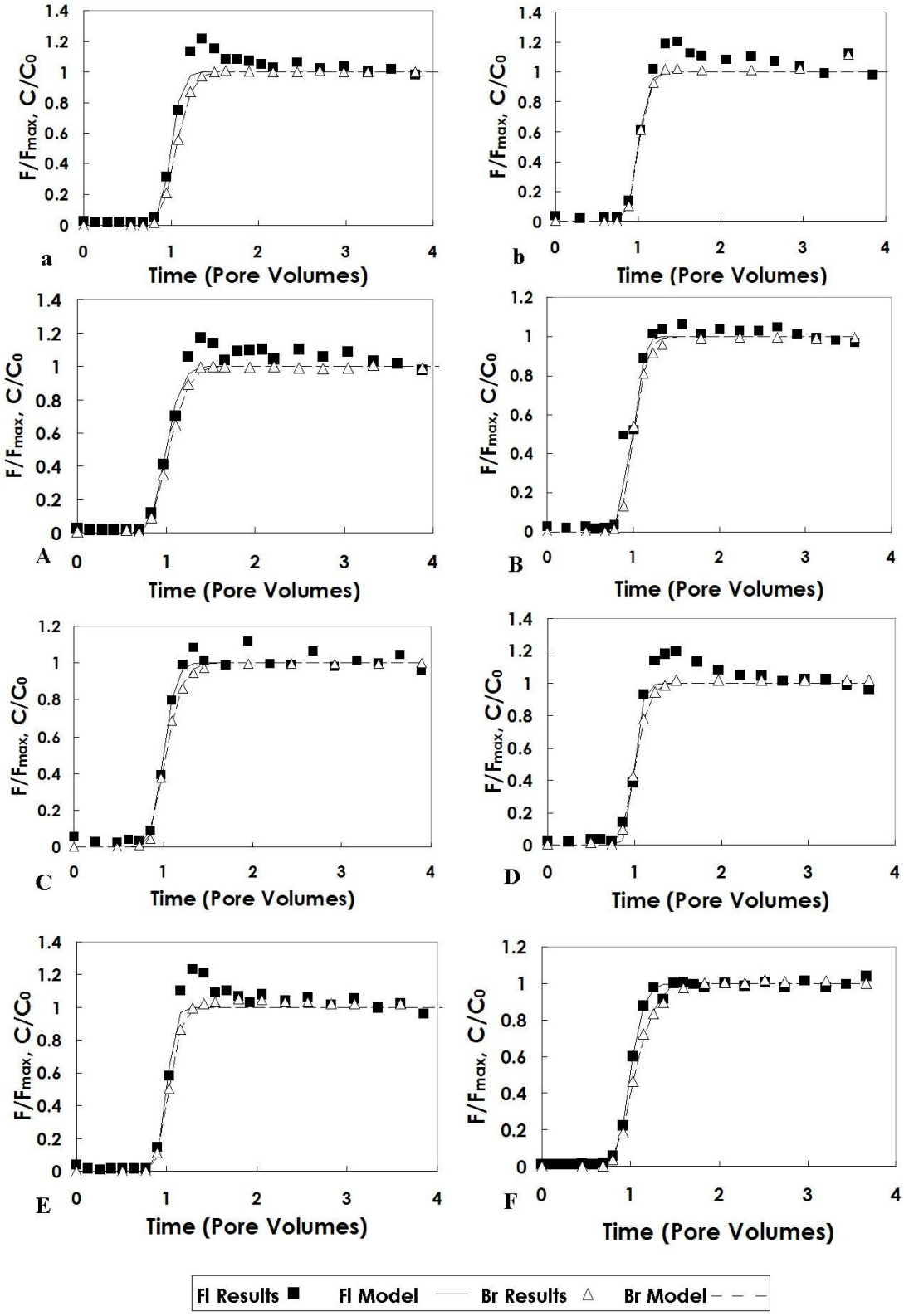

Figure 4-6: Comparison of fluorescein and Br^- BTCs during fast flow rate calibration tests for all columns

4.5.2.3. **CEC**

The CEC of the columns was estimated with PHREEQC, keeping α_L, velocity and porosity constant. For initial estimates the CEC value obtained from analysis of the sand was used. This was then varied in 0.05 meq/100g increments to obtain improved fits. Estimates of CECs were converted from meq/100g to mol sites/litre using the column empty volume, sand mass in the column and porosity [Appelo and Postma, 2005]. The best fit obtained for all columns was within the standard deviation of the CEC analysis, 4 showing very good fits for 1.59 meq/100g exactly. A high model efficiency (over 90%), was estimated for Na^+ BTC in all columns from route mean square error analysis [Berthouex and Brown, 2002; Bolster and Hornberger, 2007], and indicates the overall quality of the parameter fitting.

Table 4-9: CEC, Empty Volume, Dry Sand Mass and model efficiency of fit to Na data for all columns

	Column							
	a	b	A	B	C	D	E	F
Empty Volume (L)	1.47	1.47	1.66	1.66	1.66	1.66	1.66	1.66
Dry Sand Mass (g)	2304.6	2199.2	2636.9	2516.4	2571.4	2644	2545.5	2495.8
CEC from PHREEQC (meq/100g)	1.59	1.65	1.40	1.40	1.45	1.59	1.59	1.59
Model Efficiency PHREEQC Na fit (%)	99.22	98.70	96.75	97.37	97.44	96.56	91.52	97.95

4.5.2.4. **Cation breakthrough curves**

An example breakthrough profile for cations in the column experiments is shown in Figure 4-7. The Na BTCs were reproduced very well with PHREEQC. The background Mg^{2+} and Ca^{2+} ions increased in concentration to nearly twice their original value, just before Na^+ breakthrough. This relates to desorption of background ions and sorption of Na^+. The model slightly overestimates, but otherwise fits well, the cation BTC for most columns. The Mg^{2+} and Ca^{2+} concentration returns to near background values before the end of the test, as equilibrium conditions are approached. The concentration of K^+ increases to a maximum of 1.2 from 0.6 input values in tests at the same time as Ca^{2+} and Mg^{2+}. It then quickly returns to a stable value. However, in the modelled K^+ BTC the first peak is followed by a trough from approximately 1.5 to 3.5 pore volumes, corresponding to the main arrival of Na^+ (i.e.

K^+ is being sorbed and Na^+ desorbed), before returning to the input value. This feature is observed in the other columns tested and suggests that PHREEQC overestimates the re-sorption of K^+ and underestimates the re-sorption of Ca^{2+} and Mg^{2+}. The larger replacing power of Mg^{2+} and Ca^{2+} over K^+, when exchanging with Na^+, conforms with theory [Yong et al., 1992].

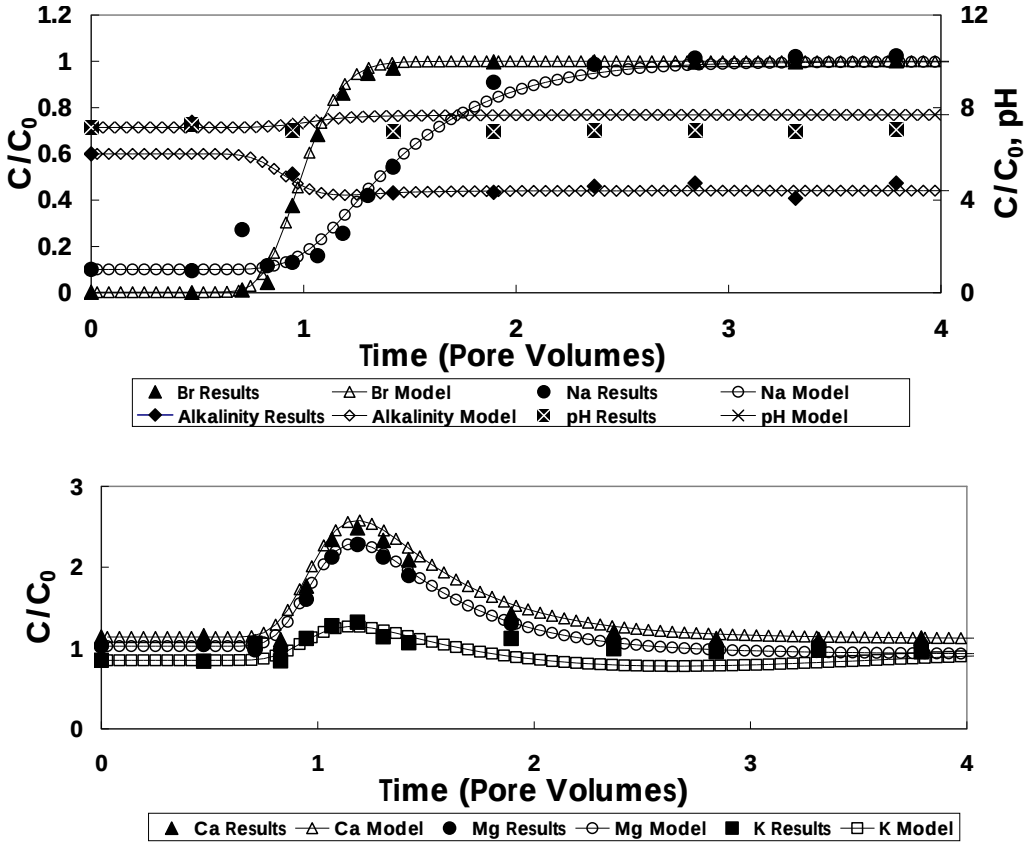

Figure 4-7: Hydraulic and CEC calibration data from column C. On the top graph pH and alkalinity are plotted on the secondary axis. Eluted cations are plotted separately on the bottom graph. The graphs for the other columns are in the Appendix E1.

4.5.2.5. **Alkalinity and pH**

Alkalinity and pH varied little during breakthrough, suggesting strong buffering in the columns. This breakthrough had no effect on the cation profiles, implying that no species was close to precipitation (e.g. PHREEQC modelling calculated the (calcite saturation index (SI) to be -1.28 at the end of the test in column C). The background pH at the start of the experiment was 7.0-7.5, whereas the tracer stock pH was close to 5.3. However after tracer breakthrough the pH was typically 6.7-7.2, not 5.3.

Similarly, the background alkalinity at the start of an experiment was close to 25 mg/l $CaCO_3$ and the stock solution was close to 4 mg/l $CaCO_3$. However after tracer breakthrough the alkalinity was typically 16-20 mg/l $CaCO_3$. PHREEQC was used to inverse model the reaction between the equilibrium solution in the columns and synthetic groundwater. This suggested that a small amount of calcite dissolution, comparable to a concentration of 1.5-4 $x10^{-4}$M, can account for the difference in alkalinity. It is possible that degassing of column samples causing partial equilibrium with atmospheric CO_2 also occurred, due to the analysis method for alkalinity. Considering these observations, SIs for calcite of -0.6 to -0.75 were required by PHREEQC to fit the solute BTCs. These values are greater than the SI indicated from end of test solutions (see above). The end of test solutions only represent one data point, while these values were required to fit the entire breakthrough, therefore some difference is expected. It was expected that the calcite SI would be closer to 0 (i.e. saturation), due to 3% calcite present in the sand [Appelo and Postma, 2005]. However when the calcite SI was allowed to reach equilibrium the alkalinity was overestimated. The rate-limiting process of calcite dissolution is the surface reaction [Appelo and Postma, 2005]. The sub-saturation of calcite may be explained if calcite is present in aggregates with a low surface area in contact with the flowing water. However, this cannot be proven with the available data. The simulated pH does not show the same trend as observed values in the experiments, but remains around neutral. The pH in control experiments varied over a similar range of values (data in Appendix E1).

4.5.3. **Ionic tracer mixtures**

Values of D and velocity obtained through inverse modelling with STANMOD for different inorganic anions are shown in Table 4-10. Values obtained with Br^- and Cl^- are within 95% confidence limits of each other. However SO_4^{2-} velocity is consistently below the minimum 95% confidence limit of Br^- or Cl^-. Some of this discrepancy may be due to analytical error. Br^- and Cl^- may be exhibiting anion exclusion effects; however this is unlikely as they have a smaller negative charge than

SO_4^{2-}. Slight sorption of SO_4^{2-} onto a small amount of positive surface sites may be occurring in the column [Yong et al., 1992]. Due to this uncertainty SO_4^{2-} derived values were not used for PHREEQC modelling. The inorganic anions were slower to breakthrough than fluorescein, although this observation may reflect the solution pH and procedure used to normalise the fluorescein data (see above). The variation in alkalinity and pH in the control column during the test was similar to that in previous tests, indicating that these species are not affected by the tracer. The pH never reached input levels, even at the lower sample ports where samples were collected for the tracer mixture tests, showing buffering reaches equilibrium near the base of the columns. Calcite SIs required by PHREEQC to fit the data varied from -0.70 to -1.30. These values are similar to those required in the column calibration tests (see above).

Table 4-10: Values of pore water velocity and D obtained through inverse modelling with STANMOD for Cl^-, Br^- and SO_4^{2-} in ionic mixture tests. Also shown are minimum and maximum 95 % confidence values.

		Cl^-			Br^-			SO_4^{2-}		
Test		value	min 95 %	max 95 %	value	min 95 %	max 95 %	value	min 95 %	max 95 %
$MgSO_4$/KBr	Velocity (m/min)				$4.48x10^{-3}$	$4.42x10^{-3}$	$4.54x10^{-3}$	$4.38x10^{-3}$	$4.22x10^{-3}$	$4.54x10^{-3}$
	D(m^2/min)				$2.39x10^{-5}$	$1.96x10^{-5}$	$2.82x10^{-5}$	$3.09x10^{-5}$	$1.65x10^{-5}$	$4.52x10^{-5}$
KBr/NaCl	Velocity (m/min)	$4.80x10^{-3}$	$4.70x10^{-3}$	$4.90x10^{-3}$	$4.84x10^{-3}$	$4.72x10^{-3}$	$4.95x10^{-3}$			
	D(m^2/min)	$1.99x10^{-5}$	$1.39x10^{-5}$	$2.59x10^{-5}$	$2.07x10^{-5}$	$1.37x10^{-5}$	$2.77x10^{-5}$			
$MgSO_4$/NaBr	Velocity (m/min)				$5.35x10^{-3}$	$5.29x10^{-3}$	$5.42x10^{-3}$	$5.22x10^{-3}$	$5.16x10^{-3}$	$5.27x10^{-3}$
	D(m^2/min)				$1.59x10^{-5}$	$1.14x10^{-5}$	$2.03x10^{-5}$	$1.68x10^{-5}$	$1.30x10^{-5}$	$2.06x10^{-5}$
$MgSO_4$/NaCl	Velocity (m/min)	$4.90x10^{-3}$	$4.79x10^{-3}$	$5.01x10^{-3}$				$4.77x10^{-3}$	$4.70x10^{-3}$	$4.84x10^{-3}$
	D(m^2/min)	$3.41x10^{-5}$	$2.23x10^{-5}$	$4.60x10^{-5}$				$3.46x10^{-5}$	$2.71x10^{-5}$	$4.22x10^{-5}$

The experiments using ionic tracer mixtures suggested that sorption of cations varied according to the composition of the mixture. The observed cation BTCs were satisfactorily simulated in most experiments by varying the cation K_A values. This is evident from the model efficiencies, which are typically >90 % for all tracer ions (Table 4-11). There are good fits for Ca^{2+} and Mg^{2+} for all tests, but model efficiencies for Na^+ and K^+ were sometimes very low when they are only in the background solution. This is partly due to the BTC for these ions showing low variation in concentration during the tests, making the method used for calculating model efficiency less suitable for these cases. The Na^+ half reaction was used as a point of reference by PHREEQC i.e. K_A of $Na^+ = 0$. Therefore the K_A value of Na^+ in the column tests is not given in Table 4-12. This also means that when a cation displaces Na^+ from an exchange site, e.g.:

$$K^+ + Na\text{-}X \rightarrow Na^+ + K\text{-}X \qquad (4.6)$$

that log K_A= log selectivity coefficient. The K_A of a cation required to fit the BTC generally increased when it was used as a tracer (Table 4-12). This shows preferential sorption of cations when present in a tracer mixture, compared with the background solution. The best model estimates of the column CECs were usually the same as the calibration test for each column, or within error of the independent laboratory-determined CEC.

Table 4-11: Estimated model efficiencies (%) for PHREEQC fits to data for ionic tracer tests. NaBr values are averages. Bold values indicate the ion is part of the tracer suite in the experiment. N/A indicates that the ion was not present or was at the same concentration in the equilibrium and tracer solutions.

Ionic Tracers	Br^-	Cl^-	SO_4^{2-}	Ca^{2+}	K^+	Mg^{2+}	Na^+
NaBr	**99.44**	N/A	N/A	89.58	-23.53	81.40	**96.94**
$MgSO_4$	N/A	N/A	**99.78**	94.25	96.97	**96.50**	27.12
KBr	**98.73**	N/A	N/A	95.45	**98.34**	79.81	-0.59
$MgSO_4$, KBr	**98.85**	N/A	**96.11**	92.35	**90.29**	**93.83**	42.58
NaBr, $MgSO_4$	**96.50**	N/A	**97.07**	92.27	76.83	**94.43**	**97.99**
NaCl, $MgSO_4$	N/A	**99.22**	**99.00**	94.49	-462.36	**96.07**	**98.49**
NaCl, KBr	**98.50**	**93.53**	N/A	86.57	**98.82**	85.99	**96.55**

Table 4-12: Log K_A values or cations and best fit CEC values estimated by PHREEQC for the ionic tracers. All NaBr calibration tests were fitted with the same log K values.

	log K_A			CEC best fit-
Ionic Tracers	Ca^{2+}	K^+	Mg^{2+}	CEC calibration test
NaBr	0.75	0.70	0.50	N/A
$MgSO_4$	0.85	0.80	1.00	0.10
KBr	0.75	2.16	0.70	0.00
$MgSO_4$, KBr	0.75	0.70	0.50	0.00
NaBr, $MgSO_4$	0.75	0.90	1.00	0.30
NaCl, $MgSO_4$	0.75	1.00	1.00	0.11
NaCl, KBr	0.75	2.45	0.70	0.00

It was not possible to get an improved fit for Mg^{2+} and K^+ in the $MgSO_4$ and KBr test (Figure 4-8) by varying K_A values. A good fit for one cation breakthrough led to underestimation of sorption in the other cation breakthrough. An unlikely CEC of 2.6 meq/100g is required in the model to estimate the average retardation of the K^+ data and results in poor simulation of solute BTCs. There is slight underestimation of Mg^{2+} and K^+ retardation. The Ca^{2+} desorption peak may be later and larger than modelled, suggested by the data point at 2 pore volumes. This would correspond to greater ion exchange than modelled and increased retardation of K^+ and Mg^{2+}, as seen. This behaviour is observed in Mg^{2+} and Na^+ tracer mixture tests, where PHREEQC underestimates desorbed Ca^{2+} and the retardation of Mg^{2+} (Figure 4-9**),** but not in other tests where K^+ was used as a tracer. A larger CEC was required to fit 3 of the 4 Mg^{2+} tests compared with the NaBr calibration tests. This implies that a larger CEC is "available" to Mg^{2+} than Na^+ and K^+. This may reflect the higher valency and smaller size of Mg^{2+}. Alternatively some exchange sites on the sand may have already been occupied by Na^+ and K^+, before the tracer arrived. Therefore ion exchange would seem to be reduced when Na^+ or K^+ was injected as a tracer, leading to an underestimation of CEC.

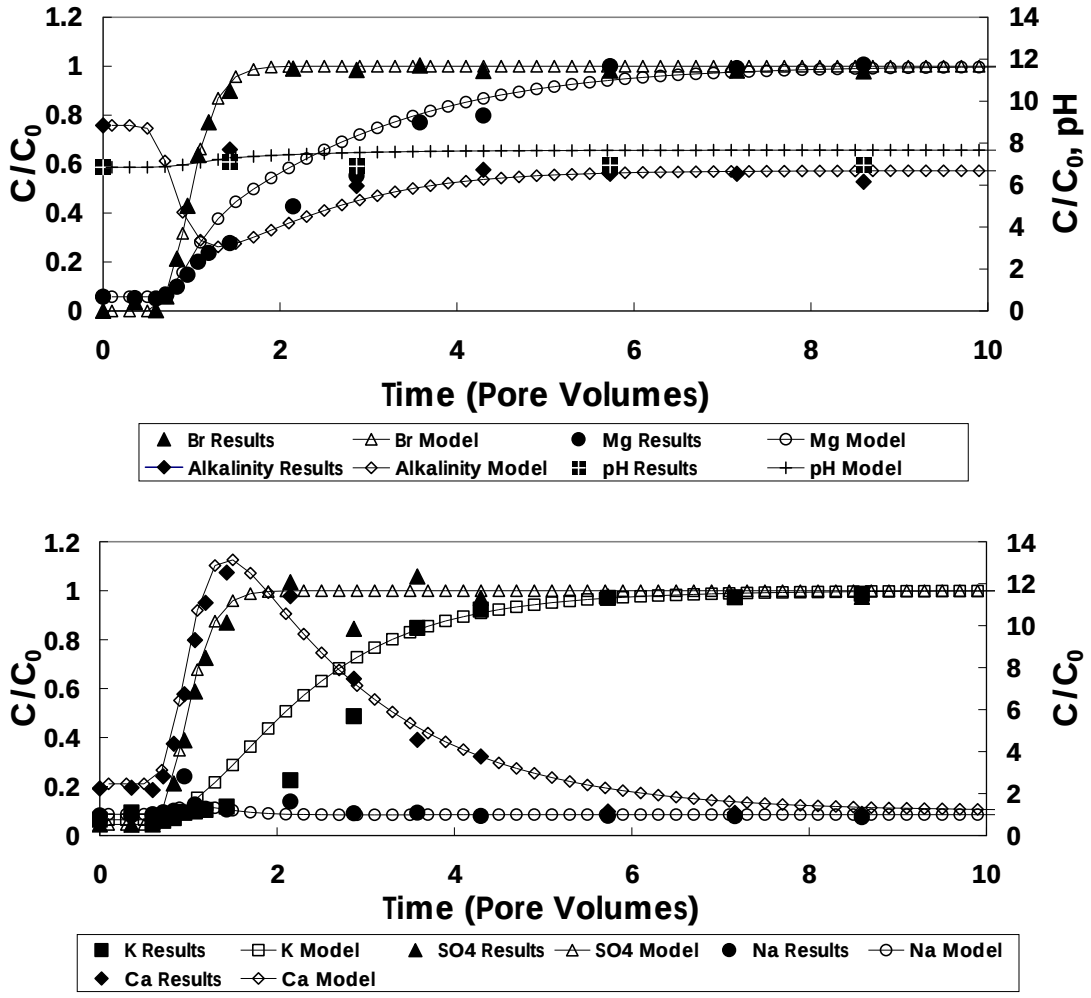

Figure 4-8: Experimental BTC and PHREEQC model BTC for the KBr and $MgSO_4$ tracer test. Results for pH, alkalinity, Na^+ and Ca^{2+} are plotted on the secondary axis.

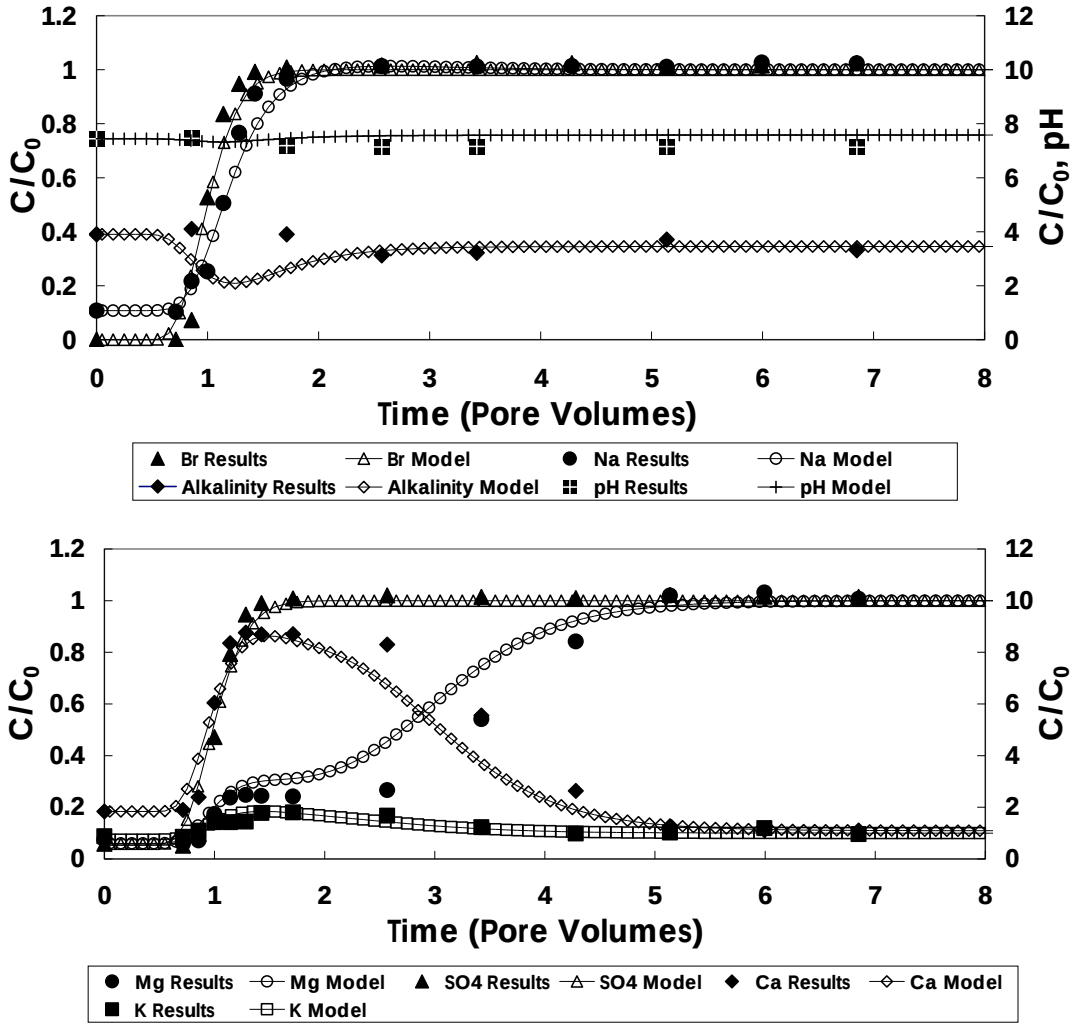

Figure 4-9: Experimental BTC and PHREEQC model BTC for the NaBr, MgSO4 tracer test. Results for pH and alkalinity are plotted on the secondary axis.

Competitive sorption between the different cations occurred in the tests, with retardation being less for species in mixtures. For example the average breakthrough of Na^+ and K^+ occurs at approximately 1.4 and 4.5 PV when used as separate tracers. However when present in a tracer mixture the average breakthrough is at 1.1 and 3 PV for Na^+ and K^+, respectively (Figure 4-7, Figure 4-10 and Figure 4-11). This implies that the tracers compete for a limited number of sorption sites, represented by the CEC (as expected from theory) [Appelo and Postma, 2005].

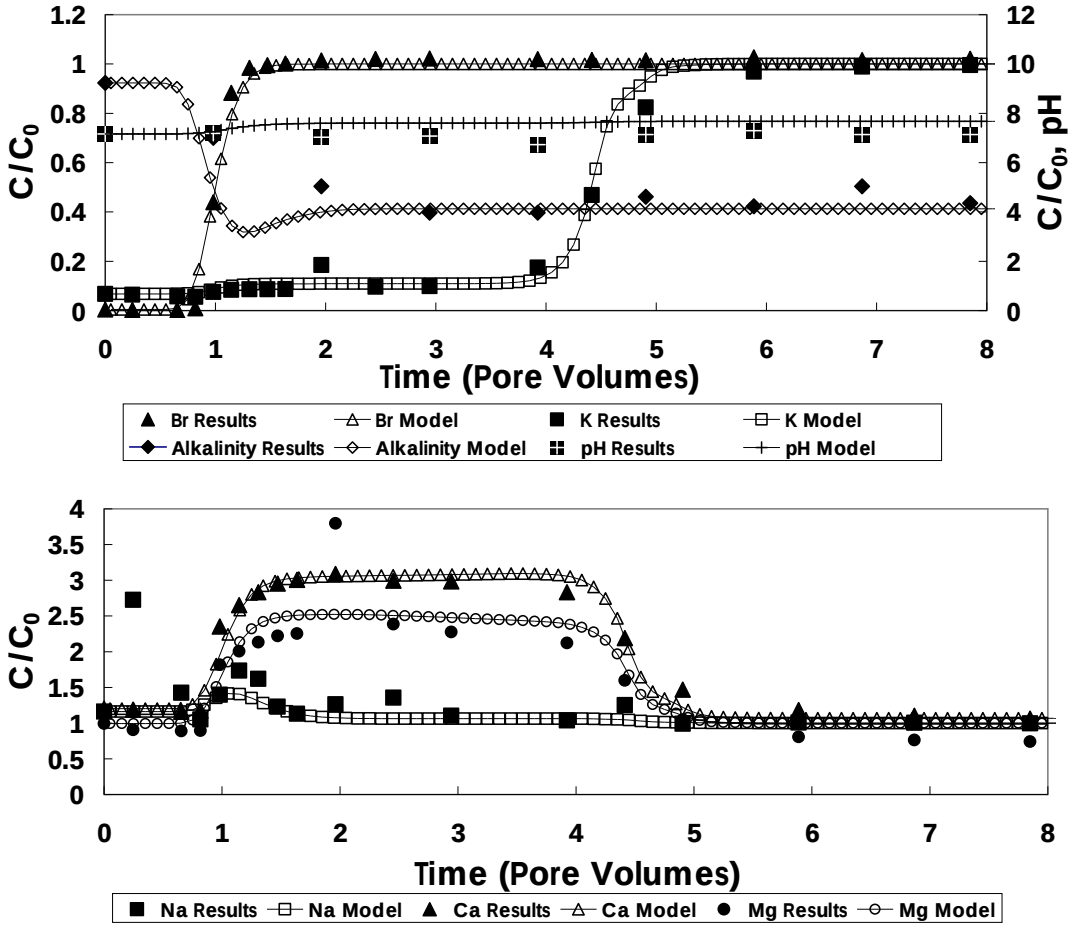

Figure 4-10: Experimental BTC and PHREEQC model BTC for the KBr tracer test. Results for pH and alkalinity are plotted on the secondary axis.

Tracer cations show an initial rise during conservative breakthrough, related to desorption of background cations. The low Na retardation observed in mixtures (Figure 4-11) is partly due to merging of this initial rise with the Na tracer breakthrough.

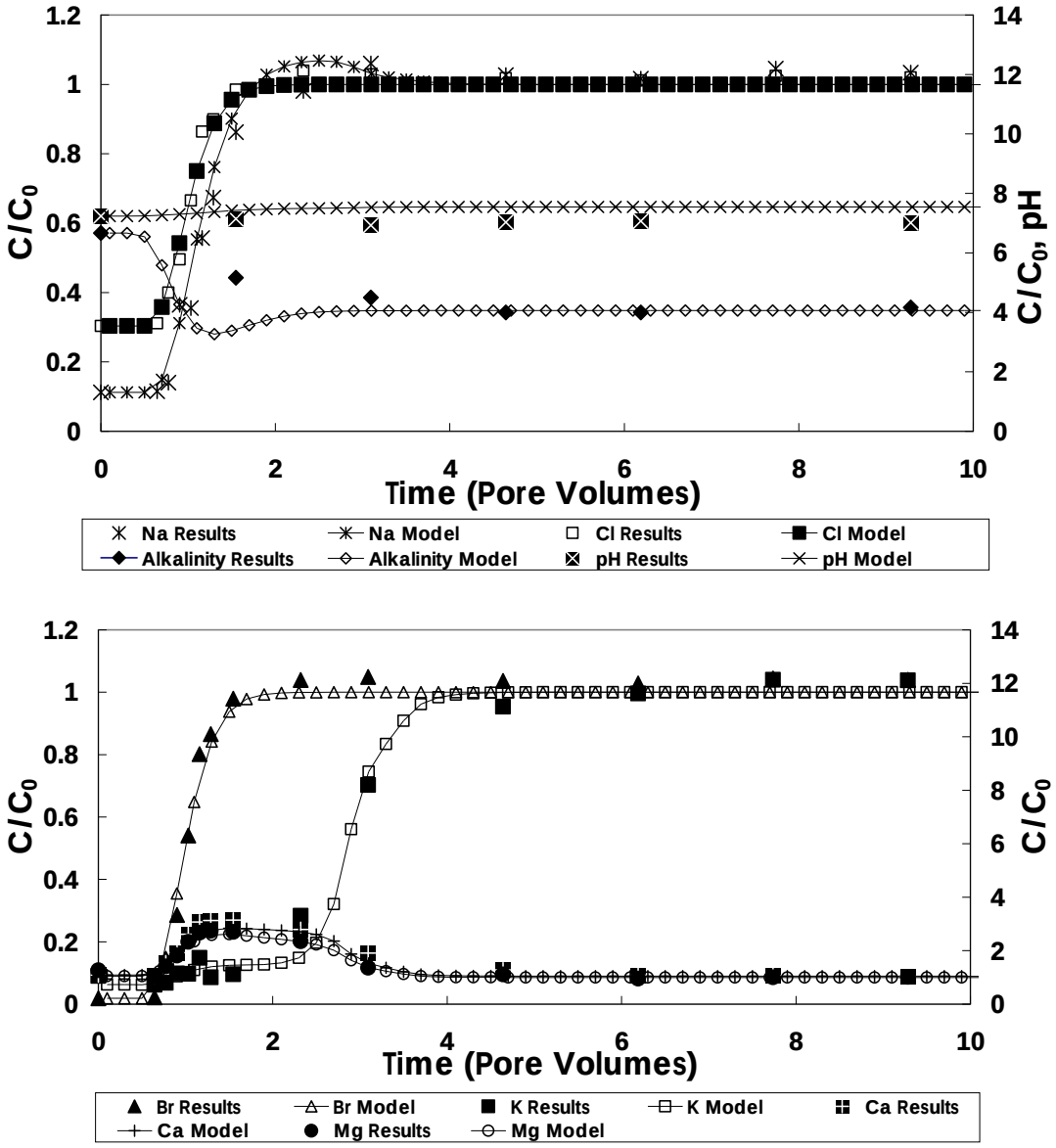

Figure 4-11: Experimental BTC and PHREEQC model BTC for the NaCl, and KBr tracer test as an example of an ionic tracer mixture. Results for pH, alkalinity, Mg^{2+} and Ca^{2+} are plotted on the secondary axis.

4.5.4. **Ni-EDTA tracer tests**

The Ni-EDTA experiments with a lower concentration were fitted better using STANMOD than those at a higher Ni-EDTA concentration. Model efficiencies of 99.5 and 99.4 % were estimated for Br concentrations of $5x10^{-3}$ M and 10^{-3} M, respectively, at 10^{-4} M Ni-EDTA, whereas at 10^{-3} M Ni-EDTA the model efficiency was 98.7 and 73.1%. Ni was slightly retarded relative to Br in the experiments. In tests where Ni-EDTA was injected at 10^{-4} M, the retardation factor for Ni was 1.08 and 1.04 for Br concentrations of $5x10^{-3}$ M and 10^{-3} M, respectively (see Figure 4-12).

These estimates of retardation were not in error of 1, showing that the observed retardation is significant and does not result from measurement error. The pH during these tests was 6.3-7.6, whereas the stock mixtures were acidic (pH 2.8-4.51). It was decided not to adjust the stock solution to neutral pH as the columns already had a high buffering capacity, observed in previous experiments. Also, adding base to the stock would have changed the background ion concentrations, which was undesirable. The neutral output pH suggests that the buffering capacity of the sand was retained from previous tests.

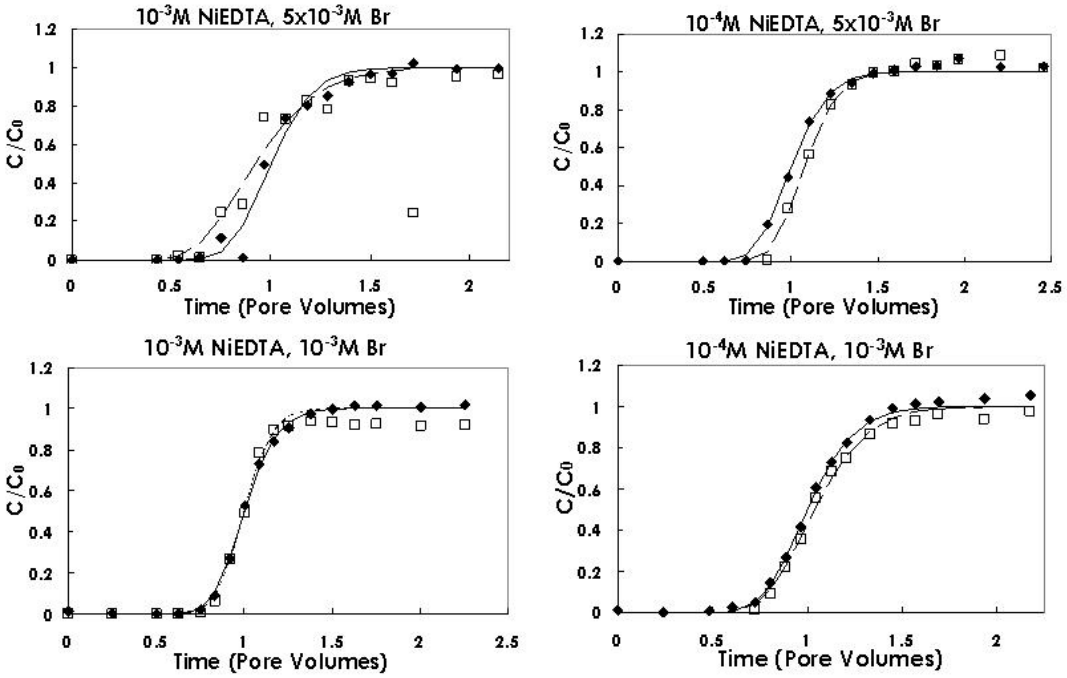

Figure 4-12: Br^- and Ni breakthrough curves for Ni-EDTA experiments and STANMOD fits. Black triangles are Br^-, squares are Ni, the solid line is the Br^- fit and the dashed line is the Ni fit.

Low sorption of the large negatively charged Ni-EDTA molecule, shown by the small retardations relative to Br^-, was observed. This is attributed to either the neutral pH increasing the number of negatively charged surface sites or a lack of suitable oxide minerals providing surface sites [Nowack et al., 1996; Nowack and Sigg, 1996]. When Ni-EDTA was injected at a concentration of 10^{-3} M, the estimated retardation factor values for Ni were 0.919 and 0.998 for Br concentrations of $5x10^{-3}$ M and $1x10^{-3}$ M, respectively. This suggests that sorption sites for Ni-EDTA were saturated at Ni-

EDTA concentrations of 10^{-3} M, leading to limited retardation relative to Br^-. Saturation of sorption sites at 10^{-3} M Ni-EDTA may be due to the large size of the Ni-EDTA molecule or absence of many positive sites at the neutral pH in experiments. The results suggest that the transport velocity of Ni-EDTA is greater than Br^-, which may be due to anionic exclusion effects at high concentrations or its large molecule size preventing transport in smaller pores.

The experimental BTCs were modelled using PHREEQC without the Ni-EDTA data. This was to check if CEC estimates obtained with Na^+ BTCs during NaBr calibration tests varied from that when Ni-EDTA was also used as a tracer. The same K_A values were used as for the NaBr calibration test BTCs. A lower CEC was needed in the Ni-EDTA tracer tests than the calibration tests to fit the Na^+ BTC (Table 4-13) The CEC estimates obtained are lower in the column tests run at 10^{-3} M Ni-EDTA than 10^{-4} M, but there is no clear trend when these values are compared against CEC estimates obtained in the NaBr calibration tests. The results suggest that competition for sorption sites between Ni-EDTA and Na^+ lowers the apparent sorption and retardation of Na^+. Solution K^+, Mg^{2+} and Ca^{2+} concentrations remain high for longer than predicted by the model (see Figure 4-13), for all tests apart from the $5x10^{-3}$ M Br^-, 10^{-4} M Ni-EDTA experiment. This suggests Ni-EDTA may restrict re-sorption of these background cations after the tracer front has passed, due to blocking of surface sites and slow or little de-sorption, as it forms inner sphere complexes [Nowack and Sigg, 1996].

Table 4-13: Estimated CECs obtained from modelling of Ni-EDTA experiments. Na concentrations are greater in the 10^{-3}M tests due to Na^+ being a waste product of Ni-EDTA formation. CEC_{NaBr} is the CEC obtained in the NaBr column calibration tests.

Ni-EDTA (M)	Na^+ (mg/l)	CEC from PHREEQC (meq/100g)	CEC-CEC_{NaBr}
1.00E-03	205.5	1.3	0.29
1.00E-03	99.5	1.35	0.05
1.00E-04	148.3	1.4	0.19
1.00E-04	54.4	1.4	0.19

Alkalinity was quite stable during the 10^{-4} M Ni-EDTA tests but nearly doubled during breakthrough for 10^{-3} M Ni-EDTA tests (Figure 4-13). This is probably due to the higher acidity of the stock used in the higher concentration tests. This most likely led to greater dissolution of calcium carbonate to buffer the pH, which increased the alkalinity. Calcite SIs of -0.56 to -0.70, similar to the values in the column calibration tests, were required to fit the data in 3 out of 4 tests with PHREEQC. In the 10^{-3} M Br^-, 10^{-4} M Ni-EDTA experiment a SI of -1.77 was required. This may indicate that calcite had become depleted in this column. The alkalinity of stock solutions was very low and not easily measured, and therefore alkalinity on graphs is presented as mg/l calcite (as it was measured), rather than normalised to stock concentrations.

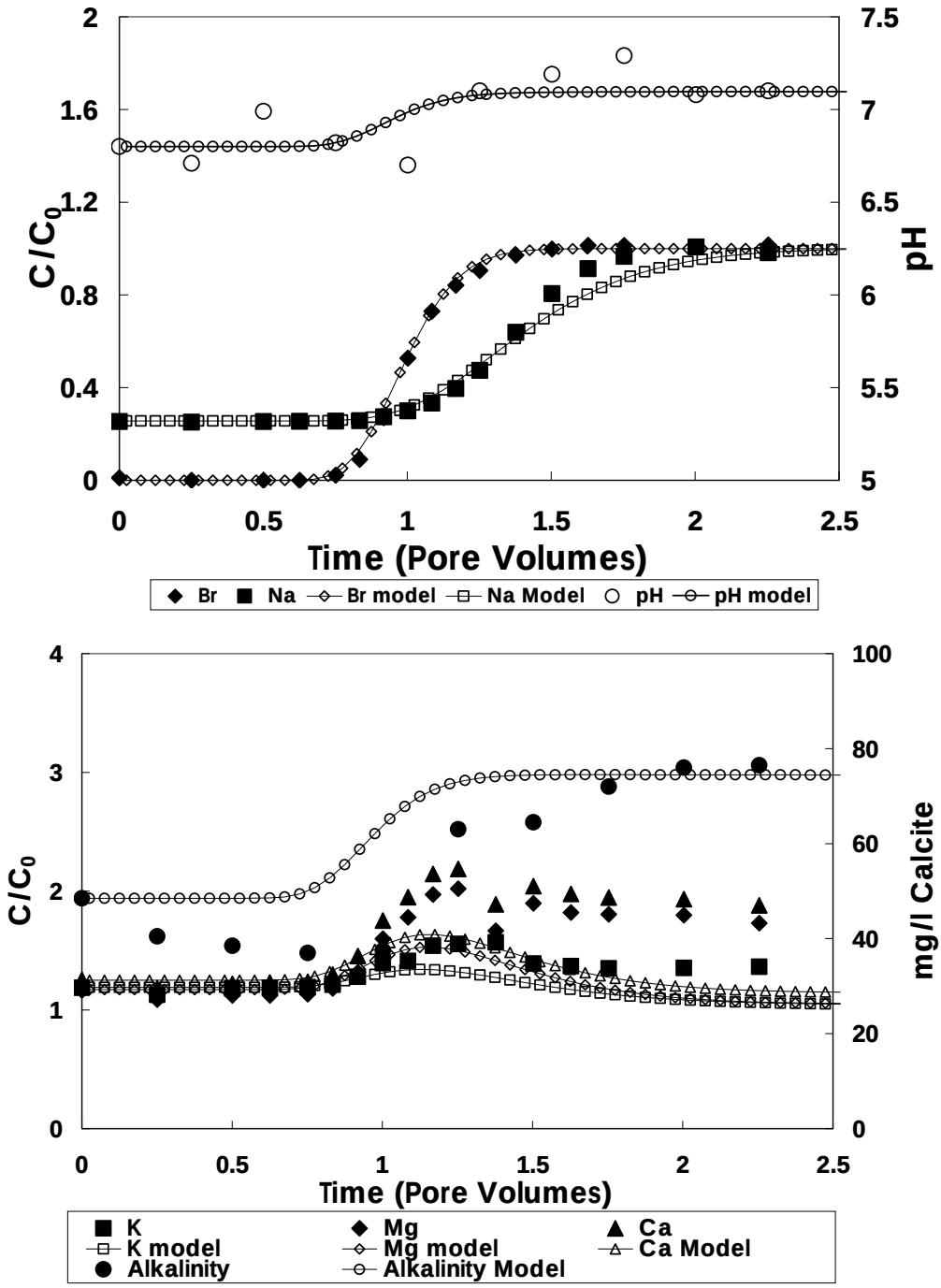

Figure 4-13: Experimental BTC (without Ni) and PHREEQC simulated BTC for 10^{-3} M NiEDTA, 10^{-3} M Br experiment. pH and alkalinity are plotted on the secondary axis. Note the higher than predicted concentration of K^+, Mg^{2+} and Ca^{2+} after initial breakthrough on the bottom graph.

4.6. **Discussion and implications for use of tracers in single well forced gradient tests**

The laboratory column experiments using single and mixed tracer compounds show that Br^- and Cl^- provide similar estimates of the hydraulic properties and may be used as conservative tracers in forced gradient tests. SO_4^{2-} showed a small amount of retardation relative to Br^- and Cl^- and is less suitable. The performance of Cl^- as a tracer does not seem to be affected when it's present in the synthetic groundwater at a high concentration. Fluorescein has mixed performance in these tests, showing significant statistical similarity between tests but generally having an earlier breakthrough than the inorganic anions. A reason for this is a high variability in measured fluorescence at peak concentrations, due to the pH effect noted. This makes normalisation of tracer concentrations difficult. Therefore fluorescein it is not recommended as a conservative tracer to quantitatively interpret aquifer properties during field tracer tests, where there is significant pH variation

On their own Na^+, Mg^{2+} and K^+ all produce tracer profiles that illustrate aquifer sorption properties over the experimental time frame of the column tests, which can be interpreted with PHREEQC. The aim for ionic tracer mixtures is to have two cations which sorb to different extents and can be distinguished from conservative behaviour at concentrations of $1x10^{-2}$ M, which is suitable for analysis and separation from the background signal. This would allow more reliable assessment of CEC when doing tracer tests in the field, when approximate values of CEC and background ion concentrations are not known. Mg^{2+} and K^+ do not seem to be suitable as reactive tracers in this respect, as they are retarded by similar amounts in a mixture and quantitative prediction of their transport behaviour is difficult. Na^+/K^+ and Na^+/Mg^{2+} binary mixtures may be useful as long as the breakthrough of the background ions can be delineated from the tracer signal with modelling. The low retardation of Na^+ in these laboratory tests would evaluate the sensitivity of single well forced gradient

tracer tests to cation sorption. Na^+ retardation may only be observed appreciably for tracer tests conducted in relatively high-CEC sediments, when used with K^+ or Mg^{2+} in a mixture. The CEC of an aquifer can vary between 0.2 to 5 meq/100g [Christensen et al., 2001], causing great variability in potential retardation of cations. Therefore using two cation tracers in a binary mixture to measure CEC is advantageous.

The selectivity coefficient which describes cation sorption is needed to fit breakthrough curves with PHREEQC. K_A values generally increased when the cation was used as a tracer. This shows preferential sorption of a cation at higher concentrations. This trend is the opposite to previous observations in the literature [Bjerg et al., 1993], however it is observed in this study at an order of magnitude larger cation concentrations. Variation in the sorption selectivity coefficient with concentration adds extra complication to modelling natural attenuation in aquifers. The sorption selectivity coefficients estimated when cations are used in a single salt tracer are similar to those when they are used with another cation in a mixture (accept for the Mg^{2+} and K^+ case). However the retardation of the cations in a mixture is decreased, suggesting competition between cations for sorption sites. If cation tracers are modelled individually in the field the estimate of CEC and/or sorption coefficient may be in error. It is suggested that a model is used that incorporates geochemical interactions between cations in mixtures.

In neutral pH conditions at low concentration Ni-EDTA transport is retarded relative to Br^-, suggesting that it is a suitable tracer to estimate the migration of heavy metal-organic ligand complexes. The laboratory results suggest that using Ni-EDTA with a cation tracer may underestimate the CEC. This may be due to Ni-EDTA competing with Na^+ for surface sorption sites on the sediment. Ni-EDTA usually has a charge of 2 minus (at pH 4-8) [Nowack and Sigg, 1996] and Na 1 plus, such that they would not be expected to compete for the same surface sorption sites. However the large EDTA molecule may sorb onto the few positively-charged surface sites and impede Na^+ sorption onto some of the negatively-charged surface sites. These results may also be

explained if a fraction of the iron oxide coating had been washed off the Permo-Triassic sand over time in the columns, reducing potential sorption site for Na^+ and Ni-EDTA. This may correlate with the slightly increased apparent porosities that were observed over time in the columns. Low retardation would mean that at neutral pH differences between Ni-EDTA and Br breakthrough curves may be difficult to see in single well forced gradient tests. Tests using Ni-EDTA would be more suited to polluted acidic sediments, where retardation would be greater. However the results show clear retardation of Ni-EDTA in neutral pH conditions and conservative/non-reactive behaviour should therefore not be assumed. Sorption of Ni-EDTA can vary on different oxide minerals [Nowack et al., 1996], and therefore retardation may varying greatly depending on the aquifer surface properties. The best results were obtained for concentrations of 10^{-4} M Ni-EDTA, approximately 8 mg/l Ni. The UK drinking water standard for Ni is 20 µg/l, [UK Government, 2000] and therefore good proof of mass recovery or natural attenuation may be required to ensure regulatory confidence in the field-scale test. Good results may be obtained with smaller concentrations, as long as they can be analysed accurately.

In conclusion, inorganic ions were more reliable conservative tracers than fluorescein. Na^+ with K^+ or Mg^{2+} are the most suitable cation tracers to be used in a binary mixture for the assessment of CEC. Retardations of cation tracers and the short time for equilibrium conditions to be reached suggest they are suitable for use in single well forced gradient tests. Ni-EDTA showed low retardation in tests and may not be suitable for use in field experiments where pH conditions are neutral, or a high degree of experimental error is expected. Interactions occur between sorbing tracers. Tracer cations were sorbed preferentially, relative to background cations. Ni-EDTA retardation depended on the input concentration used. This suggests that a model incorporating geochemical interactions should be used when estimating aquifer parameters in a forced gradient test with these tracers.

5. Performance of a biodegrading tracer for natural attenuation assessment under the influence of forced gradient transport in a porous medium

5.1. Abstract

Accurate assessment of parameters which describe the transport and biodegradation potential of pollutants in aquifers is important for the evaluation of natural attenuation or active remediation schemes. In this study column tests were performed using unconsolidated sand permeated with acetate as a model biodegrading tracer, to represent forced gradient field tracer tests that may be undertaken in a sandy aquifer to estimate *in situ* biodegradation potential. The tests were operated under pulsed and continuous injection mode over a period of 2-3 days and interpreted using mass balances with numerical modelling.

Acetate was biodegraded aerobically in the columns, with some Mn/Fe reduction also occurring. Consistent biodegradation rates, at flow rates typical of forced gradient tests, were obtained during pulsed tracer injection. Naturally occurring organic carbon in the sediment provided a significant native oxygen demand. This made changes in dissolved oxygen concentration from acetate biodegradation difficult to quantify. Alkalinity and electron balances were required to help identify the biodegradation pathways. Physical non-equilibrium transport was observed in the tests. These conditions were more predominant in pulse input tests compared with constant injection tests and at higher flow rates. The results show that acetate is a suitable tracer to quickly assess the biodegradation potential of an aquifer for natural attenuation or enhanced bioremediation at flow rates typical of forced gradient tracer tests. If an accurate electron balance is required it is recommended that oxygenated water is pumped through a test zone for a long period of time before a test takes place, to satisfy the natural oxygen demand.

5.2. **Introduction**

Quantifying the potential for contaminant biodegradation in groundwater is important for the design and interpretation of remediation schemes using natural attenuation and bioremediation. The availability of nutrients and electron acceptors (both dissolved and mineral bound) to support *in situ* microbial activity in the aquifer are important factors. Biodegradation may be limited by electron acceptor concentrations [Oya and Valocchi, 1998] or inhibited by high concentrations of an organic species [Antizar-Ladislao and Galil, 2006]. The bioavailability of organic contaminant may also need to be considered [Zhang et al., 1998; Liu et al., 2007]. Often contaminant biodegradation potential at the field-scale is greatest at the fringe of plumes [Lerner et al., 2000; Tuxen et al., 2006], where conditions are more favourable. This behaviour has also been confirmed in laboratory imaging tests and process studies [Huang et al., 2003; Elliott et al., 2010].

To deduce these factors and biodegradation behaviour at the field-scale would generally require intense sampling of a contaminant plume, which would not be feasible for most investigations. Tracer tests provide an alternative method to evaluate the biodegradation potential and pathway of a contaminant in groundwater. These provide spatially averaged bulk values, relating to the portion of the aquifer sampled, which can be used to model natural attenuation or estimate the effectiveness of remediation options. Natural gradient tests [Bugna et al., 2004; Pombo et al., 2005] can deduce the transport behaviour of a contaminant under *in situ* conditions, but often take too long to be practical for most commercial applications. Forced gradient tracer tests are an alternative. Push-pull tests can be used to interpret biodegradation processes in groundwater, by measuring compound and product concentrations, electron acceptors and the amount of a compound used to stimulate biodegradation [Istok et al., 1997]. In these tests the biodegradation capacity of the aquifer is typically described by zero- or first-order kinetics [Istok et al., 1997; Haggerty et al., 1998]. Natural gradient flow during the rest phase of a push-pull test can complicate results

and lead to mass loss. Inter-well tracer tests (e.g. Jin et al. [1995]) and dipole flow tracer tests [Sutton et al., 2000] could also be modified to assess biodegradation. These tests do not include a rest phase.

Acetate ($CH_3CO_2^-$) is readily biodegradable and is a biodegradation product of many contaminant plumes [Thornton et al., 2001; Devlin et al., 2002; Wilson et al., 2004]. It has been used as a carbon source to investigate biodegradation in aerobic, sulphate reduction and fermentation studies in the field and laboratory [Huang and Jih, 1997; Kleikemper et al., 2002; Pombo et al., 2005; Watson et al., 2005; Kneeshaw et al., 2007; Rees et al., 2007]. Also, it has been investigated as an additive to enhance bioremediation of polyaromatic hydrocarbons [Ebihara and Bishop, 2002], and has been shown to biodegrade to inorganic end-products under aerobic conditions [Watson, 2004]. Acetate was not observed to adsorb to aquifer sediments in these studies. These factors make acetate a suitable tracer to assess the biodegradation capacity of aquifers in a variety of scenarios. Simple alcohols and benzoate are also easily biodegradable compounds that can be used to assess the biodegradation capacity of an aquifer under a variety of conditions [Alter et al., 2003]. However, depending on the alcohol, organic sorption or partitioning to a non-aqueous phase may occur [Wilson, 1998; Alter et al., 2003]. Acetate is preferable to benzoate as analysis can be simply performed along side an inorganic conservative tracer using ion chromatography, whilst benzoate is analysed by HPLC.

This study investigates the influence of forced gradient conditions at the mesoscale on the performance of a reactive tracer test in a saturated granular porous media. The tracer tests were examined in laboratory columns containing sand, with acetate as a model biodegrading tracer. Tests were carried out to determine the effect of injection method and flow rate on biodegradation. The implications of the findings are considered at the field-scale.

5.3. **Method**

5.3.1. **Materials**

Sand for the column experiments was obtained from the Builders Centre Ltd, Sheffield, S2 1TA. This was a Permo-Triassic desert sand from Carlton Forest Quarry, Worksop. The sand was chosen to represent a typical red sandstone aquifer in the U.K. [Kimblin, 1995]. XRD analysis on a bulk sample showed that it is composed of predominantly quartz, with some calcite and aluminium oxides. A small amount of fine grained clay minerals are present but their characterisation was not considered crucial to the experiment. There are also iron oxide coatings on the grains. The cation exchange capacity of the sand was estimated to 1.592 ± 0.254 meq/100g using the method of Edmeades and Clinton [1981] and the particulate organic carbon (POC) content, measured using the Walkley-Black procedure, is 0.023 ± 0.003 wt% [van Reeuwijk, 1992]. Grain size analysis showed the sand is very poorly sorted and that 58.2 % of the sand has a grain size <300 μm. Grains sizes >1.18 mm in size were sieved out. This prevented any large stones creating problems with column packing or preferential flow. Calcium carbonate was measured at 3.8 % [Smalley, 2004]. All chemicals used were AnalaR grade or equivalent and obtained from Fischer Scientific or VWR.

5.3.2. **Column set-up**

Column tests were performed using uPVC columns (0.75 m x 0.053 m) which were dry packed with the sand (Figure 5-1). The sand was packed inside the columns in 5-10 cm increments, which were compacted by tamping 20 times with a rod and plastic plunger. The average hydraulic conductivity of columns (for all packed columns including those not used in these tests), measured using a constant head test, was $4.45 \times 10^{-5} \pm 1.55 \times 10^{-5}$ m/s. For each column values ranged by an average of 3.00 ± 2.08 %. Porosity was calculated from the difference between the dry and saturated mass of the column, with an average of 36.1 ± 2.8 %.

The columns were slowly saturated in a vertical position from the base upwards with synthetic groundwater (see Table 5-1) that was similar in composition to that in the unpolluted sandstone aquifer at the Site for Innovative Research on Natural Attenuation (SiREN) in Carrington, UK [unpublished Shell data]. The cation composition was similar to that in the aquifer, but the sodium concentration was very high in the aquifer and was reduced for the synthetic groundwater. Alkalinity was kept low to identify any small variation during the tests. Synthetic groundwater was used as the background composition for tracer solutions and flushing the columns after experiments for approximately 12 pore volumes (PVs). Modelling with the geochemical transport code PHREEQC [USGS, 2008] showed that this was sufficient for each column to reach chemical equilibrium. A PV is the volume of water present in the saturated column.

Tracer experiments were performed with the columns aligned horizontal and with no sample ports. This minimised oxygen diffusion into the column at the side or end that could affect dissolved oxygen readings. Input solutions were stored in sealed 10 L containers. Aseptic filtered (0.2 μm polyethersulfone membrane) air or N_2 gas was sparged through the test solutions to saturate them with oxygen or de-oxygenate them depending on requirements. The containers had a small opening to allow the escape of gas. Oxygen concentrations were measured at the start and end of each day of testing to ensure conditions remained constant and any small variation was taken into account.

The columns were operated with a flow rate of 1-2 PV every 12 hours (6.25 – 12.5 cm/hr), using a peristaltic pump. Every alternate 12 hour period the pump was switched off; this ensured a consistent flow rate within laboratory constraints. The flow rates used are similar to those of Istok et al [1997], when investigating biodegradation with push-pull tests, and are significantly slower than some flow rates used for forced gradient tracer tests investigating conservative transport [Ptak and Schmid, 1996].

Tests were performed in two identically packed columns. Tests were run sequentially and columns were not repacked during experiments. A sodium acetate (NaAc) solution was pumped through the columns prior to the experiments described until acetate biodegradation occurred (conditioning phase). This ensured that there was no lag time for biodegradation in subsequent tests. Columns were then deoxygenated prior to tests by pumping through N_2-sparged synthetic water. In the first tests (Table 5-2) NaCl plus oxygen-saturated synthetic groundwater was pumped into the column until the oxygen level stabilised. This allowed the effect of particulate organic carbon (POC) in the sand on dissolved oxygen concentrations to be assessed. In subsequent tests acetate was continuously injected with NaBr tracer solution until chemical equilibrium was reached. These tests allowed acetate biodegradation to be assessed under stable conditions. In the third and fourth set of tests, after oxygen had stabilised during purging of the tracer solution, a pulse of NaAc solution was injected and then purged. These dynamic conditions are more representative of field *in situ* tests. Two different flow rates (slow and fast pulse) were used to evaluate the effect of velocity on the biodegradation assessment.

5.3.3. **Analysis**

Water samples for chemical analysis were taken at intervals from the end of each column. Dissolved Mn and Fe were measured on a Perkin Elmer AAnalyst 200 Atomic Adsorption Spectrometer, at wavelengths of 279.5 and 248.3 nm respectively. The slit width was 1.8 nm and detection limit 0.01 mg/l for both elements. All 2.5 ml samples were filtered through a 0.2 µm polyethersulfone membrane and preserved with 100 µl of 0.1 M HCl.. Samples were stored in a -10˚C refrigerator prior to analysis.

Major inorganic ions (Ca^{2+}, Mg^{2+}, Na^{+}, K^{+}, Cl^{-}, Br^{-}, SO_4^{2-}, NO_3^{-}, PO_4^{3-}) and acetate were analysed on a Dionex DX-120 Ion Chromatograph. A RFIC™ Ionpac® A514A 4 x 250 mm Analytical Column was used for Anion analysis, with an eluent of 8 mM

Na_2CO_3 and 1 mM $NaHCO_3$. A RFIC™ Ionpac® C512A 4 x 250 mm Analytical Column was used for cation analysis, with an eluent of 20 mM Methane Sulphonic Acid. A 10 µl sample loop was used, with lower reliable detection limits of 0.6 ppm for Br^- and 0.25 mg/l for acetate (detection limits for other ions are stated in Appendix B). Samples were filtered through a 0.2 µm polyethersulfone membrane and diluted to the calibration range used on the instrument.

Alkalinity was measured on 20 ml samples during the experiments with a Hach® field test kit and digital titrator. Sulphuric acid at 0.16 N was used and values were measured to an accuracy of ± 3.82 mg/l calcite. This allowed measurements to be taken quickly after sampling. The dissolved oxygen concentrations was measured on line with a Presens® Fibrox 3 fiber–optic oxygen meter, using a 0.2 ml volume flow cell to minimise sample volume. Repeated testing showed that the meter was accurate to within 1 %. To ensure that air leakage in the plastic sample tubing used for plumbing or the sample valves did not affect the results, the sampling port was detached and the flow-through cell was attached to the end of the column. Sample pH was measured directly after collection. A probe was equilibrated in 20 ml of collected sample in a centrifuge tube. The probe was recalibrated each day with fresh standards.

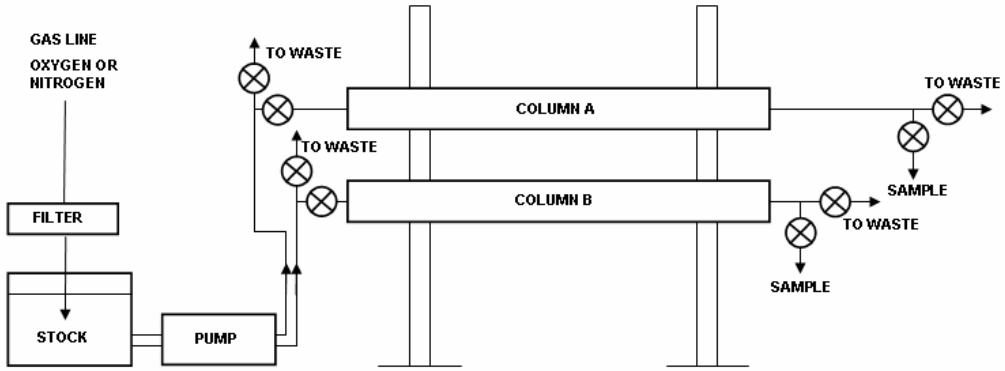

Figure 5-1: Schematic diagram of column apparatus used in the experiments

Table 5-1: Table of major ion concentrations for SiREN uncontaminated groundwater and the synthetic groundwater used in experiments.

	Concentration (mg/l)					
Water type	Ca^{2+}	K^{+}	Mg^{2+}	Na^{+}	Cl^{-}	SO_4^{2-}
SiREN groundwater	61.8	20.1	12.0	109.0	35.9	37.1
Synthetic groundwater	61.8	20.1	12.0	23.0	162.6	47.5

Table 5-2: Table of column test parameters * = numbers after the slash indicate values relating to the flushing solution injected after the tracer solution. ROT = remainder of the test. Although Cl was not always used as a tracer it was always in the background solution as part of the synthetic groundwater mix. Small scale variations between similar concentrations are due to analytical instrument variability. Test durations include hiatus periods, when the pump was switched off.

				Tracer concentration (mg/l)			
Test phase	Flow rate (ml/min)	Tracer injection time (hrs)	Test duration(hrs)	Cl^{-}	Br^{-}	Acetate	Oxygen
Conditioning	2.4	Continuous	57-81	-	81.3-92.9	43.2-43.6	8.5-9.1
Oxygen saturation	0.9-1.0	Continuous	1136.5	558.0	-	-	8.8
Constant injection	0.9	Continuous	83.3	-	925.0	41.4	8.6
Slow pulse injection	1.2	4 / ROT*	59.3	0 / 530.7*	868.2 / 0*	40.8 / 0*	8.8
Fast pulse injection	1.8	2 / ROT*	52	0 / 547.9*	890.4 / 0*	87.2 / 0*	9.2

5.4. **Results and Modelling**

5.4.1. **Normalisation of results and modelling strategy**

All time in the experiments was normalised to represent the total PVs that had passed through the column. The column PV was estimated by curve fitting of the conservative tracer breakthroughs using STANMOD, a public domain 1-D transport model [Simunek et al., 1999]. Total porosity was estimated during column preparation by weighing the column before and after saturation with water. Water was assumed to have a density of 1 kg/l. The apparent porosity, calculated from the flow rate and PV flush times, in the columns increased as more tests were performed with them. This was attributed to loss of a small proportion of the fine sand material over time.

Tracer and background solute concentrations in aqueous samples were normalised to the concentrations in the tracer stock solution, to give relative concentrations, expressed as C/C_o values. This was not possible for dissolved Mn and Fe, which were not present in the stock solutions. The stock solutions were sampled at the start and end of each day to evaluate temporal variation in the composition of these. Output sample concentrations were normalised to the stock concentrations from the same day.

Modelling (using STANMOD and the geochemical transport code PHREEQC) was undertaken to (i) estimate the hydraulic parameters of each column experiment and then to (ii) interpret solute transport and acetate biodegradation, considering changes in acetate and electron acceptor concentrations and alkalinity. The acetate biodegradation rate was also assessed. Transport parameters (dispersivity and velocity) were obtained using the conservative tracer breakthrough curves (BTC) and STANMOD. The estimated acetate biodegradation rates and conservative transport parameters were used to model acetate breakthrough in the pulse injection tests.

5.4.2. **Effect of particulate organic carbon**

Naturally occurring POC in the sediment consumed a large amount of the oxygen present in the injection solution. The sand used in the experiment had 0.023 ± 0.003 wt% POC.

This represents 0.62 ± 0.085g of POC in column A and 0.58 ± 0.081g of POC in column B. Assuming that organic carbon biodegrades according to Equation 5.1, 32 mg of oxygen is required to biodegrade 12 mg of organic carbon (present as organic matter, CH_2O, in Equation 5.1).

$$CH_2O + O_2 \rightarrow CO_2 + H_2O \qquad (5.1)$$

This gives a natural oxygen demand of 1.645 ± 0.23 g and 1.154 ± 0.22 g for columns A and B, respectively. Oxygen in the oxygenation tests was injected at 8.85 ± 0.41 mg/l. Therefore, to completely oxidise all POC in the columns, assuming it was readily oxidisable, 113.82 ± 16.58 PV of water in column A and 107.54 ± 15.66 PV of water in column B is required. However oxygen breakthrough is seen in experiments before 10 PV, suggesting that most of the organic carbon is not readily oxidisable (Figure 5-2). A constant 2-4 mg/l of oxygen utilisation is seen when it reaches equilibrium values. This may represent the oxidation of a less readily available portion of POC. Calculations show that only 10.69 ± 1.55% and 7.39 ± 1.06% of the natural oxygen demand is satisfied in column A and B, respectively, which ran for approximately 50 PV during the tests. Therefore, more than 500 PV of oxygen saturated water is required to fully satisfy the demand in the columns. It was considered that this timescale was impractical for running future tests. As the system had reached equilibrium it was decided to move onto the next phase of experimentation.

The high oxygen demand of the sand is not expected as it originates from the Sherwood sandstone aquifer, which is typically aerobic [Kimblin, 1995; Thornton et al., 2005]. Therefore the oxygen demand of the material would be expected to have been satisfied over a long period in the aquifer. The oxygen demand was present before the acetate conditioning phase (data in appendix E1), therefore it is not due to an increase biological activity or presence of residual acetate. The use of purged water flush may have de-oxygenated the sand. An oxygen demand may sometimes be seen in anaerobic conditions [Wilson et al., 2002]. Also the possible presence of physical non-equilibrium conditions in the columns (see 5.4.4) may have caused slow diffusion of oxygen between mobile and immobile pore spaces increasing the amount of time it takes for oxygen to saturate the column. Alternatively during collection of the sand and packing of the column fresh

organic carbon surfaces and surfaces previously in immobile pore spaces may have been exposed [Ball and Roberts, 1991]. This could create a natural oxygen demand not present in the aquifer. While important to understand for these experiments the natural oxygen demand observed is likely not typical of aerobic sandstone aquifer conditions.

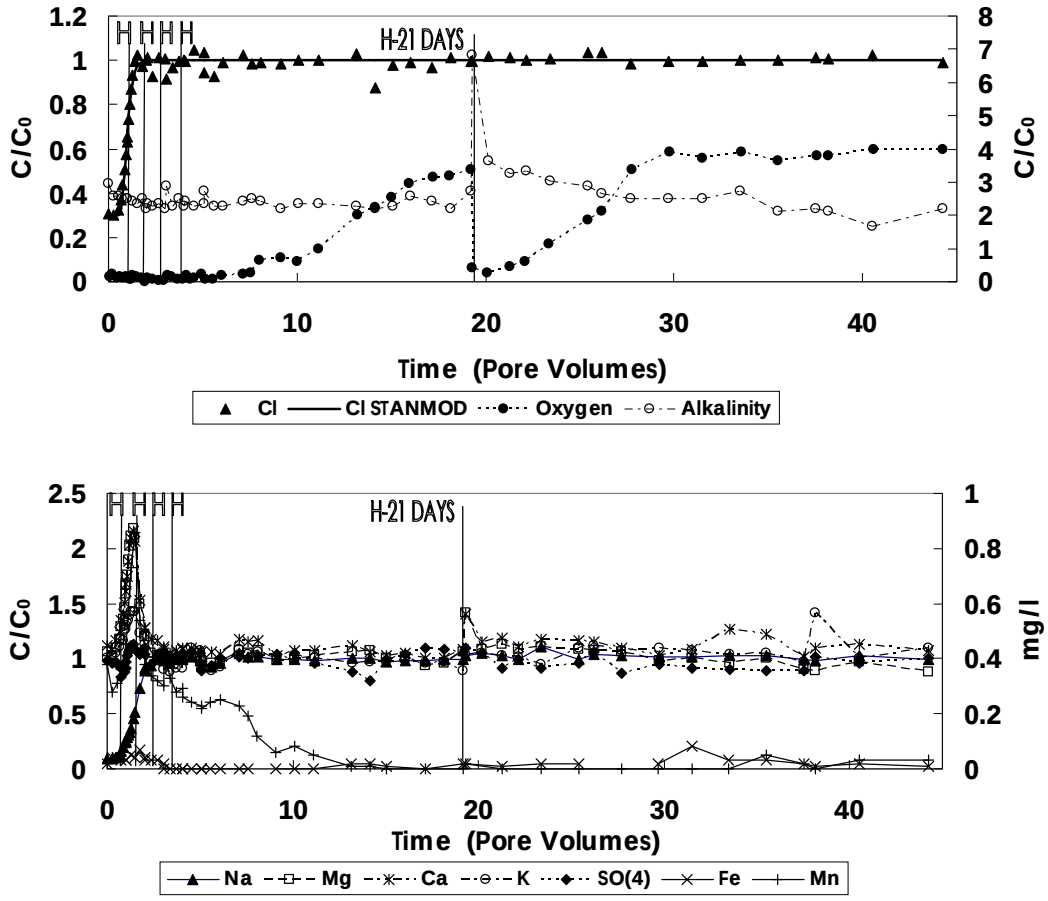

Figure 5-2: Oxygen saturation test data for column A. Alkalinity, Mn and Fe are plotted on the secondary axes. Note the long time required for oxygen to initially breakthrough and absence of full breakthrough to C/C_0 of 1.0. Under anaerobic conditions at the start of the test Mn and Fe are present. "H" on its own indicates a 12 hour hiatus. Note the increase in alkalinity and decrease in oxygen levels after the long hiatus.

During the long hiatus of the oxygen saturation test there was an increase in alkalinity and decrease in oxygen concentration. This was more prominent in column A, where oxygen decreased by 3.96 mg/l and alkalinity increased by 54 mg/l, in comparison with respectively 0.72 mg/l and 12 mg/l in column B. There was no change in the concentration of other electron acceptors during the hiatus. The results in Table 5-3

suggest that aerobic degradation of simple organic carbon (CH_2O) should not change the alkalinity. An increase in alkalinity can occur due to calcite dissolution from CO_2 accumulation during aerobic respiration [Stumm and Morgan, 1996]. From the equation:

$$CaCO_{3(s)} + CO_{2(aq)} + H_2O = Ca^{2+}{}_{(aq)} + 2HCO_3{}^{-}{}_{(aq)} \quad (5.2)$$

at pH < 10 it can be deduced that:

$$\frac{\delta \log \rho_{CO_2}}{\delta \log\left[Ca^{2+}\right]} \simeq 3 \quad (5.3)$$

The impact of CO_2 accumulation on alkalinity was investigated using the geochemical reactive transport code PHREEQC. In the experiments the alkalinity increased from 36 to 90 mg/l in column A. In PHREEQC, when adding an amount of POC equivalent to the dissolved oxygen concentration decrease from input values to the post-hiatus solute and allowing the calcite saturation index to reach equilibrium, the alkalinity rose to 73 mg/l, similar to the value measured in experiments. The alkalinity did not increase during POC biodegradation when the solution was flowing through the columns. This suggests that the build-up of CO_2 from POC biodegradation is slow, only inducing calcite dissolution during hiatuses.

Table 5-3: Equations used for alkalinity and electron balance calculations, with alkalinity contribution per mol of simple organic carbon (CH_2O) or acetate (CH_3HOO^-) biodegraded or metal precipitated.

Equation	Alkalinity contribution (eq /mol)
Natural organic carbon degradation	
$CH_2O + O_2 \rightarrow CO_2 + H_2O$	0
$CH_2O + 2MnO_2 + 4H^+ \rightarrow 2Mn^{2+} + 3H_2O + CO_2$	4
$CH_2O + 4FeOOH + 8H^+ \rightarrow 7H_2O + 4Fe^{2+} + CO_2$	8
$5CH_2O + 4NO_3^- + 4H^+ \rightarrow 2N_2 + 5CO_2 + 7H_2O$	0.8
$SO_4^{2-} + 2H^+ + 2CH_2O \rightarrow 2CO_2 + H_2S + 2H_2O$	1
Acetate biodegradation	
$CH_3COO^- + H^+ + 2O_2 \rightarrow 2CO_2 + 2H_2O$	1
$CH_3COO^- + 17H^+ + 8FeOOH \rightarrow 2CO_2 + 14H_2O + 8Fe^{2+}$	17
$CH_3COO^- + 9H^+ + 4MnO_2 \rightarrow 2CO_2 + 6H_2O + 4Mn^{2+}$	9
Metal precipitation	
$Fe^{2+} + H_2O + CO_2 \rightarrow FeCO_3 + 2H^+$	-2
$Mn^{2+} + H_2O + CO_2 \rightarrow MnCO_3 + 2H^+$	-2
$Fe^{2+} + 3H_2O \rightarrow Fe(OH)_3 + 3H^+ + e^-$	-3

5.4.3. **Assessment of acetate biodegradation**

5.4.3.1. **Interpretation of column experiments**

Acetate was biodegraded in all tests. Oxygen concentrations decrease during tests, suggesting aerobic biodegradation occurred. The nitrate concentration in the synthetic groundwater was very low and sulphate levels did not vary greatly. This suggests that nitrate- and sulphate-reduction were not important. Methanogenesis was not considered, as the column was predominantly aerobic, and the sulphate concentrations were not reduced [Chapelle, 1993]. The dissolved Mn and Fe concentrations increase slightly, near the end of the constant injection test, when anaerobic conditions develop. Sorption and re-precipitation of these metals may occur within the columns [Hunter et al., 1998; Christensen et al., 2001], such that the contribution of Mn- and Fe- reduction to acetate biodegradation may be underestimated based on the dissolved concentration of these species.

Results for the constant injection tests for column A and B are shown in Figure 5-3 and Figure 5-4, respectively. In both tests the alkalinity increased and dissolved oxygen decreased during acetate biodegradation. At the hiatuses the acetate concentration decreases and alkalinity increases. This may be due to calcite dissolution caused by CO_2 build-up as in the oxygen saturation tests (see Equations 5.2 and 5.3). Longitudinal dispersion in column A is greater than column B (α_L = 0.13 m compared with 0.011 m, as measured from STANMOD model fits). Both columns were packed and treated similarly. The difference may result from slight disturbances when turning the columns sideways and differences in the efficiency of the packing procedure. The high apparent dispersivity may relate to physical non-equilibrium transport, which is discussed below.

In the constant injection tests there is a lag between the onset of acetate biodegradation and decrease in oxygen levels. In column A the lag is less that in column B. The decrease in dissolved oxygen concentration is also more gradual in column A than column B. This may be influenced by the higher dispersion in column A. The reduction in acetate early in the experiment may be due abiotic processes. However no reduction in concentration was seen in the sterile stock solution during the experiments. The lag may be due to a

decrease in oxygen utilisation by POC biodegradation concomitant with an increase in utilisation by acetate biodegradation. This is discussed in further detail later in the chapter.

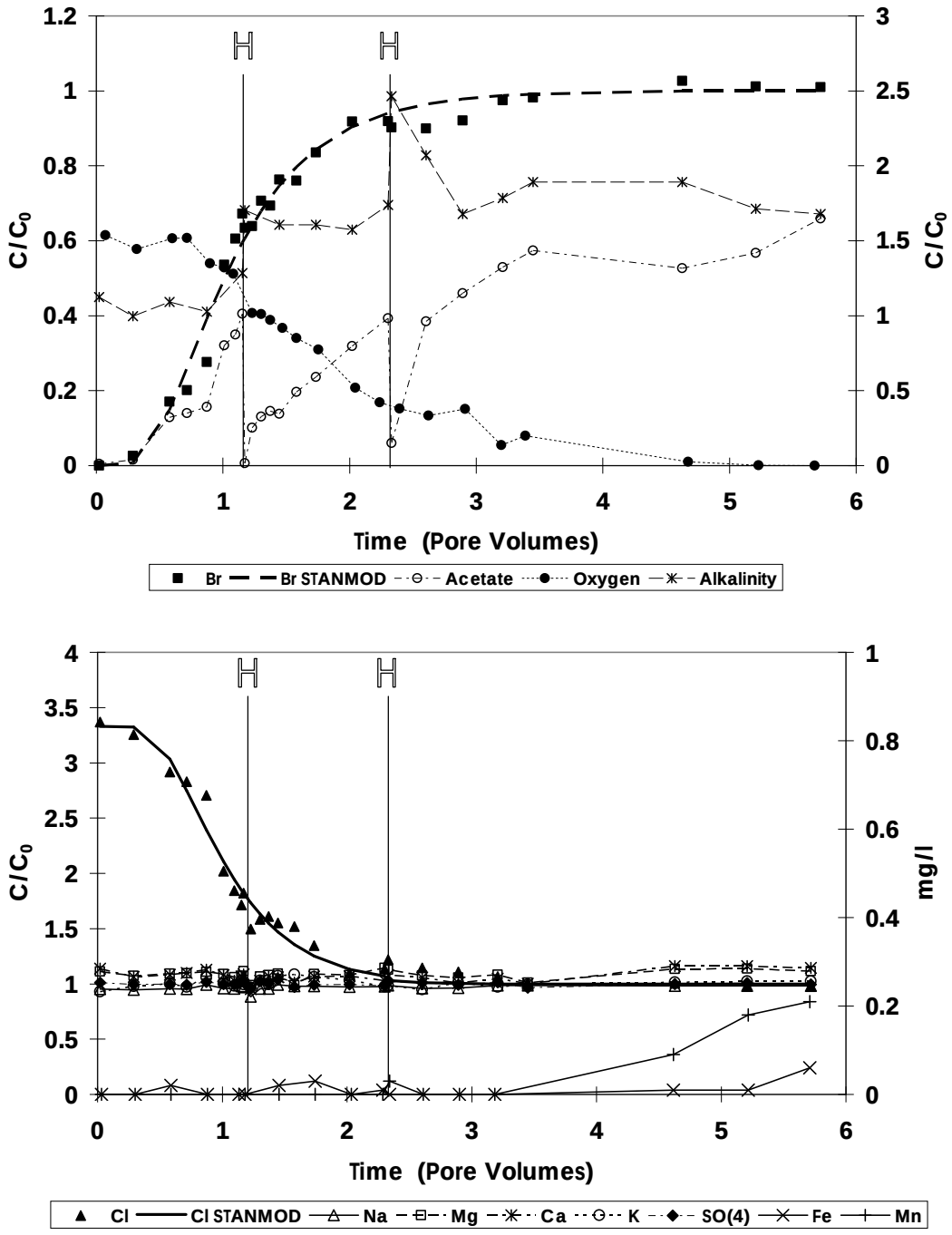

Figure 5-3: Constant injection test data for column A and STANMOD fits. Alkalinity, Mn and Fe are plotted on the secondary axes. H represents a 12 hour hiatus. Note that oxygen is the only electron acceptor that varies and its depletion slightly lags acetate biodegradation. Also note the increase in alkalinity during acetate biodegradation.

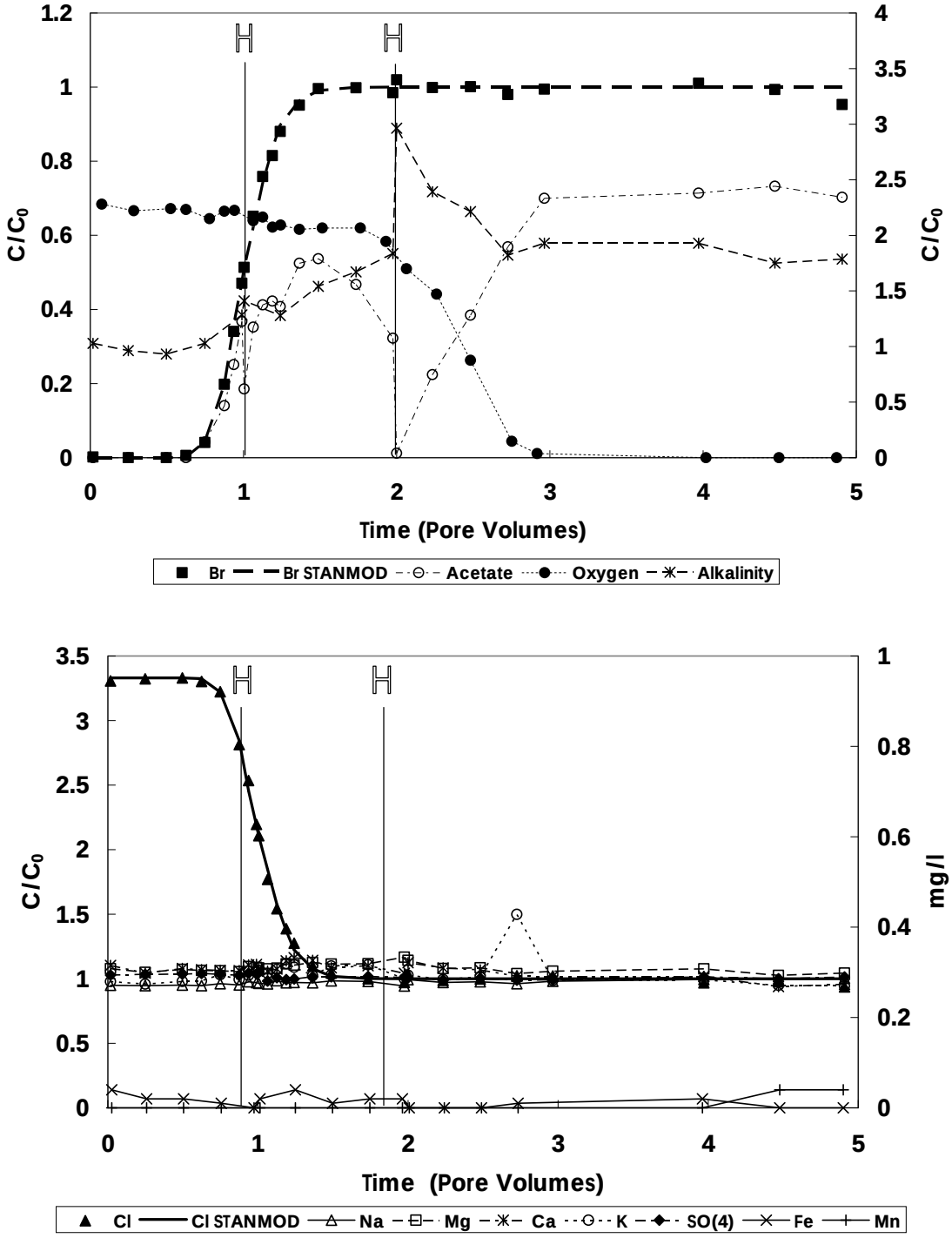

Figure 5-4: Constant injection test data for column B and STANMOD fits. Alkalinity, Mn and Fe are plotted on the secondary axes. H represents a 12 hour hiatus. Note that oxygen is the only electron acceptor that varies and its depletion lags acetate biodegradation. Also note the increase in alkalinity during acetate biodegradation.

5.4.3.2. **Electron balances**

The end of the constant injection tests (last 3 data points) provided the best data to clearly assess acetate biodegradation, as solute concentrations reached steady-state. An electron balance was performed to ascertain if the reduction in acetate levels could be explained by aerobic biodegradation. The electrons donated by observed acetate degradation were balanced against those that would be accepted by the observed decrease in oxygen concentrations. Two competing hypotheses were tested: (A) POC was aerobically biodegraded preferentially over acetate, and (B) acetate was aerobically biodegraded preferentially over POC. Hypothesis B would explain the lag between the decrease in acetate concentrations and decrease in dissolved oxygen concentrations seen in tests (see above).

For hypothesis A, the decrease in dissolved oxygen concentration from the start to end of the experiment at the sampling point was assumed to be the oxygen utilised for aerobic biodegradation of acetate. For hypothesis B the oxygen utilised is assumed to be the decrease from that injected into the column. This assumes that when acetate is injected into the column POC oxidisation stops and oxygen is utilised only to biodegrade the more labile acetate. Hypothesis A accounts for less than half the electrons produced by the acetate biodegradation observed in both columns (Figure 5-5). The balance is better for hypothesis B, but acetate biodegradation is still under-predicted by the decrease in dissolved oxygen concentration.

The biodegradation not accounted for may result partly from diffusion of some oxygen from immobile zones or oxygen leakage into the column. Greater diffusion from immobile zones would be expected from column A, which shows more physical non-equilibrium flow than column B (see section 5.3.4). Also, this may have contributed to the long time required to fully de-oxygenate the columns before experiments (not shown). Oxygen leakage is unlikely to significantly affect the results, as at the start of the column the aqueous solution is oxygen-saturated (any leakage would not add to concentrations), while at the end of the column the sample is quickly taken and analysed. Also if oxygen

leakage occurred at the end of the column, readings of 0 mg/l dissolved oxygen at the end of the constant injection tests would not arise.

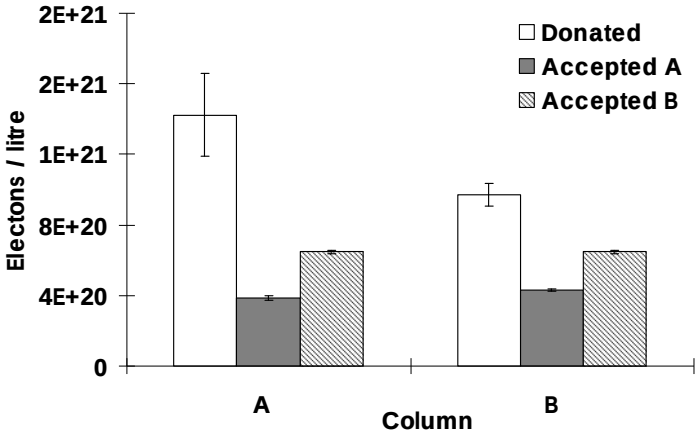

Figure 5-5: Observed donated and accepted electrons for the equilibrium phase of the constant injection test. A and B refer to hypothesis A and B, regarding aerobic degradation (see text).

Mn and Fe reduction may partially contribute to acetate biodegradation during the period analysed in the electron balance. Acetate biodegradation is greater than can be explained by aerobic biodegradation alone in parts of the constant and pulse injection tracer tests. For example in the fast pulse test in column B (Figure 5-6) the decrease in oxygen concentrations observed is significantly less than that needed to balance the acetate decrease by aerobic biodegradation. The reason for this is unclear, but could reflect an unknown source of dissolved oxygen in the experiment.

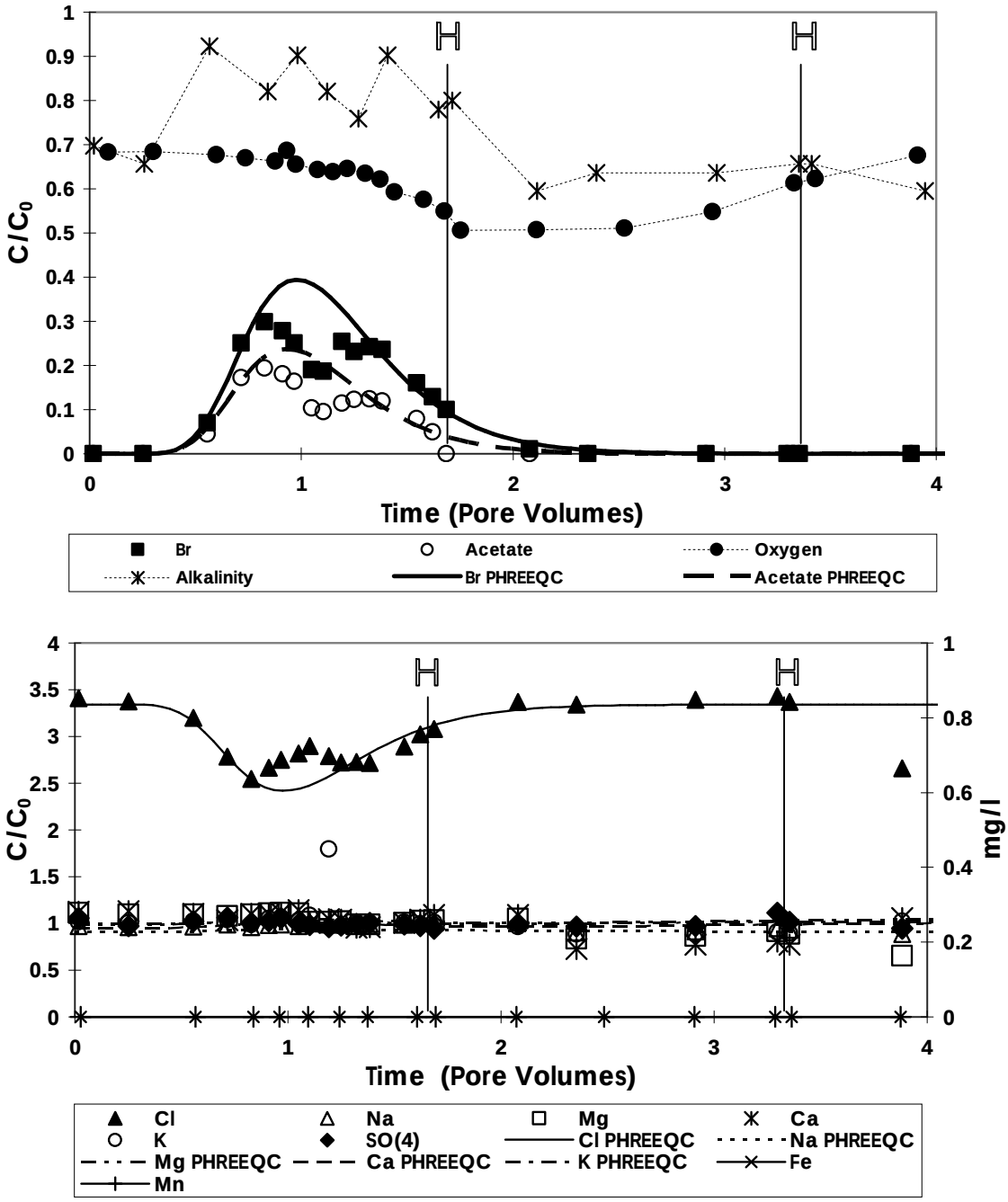

Figure 5-6: Fast pulse injection test data for column B and PHREEQC model fits. Mn and Fe are plotted on the secondary axis. H represents a 12 hour hiatus. Note that oxygen is the only electron acceptor that varies and its depletion lags acetate biodegradation. Also note the double peak for Br breakthrough, which may indicate 2 porosity zones of different flux.

5.4.3.3. **Alkalinity balances**

Alkalinity balances were performed to further investigate biodegradation pathways that may contribute to acetate biodegradation. The observed increase of alkalinity was

compared with that expected from different acetate biodegradation pathways (Table 5-3). Breakthrough of the stock solution also contributed to the alkalinity rise observed. This was estimated from values in the conditioning tests at the end of the first day, where C/C_o of acetate equalled 1, and was taken away from the observed total alkalinity to give the observed total alkalinity produced due to biodegradation. Alkalinity expected from different pathways was calculated from the decrease in acetate concentrations and equations in Table 5-3. The contribution of known aerobic biodegradation was calculated from the oxygen utilised during the tests, relative to levels at the start of the experiments. Results were integrated over the entire experiment duration to reduce inaccuracy due to alkalinity measurement error.

The contribution to alkalinity of observed aerobic biodegradation is small (Figure 5-7). Approximately 80% of the alkalinity comes from an unknown acetate biodegradation pathway. Electron acceptor profiles and electron balances (see above) imply that the unknown pathway is more aerobic biodegradation or Mn/Fe reduction. If the unknown pathway is aerobic biodegradation or Mn/Fe reduction with precipitation of $MnCO_3$ or $FeCO_3$ (rhodochrosite and siderite) the expected alkalinity is similar to that observed (Figure 5-7, Table 5-3). Mn and Fe reduction with precipitation of $MnCO_3$ or $FeCO_3$ (rhodochrosite and siderite) is not supported by the results of PHREEQC modelling, which suggest the pore fluids are significantly undersaturated with respect to these minerals, when Mn/Fe concentrations are <1mg/L (Figure 5-8). However, concentrations up to 1 mg/l do not occur in the tests, suggesting this process is not important. From the above, it is unlikely that the unknown pathway is mainly Mn-and Fe-reduction with precipitation of metal carbonates, as the columns are predominantly aerobic during tests. This suggests that aerobic biodegradation is the most likely pathway. However the unknown portion of produced alkalinity is unlikely to be all directly due to aerobic biodegradation as insufficient dissolved oxygen was added to the column to account for all the acetate biodegradation, as seen in the electron balances.

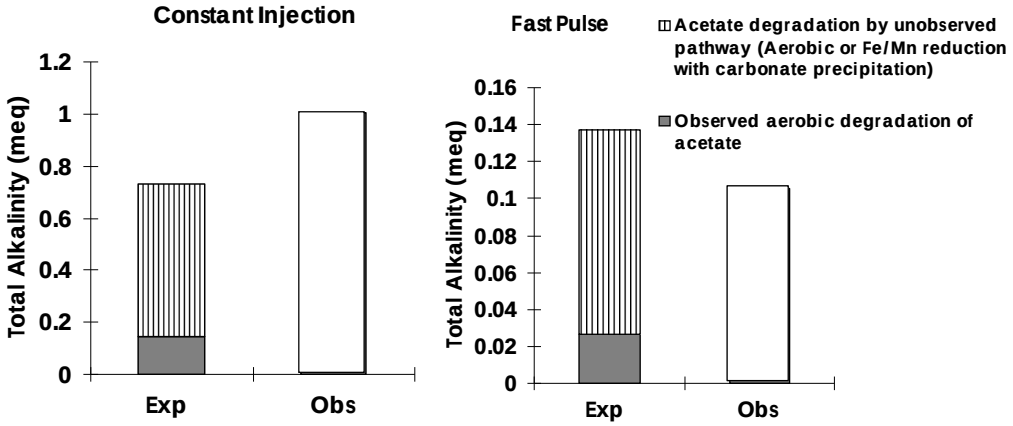

Figure 5-7: Expected and observed total alkalinity produced from acetate biodegradation and related reactions for tests in column B.

Calcite dissolution due to CO_2 build-up during the experiment hiatuses may contribute to the alkalinity, as seen in the oxygen saturation tests. The underestimation of observed alkalinity in the mass balances may also be explained if a small amount of Mn or Fe reduction with sorption of the metals was occurring, as acetate biodegradation by this pathway leads to a large rise in alkalinity (Table 5-3). This would also partially offset the electron imbalance seen in tests.

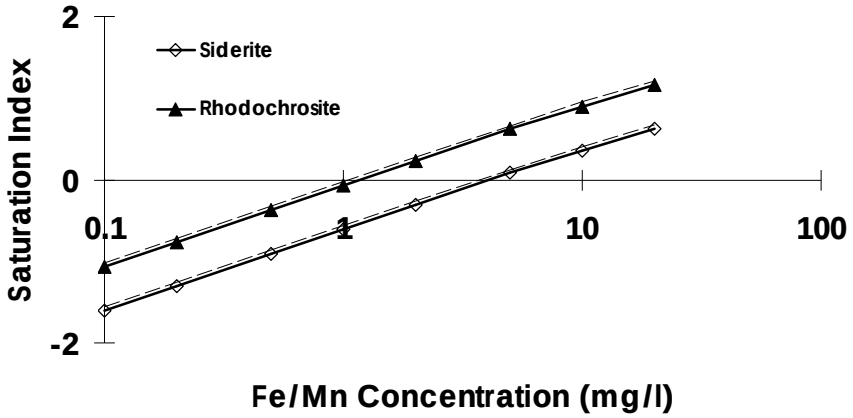

Figure 5-8: Saturation indexes calculated by PHREEQC for siderite and rhodochrosite for the constant injection test in column B, for varying input concentrations of Fe and Mn. The solid line represents the end of the test and dashed the start of the second hiatus. Negative values represent undersaturation and positive values oversaturation of pore fluids with respect to these phases.

The contribution of different acetate biodegradation pathways and calcite dissolution to alkalinity was separately verified with PHREEQC, using data from the constant injection

test in column B at the end of the second day. Acetate biodegradation was simplified by adding CH_3COONa (form of acetate added to the input solution as a tracer) to the solution as a reactant. When calcite is not present in equilibrium with the solution, aerobic biodegradation and Fe-reduction of acetate changed alkalinity to the amount expected in Table 5-3. When calcite is present in equilibrium the alkalinity change for aerobic biodegradation of acetate is increased approximately by a factor of 4. Therefore calcite dissolution can contribute significantly to alkalinity.

Overall analysis suggests that acetate biodegradation in the column experiments is likely to be mostly aerobic. Oxygen was used (before acetate arrival) by the oxidation of POC. During the test is seems aerobic biodegradation of acetate is favoured over that of natural organic carbon. This means most of the oxygen utilised by acetate biodegradation during the tests cannot be quantified exactly. The electron and alkalinity balances suggests that dissolved oxygen from an alternative source contributes to aerobic biodegradation, and some Mn and Fe reduction occurs, with sorption of the free metals onto minerals. Calcite dissolution by CO_2 from aerobic biodegradation may also be occurring, supporting the increase in alkalinity.

5.4.3.4. **Estimation of acetate biodegradation rates**

Acetate biodegradation was observed to follow first-order decay (Figure 5-9). First-order biodegradation rates were estimated for acetate in the pulse injection tests. This parameter can be used as a measure of biodegradation in the field [Haggerty et al., 1998]. This calculation does not require fitting of the data with a model. A graph of time versus $-\ln\frac{[C_{acetate}]}{[C^{c}_{acetate}]}$, where $[C_{acetate}]$ is the concentration of acetate measured at a given time and $[C^{c}_{acetate}]$ is equal to the stock concentration of acetate times the normalised concentration of Br^- (i.e. the concentration of acetate expected if it was transported conservatively), was plotted. Points were considered from the initial breakthrough of acetate until the first hiatus. Some points at earlier times were discounted, as outlying values were obtained that did not correspond with trends. These were probably due to instrument error and measurement variability at low concentrations. The decay constant obtained for column B is similar in the slow and fast pulse injection tests. The decay is

faster in column A than B and greater in the slow pulse test relative to the fast pulse test in column A. However, the overall variation in the decay constant is less than a factor of 2. This shows good reproducibility at different flow rates and in different columns. Data points from later times in the column A slow pulse test indicate a larger decay constant. Data from 294–452 minutes suggests a decay constant similar to the other tests of 0.0024 /min (R^2 =0.86). However if all the results from the first day (up to 700 minutes) are considered, the value increases to 0.0036 /min (R^2= 0.61). These points (not shown) represent acetate concentrations around 1 mg/l and may not be reliable. Therefore they are not shown on the graph. These biodegradation rates were later used to fit acetate BTCs for the pulse tests in conjunction with PHREEQC and STANMOD model fits to Br^- (see below).

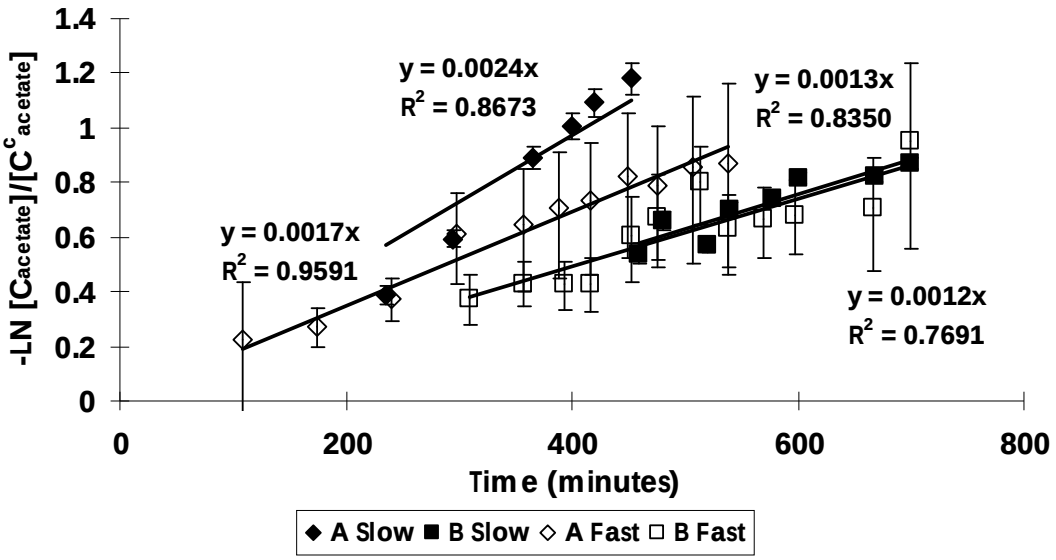

Figure 5-9: First order decay fits for acetate biodegradation for the slow and fast pulse injection tests in both columns.

5.4.4. **Physical non-equilibrium transport**

Initial modelling of conservative tracer breakthrough was performed using STANMOD. High model efficiencies [Berthouex and Brown, 2002; Bolster and Hornberger, 2007] showed the STANMOD fits obtained for Br^- were good for the constant injection tests (99.6 and 99.7 % in columns A and B respectively) and the slow pulse test in column B (86.2 %). However other pulse tests required unrealistically high values of longitudinal dispersivity (α_L) to fit the data. For example, in column A a longitudinal dispersivity of

0.49 m was required for the fast pulse test, which was previously modelled with a dispersivity of 0.13 m during constant injection. Column A pulse test breakthrough curves showed long tailing of concentrations (Figure 5-10) and BTCs also showed a secondary peak or shoulder for Br^- (e.g. Figure 5-6), which is not consistent with regular advective dispersive transport in a homogenised medium. Mass recovery of Br^- was above 92 % in all pulse tests (Table 5-4), even with less regular sampling and tailing of tracer concentrations in some experiments. The high values of longitudinal dispersivity and asymmetrical nature of conservative tracer breakthrough could be explained by physical non-equilibrium transport in the column, which was more prevalent in the pulse injection tests. Welty and Gelhar [1994] also noted that pulse injection tests were more susceptible to physical non-equilibrium transport than constant injection tests.

Table 5-4: Mass recovery for pulse tests. Percentages are rounded to 1 decimal place. Mass recovery of Br less than 100% occurs in the slow pulse injection tests indicates a tailing of breakthrough and/or underestimation of breakthrough concentrations due to analytical error. Mass recovered of acetate is much less in the slow pulse injection test as a hiatus occurred near peak concentrations.

		Column A		Column B	
Test		Br^-	Acetate	Br^-	Acetate
Slow Pulse Injection	Mass Recovery	92.7 %	17.8 %	93.4 %	22.2 %
Fast Pulse Injection	Mass Recovery	105.9 %	47.6 %	98.1 %	50.3 %

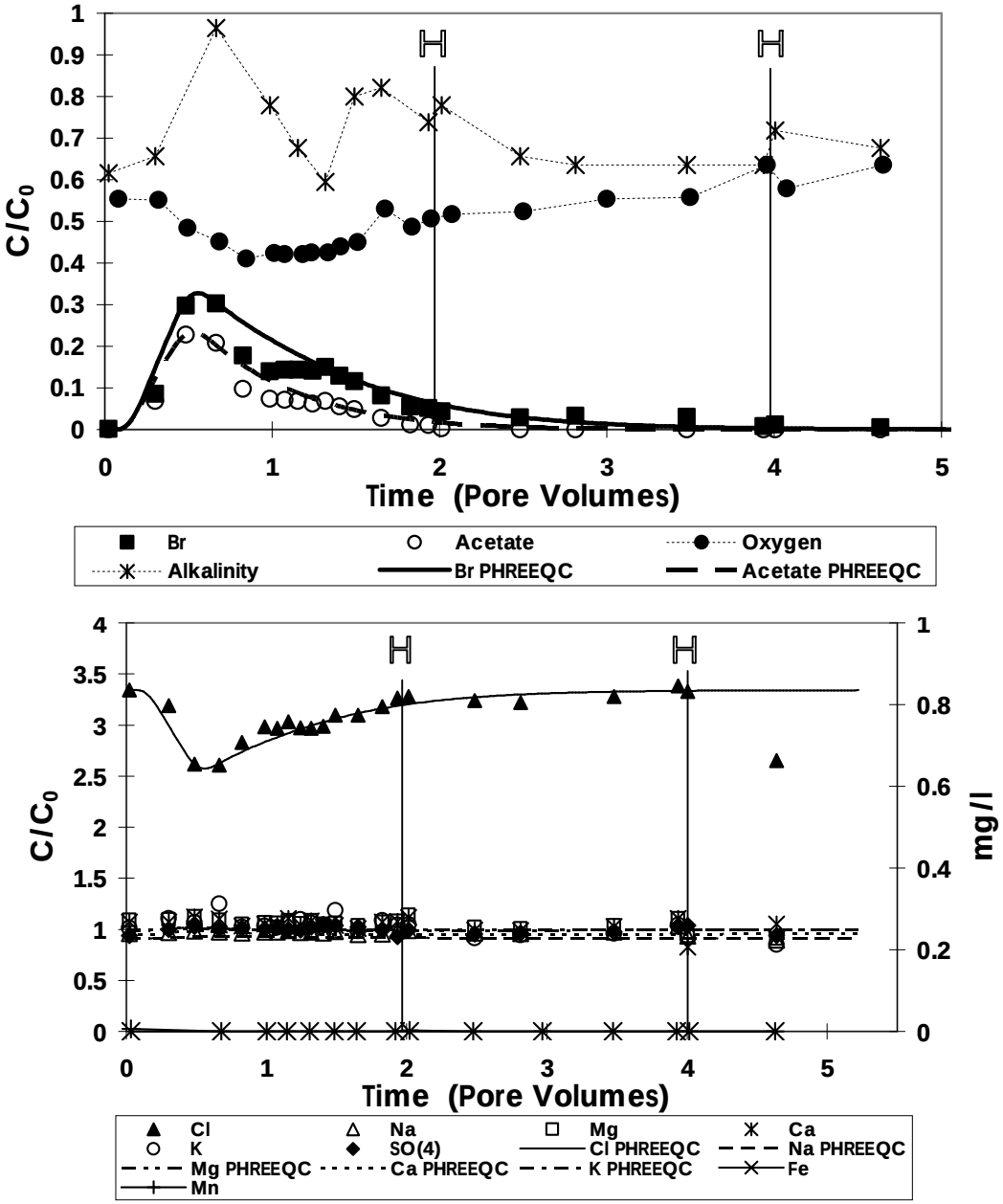

Figure 5-10: Fast pulse injection test data for column A and PHREEQC model fits. Mn and Fe are plotted on the secondary axis. H represents a 12 hour hiatus.

Physical non-equilibrium tracer transport may occur due to the presence of:

(a) Dual porosity. Mobile and immobile pore spaces, with diffusion between the two domains [Brusseau and Rao, 1989].

(b) Dual permeability. Diffusion occurs between two zones with distinctly different permeabilities. Over time advective breakthrough will occur in both zones [Gillham

et al., 1984; Guswa and Freyberg, 2000].

(c) A chemical effect. However similar tailing is seen in both the conservative tracer (Br^-) and biodegrading tracer (acetate).

(d) Some short circuiting of flow around the column walls with bulk matrix flow in the core of the column. The columns were packed to a procedure used in published studies [Thornton et al., 2000a; Thornton et al., 2000b], with loose material that would fill the column entirely. Therefore this effect would be expected to be minimal.

The constant injection test for column A took a long time to reach equilibrium values (Figure 5-3) and may also indicate the presence of non-equilibrium flow. If so this suggests that physical non-equilibrium conditions were always in column A. In column B physical non-equilibrium flow did not occur until the fast pulse test. This suggests that differences in packing between the columns may have contributed to the behaviour observed. As column B develops physical non-equilibrium over time this suggest that it may be a factor of the sand used, higher flow rates in the fast pulse tests and/or extended use of the column.

PHREEQC was used to model physical non-equilibrium transport in the pulse tests. The model can account for physical non–equilibrium transport by conceptualising the process as an immobile cell in parallel with each mobile cell. Mass transfer between the cells is simulated by a first–order exchange coefficient [Appelo and Postma, 2005]. This type of model has previously been used to model dual porosity and dual permeability scenarios (e.g. [Goltz and Roberts, 1988; Welty and Gelhar, 1994]). For column A the total porosity and dispersivity were assumed to be the same as the constant injection test in the column. For the fast pulse test in column B total porosity and dispersivity were assumed to be the same as the slow pulse test that showed equilibrium transport and was performed directly before the fast pulse test. Water velocity was calculated from the assumed total porosity and measured flow rate. The mobile and immobile porosity present and the exchange coefficient were fitted simultaneously using the model. Values obtained for the immobile porosity and the exchange coefficient (see Table 5-5) from manual fits of the data with PHREEQC were similar to other studies [Tan, 2009]. If

physical non-equilibrium conditions were always in column A (see above), the magnitude of physical non-equilibrium in the column A pulse tests may be underestimated. Initial breakthrough and tailing was modelled accurately, but peak height is overestimated and did not predict the double peaks seen. This suggests that the column is closer to dual permeability than dual porosity. Another possibility is that the finer grained material in the very poorly sorted sediment used may separate two higher permeability zones of different velocity (dual mobility zone). A model that took into account two porosity zones each with variable biodegradation, dispersivity and fluid mobility was not available. It was considered outside the remit of the study to develop a model to incorporate these features. A schematic diagram of a dual porosity, dual permeability, and dual mobility zone model is shown in Figure 5-11.

Table 5-5: Physical non–equilibrium transport parameters used to model breakthrough curves in pulse tests using PHREEQC. T represents the exchange (mass transfer) coefficient between the mobile and immobile phase, assuming first-order diffusion rates. Porosities are represented as fractions and T is in seconds.

	Column A			Column B		
Test	Θ_{mobile}	$\Theta_{immobile}$	1/T	Θ_{mobile}	$\Theta_{immobile}$	1/T
Slow Pulse Injection	0.18	0.17	$3x10^{-5}$	0.43	0	N/A
Fast Pulse Injection	0.17	0.18	$3x10^{-5}$	0.35	0.08	$3x10^{-5}$

The biodegradation rates previously estimated (see above) and conservative transport parameters obtained with PHREEQC and STANMOD were used to simulate acetate concentrations in the pulse tests. A good fit was obtained for the column B slow pulse test modelled with STANMOD. A model efficiency of 75.8 % was obtained for acetate. Reasonable fits were also obtained for the fast pulse tests. Model efficiencies for Br were 86.7 and 60.7 % and for acetate 88.0 and 65.7 % for columns A and B, respectively. The lower values for column B result from two peaks in the breakthrough curve. Model efficiencies were lower for the column A slow pulse tests. This is partly due to the low normalised solute concentrations for column A and the first hiatus occurring before the end of the pulse for both tests. Model efficiencies were -50.0 and 17.1 % for Br and acetate, respectively. The low values suggest that while modelling with immobile zones and diffusion coefficients improves the model fit over simple one-dimensional transport, the process is more complicated than conceptualised with the available modelling tools.

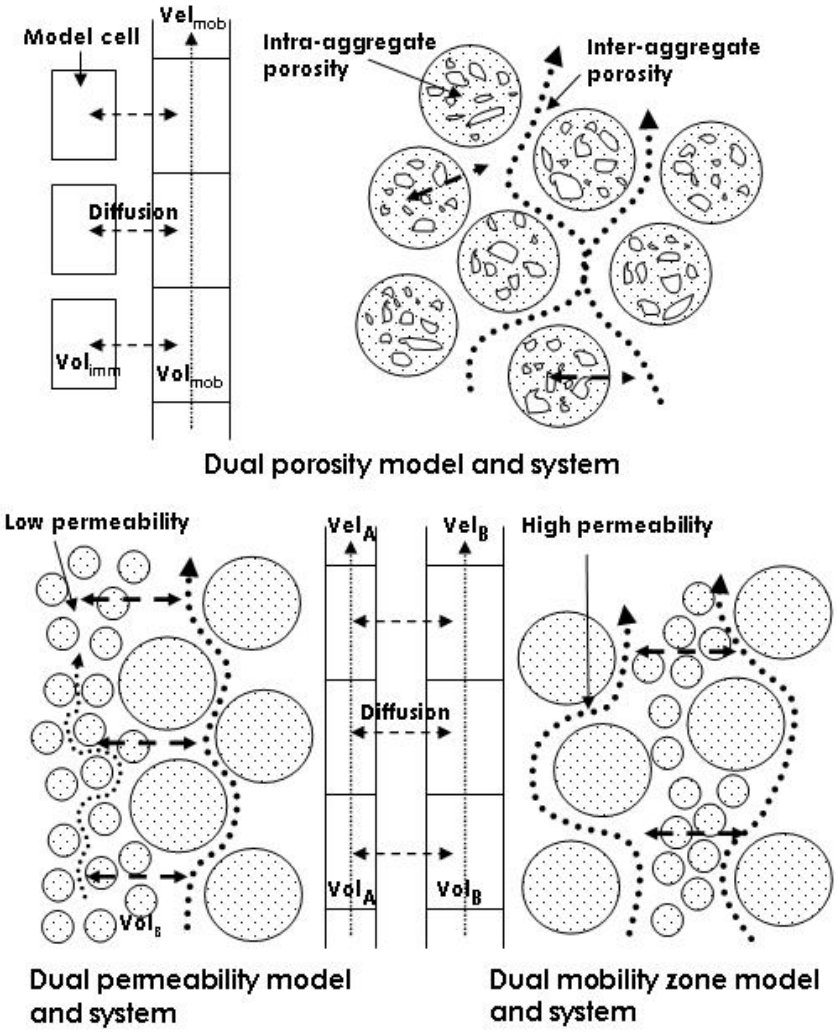

Figure 5-11: Schematic diagrams of the 1-D model and potential physical system for physical non-equilibrium flow regimes that may be present in the columns. The 1-D model is the same for dual permeability and dual mobility zone systems.

5.5. **Discussion**

5.5.1. **Assessment of biodegradation**

Column tests were performed to assess the suitability of using acetate as a model biodegrading tracer in forced gradient tracer tests for the *in situ* assessment of aquifer biodegradation potential. In the laboratory experiments the test flow rate did not significantly affect acetate biodegradation rates. Biodegradation rate has been observed to be greater at lower pore water velocities for toluene and 1,2,4-trimethylbenzene [Zheng et al., 2002], however rates only varied by an order of 2-3, similar to the variation between

columns seen in this study. Acetate was seen to degrade quickly making it suitable for use in single well forced gradient tracer tests (e.g. dipole flow and push pull tracer tests [Istok et al., 1997; Sutton et al., 2000]) that can be performed in a day. Therefore the biodegradation potential of an aquifer under natural or stimulated conditions could be quickly assessed at multiple boreholes. In preliminary conditioning tests it took 3-4 days of flushing with an acetate solution to stimulate biodegradation. If no biodegradation is seen in the first test performed at a site it should be assumed that the present biota is not yet stimulated, rather than no biodegradation is possible. Acetate should be left in the test zone and a second test performed at the same position a few days later. Alternatively a push-pull test could be performed with a rest phase of 3-4 days, however mass loss [Kim et al., 2004; Azizian et al., 2007] may occur due to background hydraulic gradients removing the tracer from the pumping wells area of influence. If the push-pull test rest phase is long biodegradation may become limited by the depletion of an electron acceptor or all acetate may be biodegraded. Either way this will give limited information on biodegradation kinetics. This is similar to what occurred at the end of the constant injection tests. However in these situations a more accurate electron balance may be obtained than shorter duration pulse tests.

The modelling studies showed that alkalinity can be used to effectively assess the type and extent of biodegradation processes. Alkalinity has been used by Hunkeler et al. [1999] to assess bioremediation in an aquifer contaminated with aromatic hydrocarbons. In this study it was used to assess potential biodegradation pathways, which may be linked to the precipitation of minerals (metal carbonates). Biodegradation pathways contribute different amounts to the measured alkalinity, which may be used to determine how a substrate biodegrades. The alkalinity balances suggested that most of the acetate biodegraded aerobically, where as the electron balances implied this was not the case. The alkalinity and electron balances together helped to show that acetate biodegradation occurs preferably over POC biodegradation in aerobic conditions and that a portion of the acetate aerobic biodegradation was supported by dissolved oxygen from an unidentified source. A small amount of acetate may have degraded via Fe/Mn-reduction, with the metal sorbing to aquifer minerals. In addition, calcite dissolution due to a build-up of CO_2

from biodegradation can explain the increased alkalinity in the columns during hiatus periods. Alkalinity measurements, along with other chemical indicators, will help deduce biodegradation pathways in the field.

5.5.2. **Effect of particulate organic carbon on electron acceptor demand**

Oxygen was the only electron acceptor that varied consistently and significantly in concentration during the column tests. However oxygen consumption is not clearly linked with acetate biodegradation. The POC in the sediment significantly affected the dissolved oxygen concentration in the pore water. The natural oxygen demand of the sediment present is more representative of anaerobic conditions [Wilson et al., 2002], than the aerobic sandstone aquifer from which the sand originated [Kimblin., 1995; Thornton et al., 2005]. The demand may originate from the purging of the column with de-oxygenated water or fresh organic carbon surfaces being exposed. Initial biodegradation of acetate occurs before a decrease in dissolved oxygen concentration. Biodegradation using other dissolved electron acceptors is likely to be minimal as aerobic conditions persisted in the columns. However, electron balances suggest that another process, either an unquantified source of oxygen allowing further aerobic biodegradation, or Mn/Fe-reduction, must be occurring to some extent in the columns. A reservoir of dissolved oxygen may be present in immobile pore spaces, supporting biodegradation. There may be other sources of dissolved oxygen that could not be quantified in these experiments. No evidence of oxygen leakage into the columns is observed. Leakage could only have occurred at the end of the columns and the slow diffusion of oxygen in water [Ferrell and Himmelblau, 1967] would mean leaked oxygen could not penetrate far into the column during test hiatuses. Before initial breakthrough of acetate the oxygen is used by microorganisms in the column to biodegrade the naturally occurring POC. When acetate arrives at a location in the column it is freely bioavailable in the aqueous phase and more readily bioavailable than the natural POC. If acetate is preferentially biodegraded over the natural POC during initial breakthrough a decrease in acetate concentration will occur without a decrease in dissolved oxygen concentration (increase in observed oxygen utilisation) or the observed decrease in oxygen will be less than expected (Figure 5-12). This is provided that dissolved oxygen is constantly being supplied to keep the

concentration high. In some pulse injection tests the decrease in oxygen concentrations occurred after most of the tracer pulse had passed. This indicates that oxygen concentration may be affected by more than POC and acetate biodegradation, and may be related to the physical non-equilibrium conditions present in the column. Although the lag between the decrease of acetate and dissolved oxygen concentrations was greater in column B, where physical non-equilibrium transport was less significant. The experimental data suggests that if in the field an accurate electron balance was required, then the zone of the test may have to be flushed with oxygen-saturated water for a long time to overcome any oxygen demand from natural POC in the aquifer sediment. This may be time consuming and not cost-effective. Also it would not be representative of the aquifer conditions. The natural oxygen demand observed is unlikely to be present in oxygenated sandstone aquifers. Therefore in aerobic aquifers flushing with oxygen-saturated would not improve electron balance data.

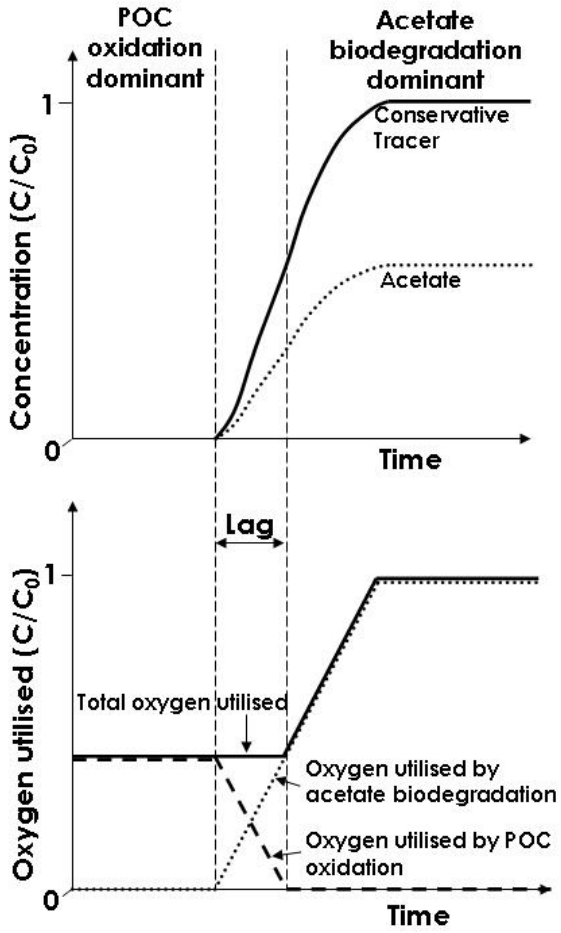

Figure 5-12: Schematic diagram of ideal tracer breakthrough and oxygen utilisation during a constant injection test with acetate when POC is present. Note the lag between the onset of acetate biodegradation and the increase in the total oxygen utilised (seen in experiments as a drop in the dissolved oxygen concentration).

5.5.3. Effect of physical non-equilibrium transport on the assessment of biodegradation

First–order rate coefficients for acetate biodegradation were estimated by plotting the natural logarithm of the normalised concentration of acetate over the normalised concentration of the conservative tracer against time. This method does not require a model to be fitted to the data to obtain a biodegradation coefficient, similar to push-pull tests [Haggerty et al., 1998]. However the method assumes that the entire mass of the biodegrading tracer seen at an observation time has been subject to biodegradation for that time. Fitting of data with PHREEQC has suggested that the flow regime in the columns is more complicated than represented by mobile and immobile zones. Double

peaks in the pulse injection tests suggest at least two zones with different column resident times (Figure 5-11). Therefore if different tracer mass travelled at different velocities through the columns, it may have been in the column for different times at the same observation point, and the assumption used to calculate simple first-order biodegradation coefficients may be in error. The fact that injection occurred over 2 or 4 hours also adds uncertainty. The slow pulse test in column A resulted in variable acetate first-order biodegradation coefficients. If later times are considered a larger biodegradation coefficient and lower R^2 value are obtained. These later times lead to an overestimation of the biodegradation rate. This may represent the slower velocity porosity zone where the acetate residence time in the column is longer, resulting in more biodegradation. Alternatively if a large amount of the immobile porosity is present as micropores then bacteria may be too large to enter them, thus inhibiting biodegradation [Roden and Scheibe, 2005]. Therefore the different porosity zones that are suggested in the experiments may have different inherent biodegradation rates. The results from the other columns show good data fits for estimates of first–order biodegradation rates. This suggests that biodegradation from the (presumed) faster flow path(s) was measured, as equal mixing between these zones is highly unlikely due to the advection rate being much quicker than diffusion. Although the data suggests that in porous media where physical non–equilibrium transport occurs two separate biodegradation rates are not always deduced, caution is recommended when estimating biodegradation rates if the conservative tracer has a double peak.

5.6. **Conclusions**

This study has evaluated the performance of a simple organic tracer to assess *in situ* biodegradation potential in unconsolidated aquifer sediment in a controlled laboratory experiment. Physical non-equilibrium transport and naturally occurring particulate organic carbon in the porous media created a complicated system in the columns, although one that may occur in a natural setting. As a model organic tracer, acetate provided consistent estimates of biodegradation rate at varying flow rates under these non-ideal conditions. Due to relatively quick biodegradation it is suitable for use in short duration, forced gradient tracer tests in the field. However the flow rate used should be

minimised to reduce the chance of physical non-equilibrium transport occurring, especially close to the pumping well. Acetate biodegrades predominantly aerobically and quickly in the tests, but the biodegradation pathway was not simple to deduce from the data obtained in the non-ideal conditions. Alkalinity mass balance and electron balance data suggests that Mn/Fe-reduction contributed to the acetate biodegradation and that some aerobic biodegradation was supported by dissolved oxygen from an unknown source. Dissolved Mn and Fe is observed in the columns only under anaerobic conditions and then at levels lower than would be expected for acetate biodegradation.

It is recommended that alkalinity and electron acceptor concentrations are measured in the field to help deduce biodegradation pathways. The natural oxygen demand of the POC seen in these experiments is unlikely to be a present in aerobic Permo-Triassic aquifers. Therefore field test electron balances should not be adversely affected by the presence of POC as they were in this study. In anaerobic conditions where an oxygen demand may be present [Wilson et al., 2002] purging of a test zone with oxygenated water to obtain good electron balances would lead to results not being representative of aquifer conditions. Therefore the results obtained would not be appropriate to assess natural attenuation. However purging with oxygen may be appropriate if biostimulation or bioaugmentation schemes (e.g. Liebeg et al. [1999] and Salanitro et al. [2000]) were being tested.

To identify sources of uncertainty in the results and process-understanding it is suggested that repeat experiments are performed with well sorted medium to coarse grained sand. This may help eliminate the physical non-equilibrium transport in the columns if this feature is related to the fine grained material creating less mobile zones, and make tracer concentrations easier to interpret for biodegradation. Also no diffusion of oxygen would occur between mobile and immobile zones which have perhaps complicated dissolved oxygen levels in this study. Experiments could also be performed with varying amount of POC to further characterise its effect on oxygen concentrations during biodegradation of acetate or other carbon sources.

6. Trichlorofluoroethene as a hydrophobic tracer to measure aquifer sorption potential

6.1. Abstract

Sorption of organic contaminants to aquifer solids is a key natural attenuation mechanism in groundwater. It affects natural and engineered biodegradation rates by controlling bioavailability. Trichlorofluoroethene (TCFE), a dense non-aqueous phase liquid and a structural analogue of tetrachloroethene (PCE), was evaluated as a partitioning tracer to measure the bulk sorption potential of aquifer sediments in forced gradient tracer tests. TCFE sorption onto natural organic carbon present in a typical aquifer sediment was evaluated using column tests with an aeolian sand. This sand was amended with varying amounts of activated charcoal to assess TCFE sorption behaviour in detail using batch tests. Thus TCFE sorption was quantified onto naturally occurring organic carbon and black carbon. To improve overall understanding of its fate in groundwater, aqueous solubility, octanol-water partitioning coefficient, and the Henry's constant of TCFE were also measured. TCFE rapidly reached a solubility limit of ~521 mg/L, indicating that tracer solutions can be readily prepared for field-scale tests. The compound has a good dynamic analytical detection range by gas chromatography, using an electron capture detector, which allows quantification of the tracer at low µg/L concentrations in field tests. Due to its moderately high dimensionless Henry's constant (1.32), care is needed during preparation of tracer stock, sampling and analysis to prevent volatile loss. A log octanol-water partitioning coefficient of 2.27 was measured, indicating moderate affinity to organic carbon. Sorption in batch tests followed a Freundlich isotherm, increased linearly with carbon concentration in the sediment and showed some variation with ionic strength. TCFE sorption was approximately two orders of magnitude greater on the black carbon compared with natural organic carbon. Results suggest that TCFE is a suitable reactive tracer to quantify the fraction of organic carbon in natural aquifers for natural attenuation assessment and remediation design. It may also be used to estimate the sorption distribution coefficient of trichloroethene (TCE) and PCE at sites contaminated by these compounds.

6.2. **Background**

Dissolved organic chemicals are common pollutants that can be detrimental to human health and the environment [Ritter et al., 2002]. There has been significant research on the behaviour of organic chemicals in *ex situ* laboratory environments [Schwarzenbach, 1993]. However the behaviour of organic pollutants in aquifers cannot be as easily predicted. The performance of both natural attenuation and engineered treatment is influenced by the affinity of a contaminant for the aquifer solids. Sorption, particularly to natural organic carbon, reduces the bioavailability of organic contaminants [Zhang et al., 1998; Liu et al., 2007], as well as retarding their migration. As such, obtaining field-scale estimates of bulk sorption potential for organic chemicals to aquifer solids can be useful in natural attenuation assessments or remedial system design. A well-accepted approach links the sediment fraction of particulate organic carbon (f_{oc}) to the sorption distribution coefficient and the retardation factor of the contaminant relative to a conservative tracer through semi-empirical relationships [Wilson, 1998]:

$$f_{oc} = \frac{K_d}{K_{oc}} \quad \text{, where } \log K_{oc} = a(\log K_{ow}) + b \tag{6.1}$$

$$R = 1 + \frac{p_b}{\Theta} * K_d \tag{6.2}$$

where K_d is the sorption distribution coefficient, K_{oc} is the partitioning constant onto organic carbon, K_{ow} is the octanol-water partitioning coefficient, R is the retardation factor of the contaminant, p_b is the bulk density of the sorbent, Θ is the porosity of the sorbent, and a and b are empirical constants. R is equal to the breakthrough time of the contaminant at a given point divided by the theoretical breakthrough time of a conservative tracer at the same point.

Variation in the magnitude of sorption of organic chemicals with type of particulate organic carbon has been widely reported [Grathwohl, 1990; Allen-King et al., 2002; Kleineidam et al., 2002; Accardi-Dey and Gschwend, 2003; Jeong et al., 2008]. As such, errors may occur when estimating the sorption of organic chemicals using measurements of aquifer f_{oc} and published K_{oc} values. Sorption of organic chemicals tends to increase as the number of surface hydrophilic functional groups decreases, and sorption tends to be

greater on particulate black carbon than amorphous organic carbon, often dominating the sorption properties of the sediment [Accardi-Dey and Gschwend, 2003; Choung and Allen-King, 2010]. In general K_{oc} can vary over orders of magnitude depending on type of carbon present. This suggests that sorption of organic chemicals may be more reliably quantified using tracer tests or batch studies, rather than relying on f_{oc} measurements and semi-empirical relationships. A good hydrophobic partitioning tracer would ideally exhibit measurable but not excessive sorption to organic carbon, moderate to high solubility, low volatility for easier handling and resist biodegradation. Ease of analysis and high analytical sensitivity are also of practical importance for on site analysis and/or wide application.

Different organic compounds have been considered for use as hydrophobic organic tracers. Light alkanes such as methane, ethane and propane are weakly hydrophobic and have been used for organic/ soil sorption tests [Wilson, 1998]. Dodecane also has suitable hydrophobic properties [Pennell et al., 1993], but like the light alkanes is volatile [Nye et al., 1994] and highly susceptible to aerobic biodegradation. Similarly, some simple alcohols sorb to soil particulate organic carbon, but readily biodegrade at concentrations less than 2 % w/vol [Whittenbury et al., 1970]. Even if tracer concentrations were increased to levels that would inhibit microorganisms, biodegradation would still affect the dispersed tail of tracer breakthrough, shifting the centre of mass and therefore impacting the estimate of retardation and thus sorption.

Phenol and perfluorinated surfactants both have a K_{ow} value that would be useful for organic tracers in low carbon or clayey aquifers [Higgins and Luthy, 2006; Rawajfih and Nsour, 2006], but are considered toxic organic contaminants [Giesy and Kannan, 2002; Antizar-Ladislao and Galil, 2004]. Phenol also biodegrades easily at low to moderate concentration [Rawajfih and Nsour, 2006]. Conversely, perfluorinated surfactants are not easily biodegraded [Giesy and Kannan, 2002], and may be potential candidates as organic tracers at low applied concentration, assuming regulatory permits could be obtained. However, low operating concentrations reduces the dynamic detection range, reducing the accuracy of tests.

Alkyl ethoxylates are chain hydrocarbons which exhibit an increase in sorption partitioning coefficient with increasing chain length in sediment with high organic carbon content [Kiewiet et al., 1996]. Studies have also suggested that adsorption is proportional to either percentage clay content [Cano and Dorn, 1996] or the amount of montmorillonite and vermiculite [Yuan and Jafvert, 1997], suggesting hydrogen bonding as a sorption mechanism. Cano and Dorn [1996] found that sorption decreased with increasing chain length, but they only used two different molecules. Yuan and Jafvert [1997] saw an increase of adsorption with chain length. There was no relationship with CEC, f_{oc}, pH or clay content, but this could reflect the narrow range of sediments tested. Alkyl ethoxylates may also biodegrade; therefore care needs to be taken with interpretation. A complicated analytical procedure makes the use of alkyl ethoxylates unsuitable for common use [Kiewiet et al., 1995]. Analysis is much simpler if the tracer is radiocarbon-labelled [Cano and Dorn, 1996], but this may be expensive and difficult to source.

Trichlorofluoroethene (TCFE) is a dense non-aqueous phase liquid (DNAPL) that, in dissolved form, has been used as a tracer to evaluate the dechlorination of trichloroethene (TCE) in contaminated water [Hageman et al., 2001]. TCFE sorption was observed, with a computed log organic matter partitioning coefficient of 2.7. Also, there was a lag of up to ~50 days prior to TCFE biodegradation under anaerobic conditions, sufficient time for a typical forced gradient tracer test to be performed. However, in laboratory tests TCFE degradation has been quicker [Field et al., 2005], and therefore degradation over short timescales cannot be assumed to be negligible. Its high volatility must also be considered in tracer experiments. TCFE analysis is possible using the same methods as for common chlorinated ethene contaminants [Vancheeswaran et al., 1999; Hageman et al., 2001; Pon and Semprini, 2004].

In this study, the suitability and practicability of using TCFE to quantify the fraction of organic carbon in aquifers was explored. Sediment with natural organic carbon was amended with particulate black carbon (activated charcoal) to evaluate sorption and

estimate potential retardation factors. Activated charcoal is a very strong sorbent for organic chemicals [Kleineidam et al., 2002], and as supplied in powder form is easy to mix with sediments. Batch tests were used to quantify TCFE sorption to black carbon. Column studies with unamended media were undertaken to measure TCFE retardation due to sorption to natural carbon. TCFE has the added benefit that it is a structural analogue of tetrachloroethene (PCE). Characterising TCFE transport behaviour may improve understanding of PCE and TCE sorption at contaminated sites, and perhaps those not yet contaminated but at risk.

6.3. **Methods**

6.3.1. **Materials**

TCFE was obtained from Apollo Scientific Ltd., Cheshire, UK. Stock solutions were prepared from the supplied chemical in methanol to a concentration of approximately 1250 mg/l. All other chemicals used were AnalaR grade or equivalent and obtained from Fischer Scientific or VWR.

General purpose grade activated charcoal supplied in powder form with an average particle size <38 µm was obtained from Fischer Scientific. Sand for the column and batch experiments was obtained from the Builders Centre (Sheffield) Ltd. This is a Permo-Triassic desert sand from Carlton Forest Quarry, Worksop. XRD analysis on a bulk sample showed that it is composed of mainly quartz with accessory calcite and aluminium oxides. There are also iron oxide coatings on the grains. Fine grained clay minerals are present in small amounts, but their characterisation was not considered important for this experiment. The particulate organic carbon content of the sand was measured as 0.023 ± 0.003 wt%, using the Walkley-Black method [van Reeuwijk, 1992]. Grain size analysis showed that the sand was very poorly sorted and 40 % of the mass used has a grain size <250 µm. Particles >1.18 mm in size were removed by sieving, to ensure consistency in packing. The sand was chosen to represent a typical red sandstone aquifer in the U.K. [Kimblin, 1995].

Clean silica sand used in the batch experiments was obtained from Filterzand Wessem (U.K) Ltd. This sand has CEC of 0.16 meq/100g and 0.0073 % organic carbon [Thornton et al., 2001]. Grain size analysis shows 25.4 % has a grain size <250 µm, and that it is better sorted than the desert sand.

6.3.2. **Chemical Analysis**

6.3.2.1. **Gas chromatograph Method**

A Clarus 500 gas chromatograph with an electron capture detector (GC-ECD) and a 25320-U fused silica capillary column (30 m x 0.53 mm x 3.0 µm film thickness, Supelco) was used to analyse dissolved TCFE in the experiments.

A 1 ml aliquot of water was withdrawn from each sample vial and transferred to 2ml gas chromatography vials. The vials were immediately sealed with silicone/PTFE septa and 1,1 dichloroethene was added as an internal standard at 5 mg/l (5 µl of a 1000 mg/l methanolic stock). Samples were shaken for 1 minute and allowed to sit for 1 minute to equilibrate. Analysis was by manual injection of a 10 µl aliquot of headspace gas using a 25 µl gas-tight syringe. The lower detection limit for the procedure was 0.01 mg/l. An analytical error of ± 10 % was mostly caused by the manual injection procedure. Sample analysis was repeated if unexpected values were obtained.

Table 6-1: Oven run program for TCFE analysis on the GC-ECD, with a total run time of 25 minutes including reset time

Oven Ramp	Rate (ºC/min)	End temperature (ºC)	Hold (min)
Initial	0	50	4
1	10	120	0
2	40	210	8

The instrument set-up parameters for the TCFE analysis are shown in Table 6-1. TCFE and the internal standard came off during the first oven ramp, while the second oven ramp helped remove impurities in the column. The time between samples was 25 minutes. An injection split ratio of 15 was used. The temperature of the ECD detector was 376 ºC, with laboratory air being used at 30.0 ml/min. An example calibration is shown in Figure 6-1. Calibration standards were made up from 1250 mg/l and 125 mg/l

methylated stock solutions, in 70 ml hypovials. Synthetic groundwater, with a composition similar to that at a Permo-Triassic sandstone site in the UK (Table 6-2), was added so as to nearly fill each hypovial. The synthetic groundwater was made to match the cation composition of the SiREN site groundwater as a priority, since cation exchange tests were performed first (see Chapter 4). The high sodium concentration in the native groundwater was reduced for the synthetic groundwater. The high alkalinity in the native groundwater was reduced in the synthetic groundwater to identify small variations in chemistry for column tests (Chapter 4 and 5). After each hypovial was filled with synthetic groundwater the required amount (7 µl to 70 µl) of methylated stock solution was added. The hypovials were then sealed with aluminium crimp top caps fitted with butyl rubber/PTFE septa. Hypovials were weighed to check the correct amount of stock solution had been added. New standards were made for each calibration and for each experimental run a quality control was made using the same method. Samples were diluted with synthetic groundwater to fit in the calibration range, which may have added error to measured values. The split ratio could be decreased to measure lower concentrations.

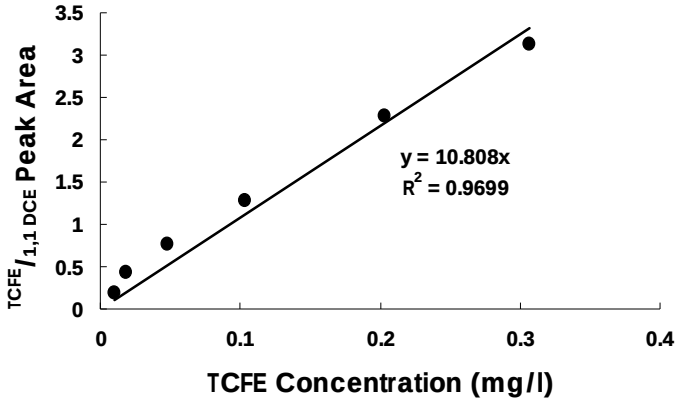

Figure 6-1: Example calibration of TCFE on GC-ECD with manual injection

Table 6-2: Chemical composition (values in mg/l) of groundwater from the UK Permo-Triassic sandstone aquifer at the SiREN site and synthetic groundwater used in experiments.

Ion	UK Permo-Triassic aquifer at the SiREN site	Synthetic groundwater
Ca^{2+}	61.7	61.7
K^{+}	20.1	20.1
Mg^{2+}	12.0	12.0
Na^{+}	109	23.0
Cl^{-}	35.8	162.4
SO_4^{2-}	37.1	47.5

6.3.2.2. **Ion Chromatograph Method**

Inorganic tracer and background ions in the synthetic groundwater were analysed on a Dionex DX-120 Ion Chromatograph. A RFIC^{TM} Ionpac$^{®}$ A514A 4 x 250 mm analytical column was used for anion analysis with an eluent of 8 mM Na_2CO_3 and 1 mM $NaHCO_3$. Cations were analysed on a RFIC^{TM} Ionpac$^{®}$ C512A 4 x 250 mm analytical column with an eluent of 20 mM methane sulphonic acid. The lower limit of detection was 0.6 mg/l for Br and 0.125 mg/l for Na, with a 10 µl sample loop. Analytical error was ± 2 % for anions and ± 4 % for cations.

6.3.3. **Batch Experiments**

All batch experiments were performed in 70 ml glass hypovials. Unless otherwise stated the activated charcoal powder was mixed with the Permo-Triassic sand at a ratio of 1:999. Five grams of the charcoal/sand media was mixed in 70 ml glass hypovials with 60 ml of synthetic groundwater**.** Triplicates were prepared for each sample and left to saturate overnight. The hypovials were then topped up with synthetic groundwater before adding the required amount of TCFE stock. The hypovials were then sealed with crimp top caps, the same as used for the calibration standards. Batches were left to equilibrate for at least 24 hours on a roller shaker at 60 rpm before sampling. This was decided as a suitable time to run experiments after a test had been performed to assess how long sorption took to reach equilibrium (see below). Quality control measures included system blanks (activated charcoal mix and synthetic groundwater) and matrix spikes (synthetic groundwater and TCFE).

Experiments were undertaken to estimate the time to reach sorption equilibrium, quantify sorption of TCFE in charcoal-amended sand mixes, and evaluate the effect of TCFE solution concentration and different ionic strength on sorption. In the equilibrium time experiment, samples were taken at 1, 4, 8, 24, 72 and 168 hours. Activated charcoal/sand mixes were tested at 0, 0.01, 0.05, 0.1, 0.2, 0.5 and 1% charcoal by mass and a TCFE concentration of 1 mg/l. These same activated charcoal/sand blends were also tested using the silica sand to investigate whether the Fe oxide grain coatings on the Permo-Triassic sand or its organic carbon content significantly affected TCFE sorption. TCFE sorption isotherms were deduced using a variable TCFE concentration and fixed % carbon in the charcoal/sand mix. TCFE was added such that the starting concentration in the vials was 0.1, 0.2, 0.5, 1, 2, 5 and 10 mg/l, with a 0.1% activated charcoal/sand mix. It is standard practice to include a conservative tracer with sorbing tracers to directly resolve retardation factors. The most common conservative tracers such as bromide or chloride, added as salts. Due to typically high detection limits, such salts are often used at concentrations ranging from 100s to 1000s of mg/l, which increases the ionic strength of the tracer water and may affect TCFE sorption [Cheng and Reinhard, 2006]. High salt concentrations may also result in density effects in the injected water [Schincariol and Schwartz, 1990]. To evaluate any potential adverse effects over a wide range of ionic strength, NaBr was added to synthetic groundwater to produce concentrations of 0, 103, 1029, 5145 and 10289 mg/l, with TCFE at 1 mg/l and 0.1 % charcoal in the charcoal/sand mix. A measurement in UHQ water was also performed. The amount of activated charcoal/sand mix was chosen to achieve measurable TCFE sorption.

6.3.4. **Solubility, Octanol-Water and Henry's Constant Tests**

Solubility tests were undertaken to help design the octanol-water experiments for TCFE and to assess the ease of dissolution. As a first approximation, a solubility of 944.9 mg/l was estimated using the structurally estimated K_{ow} value (see below) and the empirical equation 2-2 of Lyman et al [1990]: ;

$$LogS = 1.37 LogK_{ow} + 7.26 \qquad (6.3)$$

This equation had the lowest error value for TCE, which has a similar structure to TCFE, therefore was chosen to estimate the TCFE value. Pure TCFE was added to 10 ml

hypovials containing UHQ water to give a three fold excess of TCFE relative to the estimated solubility [Bowman and Sans, 1983]. Approximately 1 mg of Sudan IV dye was added to each hypovial. Sudan IV is insoluble in water but soluble in organic liquids, resulting in red dyed TCFE non aqueous phase liquid (NAPL). Therefore it was used as an indicator to check that NAPL was always present during the test. The hypovials were sealed with crimp top caps fitted with butyl rubber/PTFE seals and left at room temperature on a roller shaker at 60 rpm. The hypovials were taken off the shaker a day before sampling so that the dense TCFE NAPL fell to the bottom and reduced the risk of accidentally entraining NAPL in the aqueous sample taken for analysis.

Octanol-water partitioning tests were performed in 21ml hypovials. A ~200 mg/l aqueous TCFE stock was made up in 70 ml hypovials for each batch of tests, by adding TCFE NAPL directly to UHQ water. From the solubility tests it was found that the required amount of NAPL would quickly dissolve in water. This ensured the system was not complicated by the presence of methanol from the stock solution that was used in the batch experiments and minimised volatile loss in the stock solutions. Approximately 4 ml of octanol was first added to a vial, followed by UHQ water and an aliquot of the TCFE aqueous stock to achieve total TCFE concentrations of 5, 10, 15, 20, and 30 mg/l, in triplicate vials. Care was taken to avoid producing emulsions. Vials were then capped headspace-free with crimp tops and butyl rubber/PTFE seals. A sample of the stock solution was taken before the first and after the last hypovial was set up, to correct for any losses via volatilisation. The vials were inverted to prevent diffusion through the septa and put on an orbital shaker at 20-40 rpm for 1 day. The estimated log K_{ow} of TCFE from structural group contributions is 2.525 [Schwarzenbach, 1993], far less than 5 recommended as the upper limit for the simple shake study used here. Vials were discounted if a water/octanol emulsion had formed.

To estimate a Henry's constant for TCFE the aqueous concentration was measured in capped 70 ml hypovials before and after removing 20, 40 or 50 ml of UHQ water. Testing of a greater range was limited by instrument breakdown. The initial water concentration in vials was ~0.4 mg/l. Air was allowed into the vials via a needle in the

septa during water removal to allow pressure equilibration. Hypovials were shaken for 1 minute before re-measuring. The water concentration before ($C_{i,W}$) and after (C_W) water removal was measured and the gas concentration (C_G) was estimated from the mass balance equation:

$$C_{W,i}V_W = C_W V_W + C_G V_G \quad (6.4)$$

where, V_W and V_G are the volume of water and the volume of gas after water removal respectively. Therefore Henry's constant could be estimated.

6.3.5. **Column Experiments**

Column tests were performed in 0.75 m long uPVC columns, with an internal diameter of 0.053 m. A further explanation of the columns is in Chapter 4. Tedlar bags were used to store the input solution and soft tubing was avoided to minimise TCFE loss by adsorption upstream of the column. The sampling bags were filled with synthetic groundwater and conservative tracer (NaBr) solution, then injected with TCFE methanolic stock and thoroughly mixed just before the start of the experiment. The input TCFE concentration was 0.6 mg/l and bromide was 90 mg/l as NaBr.

The columns were subject to tracer-tagged water injection at a flow rate of 2.6 ml/min, which corresponds to 0.225 pore volumes an hour. The resulting average linear water velocity of ~0.17 m/hr is similar to published forced-gradient tests [Ptak and Schmid, 1996; Istok et al., 1997]. Samples were collected from T-fittings connected to the column outlet port, directly into a plastic syringe to minimise air contact. Samples were immediately transferred to 10 ml crimp top glass vials (no headspace) and stored upside down at -10°C until analysed.

A column containing 1-1.4 mm silicon beads was used as a control to determine any sorption of TCFE onto the column apparatus. Batch tests were also performed with these silica beads for the same reason. Tests were then performed with the Permo-Triassic sand (no charcoal added).

6.4. **Results and Modelling**

6.4.1. **Sorption equilibration time**

Figure 6-2 shows that TCFE partitioning between the aqueous phase and Permo-Triassic sand media with 0.1 % activated charcoal quickly reached equilibrium. There was no significant decrease in TCFE concentration in the matrix spikes (controls), showing that the decrease is not due to diffusion through the septa. Steady TCFE concentrations in sample batches and matrix spikes also suggest no TCFE biodegradation. Less than <0.01 mg/l TCFE was measured in all system blanks, indicating minimal cross-contamination over the experimental and measurement process. The averaged sorbed mass over the entire experiment was 0.004 ± 0.0005 mg TCFE per g of sediment. Variation between samples and triplicates may be due to analytical error from manual injection, incomplete mixing in the sand/charcoal mix and slight differences in the small amount of TCFE stock added to the batches. The rapid achievement of an equilibrium concentration suggests that TCFE sorbed to the surface of the activated charcoal particles, and that diffusion-controlled intra-granular transport and subsequent sorption was not important [Nguyen and Ball, 2006; Pignatello et al., 2006; Nguyen et al., 2007]. This would have been evident as a slow decrease in TCFE solution concentration in batch tests over time.

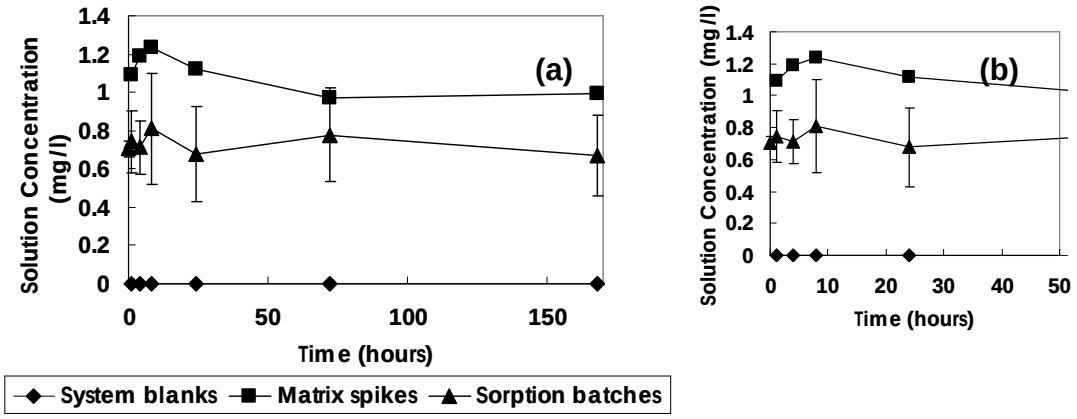

Figure 6-2: Distribution and temporal history of a 1 mg/l addition of TCFE into Permo-Triassic sand with 0.1% activated charcoal (sorption batches). System blanks have no TCFE added and matrix spikes (controls) have no sand or charcoal added. (a) whole experiment, (b) shows detail of early behaviour.

6.4.2. **Isotherm Modelling**

TCFE concentrations ranging from 0.1 to 10 mg/l were added to the hypovials containing the sand/0.1 % activated charcoal mix to estimate TCFE sorption parameters. The decrease in TCFE aqueous concentration was assumed to result from sorption, presumably to the activated charcoal in the mixture.

A non-linear sorption isotherm was obtained, and therefore Freundlich and Langmuir models were used to estimate TCFE sorption parameters (Figure 6-3). This tested whether TCFE sorption was limited by the number of sorption sites available. For both plots error is generated from variation between triplicates. The large x-axis error bar for the point ~30 l/mg on the Langmuir isotherm plot is due to variation at very low concentrations. Error may originate from differences in the amount of charcoal or TCFE added to the batch or analytical error.

The superior fit of the Freundlich isotherm suggests that saturation of TCFE on the sorbing surface was not close to being reached. For the Freundlich isotherm equation:

$$C_{sorb} = KC_{sol}^{\ n} \qquad (6.5)$$

where C_{sorb} is the sorbed concentration and C_{sol} is the solution concentration. The constant K equals 4.63×10^{-3} (mg/g)/((mg/l)^n) and the constant n equals 0.495 (mg/g)/(log mg/l). This approximates to a log sorption distribution coefficient to activated charcoal of 4.6. If it is assumed sorption is wholly hydrophobic and linked only to activated charcoal, then at a solution concentration of 1 mg/l, this gives an estimated TCFE retardation factor of 9.9 for 0.023 % carbon (the same as the Permo–Triassic sand) and a retardation factor of 39.6 for 0.1 % carbon. For the Langmuir sorption isotherm equation:

$$C_{sorb} = \frac{Q^0 KC_{sol}}{1 + KC_{sol}} \qquad (6.6)$$

where Q^O is the maximum sorption capacity, the data is plotted as the double reciprocal or the Lineweaver-Burke equation:

$$\frac{1}{C_{sorb}} = \frac{1}{KQ^0} x \frac{1}{C_{sol}} + \frac{1}{Q^0} \qquad (6.7)$$

A Q^O of $5.62x10^{-3}$ mg/g and K of 4.98/mg is obtained. At a solution concentration of 1 mg/l this gives a TCFE retardation factor estimate of 10.0 for 0.023% carbon and a retardation factor of 40.0 for 0.1% carbon. However, it is clear in Figure 6-3 that the data do not follow a Langmuir curve, so this value is likely a slight overestimate.

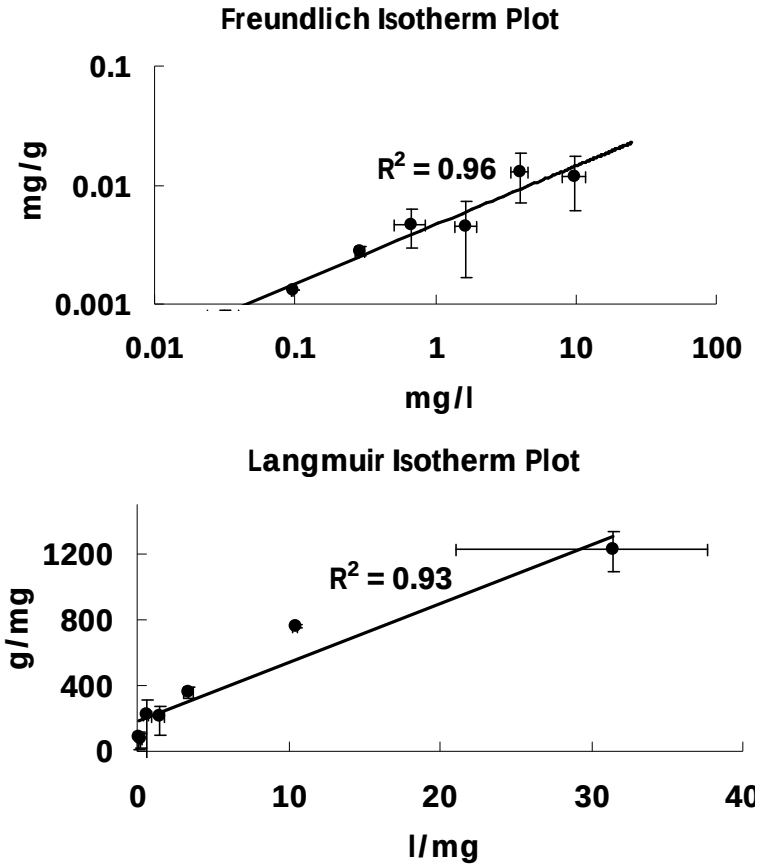

Figure 6-3: Freundlich and Langmuir isotherm plots for 0.1% activated charcoal in Permo-Triassic sand mix. Adsorbed TCFE concentrations are plotted on the y-axis and solution concentration on the x-axis.

6.4.3. **Variation of TCFE sorption with activated charcoal concentration**

There is a linear increase of TCFE adsorption per g sediment as the percentage of activated charcoal increases (Figure 6-4). TCFE has a small residual electronegativity arising from the carbon-fluorine bond, which has a slightly higher negativity than the carbon-chloride bonds. Nevertheless this small charge is unlikely to cause significant adsorption to acidic or basic surface groups [Schwarzenbach, 1993] on the surface of the activated charcoal [Tsutsumi et al., 1993; Stavropoulos et al., 2008]. It is therefore

assumed that sorption in this case is dominated by the hydrophobic surfaces. The moderate-strong hydrophobic tendency of TCFE is evident in the octanol-water partitioning test (see below).

The trend lines in Figure 6-4 are not parallel and tend to zero at low activated charcoal concentrations. This indicates that there is no sorption to the native sand. In turn this shows that the higher organic carbon content of the Permo-Triassic sand or the presence of iron oxide coatings on it did not significantly increase sorption of TCFE. At the higher activated charcoal concentrations silica sand values are within triplicate error Permo-Triassic sand values, supporting this interpretation. Also, a paired student t-test showed that, at a 95 % confidence level, the sorption onto the Permo-Triassic sand/activated charcoal and silica sand/activated charcoal mixes is the same.

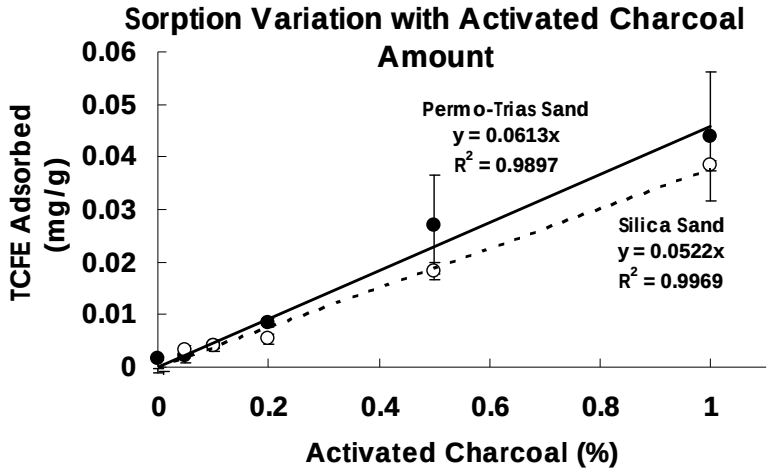

Figure 6-4: Sorption of TCFE on activated charcoal-amended Permo-Triassic sand and charcoal-amended silica sand, with varying amounts of activate charcoal by % mass.

6.4.4. Variation of TCFE sorption with ionic strength

There was a general decrease in TCFE sorption with increasing ionic strength, but without a clear trend (Figure 6-5). The ionic strength was calculated from the measured total ion concentrations and Debye-Hückel theory [Appelo and Postma, 2005], using the equation:

$$I = \tfrac{1}{2} \sum m_i z_i^2 \qquad (6.8)$$

where I is ionic strength, m_i is the molality of ion i and z_i is the charge of the ion. The UHQ water experimental point had an ionic strength of ~0.001 M, implying some

leaching of water soluble ions present on the activated charcoal/sand mix. These ions included Cl^-, PO_4^{3-}, SO_4^{2-}, Na^+, Mg^{2+}, K^+ and Ca^{2+}. Displacement of these ions did not increase at higher ionic strength. At increasing ionic strength Br^- and Na^+ were desorbed from the charcoal/sand mix when TCFE was added (Figure 6-6). The "sediment-salt" batches represent the activated charcoal/sand mix equilibrated with the salt solution (minus TCFE). For the "sediment-salt-TCFE" batches 1 mg/l of TCFE was added, after the activated charcoal/sand mix had equilibrated with the salt solution for a day. Therefore "sediment-salt-TCFE" minus "sediment-salt" aqueous concentrations of ions represents the ions desorbed when TCFE was added. The "sediment-salt" concentrations were within 10 % of the "sediment-salt-TCFE" concentrations at high ionic strengths and samples had to be heavily diluted for analysis. Therefore triplicate variation lead to an increase of y-axis error with ionic strength in Figure 6-6, and is the cause of the very large error at ~0.6 M ionic strength. The results imply that TCFE may interact with inorganic ions for sorption sites. The presence of cations on hydrophobic surfaces has been shown to reduce sorption of organic chemicals [Cheng and Reinhard, 2006] and sorbed organics may block micropores preventing the sorption of ions [Pignatello et al., 2006]. Alternatively varying ionic strength may affect TCFE solubility and related analysis. Higher salt concentrations will decrease TCFE solubility and increase the amount of TCFE in the headspace of the sample vial [Peng and Wan, 1998], leading to an underestimation of sorption. However, this would not explain the Br^- and Na^+ results. There may have been less variability in TCFE sorption if individual calibrations were performed at each ionic strength. Greater variation is seen in the TCFE and ion data above 0.02 M ionic strength (1029 mg/l NaBr added). Therefore it is recommended that ion tracer concentrations are kept below ~ 1000 mg/l when performing tracer tests with TCFE.

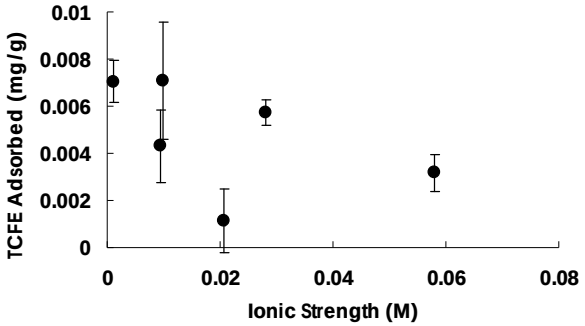

Figure 6-5: TCFE adsorbed onto 0.1 % activated charcoal/sand mix at different ionic strengths, when TCFE was added at 1.7 mg/l.

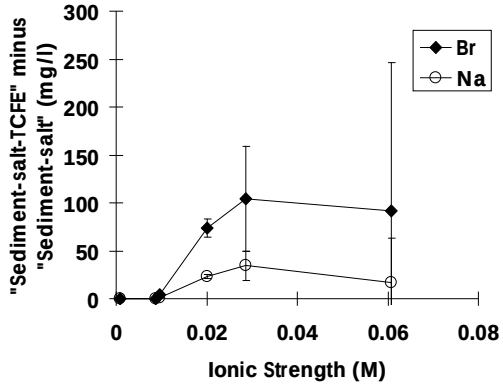

Figure 6-6: Desorption of Br^- and Na from 0.1% activated charcoal/sand mix at different ionic strengths, when TCFE was added at 1.7 mg/l.

6.4.5. Solubility, Henry's Constant Tests and Octanol-Water

In the solubility experiment, the aqueous TCFE concentration measured 24 hours after the TCFE NAPL was added to the hypovial, was 487.9 ± 47.7 mg/l. The TCFE concentration remained relatively constant over the next 28 days (Figure 6-7). An average TCFE concentration of 521.1 ± 54.3 mg/l was measured, which is assumed to be the TCFE solubility as NAPL was still present in the vials. The amount of TCFE NAPL present in the hypovials decreased during the monitoring period, presumably due to diffusion of NAPL through the septa, after sorbing onto it, driven by a high concentration gradient. The measured solubility is between reported values for TCE (~1400 mg/l) and PCE (~300 mg/l) at room temperature [Knauss et al., 2000]. TCFE concentrations were close to saturation after 24 hours and when added to the hypovials, the NAPL formed a film on the bottom of the vials. Tests using a goniometer gave a TCFE contact angle in UHQ water on quartz of 115˚ (angle between the quartz/water and the water/TCFE interface), indicating it was mildly wetting. The increased surface area of the TCFE

NAPL results in rapid mass transfer to the aqueous phase and attainment of solubility. The data shows that TCFE solutions for field tracer test injection can be prepared quickly.

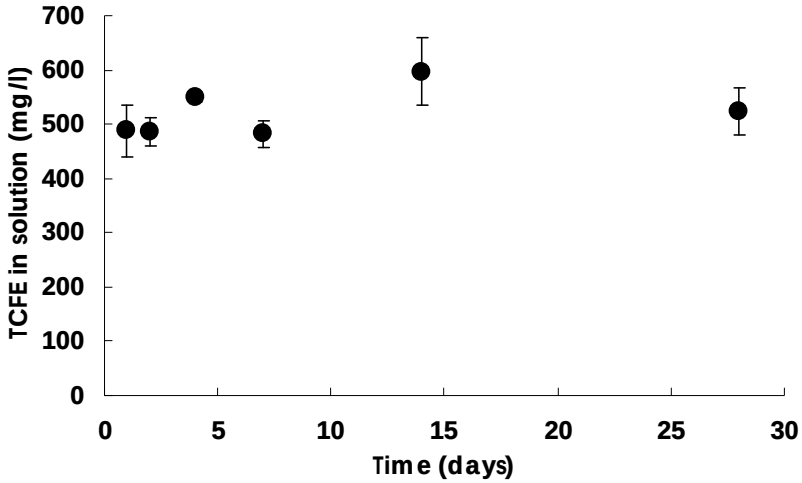

Figure 6-7: TCFE concentrations in aqueous solution over time under presence of TCFE NAPL.

Figure 6-8 shows the data from the TCFE octanol-water partitioning experiment. Data points were considered individually rather than triplicate averages, as 7 of 21 points had to be discounted due to the formation of water-octanol emulsions. A log K_{ow} of 2.27 (R^2 = 0.93) for TCFE was estimated by linear regression of the data. This compares well with the value of 2.53 estimated from the TCFE structure [Schwarzenbach, 1993]. The experimental value is similar to that reported for TCE (~2.29) [Schwarzenbach et al., 1983]and less than that for PCE (2.53-2.88) [Karickhoff, 1981; Schwarzenbach et al., 1983; Schwarzenbach and Westall, 1985]. Log K_{oc} can be estimated from log K_{ow} using empirical relationships. Xia and Ball [1999] obtained the following equation for the sorption behaviour of non-polar organic chemicals on natural sorbents:

$$LogK_{oc} = 1.10LogK_{ow} - 0.99 \quad (6.9)$$

The equation had an average variation of 0.31 log units from measured values. Using the TCFE log K_{ow} obtained in this study and Equation 6.9 gives a log K_{oc} for TCFE of 1.50. If the same deviation applies here as in Xia and Ball [1999] the log K_{oc} is between 1.19 and 1.81. Razzaque and Grathwohl [2008] obtained an empirical relationship with a lower average variation from measured values of 0.25, from sorption studies using sediments and soils:

$$LogK_{oc} = 0.94LogK_{ow} - 0.39 \quad (6.10)$$

Using this equation and the low K_{ow} obtained experimentally for TCFE, a log K_{oc} of 1.79 is found. Considering the average variation the experimental log K_{oc} is between 1.54 and 2.04. The K_{oc} values estimated above from Equations 6.9 and 6.10 and the measured K_{ow} are approximately three orders of magnitude less than the TCFE sorption distribution coefficient to activated charcoal (log value of 4.6), estimated from batch tests. This is probably due to the higher sorption capacity of black carbon over natural organic carbon [Accardi-Dey and Gschwend, 2003]. Values of TCFE K_{oc} derived from Equations 6.9 and 6.10 can be used to estimate the average f_{oc} in the sampled volume of a tracer test. First, the retardation of TCFE relative to the conservative tracer must be determined, along with the bulk density and porosity of the test zone. Then Equation 6.2 can be used to estimate K_d. Finally the measured K_d and the TCFE K_{oc} can be used in Equation 6.1 to estimate $f_{oc.}$ These semi-empirical relationships require the user to assume that sorption is entirely hydrophobic (i.e. a function only of the particulate organic carbon in the porous media).

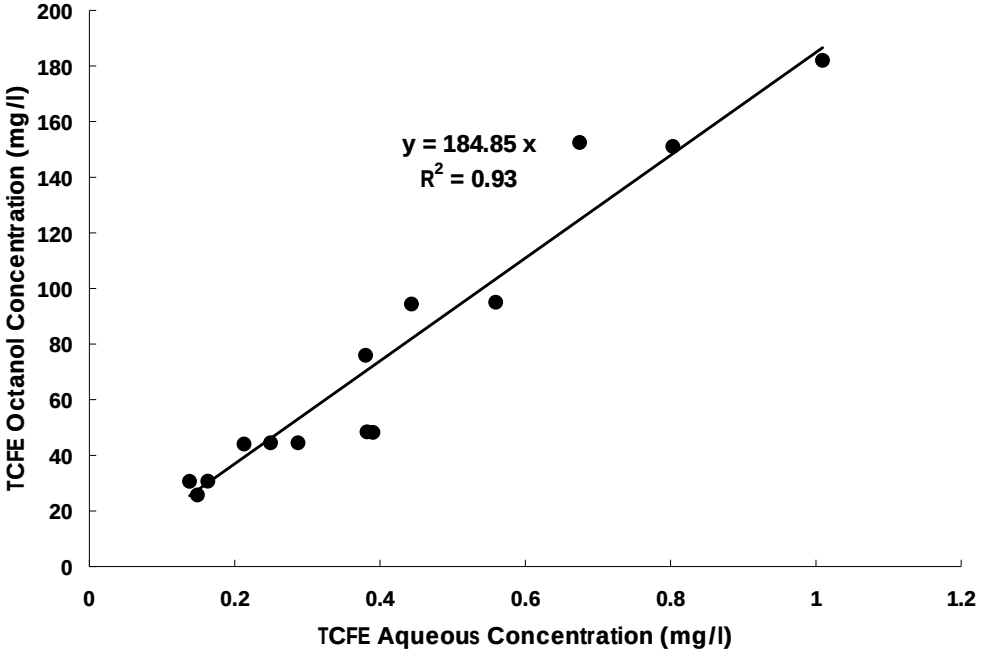

Figure 6-8: TCFE concentration plotted for octanol-water tests.

Figure 6-9 shows the data used to determine Henry's constant or TCFE. A dimensionless H_{TCFE} value of 1.32 (mg/l gas/ mg/l water) was obtained. The concentration of TCFE in the gas phase was obtained by mass balance (Equation 6.4). This is similar to the value of

1.39 cited by Vancheeswaran et al. [1999] and larger than literature values for TCE (~0.4) and PCE (0.69) at room temperature [Peng and Wan, 1997]. It implies that the high volatility of TCFE is caused by the fluorine in the structure. Many simple structure organic compounds containing fluorine have high volatility [Key et al., 1997]. This feature makes TCFE suitable for headspace analysis, but means care is needed to prevent loss during preparation, sampling and analysis. It is not very suitable for use as a tracer in the unsaturated zone.

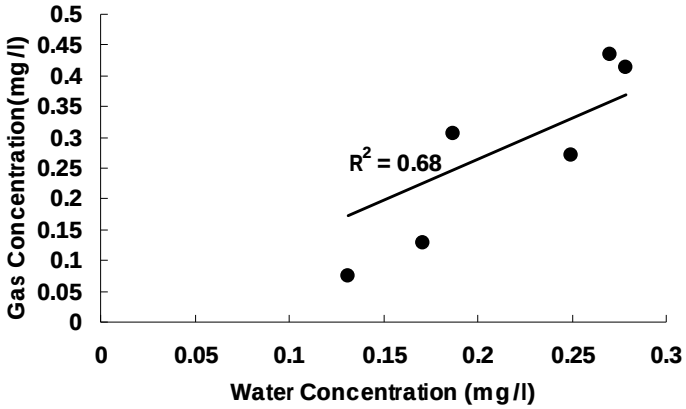

Figure 6-9: TCFE concentrations plotted for the determination of Henry's constant

6.4.6. Column Experiments

The column experiments were modelled using STANMOD, a public-domain 1-D reactive transport model [Simunek et al., 1999]. The pore water velocity was estimated by fitting the model to the Br tracer breakthrough, assumed to be conservative. The retardation factor of TCFE was estimated by inverse modelling with STANMOD, using this pore water velocity. The first column experiment was performed using clean silica beads to deduce if TCFE adsorbs to the uPVC column (see Appendix B). A TCFE retardation factor of 1.08 and K_d of 0.0160 ml/g was estimated using STANMOD. As both TCFE and Br breakthrough occurs at a relative concentration of 1.0, degradation of TCFE is unlikely. There was no sorption of TCFE onto the silica beads in the control batch tests. The slight TCFE retardation in the column experiment is presumed to arise from a small amount of sorption (2.34 mg TCFE per m^2 of uPVC surface area) to the column walls.

The breakthrough data in the Permo-Triassic sand (no activated charcoal added) column experiment was simulated well using STANMOD (Figure 6-10). Bromide is fitted with

model efficiencies [Berthouex and Brown, 2002; Bolster and Hornberger, 2007] of 98.9 and 99.8% for columns A and B respectively, while efficiencies of 98.0 and 89.9% are obtained for TCFE. A TCFE retardation factor of 1.24 and 1.39 was estimated for column A and B, respectively. These values are in between the retardation factors of TCE (1.1-1.2) and PCE (1.6-1.8) measured at the CFB Borden, Canada, sand aquifer ($\boldsymbol{f}_{oc}$ = 0.00021), by Rivett and Allen-King [2003]. When sorption competition effects were discounted in laboratory tests [Rivett and Allen-King, 2003], the retardation factor of TCE increased to 1.1-1.4, similar to the values of TCFE in this study. Accounting for the TCFE sorbed to the column walls, a TCFE K_d of 0.056 and 0.097 ml/g was estimated for the Permo-Triassic sand for columns A and B, respectively. The TCFE K_{oc} derived from the octanol-water experiments was used with column test-derived K_d values to estimate the $\boldsymbol{f}_{oc}$ present (Equation 6.1,Table 6-3). The $\boldsymbol{f}_{oc}$ estimated in this way is higher than the Walkley-Black method measured value for the sand (0.00023). Estimates of $\boldsymbol{f}_{oc}$ (Table 6-3) are closer to the measured value when the K_{oc} used (from Equation 6.7 or 6.8) is the equation-derived value plus the average variation. This suggests that the K_{oc} values derived with Equations 6.7 and 6.8 underestimate the true value for TCFE. However some of the difference may be due to error in the Walkley-Black $\boldsymbol{f}_{oc}$ value, as it close to the resolution of the method. A separate estimate of K_{oc} for TCFE can be obtained from the column data, using Equations 6.1 and 6.2. Using the column retardation factor of TCFE and $\boldsymbol{f}_{oc}$ measured by the Walkley-Black analysis gives a dimensionless log K_{oc} value of 2.39 and 2.63 for columns A and B, respectively. These correspond well with a log organic matter partitioning coefficient (which would be expected to have a similar value to K_{oc}) of 2.70 obtained by Hageman et al. [2001], using TCFE data from a push-pull field tracer test. The variability between columns may imply an uneven distribution of organic carbon in the sand. TCFE shows a similar initial breakthrough to Br and an increased dispersivity. This suggests that TCFE sorption in the column is limited by mass transfer to sorption sites [Brusseau and Rao, 1989]. This physical non-equilibrium was not seen in the batch experiments. This is probably due to a lower particle surface area in contact with water for TCFE sorption in the column tests than the batch tests, as flow is along a fraction of the total porosity. Sorption is also expected to be slower onto low organic carbon sands [Ball and Roberts, 1991] than activated charcoal.

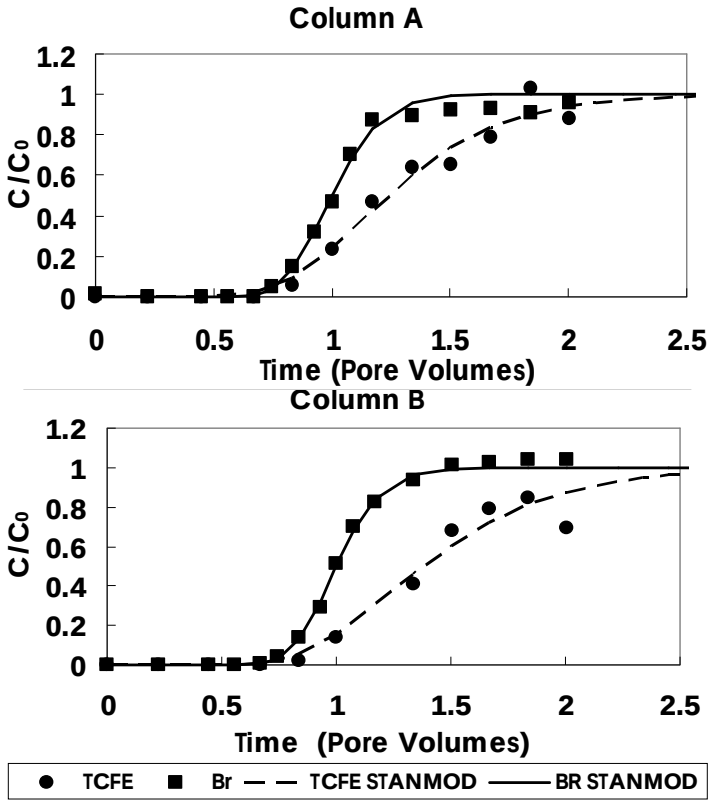

Figure 6-10: Solute breakthrough for TCFE and Br in columns of Permo-Triassic sand. Solute concentration is normalised to input concentration (C/C_0). Time is normalised to residence time of 1 pore volume in the column.

Table 6-3: Estimated f_{oc} in columns. Values calculated from TCFE retardation in column experiments and K_{oc} values derived from Equations 6.7 [Xia and Ball, 1999] and 6.8 [Razzaque and Grathwohl, 2008]. Eqn K_{oc} = value estimated from equation K_{oc}, min K_{oc} = value estimated from equation K_{oc} minus average variation, max K_{oc} = value estimated from equation K_{oc} plus average variation.

	Xia and Ball [1999]			Razzaque and Grathwohl [2008]		
	min K_{oc}	eqn K_{oc}	max K_{oc}	min K_{oc}	eqn K_{oc}	max K_{oc}
Column A	0.00358	0.00175	0.00086	0.00161	0.00091	0.00051
Column B	0.00624	0.00306	0.00150	0.00280	0.00158	0.00089

6.5. **Discussion**

An important technical and practical issue is whether TCFE can be used effectively as a partitioning tracer at field-scale to estimate the potential for sorption of hydrophobic organic chemicals to aquifers. TCFE quickly dissolved at high concentration to give a solubility of ~521 mg/l. This shows a saturated TCFE solution could be prepared within 24 hours, and at a sufficiently high concentration that large volume injections at ~ 1-5 mg/l would be possible by spiking TCFE from a saturated reservoir into an injection flow

using a peristaltic pump and in-line mixer. TCFE was found to be moderately volatile, with a dimensionless Henry's constant of 1.32, which is greater than that of TCE and PCE. This means care is required in the preparation of tracer mixtures and sample analysis to ensure high quality data. An empty column test indicated that TCFE will sorb slightly to uPVC, a common material used in the construction of groundwater monitoring well screens [Gillham and O'Hannesin, 1990]. However, this is expected to have a negligible effect on tracer test performance under steady-state conditions, due to the higher retardation of TCFE from sorption to natural or artificial carbon materials. TCFE has been shown to be easily and accurately measured by manual headspace chromatography on a GC-ECD. Measurement is also possible on GC/MS [Hageman et al., 2001; Field et al., 2005] and analytical variability would be reduced if a headspace auto-sampler were used. Using GC-ECD analysis there is a lower limit of detection of ~0.01 mg/l. This could be improved using a larger water sample size to increase TCFE mass, changing the air/water ratio in the analysis vial to focus TCFE mass in the headspace, injecting a greater headspace gas volume onto the GC-ECD and salting the aqueous sample to drive TCFE into the headspace. Therefore, if TCFE was injected at ~1 mg/l a good dynamic detection range of 3 orders of magnitude is possible. This allows concentrations to be accurately measured far along a breakthrough curve, leading to better estimates of breakthrough and mass balances.

A second issue is the specific suitability of TCFE as a tracer to estimate the retardation of organic chemicals by sorption onto particulate organic carbon in porous media. A good tracer should adsorb onto hydrophobic surfaces kinetically fast over a practical range of concentrations. Using the K_{ow} for TCFE estimated from the octanol–water partitioning tests and empirical relationships in the literature, a minimum estimate of f_{oc} (0.00051) was obtained from the Permo–Triassic sand column test data. This is an overestimate of the f_{oc} obtained using the Walkley–Black procedure (0.00023). However the TCFE log K_{oc} value of ~2.5, obtained from the column test data and Walkley-Black measured f_{oc} alone was similar to values derived from field tests [Hageman et al., 2001]. Therefore it is recommended that this value is used for field testing rather than the K_{oc} derived from the K_{ow} estimate. The retardation of TCFE relative to Br in the column tests was 1.24-1.39,

indicating that TCFE will be clearly retarded at the low f_{oc} typically found in sandy aquifers [Ball et al., 1990]. The TCFE retardation factor estimated from the Freundlich isotherm was 37.7 with 0.1 % activated charcoal in the charcoal/sand mix and 9.4 with 0.023 % activated charcoal. The higher TCFE retardation estimated from the batch tests relative to the column tests is attributed to the larger sorption capacity of black carbon over natural organic carbon [Accardi-Dey and Gschwend, 2003]. It could also reflect a higher particle surface area available for TCFE sorption in the batch tests relative to column tests where flow is along a fraction of the total porosity. If a large amount of black carbon was present in the sediment TCFE breakthrough is likely to be highly retarded. The estimated retardation factors shows that TCFE is suitable for measuring hydrophobic sorption at low concentrations of black or natural organic carbon. A forced gradient tracer test lasting a few days at most should cover the range of solute retardation predicted by the experiments.

An ideal tracer should resist degradation by biological and abiotic mechanisms. No degradation of TCFE was observed in the sorption equilibration time experiment containing the matrix spikes. There was full breakthrough (C/C_0 = 1.0) of TCFE in column experiments, suggesting TCFE does not readily biodegrade under the aerobic conditions used. The duration of these experiments was similar to that of single well forced gradient tests. TCFE may biodegrade anaerobically, via sequential dechlorination, similar to other halogenated organic chemicals [Vancheeswaran et al., 1999; Field et al., 2005]. However Hageman et al. [2001] showed in field tests that there is typically a lag phase of up to ~50 days prior to TCFE biodegradation and no dechlorination was seen in groundwater not previously exposed to TCE. Therefore it should be possible to perform a partitioning forced gradient test before the onset of TCFE biodegradation, particularly when assessing the potential for sorption of organic chemicals in aerobic aquifers or plumes where biodegradation of highly halogenated organic chemicals is not occurring.

It has been demonstrated that TCFE could be used to estimate f_{oc} in media with a low particulate organic carbon content and thus predict the retardation of important organic contaminants in groundwater (e.g. TCE and PCE). TCFE could also be used to predict the

retardation of organic contaminants in media containing low concentrations of black carbon (e.g. alluvial aquifers [Karapanagioti et al., 1999]). The structural similarity of TCFE to TCE and PCE implies that it can be used to estimate the retardation and biodegradation of these contaminants at polluted sites, to evaluate remediation strategies. A better estimate of plume retardation is likely if the test is performed in the high concentration polluted zone rather than unpolluted aquifer, as retardation will decrease at higher concentration and when TCE and PCE are both present [Rivett and Allen-King, 2003]. At non-chlorinated contaminated sites, TCFE may offer the means to quantify factors controlling contaminant bioavailability, an important aspect supporting natural attenuation and the design of bioremediation systems.

7. Discussion and synthesis, future work and conclusions

7.1. Discussion and synthesis

In this thesis, experiments and modelling were performed to assess the suitability of single well forced gradient tests to estimate conservative and reactive transport properties of aquifers. Ultraviolet imaging tests were performed in a pseudo 2-D aquifer model and were modelled with HydroGeoSphere©, a fate and transport model [Therrien et al., 2005] (Chapters 2 and 3), in finite difference mode. Dipole flow tracer test (DFTT) breakthrough curves sampled the aquifer closer to the well than push pull tests (PPTs). Tracer that contributed to the breakthrough peak (equal to ~50 % of the total injected tracer) travelled within ~2 cm (~0.3 x central packer length) of the well screen. PPTs run for a similar time and a lower flow rate sampled a distance of ~7 cm from the well into the aquifer. Equations were proposed in Chapter 2 to help design DFTTs. It was deduced that a large flow rate (10 l/min), long central packer (~1.4 m) and long duration (~2 days) are required to measure aquifer properties in the extraction well breakthrough curve ~70 cm into an aquifer, with a porosity of 0.37. As a general rule, the central packer should be at least three times as long as the desired sampling distance. A test needs to be carefully designed so that estimated parameters are representative of the aquifer rather than any potential drilling-induced disturbed zone near the well screen, i.e. the test needs to sample further out into the aquifer than the radius of the disturbed zone. Estimates of dispersivity from DFTTs were much closer to literature values for similar experiments [Corapcioglu and Fedirchuk, 1999; Huang et al., 2002; Olsson and Grathwohl, 2007; Rees et al., 2007] than those from PPTs (Chapter 2). The difference in dispersivity estimated by the two methods suggests that the near-well environment sampled is below the representative elementary volume of the bead pack, or that at this scale dispersion is test-dependant [Domenico and Schwartz, 1990; Neuweiler et al., 2001]. In either case this increases uncertainty in estimates of aquifer dispersivity obtained with single well forced gradient tracer tests. The closer to expected dispersivity estimates provided by DFTTs and the fact that hydraulic conductivity can be estimated from variations of pressure head in the well chambers in DFTTs [Sutton et al., 2000], suggest they are more suitable tests for measuring the conservative transport properties of an aquifer. Dispersivity is scale-

dependant at low aquifer volumes, and generally increases with the scale of measurement, as a test samples greater aquifer heterogeneity [Domenico and Schwartz, 1990]. If the dispersivity obtained in field DFTTs or PPTs was applied to plume migration over a large area it may underestimate contaminant dispersion. Also, the difference in dispersivity estimated from DFTTs and PPTs in this study may not be up scalable to the field scale.

As described in Chapter 3 breakthrough curves for the DFTT extraction chamber are sensitive to heterogeneity in hydraulic conductivity (represented in the tests by layers with different bead size). However, this does not significantly affect the area sampled by the breakthrough peak, at the scale tested. The opposite is true for PPTs. Heterogeneity in the DFTT tests was successfully modelled. The effect of layered heterogeneity on extraction chamber breakthrough in field scale tests is expected to be similar to the laboratory scale. However, the absence of near-well boundary conditions in the field may reduce flow in low hydraulic conductivity layers and increase flow in high hydraulic conductivity layers. By performing multiple DFTTs in a borehole at depth increments equal to the dipole apparatus shoulder length, it may be possible to deduce the position of a layered heterogeneity and its permeability, relative to the background media. The identification of high hydraulic conductivity zones, which can represent preferential flow paths for contaminant transport [Devlin et al., 2002; Wilson et al., 2004], is likely to greatly improve predictions of natural attenuation or the design and performance of remediation treatment schemes. The scale of hydraulic heterogeneity that can be determined is related to the dipole apparatus central packer length (Figure 7-1). Potentially significant variations may not be detected if this length is too small and too great significance may be given to inconsequential features (such as the low permeability lens in Figure 7-1). If it is too large preferential flow paths will not be detected. In the experiments conducted there was good resolution of this feature with the central packer approximately twice as long as the thickness of the layered permeability. When a low hydraulic conductivity layer bisects the central packer only a small portion of the injected mass will contribute to a DFTT breakthrough curve peak (Figure 7-2). In this scenario the signal of a sorbing or biodegrading tracer may be very small and difficult to accurately

quantify. Therefore injected tracer concentrations must be large enough to account for the possible presence of a low hydraulic conductivity layer, and hence give greater analytical accuracy. Suitable tracer concentrations are discussed later in this chapter. Heterogeneity in hydraulic conductivity in the field will be more complex in sand and sandstone aquifers than in the experiments performed, with the presence of discontinuous layers and

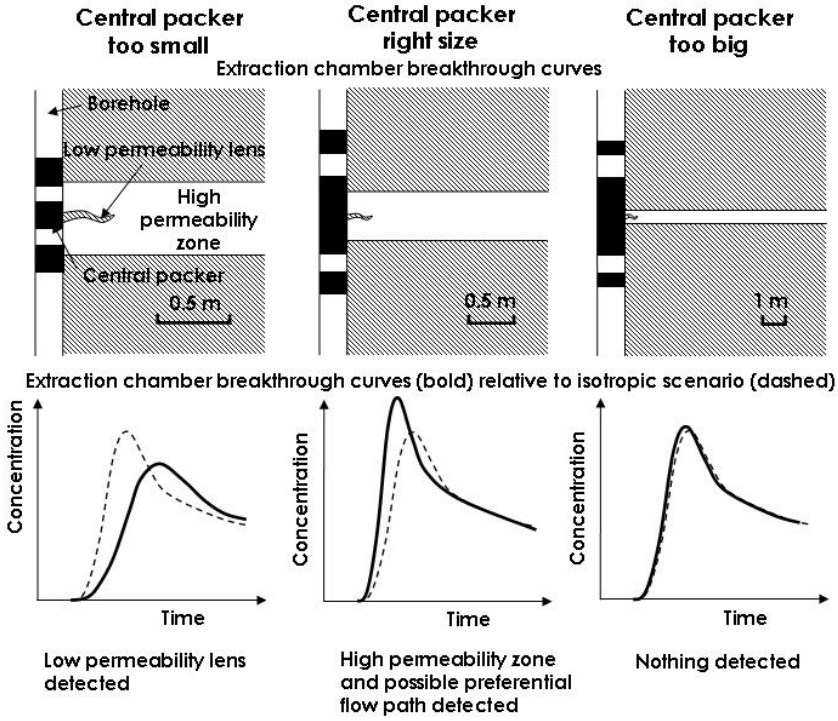

Figure 7-1: Schematic diagram to show relationship between size of DFTT central packer and the permeability heterogeneity that will be deduced. Note the change of scale in the different scenarios.

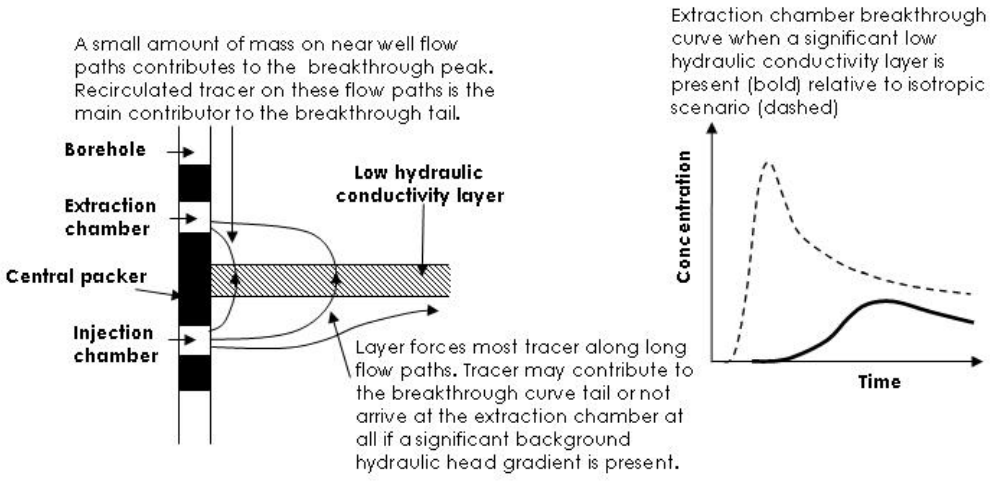

Figure 7-2: Schematic diagram to show the effect of a significant low hydraulic conductivity layer on tracer flow paths in a DFTT.

lenses [Sudicky, 1986; Stauffer, 2007]. This could complicate breakthrough curve signals and DFTTs may have to be performed at multiple boreholes to give a reasonable estimate of the heterogeneity present.

The imaging tests showed that the geometry of a PPT tracer cloud is significantly biased by the presence of layers of contrasting permeability. Injection, and subsequent advection, is greater in the high permeability zones. Therefore the breakthrough curve is biased towards the high permeability zones. Inverse modelling of the PPTs corroborated observations, but suggested that the effects should be greater. It is possible that variations in bead pack bulk density near the well supported some vertical flow, preventing migration further away from the well. If a high hydraulic conductivity zone is present as a sand pack or zone disturbed by drilling in the field it is likely that any signal will be biased towards the properties of the sand pack or zone. For PPTs a sand pack or disturbed zone is likely to cause significant vertical migration of the tracer, leading to mass loss and/or significant tailing of concentrations in the extraction phase breakthrough curve [Kim et al., 2004; Azizian et al., 2007]. In Chapter 2, DFTT breakthrough curve peaks are shown to sample an area close to the well screen, and therefore DFTTs are also likely to be affected by the presence of a higher hydraulic conductivity zone. Tracer flow will short circuit through the more hydraulically conductive material, bypassing the aquifer and leading to an early high concentration peak in the breakthrough curve [Sutton et al., 2000]. In PPTs, tracer may also be retained in low permeability layers, which may lead to greater tailing in breakthrough curve profiles.

Overall, the imaging tests suggested that PPTs may yield more representative aquifer reactive properties compared with DFTTs, as PPTs sample a greater distance into the aquifer, with a breakthrough curve that does not vary with heterogeneity in hydraulic conductivity. Thus they can be more easily modelled. However this does not take into account the clarity of signal that different reactive tracers in these tests produce. Results from tracer studies in Chapters 4-6 were combined with the HydroGeoSphere© models of DFTTs and PPTs with the same set-up parameters as in Chapters 2 and 3 (Table 7-1), to predict the signal of the reactive tracers in isotropic conditions in single well forced

gradient tracer tests. Modelling was performed with the low profile box set-up. This allowed direct comparison of simulated breakthroughs and Chapter 2 tests. To determine whether the simulated arrival of the conservative tracer and the reactive tracer was significantly different in DFTTs (i.e. could be measured in a field test), the root mean square error (RMSE) between the conservative and reactive model simulations was compared to that between the experimental data and the model fit in the first isotropic imaging test. Since the model does not account for recirculating tracer, only the experimental data up to 8 t_d was used (Chapter 2), as this is the time where significant deviation between the non-recirculating model and recirculating experiment was observed to start in experiments. If the RMSE is greater between the two model simulations than the data and model fit, it means that the difference between reactive and conservative signals is outside of measurement error and could be used to estimate aquifer parameters. For PPTs the RMSE analysis was performed, using the same method as for DFTTs, with models and data being compared over the entire PPT extraction phase.

Table 7-1: Set-up parameters for HydroGeoSphere© models

Dipole flow tracer tests		Push-pull tracer tests	
Chamber length	3.7 cm	Chamber length	3.7 cm
End packer length	3 cm	Packer length	6.7 cm
Central packer length	6.7 cm		
Flow rate	5.6 ml/min	Flow rate	3 ml/min
Tracer injection period	15 min	Tracer injection period	80 min
		Total injection period	120 min

Column experiments in Chapter 5 showed that acetate, because it is highly labile, could be useful as a biodegradation tracer for short duration single well forced gradient tracer tests. It should be possible to use acetate to assess biodegradation potential and rate under aerobic and anaerobic conditions [Huang and Jih, 1997; Kleikemper et al., 2002; Pombo et al., 2005; Watson et al., 2005; Kneeshaw et al., 2007; Rees et al., 2007], by measuring a reduction in its concentration relative to a conservative tracer. In column tests biodegradation rates were consistent with varying pore water flow rates and resident times. This allows flexibility in field test design. Acetate breakthrough curves were determined using HydroGeoSphere©, under conditions of isotropic hydraulic

conductivity, for the fastest (0.0024 /min) and slowest (0.0012 /min) first-order biodegradation rates calculated for acetate from column test data in Chapter 5. For DFTTs there was little deviation from the conservative tracer signal, even for the fastest biodegradation rate (Figure 7-3). The RMSE analysis shows that biodegradation of acetate could not be convincingly measured using DFTTs, as the signal is within measurement error of the conservative signal. In field tests noise in extraction chamber breakthrough curves may occur due to grain size heterogeneity not present in the model. This would reduce certainty when inverse modelling breakthrough curves and hence the potential to accurately measure biodegradation at the field-scale with a DFTT. The greatest deviation from conservative tracer concentrations is likely to occur in the breakthrough tail, which presently cannot be modelled with HydroGeoSphere©. The residence time of the tail would be difficult to calculate as the tracer that contributes to it is mostly recirculated. When the flow rate was halved and injection period doubled in the model (i.e. the total injected tracer volume kept the same) (not shown), acetate values were ~10 % less than conservative values at the breakthrough peak. However RMSE showed that the difference in tracer breakthroughs was still not significant. In the field tracer concentrations would be reduced by the presence of any low hydraulic conductivity layers between the well chambers. In addition, normalised breakthrough concentrations are expected to be an order of magnitude less in field tests ($\sim C/C_0 = 0.01$) than the imaging tests performed [Sutton et al., 2000; Roos, 2009], due to greater advective spreading and dilution of the tracer plume in fully 3-D conditions. Acetate would be required to be added at ~500 mg/l for concentrations at the extraction chamber to be accurately quantified by ion chromatography. This concentration is over 5 times that used in Chapter 5, and biodegradation is likely to be limited by electron acceptor concentrations. Also analysis has suggested that concentrations would need to reduce by over ~10 % (50 mg/l) to show clear deviation from the conservative tracer. This shows that DFTTs have a high detection limit for measuring biodegradation with these model set-up parameters. Improved resolution may be achieved with a longer central packer, which would increase aquifer residence time and hence extent of acetate biodegradation, and longer tracer injection, which would increase the magnitude of the extraction chamber breakthrough peak and hence analytical accuracy. Therefore analysis of

biodegradation may still be possible with DFTTs in the breakthrough tail if the test is carefully designed. Alternatively tests could be run in non-recirculating mode allowing longer injection of tracer at a lower concentration and a higher concentration breakthrough curve. However this would lead to a large amount of water that would need to be disposed of, similar to PPTs. As shown in Chapter 5, electron and alkalinity balances can be used to help assess the biodegradation pathway. In pulse injection column tests, during acetate biodegradation, normalised acetate concentrations were clearly lower than normalised conservative tracer concentrations. Electron and alkalinity signals showed less clear variation from pre-biodegradation values. Therefore, as in field tests acetate breakthrough is predicted to be not significantly different from conservative tracer breakthrough, it is also likely that changes in electron acceptor concentrations and alkalinity caused by biodegradation would be in error of background values. Consequently alkalinity and electron acceptor signals may not be useful for the assessment of biodegradation with DFTTs. These factors suggest that DFTTs are unsuitable for simple determination of biodegradation potential in the field.

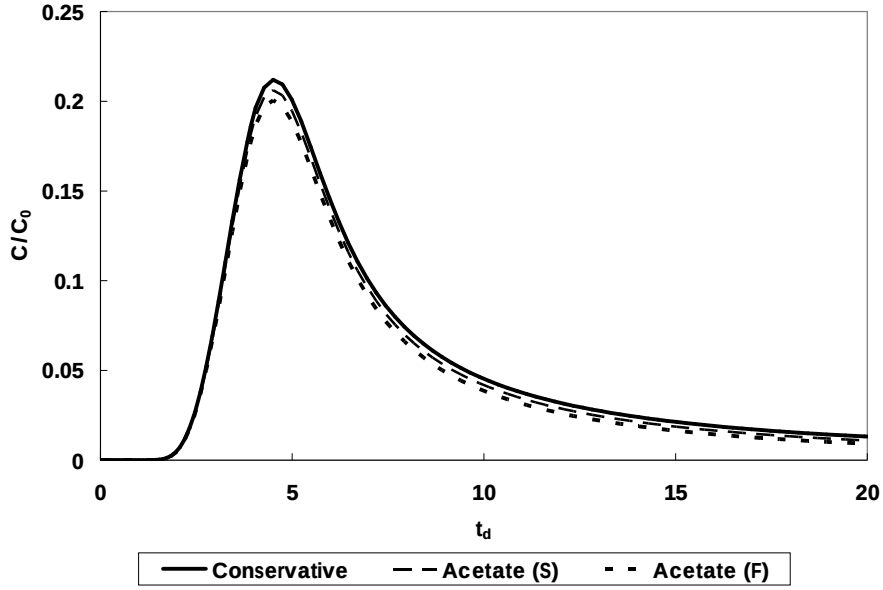

Figure 7-3: Simulated DFTT breakthrough of acetate in extraction well with no recirculation, plotted with simulated conservative tracer breakthrough. (S) = slowest degradation rate measured in experiments and (F) = fastest. Normalised concentrations are plotted against time. Time is normalised to the test charactistic time (Chapter 2).

There is much greater deviation in the acetate signal from conservative tracer concentrations in the PPT simulations (Figure 7-4). Statistical analysis suggests that the biodegradation potential of an aquifer can be estimated using acetate in PPTs, even with a relatively short residence time. Normalised peak breakthrough concentrations are expected to be similar in field tests [Istok et al., 1997]. Therefore a low acetate concentration of ~ 50 mg/l similar to column tests in Chapter 5 could be used to assess biodegradation in field tests. As for DFTTs a small amount of signal noise would be expected to slightly reduce certainty when inverse modelling breakthrough curves. Because tracer mass moves out from the well and back again as one slug, the residence of all tracer extracted at a given time is similar, irrespective of any spatial variability in hydraulic conductivity. Also biodegradation rates in PPTs can be assessed by simply comparing conservative and reactive tracer concentrations over time, without the need for a model fit [Haggerty et al., 1998]. As there is clear deviation of acetate from the conservative tracer signal, electron acceptor [Istok et al., 1997] and alkalinity budgets should be possible in field tests to assist the identification of biodegradation pathways. As observed in imaging tests, tracer in PPTs will migrate preferentially in zones with high hydraulic conductivity. Therefore the biodegradation potential is likely to be a measure of the highest flux paths in the aquifer. If high flux paths are not considered in estimates of

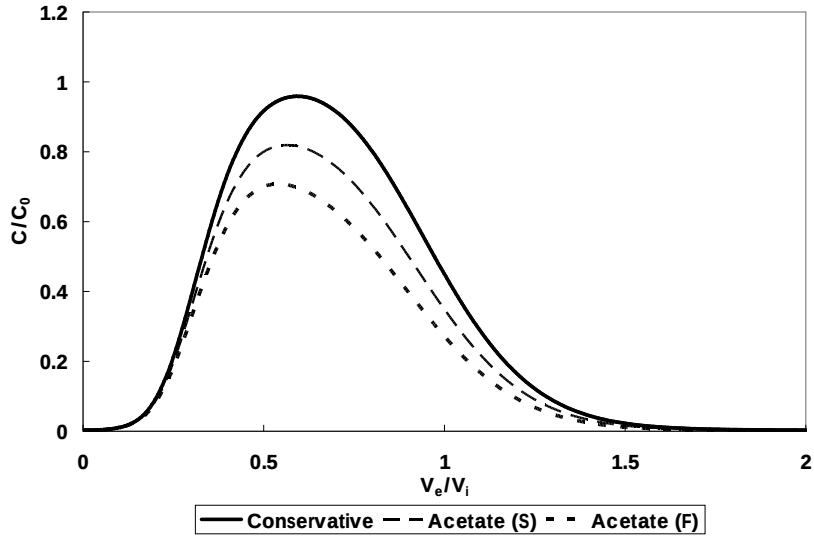

Figure 7-4: Simulated acetate breakthrough for PPT extraction phase plotted with simulated conservative tracer breakthrough. (S) = slowest degradation rate measured in experiments and (F) = fastest. Normalised concentrations are plotted against volume of extracted water over the total volume of water injected.

natural attenuation organic contaminants will migrate further down gradient than expected before they are fully biodegraded. Despite these issues it is clear from modelling that PPTs are the preferred single well forced gradient test for investigating biodegradation at the field scale.

Acetate is a quickly biodegrading compound, which was used in this study to investigate the effectiveness of DFTTs and PPTs to assess biodegradation in aerobic conditions. At polluted sites a suitable biodegradation compound would degrade similarly to the contaminant studied, being limited by the same factors, but would be distinguishable from it by chemical analysis. For example trichlorofluoroethene (TCFE) for TCE or PCE [Vancheeswaran et al., 1999; Hageman et al., 2001], deuterated surrogates of toluene and xylene in a BTEX contaminated aquifer [Reusser et al., 2002], or ethylene and propane as chlorinated aromatic hydrocarbon surrogates [Kim et al., 2004; Kim et al., 2006]. If the surrogate is degrading it is likely that so is the pollutant compound. Forced gradient tracer tests could also be used to investigate the effectiveness of biostimulation and bioaugmentation schemes, before they are applied at a wider scale. Some studies have already been performed with PPTs (e.g. Kim et al. [2006] and Azizian et al. [2005]). Biodegradation may be stimulated by adding simple organic molecules as electron donors [Major et al., 2002], adding electron acceptors such as oxygen [Salanitro et al., 2000] or adding a mixture of macro and micronutrients [Liebeg et al., 1999]. Bioaugmentation occurs when bacteria are added to the aquifer that are known to biodegrade the contaminant present, for example the addition of *Dehalococcoides* to bioaugment the biodegradation of PCE [Lendvay et al., 2003]. Tests could be quickly performed to assess the optimum set-up of a bioremediation scheme.

In Chapter 6 the suitability of TCFE as a tracer to predict hydrophobic sorption of organic contaminants, and the fraction of organic carbon in an aquifer, was investigated. TCFE was found to have a solubility of ~521 mg/l, dissolve quickly and have a dimensionless Henry's constant of 1.32. This showed that test solutions can be readily made, but care is needed to prevent loss by volatilisation. Sorption of TCFE onto activated charcoal

(particulate black carbon) and natural organic carbon was investigated in batch and column experiments. At 0.023 wt% carbon retardation factors for TCFE were estimated to be ~9.4 for activated charcoal and ~1.3 for organic carbon. This range suggests that TCFE is suitable for measuring sorption onto particulate organic carbon at amounts that may be found in sandstone aquifers [Ball et al., 1990] and can also be used to estimate sorption when a low amount of black carbon is present (e.g. alluvial aquifers [Karapanagioti et al., 1999]). Breakthrough of TCFE in DFTTs and PPTs was estimated using the model for two scenarios: sorption onto naturally occurring organic carbon (0.023 wt%), and sorption onto activated charcoal at the same concentration. The sorption distribution coefficient for the natural organic carbon scenario was estimated from the average retardation in column tests (Equation 6.2). For the activated charcoal case it was taken from the Freundlich isotherm, for 1 mg/l TCFE. For these calculations the bulk density was assumed to be 2000 kg/ m^3 and porosity of 0.37 (values used in HydroGeoSphere© models). In DFTTs solute flow through the test zone is in one overall direction from the injection to extraction chamber during the test. Therefore the sorbing tracer breakthrough curve is expected to be retarded relative to a conservative tracer. Also, the sorbing tracer mass flux entering the extraction chamber at peak breakthrough is less than for the conservative tracer, due to it having a lower velocity. Therefore the sorbing tracer peak concentration is expected to be lower relative to the conservative tracer. In PPTs the direction of solute flow reverses halfway through the test. Therefore injection and extraction phase sorbing tracer retardations are expected to roughly cancel. Sorption is measurable from an increase in apparent tracer dispersivity [Schroth et al., 2001]. For the natural organic carbon simulation in the DFTT (Figure 7-5) there is a small but distinct separation (statistically significant) between conservative (peak at 5.23 t_d) and sorbing (peak at 4.50 t_d) tracer breakthrough. Conversely, there was no statistically significant separation between the two tracers in the simulated PPT (Figure 7-6). These simulations suggest that estimating low fractions of organic carbon using sorbing tracers would be best achieved using DFTTs. In field tests increased signal noise would lower the detection limit of both methods, further favouring measurement with DFTTs. The separation between sorbing and conservative tracers is far greater when activated charcoal is present. In the simulated DFTT, TCFE peak breakthrough is much

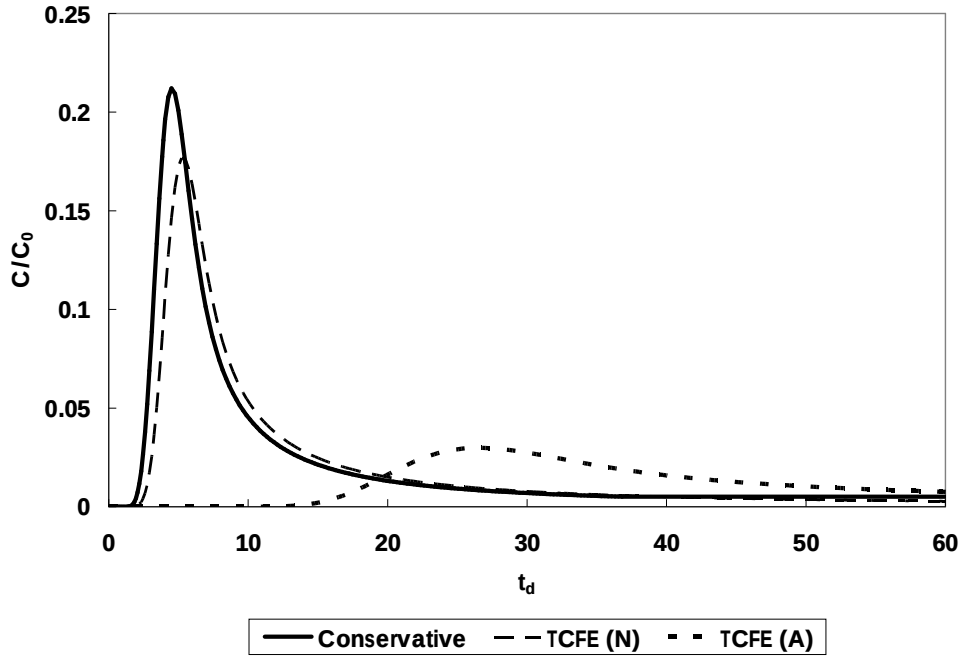

Figure 7-5: Simulated breakthrough of TCFE in DFTT extraction well with no recirculation, plotted with simulated conservative tracer breakthrough. (N) = natural organic carbon present at 0.023 wt% and (A) = activated charcoal present at 0.023 wt%.

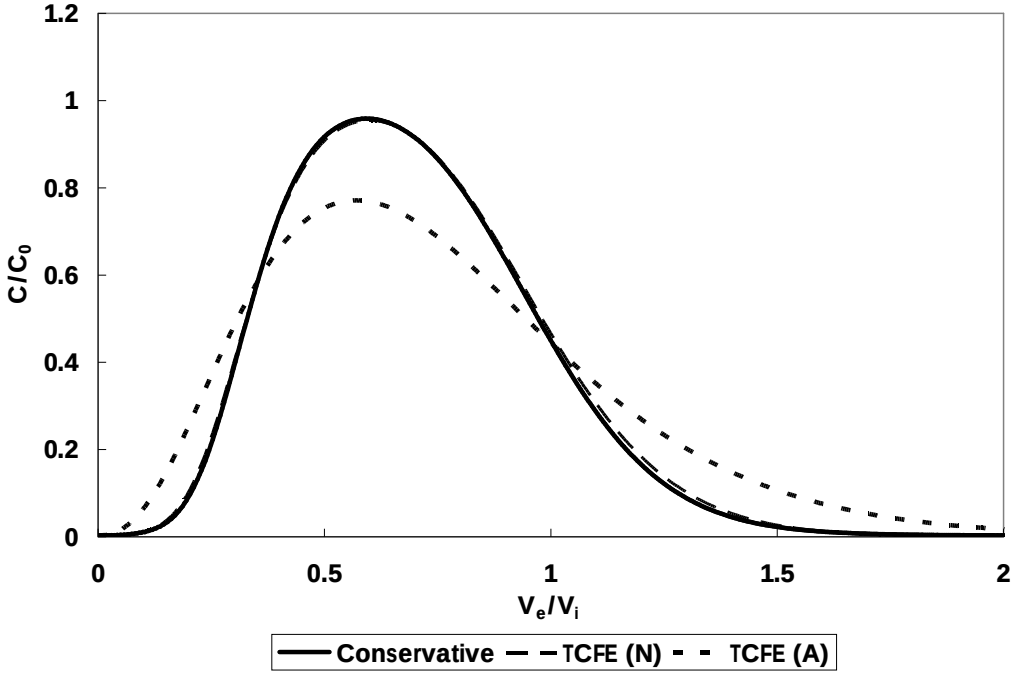

Figure 7-6: Simulated breakthrough of TCFE in PPT extraction phase with no recirculation, plotted with simulated conservative tracer breakthrough. (N) = natural organic carbon present at 0.023 wt% and (A) = activated charcoal present at 0.023 wt%.

later (26.52 t_d) and at a lower concentration than conservative tracer breakthrough. In aquifers with significant anisotropy or higher fractions of particulate carbon, attenuation of the organic sorbing tracer (TCFE) may be too great to resolve breakthrough. Synthesised breakthrough curves suggest DFTTs give clear peaks up to a retardation factor of ~10. If equal extraction and injection flow rates can be ensured, non-recirculating tests can be performed and analysed with a simple model. Recirculation of tracer will broaden peaks and is more likely to reduce certainty in estimated parameters at higher retardations. For the PPT scenario, the simulated organic sorbing tracer profile shows distinct separation from the conservative tracer breakthrough. The TCFE signal has an earlier peak breakthrough than the conservative tracer by ~0.05 V_e/V_i, but a later mean breakthrough by ~0.02 V_e/V_i. Both tracers have a similar mass balance, with > 98 % injected mass being recovered by 2 V_e/V_i. The early peak is likely to represent sorption of tracer injected at the end of the slug, which has not travelled far into the model and has been extracted quickly. The late mean arrival likely represents sorption and delayed extraction of tracer injected at the start of the test, far into the model. A long extraction phase would be needed to ensure that the tail concentration of the sorbing tracer is captured well. The accuracy of sorption estimates obtained using PPTs is reported to be lower when retardation factors are over ~20 and in the presence of layered hydraulic conductivity heterogeneity [Schroth et al., 2001]. Therefore PPTs may not be a suitable method to assess sorption at field-scale in zones of high heterogeneity or if a high fraction of black carbon is present in the porous media. Analysis suggests that both tests should be able to estimate sorption when a low amount of black carbon is present and that DFTTs are the preferable test if estimating the fraction of organic carbon.

In Chapter 4, column tests were undertaken to assess the suitability of sodium, magnesium and potassium to measure the cation exchange capacity (CEC) of an aquifer. Single well forced gradient cation breakthrough curves were simulated by assuming that average retardation factors (and hence sorption distribution coefficients) obtained for 1-D flow in DFTTs and PPTs were the same as in column tests containing Permo-Triassic sand (Chapter 4). This was a simplified modelling approach as HGS does not include a geochemical transport code taking into account ion exchange (e.g. PHREEQC [USGS,

2008]), as used in the column tests. In column tests ion exchange increased the dispersion of tracer breakthrough relative to the conservative tracer. Therefore the dispersion of sorbing tracers in simulations may be underestimated. Sodium (peak at 5.48 t_d) was clearly separated from the conservative tracer (peak at 4.50 t_d) for DFTTs (Figure 7-7). Magnesium (peak at 10.13 t_d) and potassium (peak at 13.56 t_d) are displaced further from the conservative tracer, with lower peak concentrations. The RMSE analysis suggests that the CEC could be measured in DFTTs using all cations. For the PPT model, sodium is near indistinguishable from the conservative tracer breakthrough, while magnesium and potassium are very similar (Figure 7-8). The RMSE analysis suggests that only potassium could be used to estimate CEC with any confidence. However, in field tests, if a large amount of noise was present in tracer breakthrough curves none of the cations tested would be suitable for use with PPTs. The difficulty of PPTs in distinguishing low to moderately retarding tracers from conservative breakthrough (i.e. a high detection limit) has previously been noted [Schroth et al., 2001]. This shows that for retardation factors up to ~4, the DFTT is by far the more sensitive method for measuring CEC. It also shows for DFTTs that unless a low CEC is estimated sodium is a more suitable tracer than potassium or magnesium, as a test could be performed over a shorter period. In column tests it was suggested that a tracer mixture of sodium with potassium or magnesium can estimate CEC in aquifers without prior knowledge of the expected range, when used with a DFTT. A simulation of this tracer mixture is shown in Figure 7-9. The tracer mixture is useful as CEC typically varies between 0.2 and 5 meq/100g in aquifers [Christensen et al., 2001], while in this study a sand with a mid-range CEC (1.592 meq/100g) was used. In “low” CEC sediments potassium or magnesium would be more suitable to measure CEC, whereas sodium would be preferred in “high” CEC sediments. Finer grained sediment is likely to have a higher CEC, as apparent in the CEC analysis in Chapter 4 and found for clay rich sediments in the literature [Christensen et al., 2001]. Due to the combination of horizontal and vertical flow, a DFTT will integrate sorption from layers of different permeability, which are likely to have different grain sizes and CEC (see above). If breakthrough curves suggest there is a high permeability contrast in the subsurface (shown by varying breakthrough curve geometry with depth of the dipole apparatus in the well screen), the CEC may be an overestimate of the effective value for

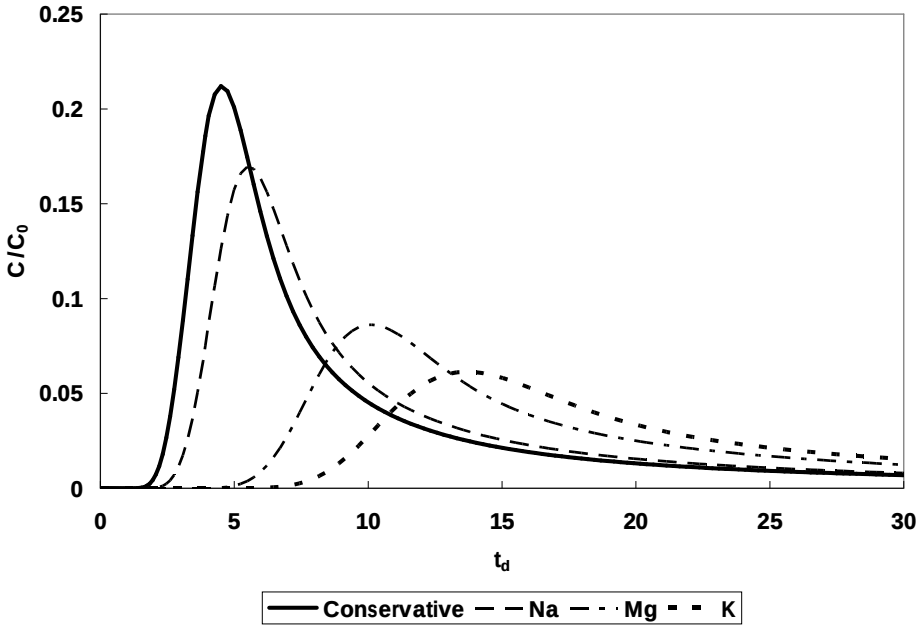

Figure 7-7: Simulated breakthrough of cations in DFTT extraction well in separate tests with no recirculation.

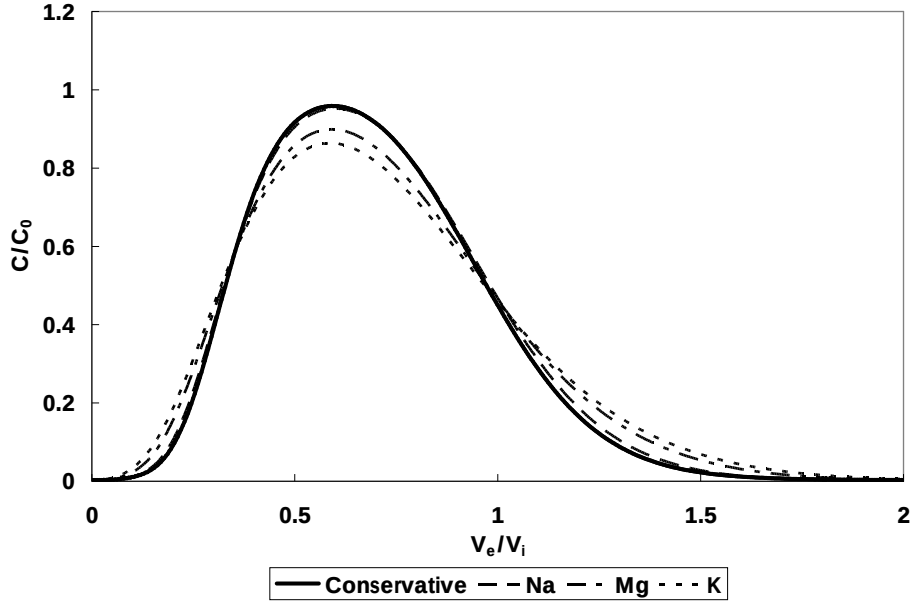

Figure 7-8: Simulated breakthrough of cations in PPT extraction phase in separate tests.

contaminant transport. This is because spatial variability in permeability is likely to produce a range of contaminant mass flux paths [Wilson et al., 2004]. High permeability/low CEC zones are likely to also be high contaminant mass flux paths and *vice versa* [Stauffer, 2007]. Therefore the effective CEC for natural attenuation will be biased towards the high permeability zones and be less than the value estimated in the

DFTT. To accurately assess CEC in high permeability zones when strong layering exists in the aquifer, it is recommended that tests are first performed at multiple depths to identify the location of high permeability layers (see above). Then a test could be performed at the required depth to estimate CEC in an identified high permeability zone. Despite this uncertainty in CEC values in zones where layered permeability exists, the higher sensitivity of DFTTs at low retardations make them the more suitable single well forced gradient test for estimating CEC.

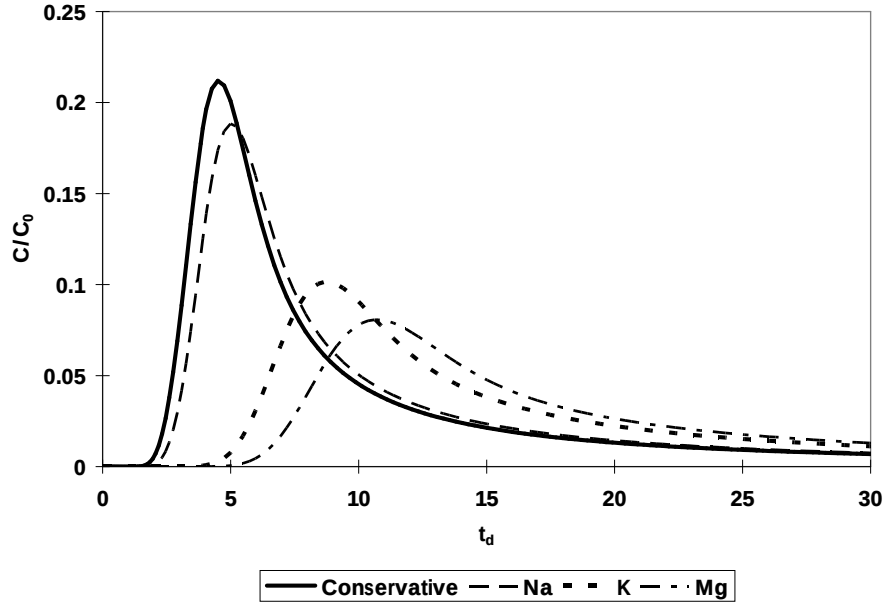

Figure 7-9: Simulated breakthrough of sodium with potassium or magnesium, in a tracer mixture for the DFTT extraction well, with no recirculation. Potassium and magnesium are run in separate tests with sodium. The sodium signal is the same for both tests.

Also in Chapter 4, Ni-EDTA was investigated as a tracer to estimate the sorption and migration of metals complexed with EDTA (as a model organic complexing agent). The sorption distribution coefficient for Ni-EDTA was estimated the same way as for the cations (see above). In column tests the average retardation factor of Ni-EDTA was 1.06, when injected at 10^{-4} M. Using this retardation factor in the HydroGeoSphere© model, there was no clear separation of Ni-EDTA from the estimated conservative tracer signal for the PPT simulation (data not shown). There was a slight separation of the tracers in the DFTT simulation (Figure 7-10), but the RMSE analysis suggests that neither single well test is suitable for measuring the retardation of Ni-EDTA. These simulations show that Ni-EDTA is not suitable as a tracer in single well forced gradient tracer tests under

neutral pH aquifer conditions. It would be better suited for use in acidic pH conditions [Davis et al., 2000], where greater retardation is expected.

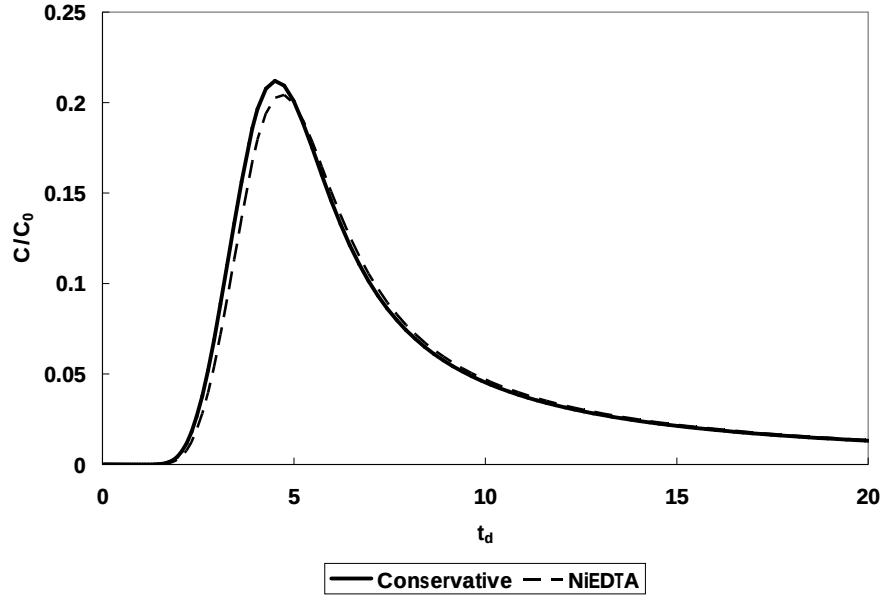

Figure 7-10: Simulated breakthrough of Ni-EDTA in DFTT extraction well, with no recirculation.

As for biodegradation tests, it is important in sorption tests to choose a suitable input concentration. This should be high enough to produce a quantifiable breakthrough curve, but low enough so that it does not saturate the limited number of surface sorption sites on aquifer mineral surfaces [Appelo and Postma, 2005]. In 3-D field tests this issue is more significant for DFTTs, as breakthrough curve peak concentrations [Sutton et al., 2000; Roos, 2009] are approximately an order magnitude less than the low-profile box models presented here. Therefore good analytical accuracy is required to quantify the tracer at concentrations two orders of magnitude less than input concentrations. If there is no significant retardation of the sorbing tracer relative to the conservative tracer, when it is expected from predicted aquifer properties, it is likely that the tracer concentration is too high. Surface sites in near-well flow paths (that dominate the breakthrough peak in DFTTs) may be saturated by the sorbing tracer at a fraction of injection concentrations, leading to no observable retardation in the tracer. If concentrations used for DFTTs are too low, it will lead to unacceptable analytical error in measurements and hence more likely that reactive tracer concentrations will be in error of conservative tracer values. Cation injection concentrations of ~500 mg/l and TCFE injection concentrations of ~5

mg/l should be satisfactory for DFTT breakthrough curves to be accurately measured. Greater cation concentrations should not be used to limit density effects [Schincariol and Schwartz, 1990], which may affect breakthrough. Lower concentrations of these tracers can be used for PPTs, as peak breakthrough concentrations in simulations are similar to field tests [Istok et al., 1997]. Cation injection concentrations of ~ 50 mg/l and TCFE injection concentrations of ~ 0.5 mg/l would be sufficient to ensure clear breakthrough and resolution. Modelling in this chapter suggests DFTTs are suitable for measuring retardation factors up to ~10. Therefore the sorbing tracer chosen should have a retardation factor < 10 for the likely range of parameter values in the test zone.

Bromide was found to be a more reliable conservative tracer than fluorescein. This was mainly due to variation in fluorescein fluorescence with changes in pH. If fluorescein is used in the field it is important that the injection solution has the same pH as the groundwater. If the groundwater pH is higher than the injection solution, tracer breakthrough curve concentrations may be overestimated, and *vice versa*. Failing to take pH into account may result in poor inverse modelling and erroneous estimation of aquifer hydraulic and reactive parameters. Fluorescein gave consistent dispersivity estimates at different flow rates in column tests and would be a suitable tracer if pH was taken into account. Of the inorganic anions tested bromide and chloride gave similar estimates of velocity and dispersivity, but sulphate showed a significantly slower velocity. This may have been due to sulphate sorption onto positively charged surface sites on the aquifer minerals [Yong et al., 1992]. The performance of chloride as a tracer was not greatly affected by a high background concentration in column tests. However, to maximise detection range it is recommended that the conservative tracer chosen is present at low concentrations in the aquifer tested. Suitable anion injection concentrations for tests are the same as for cations (see above).

If multiple reactive tracers are used in a mixture, an important issue is determining the duration of the test. Assessments of conservative parameters and sorption can be made with a test (DFTT or PPT) of 1-3 day duration, depending on set-up parameters. However a longer duration may be needed to estimate biodegradation parameters if the

biodegradation reaction kinetics are slow, or there is a lag period before biodegradation. This is easier to consider for PPTs as a long hiatus phase could be planned between the injection and extraction phases of the test, although if it is too long and the background hydraulic gradient could remove tracer from the test zone. For DFTTs a test may have to be run for a long time to observe a small amount of biodegradation in the tail. If TCFE is used as a tracer in a mixture with an aerobically biodegrading compound (e.g. acetate), it may be undesirable to have a long hiatus in a PPT. The biodegrading tracer may deplete the aquifer of oxygen creating anaerobic conditions, which may induce dechlorination of TCFE. This can occur in the field within a few days [Hageman et al., 2001]. Biodegradation of TCFE could be identified from a comparison of TCFE and conservative tracer mass balances. However, this may still lead to errors in sorption estimates. In Chapter 6 it was found at above NaBr concentrations of ~1000 mg/l TCFE may interact with inorganic ions, affecting sorption of TCFE. Therefore inorganic ion concentrations should be kept low to avoid this, as well as density effects (see above). When used in a mixture tracer concentrations may need to be lower than when used separately to prevent density affects. Ideally total concentrations should not exceed 1000 mg/l [Schincariol and Schwartz, 1990].

The numerical modelling suggests that overall there is greater confidence in measured tracer retardation, and hence estimates of CEC and fraction of organic carbon, using DFTTs rather than PPTs. Conversely, better estimates of biodegradation parameters are likely to be obtained using PPTs. Imaging tests in Chapter 2 and 3 suggested DFTTs are more suitable for measuring conservative transport parameters than PPTs, but the tests need to be carefully designed and concentration breakthrough curves are very sensitive to discrete mesoscale aquifer permeability variations. Multiple PPTs could be performed in direct-push wells to quickly characterise the aquifer biodegradation potential or effectiveness of a bioremediation scheme. An injection flow rate of 1 l/min over 12 hours would allow tests to sample ~0.5 m into the aquifer (assuming spherical flow). In this case packers should be ~0.5 m long to minimise loss of tracer to open well segments. To measure CEC and fraction of organic carbon with PPTs tracers would need to be retarded by a factor ~4-20, to measure the aquifer parameters satisfactorily. TCFE may be suitable

to measure sorption onto black carbon in a PPT. However, separate analysis might be required to characterise conservative transport parameters, as PPTs may underestimate dispersivity (Chapter 2). If DFTTs were used to assess aquifer transport parameters and heterogeneity in permeability, separate analysis would likely be required to assess the biodegradation potential or effectiveness of bioremediation schemes, due to the detection limit of DFTTs to measure biodegradation being high (see above). A DFTT run at 1 l/min and with a central packer of ~0.68 m over 2-3 days will sample a distance of approximately 0.34 m into the aquifer and detect heterogeneity in hydraulic conductivity at the same scale. Alternatively, a longer packer and higher flow rate can be used to sample further into the aquifer and detect heterogeneity at a larger scale. Performing at least one DFTT and PPT in the same borehole would be the simplest method to estimate all desired reactive and conservative transport parameters *in situ*, over a short time frame. Testing over multiple boreholes at a site and performing multiple DFTTs at different depths to characterise heterogeneity in permeability would increase certainty in estimated parameters.

7.2. **Future Work**

There is great potential to further asses the value of PPTs and DFTTs using modelling and the imaging box. The sensitivity of PPTs to background hydraulic gradients should be investigated in isotropic conditions and with various high hydraulic conductivity layers, for different test pumping rates. This is important as high groundwater flow velocities can lead to significant test asymmetry and potential tracer loss (as observed during imaging test method development). This is not very suitable for testing with the current imaging box set-up as the water table would need to be controlled accurately over a range of a few centimetres, at discretisations of millimetres, to get the desired hydraulic head gradients across the box. To solve this various groundwater flow velocities could be simulated by water being pumped slowly in from one end of the box and out the other, similar to the tests of Chiogna et al. [2010]. Work by Lekamge [2010] has shown that the detection limits for fraction of organic carbon with DFTTs using TCFE varies significantly with flow rate and central packer length. Further investigation of this for DFTTs and PPTs, as well as the detection limit to reliably measure CEC and

biodegradation rates should be performed through modelling for different tracers and set-up parameters. This would greatly aid the design of tests for use with reactive tracers.

It has been observed in field DFTTs conducted in the CFB Borden aquifer (Canada) (unpublished data) that tracer is not always observed in the extraction well. This may have been due to the presence of a low hydraulic conductivity layer between the two chambers of the dipole (Chapter 3). The contrast required to cause absence of tracer breakthrough and whether the result obtained compares favourably with the effect of bulk anisotropy on tracer breakthrough predicted by Sutton et al [2000] remains unknown. Numerical models used to examine this would need to have larger dimensions than those in this study and incorporate tracer migration in three dimensions, to prevent near-well boundaries forcing tracer across a low permeability zone. If further work is performed to find the dependence of constant A and angle α (as defined in Equation 2.3 and 2.4) on DFTT set-up parameters and time into a test, the area of sampling measured in extraction well breakthrough curves can be accurately predicted. This would allow quick and effective design of DFTTs.

The ultraviolet imaging technique can be further used to investigate the performance of forced gradient tracer tests. With direct visualisation of results, forced gradient solute transport can be studied in much finer detail than similar laboratory scale tests, such as column experiments and larger box models with multi-level samplers (e.g. Danquiny et al. [2004]). Experimental set-ups can be used to investigate deviation from predicted flow in forced gradient near-well conditions that would not be possible using modelling alone. Also, experimental set-ups and in-well apparatus configurations can be quickly modified. The performance of multiple well tests such as inter-well tracer tests and horizontal dipole tests [Ptak and Schmid, 1996; Goltz et al., 2008] could be examined. Also, different sized beads could be used to investigate the effect of random and more regular physical heterogeneity on tracer and test performance.

Further work should be performed on characterising TCFE sorption. A study comparing TCFE sorption with trichloroethene and tetrachloroethene sorption onto a range of sediments and carbon types would qualify the value of TCFE as a proxy to assess sorption of trichloroethene and tetrachloroethene in aquifers. Column and field tests should also be performed using TCFE as a tracer in a trichloroethene- or tetrachloroethene-contaminated system. This will show if it can be used successfully as a proxy tracer in polluted environments. It has been suggested in this discussion that TCFE may biodegrade over long periods if oxygen has been depleted in the aquifer by the presence of a biodegrading tracer. This would reduce confidence in sorption estimates from single well forced gradient tests and may create unrepresentative conditions of the system under study. Long duration column and field tests should be undertaken to assess this possibility.

Field tests can be undertaken to assess the performance of reactive tracer mixtures. However, it is recommended that the processes evaluated are first investigated in the laboratory and with modelling to increase the chances of success in the field. Field tests should not be carried out in wells with sand packs or those drilled with hollow stem augers, as this will lead to short circuiting of flow in DFTTs and poor mass recovery over the test timescales for PPTs. It is recommended that test set-up parameters and tracer concentrations used are similar to those suggested in the discussion.

7.3. **Conclusions**

1. Forced gradient tracer tests can be successfully performed and analysed in a small scale pseudo 2-D model aquifer, in conjunction with ultraviolet fluorescent imaging of the tracer plume. There is potential to perform further tests using the method to characterise forced gradient tests in conjunction with modelling.
2. Dipole flow tracer test breakthrough curves are highly sensitive to the position (relative to the well apparatus) of any layered permeability heterogeneity. Inverse modelling is an effective approach to understanding such systems. Multiple tests at different depths in a well could be performed to identify the location of a layer and its permeability relative to the background media. The test is suitable for measuring low

to moderately sorbing tracers (up to a retardation factor of ~ 10). If equal extraction and injection flow rates can be ensured, non-recirculating tests can be performed and analysed with a simple model. The test is not overly suitable for biodegrading tracers, in part due to a high lower detection limit. For all tracers, care is needed to ensure a clear signal, but to avoid any saturation or inhibition effects. Typically, tracer contributing to the extraction chamber breakthrough curve peak has migrated through a volume of aquifer in close proximity to the test well. This volume increases (and reaches further from the well) as the length of the central packer increases. A test pumping rate should be large enough to sample a significant distance into the aquifer, but low enough so that effects due to potential physical non-equilibrium transport are minimised. The test is most suitable for measuring aquifer parameters in zones with low anisotropy. Dipole flow tracer tests are likely to give a more accurate estimate of aquifer dispersivity in the near-well environment than push-pull tests and are preferable for measuring the conservative transport properties of an aquifer.

3. Push-pull tracer test breakthrough curves are less sensitive to heterogeneity in hydraulic conductivity. However physical heterogeneity strongly affects the geometry of the test tracer plume and may bias estimated parameters to high permeability zones. Physical heterogeneity may also result in mass loss to open well segments or the surrounding aquifer. Push-pull tests sample a greater distance into the aquifer than dipole flow tracer tests and effective tracer tests are simpler to design. The test is suitable for use with biodegrading tracers and assessing the effectiveness of bioremediation schemes. The test is largely unsuitable for sorbing tracers with low to moderate retardation due to a high lower detection limit for these. Highly sorbing tracers are likely to require a large extraction period to capture the entire tracer breakthrough history.
4. Near-well preferential flow paths caused by variation in aquifer bulk density are likely to be present in single well forced gradient tests. These features may not be evident on test well breakthrough curves when they only make up a small portion of the total flow, but will cause short circuiting or mass loss, if significant. This could lead to inaccuracy in field test interpretation or unsuccessful tests being performed.
5. Bromide and chloride were found to be more reliable conservative (non-reactive)

tracers than fluorescein and sulphate. Sodium with potassium (or magnesium) are suitable tracers to quickly assess the cation exchange capacity of an aquifer, using a dipole flow tracer test, with no prior knowledge of the aquifer sediment properties. Ni-EDTA is best suited for use as a reactive tracer to assess organic-metallic complex sorption in low pH conditions.

6. Acetate biodegraded quickly and at a consistent rate for different pore water velocities, similar to those used in forced gradient tracer tests. This makes it a suitable tracer to estimate the biodegradation potential of simple organic compounds in field tests of suitable duration. Such tests should be performed with alkalinity and electron balances, to determine the biodegradation pathway. The biodegradation surrogate chosen for a field test should biodegrade similarly to the contaminant under study.
7. Trichlorofluoroethene has suitable properties for use as a tracer to measure the fraction of organic carbon in aquifer sediments and as a proxy for trichloroethene or tetrachloroethene sorption. Care is needed to ensure sample preservation in field tests, due to the volatility of trichlorofluoroethene.
8. Dipole flow tracer tests and push-pull tests are not suitable for the use of conservative, biodegrading and sorbing tracers in a single mixture to assess aquifer transport parameters for estimates of natural attenuation and remediation schemes. It is recommended that push-pull tests are used to measure aquifer biodegradation potential, while dipole flow tracer tests are used to measure aquifer conservative transport parameters and parameters relating to the retardation of sorbing tracers.

8. **References**

Accardi-Dey, A., and P. M. Gschwend (2003), Reinterpreting literature sorption data considering both absorption into organic carbon and adsorption onto black carbon, *Environmental Science and Technology*, *37*, 99-106.

Adeel, Z., and R. G. Luthy (1995), Sorption And Transport Kinetics Of A Nonionic Surfactant Through An Aquifer Sediment, *Environmental Science & Technology*, *29*, 1032-1042.

Allen-King, R. M., P. Grathwohl, and W. P. Ball (2002), New modeling paradigms for the sorption of hydrophobic organic chemicals to heterogeneous carbonaceous matter in soils, sediments, and rocks, *Advances in Water Resources*, *25*, 985-1016.

Alter, S. R., M. L. Brusseau, J. J. Piatt, A. Ray-Maitra, J. M. Wang, and R. B. Cain (2003), Use of tracer tests to evaluate the impact of enhanced-solubilization flushing on in-situ biodegradation, *Journal Of Contaminant Hydrology*, *64*, 191-202.

Alvarez, P. J. J., and W. A. Ilman (2006), *Bioremediation and Natural Attenuation: Process Fundamentals and Mathematical Models*, Wiley-Interscience.

Andersson, P., J. Byegard, E. L. Tullborg, T. Doe, J. Hermanson, and A. Winberge (2004), In situ tracer tests to determine retention properties of a block scale fracture network in granitic rock at the Aspo Hard Rock Laboratory, Sweden, *Journal Of Contaminant Hydrology*, *70*, 271-297.

Antizar-Ladislao, B., and N. I. Galil (2006), Enhanced in situ bioremediation of phenol in bioestimulated unsaturated and saturated sand-bed columns, *Water Environment Research*, *78*, 2447.

Appelo, C. A. J., and D. Postma (2005), *Geochemistry, groundwater and pollution: 2nd edition*, A.A. Balkema.

Azizian, M. F., J. D. Istok, and L. Semprini (2005), Push-pull test evaluation of the in situ aerobic cometabolism of chlorinated ethenes by toluene-utilizing microorganisms, *Water Science And Technology*, *52*, 35-40.

Azizian, M. F., J. D. Istok, and L. Semprini (2007), Evaluation of the in-situ aerobic cometabolism of chlorinated ethenes by toluene-utilizing microorganisms using push-pull tests, *Journal Of Contaminant Hydrology*, *90*, 105-124.

Ball, W. P., C. Buehler, T. C. Harmon, D. M. Mackay, and P. V. Roberts (1990), Characterization of a sandy aquifer material at the grain scale, *Journal of Contaminant Hydrology*, *5*, 253-295.

Ball, W. P., and P. V. Roberts (1991), Long-term sorption of halogenated organic chemicals by aquifer material. 1. Equilibrium, *Environmental Science and Technology*, *25*, 1223-1249.

Banks, D., A. Kjersti Midtgard, B. Frengstad, J. Reidar Krog, and T. Strand (1998), The chemistry of Norwegian groundwaters: II. The chemistry of 72 groundwaters from Quaternary sedimentary aquifers, *Science of the Total Environment*, *222*, 93-105.

Bauer, P., S. Attinger, and W. Kinzelbach (2001), Transport of a decay chain in homogenous porous media: analytical solutions, *Journal of Contaminant Hydrology*, *49*, 217-239.

Bear, J. (1972), *Dynamics of Fluids in Porous Media*, American Elsevier, New York.
Berthouex, P. M., and L. C. Brown (2002), *Statistics for Environmenatal Engineers:Second Edition*, Second ed., Lewis Publishers.
Bjerg, P. L., H. C. Ammentorp, and T. H. Christensen (1993), Model simulations of a field experiment on cation exchange-affected multicomponent solute transport in a sandy aquifer, *Journal of Contaminant Hydrology*, *12*, 291-311.
Bjerg, P. L., and T. H. Christensen (1993), A Field Experiment On Cation Exchange-Affected Multicomponent Solute Transport In A Sandy Aquifer, *Journal Of Contaminant Hydrology*, *12*, 269-290.
Bolster, C. H., and G. M. Hornberger (2007), On the Use of Linearized Langmuir Equations, *Soil Science Society Of America Journal*, *71*, 1796-1806.
Bottrell, S. H., S. F. Thornton, M. J. Spence, S. Allshorn, and K. H. Spence (2010), Assessment of the use of fluorescent tracers in a contaminated Chalk aquifer, *Quarterly Journal of Engineering Geology and Hydrogeology*, *43*, 195-206.
Bowman, B. T., and W. W. Sans (1983), Further water solubility determinations of insecticidal compounds, *Journal of Environmental Science and Health - Part B Pesticides, Food Contaminants, and Agricultural Wastes*, *18*, 221-227.
Bowman, R. S., and J. F. Gibbens (1992), Difluorobenzoates As Nonreactive Tracers In Soil And Ground-Water, *Ground Water*, *30*, 8-14.
Bridge, J. (2007), High-Resolution Measurement of Colloid Transport in Variably Saturated Quartz Sand Using Time Lapse Fluorescence Imaging, D.Phil thesis, University of Sheffield.
Brown, M. C., D.C. Ford (1971), Quantitative tracer methods for investigation of karst hydrology systems, with reference to the Maligne Basin area, *Transactions of the Cave Research Group of Great Britain*, *13*, 37-51.
Brusseau, M. L., and P. S. C. Rao (1989), Sorption Nonideality During Organic Contaminant Transport In Porous-Media, *Critical Reviews In Environmental Control*, *19*, 33-99.
Bugna, G. C., J. P. Chanton, C. A. Kelley, T. B. Stauffer, W. G. MacIntyre, and E. L. Libelo (2004), A field test of delta C-13 as a tracer of aerobic hydrocarbon degradation, *Organic Geochemistry*, *35*, 123-135.
Cano, M. L., and P. B. Dorn (1996), Sorption of two model alcohol ethoxylate surfactants to sediments, *Chemosphere*, *33*, 981-994.
Cantrell, K. J., D. I. Kaplan, and T. W. Wietsma (1995), Zero-valent iron for the in situ remediation of selected metals in groundwater, *Journal of Hazardous Materials*, *42*, 201-212.
Cassiani, G., L. F. Burbery, and M. Giustiniani (2005), A note on in situ estimates of sorption using push-pull tests, *Water Resources Research*, *41*, W03005.
Ceazan, M. L., E.M. Thurman, R.L. Smith (1989), Retardation of ammonium and potassium through a contaminated sand and gravel aquifer: The role of cation exchange, *Environmental Science and Technology*, *23*, 1402-1408.
Chao, H.-C., H. Rajaram, and T. Illangasekare (2000a), Intermediate-scale experiments and numerical simulations of transport under radial flow in a two-dimensional heterogeneous porous medium, *Water Resources Research*, *36*, 2869-2884.

Chao, H.-S., H. Rajaram, and T. Illangasekare (2000b), Intermediate-scale experiments and numerical simulations of transport under radial flow in a two-dimensional heterogeneous porous medium, *Water Resources Research*, *36*, 2869-2884.

Chapelle, F. H. (1993), *Ground-Water Microbiology and Geochemistry*, John Wiley and Sons, Inc, New York.

Cheng, H. F., and M. Reinhard (2006), Sorption of trichloroethylene in hydrophobic micropores of dealuminated Y zeolites and natural minerals, *Environmental Science and Technology*, *40*, 7694-7701.

Chiogna, G., C. Eberhardt, P. Grathwohl, O. A. Cirpka, and M. Rolle (2010), Evidence of compound-dependent hydrodynamic and mechanical transverse dispersion by multitracer laboratory experiments, *Environmental Science and Technology*, *44*, 688-693.

Choung, S., and R. M. Allen-King (2010), Can chlorofluorocarbon sorption to black carbon (Char) affect groundwater age determinations? *Environmental Science and Technology*, *44*, 4459-4464.

Christensen, T. H., P. Kjeldsen, P. L. Bjerg, D. L. Jensen, J. B. Christensen, A. Baun, H. J. Albrechtsen, and G. Heron (2001), Biogeochemistry of landfill leachate plumes, *Applied Geochemistry*, *16*, 659-718.

Cirpka, O. A., Å. Olsson, Q. Ju, M. A. Rahman, and P. Grathwohl (2006), Determination of Transverse Dispersion Coefficients from Reactive Plume Lengths, *Ground Water*, *44*, 212-221.

Clement, T. P., Y. Sun, B. S. Hooker, and J. N. Petersen (1998), Modeling multispecies reactive transport in ground water, *Ground Water Monitoring and Remediation*, *18*, 79-92.

Corapcioglu, M. Y., and P. Fedirchuk (1999), Glass bead micromodel study of solute transport, *Journal of Contaminant Hydrology*, *36*, 209-230.

Dahan, O., and Z. Ronen (2001), Analytical procedure for simultaneous use of seven fluorobenzoates in multitracer tests, *Ground Water*, *39*, 366-370.

Dance, J. T., and Reardon, E.J. (1983), Migration of contaminants in groundwater at a landfill: A Case Study, *Journal Of Hydrology*, *63*, 109-130.

Danquigny, C., P. Ackerer, and J. P. Carlier (2004), Laboratory tracer tests on three-dimensional reconstructed heterogeneous porous media, *Journal of Hydrology*, *294*, 196-212.

Dasch, J. M., A. S. Abdul, D. N. Rai, T. L. Gibson, and L. Grovsvenor (1997), Synergistic application of four remedial techniques at an industrial site, *Ground Water Monitoring and Remediation*, *17*, 194-209.

Davis, B. M., J. D. Istok, and L. Semprini (2002), Push-pull partitioning tracer tests using radon-222 to quantify non-aqueous phase liquid contamination, *Journal of Contaminant Hydrology*, *58*, 129-146.

Davis, B. M., J. D. Istok, and L. Semprini (2005), Numerical simulations of radon as an in situ partitioning tracer for quantifying NAPL contamination using push-pull tests, *Journal Of Contaminant Hydrology*, *78*, 87-103.

Davis, J. A., D. B. Kent, J. A. Coston, K. M. Hess, and J. L. Joye (2000), Multispecies reactive tracer test in an aquifer with spatially variable chemical conditions, *Water Resources Research*, *36*, 119-134.

Davis, S. N., D.J. Campbell, H.W. Bentley, T.J.Flynn (1985), Ground-Water Tracers, National Water Well Association, Worthington, Ohio.

Devlin, J. F., M. McMaster, and J. F. Barker (2002), Hydrogeologic assessment of in situ natural attenuation in a controlled field experiment, *Water Resources Research, 38*, 1002-1013.

Domenico, P. A., and W. S. Schwartz (1990), *Physical and Chemical Hydrogeology*, John Wiley and Sons, Inc.

Eagle, B. (2006), Parameterisation of a permo Triassic sand medium through the use of laboratory column tests, with the development and application of tracer cocktails, M.Sc. Thesis, University of Sheffield.

Ebihara, T., and P. L. Bishop (2002), Influence of supplemental acetate on bioremediation for dissolved polycyclic aromatic hydrocarbons, *Journal of Environmental Engineering*, *128*, 505-513.

Edmeades, C. E., and O. E. Clinton (1981), A simple rapid method for the measurement of exchangeavle cations and effective cation exchange capacity, *Communications in Soil Science and Plant Analysis*, *12*, 683-685.

Edward, F. N., A. R. John, A. A. Nicholas, L. M. Eugene, M. M. David, and T. Terry (2009), Monitored Natural Attenuation of Manufactured Gas Plant Tar Mono- and Polycyclic Aromatic Hydrocarbons in Ground Water: A 14-Year Field Study, *Ground Water Monitoring & Remediation*, *29*, 66-76.

Elliott, D. R., Scholes J.D., S. F. Thornton, A. Rizoulis, Banwart S.A., and S. A. Rolfe (2010), Dynamic changes in microbial community structure and function in a phenol-degrading microcosms inoculated with cells from a contaminated aquifer, *FEMS Microbiology Ecology*, *71*, 247-259.

Ferrell, R. T., and D. M. Himmelblau (1967), Diffusion coefficients of nitrogen and oxygen in water, *Journal of Chemical and Engineering Data*, *12*, 111.

Fetter, C. W. (1994), *Applied hydrogeology*, 3rd ed., Maxwell Macmillan International.

Field, J. A., R. L. Reed, J. D. Istok, L. Semprini, P. Bennett, and T. E. Buscheck (2005), Trichlorofluoroethene: A reactive tracer for evaluating reductive dechlorination in large-diameter permeable columns, *Ground Water Monitoring and Remediation*, *25*, 68-77.

Flynn, R. M., and M. Sinreich (2010), Characterisation of virus transport and attenuation in epikarst using short pulse and prolonged injection multi-tracer testing, *Water Research*, *44*, 1138-1149.

Freyberg, D. L. (1986), A natural gradient experiment on solute transport in a sand aquifer 2. Spatial moments and the advection and dispersion of nonreactive tracers, *Water Resources Research*, *22*, 2031-2046.

Gaganis, P., E. D. Skouras, M. A. Theodoropoulou, C. D. Tsakiroglou, and V. N. Burganos (2005), On the evaluation of dispersion coefficients from visualization experiments in artificial porous media, *Journal of Hydrology*, *307*, 79-91.

Gelhar, L. W., and M. A. Collins (1971), General analysis of longitudinal dispersion in nonuniform, *Water Resources Research*, *7*, 1511-1521.

Gelhar, L. W., A. L. Gutjahr, and R. L. Naff (1979), Stochastic analysis of macrodispersion in a stratified aquifer, *Water Resources Research*, *15*, 1387-1397.

Geyer, T., S. Birk, T. Licha, R. Liedl, and M. Sauter (2007), Multitracer test appoach to characterise reactive transport in karst aquifers, *Ground Water, 45*, 36-45.

Ghanem, A., S. S. Thomas, M. M. Adel, and G. J. Thoma (2003), Investigation of Fluorescent Dyes as Partitioning Tracers for Subsurface Nonaqueous Phase Liquid (NAPL) Characterization, *Journal of Environmental Engineering, 129*, 740-744.

Giesy, J. P., and K. Kannan (2002), Perfluorochemical surfactants in the environment, *Environmental Science and Technology, 36*, 146-152.

Gillham, R. W., E. A. Sudicky, J. A. Cherry, and E. O. Frind (1984), An Advection-Diffusion Concept for Solute Transport in Heterogeneous Unconsolidated Geological Deposits, *Water Resources Research, 20*, 369-378.

Gillham, R. W., and S. F. O'Hannesin (1990), Sorption of Aromatic Hydrocarbons by Materials in Construction of Ground-Water Sampling Wells, in *Ground Water and Vadose Zone Monitoring*, edited by D. M. Nielsen and A. I. Johnson, pp. 108-122, American Society for Testing and Materials, Philadelphia.

Goltz, M. N., and P. V. Roberts (1988), Simulations of physical nonequilibrium solute transport models: Application to a large-scale field experiment, *Journal of Contaminant Hydrology, 3*, 37-63.

Goltz, M. N., J. Huang, M. E. Close, M. J. Flintoft, and L. Pang (2008), Use of tandem circulation wells to measure hydraulic conductivity without groundwater extraction, *Journal of Contaminant Hydrology, 100*, 127-136.

Grathwohl, P. (1990), Influence of organic matter from soils and sediments from various origins on the sorption of some chlorinated aliphatic hydrocarbons: Implications on Koc correlations, *Environmental Science & Technology, 24*, 1687-1693.

Guswa, A. J., and D. L. Freyberg (2000), Slow advection and diffusion through low permeability inclusions, *Journal Of Contaminant Hydrology, 46*, 205.

Hageman, K. J., J. D. Istok, J. A. Field, T. E. Buscheck, and L. Semprini (2001), In situ anaerobic transformation of trichlorofluoroethene in trichloroethene-contaminated groundwater, *Environmental Science and Technology, 35*, 1729-1735.

Hageman, K. J., J. A. Field, J. D. Istok, and M. H. Schroth (2003), "Forced mass balance" technique for estimating in situ transformation rates of sorbing solutes in groundwater, *Environmental Science and Technology, 37*, 3920-3925.

Haggerty, R., M. H. Schroth, and J. D. Istok (1998), Simplified method of "push-pull" test data analysis for determining in situ reaction rate coefficients, *Ground Water, 36*, 314-324.

Ham, P. A. S., R. J. Schotting, H. Prommer, and G. B. Davis (2004), Effects of hydrodynamic dispersion on plume lengths for instantaneous bimolecular reactions, *Advances in Water Resources, 27*, 803-813.

Hess, K. M., J. A. Davis, D. B. Kent, and J. A. Coston (2002), Multispecies reactive tracer test in an aquifer with spatially variable chemical conditions, Cape Cod, Massachusetts: Dispersive transport of bromide and nickel, *Water Resources Research, 38*, 1161-1177.

Higgins, C. P., and R. G. Luthy (2006), Sorption of perfluorinated surfactants on sediments, *Environmental Science & Technology, 40*, 7251-7256.

Hoopes, J. A., and D. R. Harleman (1967), Wastewater recharge and dispersion in porous media, *Journal of the Hydraulics Division, ASCE, 93*, 51-71.

Huang, J., and M. Goltz (2006), Analytical Solutions for Solute Transport in a Spherically Symmetric Divergent Flow Field, *Transport in Porous Media, 63*, 305-321.

Huang, J. S., and C. G. Jih (1997), Deep-biofilm kinetics of substrate utilization in anaerobic filters, *Water Research, 31*, 2309-2317.

Huang, W. E., C. C. Smith, D. N. Lerner, S. F. Thornton, and A. Oram (2002), Physical modelling of solute transport in porous media: evaluation of an imaging technique using UV excited fluorescent dye, *Water Research, 36*, 1843-1853.

Huang, W. E., S. E. Oswald, D. N. Lerner, C. C. Smith, and C. Zheng (2003), Dissolved Oxygen Imaging in a Porous Medium to Investigate Biodegradation in a Plume with Limited Electron Acceptor Supply, *Environmental Science & Technology, 37*, 1905-1911.

Hunkeler, D., D. Jorger, K. Haberli, P. Hohener, and J. Zeyer (1998), Petroleum hydrocarbon mineralization in anaerobic laboratory aquifer columns, *Journal of Contaminant Hydrology, 32*, 41-61.

Hunkeler, D., P. Hohener, S. Bernasconi, and J. Zeyer (1999), Engineered in situ bioremediation of a petroleum hydrocarbon-contaminated aquifer: Assessment of mineralization based on alkalinity, inorganic carbon and stable carbon isotope balances, *Journal Of Contaminant Hydrology, 37*, 201.

Hunter, K. S., Y. Wang, and P. Van Cappellen (1998), Kinetic modeling of microbially-driven redox chemistry of subsurface environments: Coupling transport, microbial metabolism and geochemistry, *Journal of Hydrology, 209*, 53-80.

Hvilshoj, S., K. H. Jensen, and B. Madsen (2000), Single-well dipole flow tests: Parameter estimation and field testing, *Ground Water, 38*, 53-62.

Istok, J. D., M. D. Humphrey, M. H. Schroth, M. R. Hyman, and K. T. Oreilly (1997), Single-well, "push-pull" test for in situ determination of microbial activities, *Ground Water, 35*, 619-631.

Istok, J. D., J. A. Field, M. H. Schroth, T. E. Sawyer, and M. D. Humphrey (1999), Laboratory and field investigation of surfactant sorption using single-well, "push-pull" tests, *Ground Water, 37*, 589-598.

Istok, J. D., J. A. Field, M. H. Schroth, B. M. Davis, and V. Dwarakanath (2002), Single-well "push-pull" partitioning tracer test for NAPL detection in the subsurface, *Environmental Science and Technology, 36*, 2708-2716.

Jaeger, S., M. Ehni, C. Eberhardt, M. Rolle, P. Grathwohl, and G. Gauglitz (2009), CCD camera image analysis for mapping solute concentrations in saturated porous media, *Analytical and Bioanalytical Chemistry, 395*, 1867-1876.

Jaynes, D. B. (1994), Evaluation Of Fluorobenzoate Tracers In Surface Soils, *Ground Water, 32*, 532-538.

Jeong, S., M. M. Wander, S. Kleineidam, P. Grathwohl, B. Ligouis, and C. J. Werth (2008), The role of condensed carbonaceous materials on the sorption of hydrophobic organic contaminants in subsurface sediments, *Environmental Science and Technology, 42*, 1458-1464.

Jin, M. Q., M. Delshad, V. Dwarakanath, D. C. McKinney, G. A. Pope, K. Sepehrnoori, C. E. Tilburg, and R. E. Jackson (1995), Partitioning Tracer Test For

Detection, Estimation, And Remediation Performance Assessment Of Subsurface Nonaqueous Phase Liquids, *Water Resources Research*, *31*, 1201-1211.

Johnston, C. D., J. L. Rayner, and D. Briegel (2002), Effectiveness of in situ air sparging for removing NAPL gasoline from a sandy aquifer near Perth, Western Australia, *Journal of Contaminant Hydrology*, *59*, 87-111.

Jones, E. H., and C. C. Smith (2005), Non-equilibrium partitioning tracer transport in porous media: 2-D physical modelling and imaging using a partitioning fluorescent dye, *Water Research*, *39*, 5099-5111.

Kabala, Z. J. (1993), The Dipole Flow Test - A New Single-Borehole Test For Aquifer Characterization, *Water Resources Research*, *29*, 99-107.

Karapanagioti, H. K., S. Kleineidam, D. A. Sabatini, P. Grathwohl, and B. Ligouis (1999), Impacts of Heterogeneous Organic Matter on Phenanthrene Sorption: Equilibrium and Kinetic Studies with Aquifer Material, *Environmental Science & Technology*, *34*, 406-414.

Karickhoff, S. W. (1981), Semi-empirical estimation of sorption of hydrophobic pollutants on natural sediments and soils, *Chemosphere*, *10*, 833-846.

Kasnavia, T., V. De, and A. S. David (1999), Fluorescent Dye and Media Properties Affecting Sorption and Tracer Selection, *Ground Water*, *37*, 376-381.

Katz, B. G., A. R. Chelette, and T. R. Pratt (2004), Use of chemical and isotopic tracers to assess nitrate contamination and ground-water age, Woodville Karst Plain, USA, *Journal Of Hydrology*, *289*, 36-61.

Kent, D. B., J. A. Davis, L. C. D. Anderson, B. A. Rea, and J. A. Coston (2002), Effect of adsorbed metal ions on the transport of Zn- and Ni-EDTA complexes in a sand and gravel aquifer, *Geochimica Et Cosmochimica Acta*, *66*, 3017-3036.

Key, B. D., R. D. Howell, and C. S. Criddle (1997), Fluorinated organics in the biosphere, *Environmental Science and Technology*, *31*, 2445-2454.

Kiewiet, A. T., J. M. D. Vandersteen, and J. R. Parsons (1995), Trace Analysis Of Ethoxylated Nonionic Surfactants In Samples Of Influent And Effluent Of Sewage-Treatment Plants By High-Performance Liquid-Chromatography, *Analytical Chemistry*, *67*, 4409-4415.

Kiewiet, A. T., K. G. M. De Beer, J. R. Parsons, and H. A. J. Govers (1996), Sorption of linear alcohol ethoxylates on suspended sediment, *Chemosphere*, *32*, 675-680.

Kim, Y., J. D. Istok, and L. Semprini (2004), Push-pull tests for assessing in situ aerobic cometabloism, *Ground Water*, *42*, 329-327.

Kim, Y., J. H. Kim, B. H. Son, and S. W. Oa (2005), A single well push-pull test method for in situ determination of denitrification rates in a nitrate-contaminated groundwater aquifer, *Water Science And Technology*, *52*, 77-86.

Kimblin, R. T. (1995), The chemistry and origin of groundwater in Triassic sandstone and Quaternary deposits, northwest England and some UK comparisons, *Journal of Hydrology*, *172*, 293-311.

Kleikemper, J., M. H. Schroth, W. V. Sigler, M. Schmucki, S. M. Bernasconi, and J. Zeyer (2002), Activity and diversity of sulfate-reducing bacteria in a petroleum hydrocarbon-contaminated aquifer, *Applied And Environmental Microbiology*, *68*, 1516-1523.

Kleineidam, S., C. Schth, and P. Grathwohl (2002), Solubility-normalized combined adsorption-partitioning sorption isotherms for organic pollutants, *Environmental Science and Technology*, *36*, 4689-4697.

Knauss, K. G., M. J. Dibley, R. N. Leif, D. A. Mew, and R. D. Aines (2000), The aqueous solubility of trichloroethene (TCE) and tetrachloroethene (PCE) as a function of temperature, *Applied Geochemistry*, *15*, 501-512.

Kneeshaw, T. A., J. T. McGuire, E. W. Smith, and I. M. Cozzarelli (2007), Evaluation of sulfate reduction at experimentally induced mixing interfaces using small-scale push-pull tests in an aquifer-wetland system, *Applied Geochemistry*, *22*, 2618-2629.

Knezovich, J. P., F. L. Harrison, and R. G. Wilhelm (1987), The bioavailability of sediment-sorbed organic chemicals: A review, *Water, Air, and Soil Pollution*, *32*, 233-245.

Ko, S. O., and S. H. Ji (2007), In situ push-pull tests for the determination of TCE degradation and permanganate consumption rates, *Environmental Geology*, *53*, 359-364.

Korte, N., P. M. Kearl, R. L. Siegrist, M. T. Muck, and R. M. Schlosser (2000), An evaluation of horizontal recirculation using single-well tests, pumping tests, tracer tests, and the colloidal borescope, *Ground Water Monitoring and Remediation*, *20*, 78-85.

Landmeyer, J. E., F. H. Chapelle, M. D. Petkewich, and P. M. Bradley (1998), Assessment of natural attenuation of aromatic hydrocarbons in groundwater near a former manufactured-gas plant, South Carolina, USA, *Environmental Geology*, *34*, 279-292.

Lawrence, A., and P. L. McCarty (1970), Unified basis for biological treatment design and operation, *Journal of Sanitary Engineering Division, ASCE*, *96*, 757-778.

LeBlanc, D. R., S. P. Garabedian, K. M. Hess, L. W. Gelhar, R. D. Quadri, K. G. Stollenwerk, and W. W. Wood (1991), Large-Scale Natural Gradient Trace Test in Sand and Gravel,Cape Cod, Massachusetts. 1. Experimental Design and Observed Traceer Movement, *Water Resources Research*, *27*, 895-910.

Lekamge, L. R. S. K. (2010), Designing a Dipole Flow Tracer Test setup to measure low level Foc values in aquifers, University of Sheffield, MSc Thesis.

Lendvay, J. M., F. E. Loffler, M. Diollhopf, M. R. Aiello, G. Daniels, B. Z. Fathepure, M. Gebhard, R. Heiner, R. Helton, J. Shi, R. Krajmalnik-Brown, E. Petrovskis, R.Hickey, J. M. Tiedje and P. Adrians (2003). Bioreactive barriers: A comparison of bioaugmentation and biostimulation for chlorinated solvent remediation. *Environmental Science and Technology*, *37*, 1422-1431.

Lerner, D. N., S. F. Thornton, M. J. Spence, S. A. Banwart, S. H. Bottrell, J. J. Higgo, H. E. H. Mallinson, R. W. Pickup, and G. M. Williams (2000), Inneffective natural attenuation of degradable organic compounds in a phenol-contaminated aquifer, *Ground Water*, *38*, 922-928.

Liebeg, E. W., and T. J. Cutright (1999) The investigation of enhanced bioremediation throught the addition of macro and micro nutrients in a PAH contaminated soil. *International Biodeterioration and Biodegradation*, *44*, 55-64.

Liu, L., J. A. Tindall, M. J. Friedel, and W. Zhang (2007), Biodegradation of organic chemicals in soil/water microcosms system: Model development, *Water, Air, and Soil Pollution, 178*, 131-143.

Lu, G., T. P. Clement, C. Zheng, and T. H. Wiedemeier (1999), Natural attenuation of BTEX compounds: Model development and field-scale application, *Ground Water, 37*, 707-717.

Lyman, W. J., Reehl, W.F., Rosenblatt, D.H. (1990), *Handbook of Chemical Estimation Methods*, American Chemical Society.

Mackay, D. M., W. P. Ball, and M. G. Durant (1986), Variability of aquifer sorption properties in a field experiment on groundwater transport of organic solutes: Methods and preliminary results, *Journal of Contaminant Hydrology*, *1*, 119-132.

Maier, U., and P. Grathwohl (2006), Numerical experiments and field results on the size of steady state plumes, *Journal of Contaminant Hydrology*, *85*, 33-52.

Major, D.W., M. L. McMaster, E. E. Cox, E. A. Edwards, S. M. Dworatzek, E. R. Hendrickson, M. G. Starr, J. A. Payne, and L. W. Buonamici (2002). Field demonstration of successful bioaugmentation to achieve dechlorination of tetrachloroethene to ethene. *Environmental Science and Technology*, *36*, 5106-5116.

Mailloux, B. J., S. Devlin, M. E. Fuller, T. C. Onstott, M. F. DeFlaun, K. H. Choi, M. Green-Blum, D. J. P. Swift, J. McCarthy, and H. Dong (2007), The limited role of aquifer heterogeneity on metal reduction in an Atlantic coastal plain determined by push-pull tests, *Applied Geochemistry*, *22*, 974-995.

Mathias, S. A. (2010), Transient Divergent Flow and Transport in an Infinite Anisotropic Porous Formation, *Ground Water*, *48*, 438-441.

Neuweiler, I., S. Attinger, and W. Kinzelnbach (2001), Macrodispersion in a radially diverging flow field with finite peclet numbers 1. Perturbation theory approach, *Water Resources Research*, *37*, 481-493.

Nguyen, T. H., and W. P. Ball (2006), Absorption and adsorption of hydrophobic organic contaminants to diesel and hexane soot, *Environmental Science & Technology*, *40*, 2958-2964.

Nguyen, T. H., H. H. Cho, D. L. Poster, and W. P. Ball (2007), Evidence for a pore-filling mechanism in the adsorption of aromatic hydrocarbons to a natural wood char, *Environmental Science & Technology*, *41*, 1212-1217.

North, J. (2008), Capturing and quantifying a dipole flow tracer test using a novel imaging technique, MSc Thesis, University of Sheffield.

Nowack, B., T. Lutzenkirchen, P. Behra, and L. Sigg (1996), Modeling the adsorption of metal-EDTA complexes onto oxides, *Environmental Science & Technology*, *30*, 2397-2405.

Nowack, B., and L. Sigg (1996), Adsorption of EDTA and metal-EDTA complexes onto goethite, *Journal Of Colloid And Interface Science*, *177*, 106-121.

Nowack, B., and L. Sigg (1997), Dissolution of Fe(III)(hydr)oxides by metal-EDTA complexes, *Geochimica Et Cosmochimica Acta*, *61*, 951-963.

Nye, P. H., Z. Gerstl, and T. Galin (1994), Prediction Of Sorption By Soils Of Volatile Hydrocarbon Mixtures, *Journal Of Environmental Quality*, *23*, 1031-1037.

Oates, P. M., C. Castenson, C. F. Harvey, M. Polz, and P. Culligan (2005), Illuminating reactive microbial transport in saturated porous media: Demonstration of a visualization method and conceptual transport model, *Journal of Contaminant Hydrology*, *77*, 233-245.

Olsson, Ã., and P. Grathwohl (2007), Transverse dispersion of non-reactive tracers in porous media: A new nonlinear relationship to predict dispersion coefficients, *Journal of Contaminant Hydrology*, *92*, 149-161.

Oya, S., and A. J. Valocchi (1998), Transport and biodegradation of solutes in stratified aquifers under enhanced in situ bioremediation conditions, *Water Resources Research*, *34*, 3323-3334.

Peng, J., and A. Wan (1997), Measurement of Henry's constants of high-volatility organic compounds using a headspace autosampler, *Environmental Science and Technology*, *31*, 2998-3003.

Peng, J., and A. Wan (1998), Effect of ionic strength on Henry's constants of volatile organic compound, *Chemosphere*, *36*, 2731-2740.

Pennell, K. D., L. M. Abriola, and W. J. Weber (1993), Surfactant-Enhanced Solubilization Of Residual Dodecane In Soil Columns.1. Experimental Investigation, *Environmental Science & Technology*, *27*, 2332-2340.

Pickens, J. F., R. E. Jackson, K. J. Inch, and W. F. Merritt (1981), Measurement of distribution coefficients using a radial injection dual-tracer test, *Water Resources Research*, *17*, 529-544.

Pignatello, J. J., S. Kwon, and Y. F. Lu (2006), Effect of natural organic substances on the surface and adsorptive properties of environmental black carbon (char): Attenuation of surface activity by humic and fulvic acids, *Environmental Science & Technology*, *40*, 7757-7763.

Pitterle, M. T., R. G. Andersen, J. T. Novak, and M. A. Widdowson (2005), Push-pull tests to quantify in situ degradation rates at a phytoremediation site, *Environmental Science & Technology*, *39*, 9317-9323.

Pombo, S. A., J. Kleikemper, M. H. Schroth, and J. Zeyer (2005), Field-scale isotopic labeling of phospholipid acetate-degrading sulfate-reducing fatty acids from bacteria, *Fems Microbiology Ecology*, *51*, 197-207.

Pon, G., and L. Semprini (2004), Anaerobic reductive dechlorination of 1-chloro-1-fluoroethene to track the transformation of vinyl chloride, *Environmental Science & Technology*, *38*, 6803-6808.

Ptak, T., and G. Schmid (1996), Dual-tracer transport experiments in a physically and chemically heterogeneous porous aquifer: effective transport parameters and spatial variability, *Journal of Hydrology*, *183*, 117-138.

Ptak, T., M. Piepenbrink, and E. Martac (2004), Tracer tests for the investigation of heterogeneous porous media and stochastic modelling of flow and transport - a review of some recent developments, *Journal Of Hydrology*, *294*, 122-163.

Rawajfih, Z., and N. Nsour (2006), Characteristics of phenol and chlorinated phenols sorption onto surfactant-modified bentonite, *Journal Of Colloid And Interface Science*, *298*, 39-49.

Razzaque, M. M., and P. Grathwohl (2008), Predicting organic carbon-water partitioning of hydrophobic organic chemicals in soils and sediments based on water solubility, *Water Research*, *42*, 3775-3780.

Rees, H. C., S. E. Oswald, S. A. Banwart, R. W. Pickup, and D. N. Lerner (2007), Biodegradation Processes in a Laboratory-Scale Groundwater Contaminant Plume Assessed by Fluorescence Imaging and Microbial Analysis, *Appl. Environ. Microbiol.*, *73*, 3865-3876.

Reznek, S., W. Hayden, and M. Lee (1979), Fluorescein Tracer Technique For Detection Of Groundwater Contamination, *Journal American Water Works Association*, *71*, 586-587.

Reusser, D. E., J. D. Istok, H. R. Beller, J. A. Field (2002). In situ transformation of deuterated toluene and xylene to benzylsuccinic acid analogues in BTEX-contamaninated aquifers. *Environmental Science and Technology*, *36*, 4127-4134.

Ritter, L., K. Solomon, P. Sibley, K. Hall, P. Keen, G. Mattu, and B. Linton (2002), Sources, pathways, and relative risks of contaminants in surface water and groundwater: A perspective prepared for the Walkerton inquiry, *Journal of Toxicology and Environmental Health - Part A*, *65*, 1-142.

Rivett, M. O. and R. M. Allen-King (2003). A controlled field experiment on groundwater contamination by a multicomponent DNAPL: Dissolved plume migration. *Journal of Contaminant Hydrology*, *66*, 117-146.

Roden, E. E., and T. D. Scheibe (2005), Conceptual and numerical model of uranium(VI) reductive immobilization in fractured subsurface sediments, *Chemosphere*, *59*, 617.

Rolle, M., C. Eberhardt, G. Chiogna, O. A. Cirpka, and P. Grathwohl (2009), Enhancement of dilution and transverse reactive mixing in porous media: Experiments and model-based interpretation, *Journal of Contaminant Hydrology*, *110*, 130-142.

Roos, G. N. (2009), Development of the Dipole Flow and Reactive Tracer Test (DFRTT) for Aquifer Parameter Estimation, M.A.Sc Thesis, University of Waterloo.

Sabatini, D. A., and T. Al Austin (1991), Characteristics of Rhodamine WT and Fluorescein as Adsorbing Ground-Water Tracers, *Ground Water*, *29*, 341-349.

Salanitro, J. P., P. C. Johnson, G. E. Spinnler, P. M. Maner, H. L.Wisniewski, C. Bruce (2000). Field-scale demonstration of enhanced MTBE bioremediation through aquifer bioaugmentation and oxygenation. *Environmental Science and Technology*, *34*, 4152-4162.

Sanford, W. E., P. G. Cook, and J. C. Dighton (2002), Analysis of a vertical dipole tracer test in highly fractured rock, *Ground Water*, *40*, 535-542.

Schincariol, R. A., and F. W. Schwartz (1990), An experimental investigation of variable density flow and mixing in homogeneous and heterogeneous media, *Water Resources Research*, *26*, 2317-2329.

Schroth, M. H., J. D. Istok, M. R. Hyman, and K. T. Oreilly (1997), Field-scale measurements of in situ microbial metabolic activities, in *In Situ And On-Site Bioremediation, Vol 2*, edited, pp. 387-392.

Schroth, M. H., J. D. Istok, and R. Haggerty (2001), In situ evaluation of solute retardation using single-well push-pull tests, *Advances In Water Resources*, *24*, 105-117.

Schroth, M. H., and J. D. Istok (2005), Approximate solution for solute transport during spherical-flow push-pull tests, *Ground Water*, *43*, 280-284.

Schwarzenbach, R. P., W. Giger, E. Hoehn, and J. K. Schneider (1983), Behavior of Organic Compounds during Infiltration of River Water to Groundwater. Field Studies, *Environmental Science and Technology*, *17*, 472-479.

Schwarzenbach, R. P., and J. Westall (1985), Sorption of hydrophobic trace organic compounds in groundwater systems, *Water Science and Technology*, *17*, 39-55.

Schwarzenbach, R. P., Gschwend, P.M., Imboden, D.M. (1993), *Environmental Organic Chemistry*, Wiley-Interscience, New York.

Simunek, J., M. Th. van Genuchten, M. Sejna, N. Toride, and F. J. Leij (1999), The STANMOD computer software for evaluating solute transport in porous media using analytical solutions of convection-dispersion equation. Versions 1.0 and 2.0, edited, p. 32pp, IGWMC - TPS - 71, International Ground Water Modeling Center, Colorado School of Mines, Golden, Colorado.

Smalley, A. (2004), Commissioning Plan: Sandbox Test Facility, edited, University of Sheffield.

Smart, P. L., and I. M. S. Laidlaw (1977), An Evaluation of Some Fluorescent Dyes for Water-Tracing, *Water Resources Research*, *13*, 15-33.

Sposito, G., et al (1983), Cation Selectivity in Sodium-Calcium, Sodium-Magnesium, and Calcium-Magnesium Exchange on Eyoming Bentonite at 298K, *Soil Science Society Of America Journal*, *47*, 917-921.

Stamm, J. (1995), Vertical circulation flows for vadose and groundwater zone in situ (bio-)remediation, in *In Situ Aeration: Air Sparging, Bioventing, And Related Remediation Processes*, edited, pp. 483-493.

Stauffer, F. (2007), Impact of highly permeable sediment units with inclined bedding on solute transport in aquifers, *Advances in Water Resources*, *30*, 2194-2201.

Stavropoulos, G. G., P. Samaras, and G. P. Sakellaropoulos (2008), Effect of activated carbons modification on porosity, surface structure and phenol adsorption, *Journal Of Hazardous Materials*, *151*, 414-421.

Stumm, W., and J. J. Morgan (1996), *Aquatic Chemistry: Third Edition*, Wiley-Interscience.

Sudicky, E. A., J. A. Cherry, and E. O. Frind (1983), Migration of contaminants in groundwater at a landfill: A case study: 4. A natural-gradient dispersion test, *Journal of Hydrology*, *63*, 81-108.

Sudicky, E. A. (1986), Natural gradient experiment on solute transport in a sand aquifer: Spatial variability of hydraulic conductivity and its role in the dispersion process, *Water Resources Research*, *22*, 2069-2082.

Sutton, D. J., Z. J. Kabala, D. E. Schaad, and N. C. Ruud (2000), The dipole-flow test with a tracer: a new single-borehole tracer test for aquifer characterization, *Journal Of Contaminant Hydrology*, *44*, 71-101.

Tan, X. (2009), Developing a Practical Methodology to Predict Quantitatively Ammonium Sorption in Red-Bed Sandstone, D Phil Thesis, University of Sheffield.

Therrien, R., R. G. Mclaren, E. A. Sudicky, and R. M. Panday (2005), HydroGeoSphere: A three -dimensional numerical model describing fully - integrated subsurface and surface flow and solute transport. Copyright R. Therrien, E.A. Sudicky, R.G. McLaren Groundwater Simulations Group, edited.

Thornton, S. F., D. N. Lerner, and J. H. Tellam (1996), Attenuation of landfill leachate-Triassic sandstone interactions, edited by D. o. t. Environment.

Thornton, S. F., M. I. Bright, D. N. Lerner, and J. H. Tellam (2000a), Attenuation of landfill leachate by UK Triassic sandstone aquifer materials 2. Sorption and degradation of organic pollutants in laboratory columns, *Journal Of Contaminant Hydrology*, *43*, 355-383.

Thornton, S. F., J. H. Tellam, and D. N. Lerner (2000b), Attenuation of landfill leachate by UK Triassic sandstone aquifer materials 1. Fate of inorganic pollutants in laboratory columns, *Journal Of Contaminant Hydrology*, *43*, 327-354.

Thornton, S. F., D. N. Lerner, and J. H. Tellam (2001), Attenuation of Landfill leachate by clay liner materials in laboratory columns: 2. Behaviour of inorganic contaminants, *Waste Management and Research*, *19*, 70-88.

Thornton, S. F., S. Quigley, M. J. Spence, S. A. Banwart, S. Bottrell, and D. N. Lerner (2001), Processes controlling the distribution and natural attenuation of dissolved phenolic compounds in a deep sandstone aquifer, *Journal of Contaminant Hydrology*, *53*, 233-267.

Thornton, S. F., J. H. Tellam and D. N. Lerner (2005). Experimental and modelling approaches for the assessment of chemical impacts of leachate migration from landfills: A case study of a site on the Triassic sandstone aquifer in the UK East Midlands. *Geotechnical and Geological Engineering*, *23*, 811-829.

Tiedeman, C. R., and P. A. Hsieh (2004), Evaluation of longitudinal dispersivity estimates from simulated forced- and natural-gradient tracer tests in heterogeneous aquifers, *Water Resources Research*, *40*, W01512.

Tsutsumi, K., Y. Matsushima, and A. Matsumoto (1993), Surface heterogeneity of modified active carbons, *Langmuir*, *9*, 2665-2669.

Tuxen, N., H.-J. Albrechtsen, and P. L. Bjerg (2006), Identification of a reactive degradation zone at a landfill leachate plume fringe using high resolution sampling and incubation techniques, *Journal of Contaminant Hydrology*, *85*, 179-194.

UK Government (2000), 2000 No.3148. Water, England and Wales: The Water Supply (Water Quality) Regulations 2000, edited.

USGS (2008), PHREEQC (Version 2)--A Computer Program for Speciation, Batch-Reaction, One-Dimensional Transport, and Inverse Geochemical Calculations. http://wwwbrr.cr.usgs.gov/projects/GWC_coupled/phreeqc/, edited.

Valocchi, A. J., R. L. Street, and P. V. Roberts (1981), Transport of ion-exchanging solutes in groundwater: chromatographic theory and field simulation, *Water Resources Research*, *17*, 1517-1527.

van Reeuwijk, L. P. (Ed.) (1992), *Procedures for Soil Analysis*, 3rd ed., International Soil Reference and Information Centre.

Vancheeswaran, S., M. R. Hyman, and L. Semprini (1999), Anaerobic biotransformation of trichlorofluoroethene in groundwater microcosms, *Environmental Science and Technology*, *33*, 2040-2045.

Vandenbohede, A., A. Louwyck, and L. Lebbe (2008), Identification and reliability of microbial aerobic respiration and denitrification kinetics using a single-well push-pull field test, *Journal Of Contaminant Hydrology*, *95*, 42-56.

Vasudevan, D., R. L. Fimmen, and A. B. Francisco (2001), Tracer-grade rhodamine WT: Structure of constituent isomers and their sorption behavior, *Environmental Science & Technology*, *35*, 4089-4096.

Voegelin, A., V. M. Vulava, and R. Kretzschmar (2001), Reaction-based model describing competitive sorption and transport of Cd, Zn, and Ni in an acidic soil, *Environmental Science & Technology*, *35*, 1651-1657.

Watson, I. A. (2004), Modelling of natural attenuation processes in groundwater using adaptive and parallel numerical methods, PhD Thesis, University of Sheffield.

Watson, I. A., S. E. Oswald, S. A. Banwart, R. S. Crouch, and S. F. Thornton (2005), Modeling the dynamics of fermentation and respiratory processes in a groundwater plume of phenolic contaminants interpreted from laboratory- to field-scale, *Environmental Science and Technology*, *39*, 8829-8839.

Welty, C., and L. W. Gelhar (1994), Evaluation of longitudinal dispersivity from nonuniform flow tracer tests, *Journal of Hydrology*, *153*, 71.

Werth, C. J., O. A. Cirpka, and P. Grathwohl (2006), Enhanced mixing and reaction through flow focusing in heterogeneous porous media, *Water Resources Research*, *42*, W12414.

Whittenbury, R., K. C. Phillips, and Wilkinson.J.F. (1970), Enrichment, Isolation And Some Properties Of Methane-Utilizing Bacteria, *Journal Of General Microbiology*, *61*, 205-218.

Wilkin, R. T., R. W. Puls, and G. W. Sewell (2003), Long-term performance of permeable reactive barriers using zero-valent iron: geochemical and microbiological effects, *Ground water*, *41*, 493-503.

Wilson, J. L., and P. J. Miller (1978), Two-dimensional plume in uniform groundwater, *Journal of the Hydraulics Division, ASCE*, *104*, 503-514.

Wilson, R. D., and D. M. Mackay (1993), The Use Of Sulfur-Hexafluoride As A Conservative Tracer In Saturated Sandy Media, *Ground Water*, *31*, 719-724.

Wilson, R. D., D. M. Mackay, and J. A. Cherry (1997), Arrays of unpumped wells for plume migration control by semi-passive in situ remediation, *Ground Water Monitoring and Remediation*, *17*, 185-193.

Wilson, R. D. (1998), Partitioning Tracers for Soil Characterisation, in *Encyclopedia of Environmental Analysis and Remediation*, edited by R. A. Meyers, pp. 3415-3436, John Wiley and Sons, Inc.

Wilson, R. D., D. M. Mackay, and K. M. Scow (2002), In Situ MITBE Biodegredation Supported by Diffusive Oxygen Release, *Environmental Science and Technology*, *36*, 190-199.

Wilson, R. D., S. F. Thornton, and D. M. MacKay (2004), Challenges in monitoring the natural attenuation of spatially variable plumes, *Biodegradation*, *15*, 359-369.

Xia, G. S., and W. P. Ball (1999), Adsorption-partitioning uptake of nine low-polarity organic chemicals on a natural sorbent, *Environmental Science & Technology*, *33*, 262-269.

Xiang, J., and Z. J. Kabala (1997), Performance of the steady-state dipole flow test in layered aquifers, *Hydrological Processes*, *11*, 1595-1605.

Yong, R. N., A. M. O. Mohamed, and B. P. Warkentin (1992), *Principles of Contaminant Transport in Soils*, Elsevier.

Yuan, C., and C. T. Jafvert (1997), Sorption of linear alcohol ethoxylate surfactant homologs to soils, *Journal Of Contaminant Hydrology*, *28*, 311-325.

Zhang, W. X., E. J. Bouwer, and W. P. Ball (1998), Bioavailability of hydrophobic organic contaminants: Effects and implications of sorption-related mass transfer on bioremediation, *Ground Water Monitoring And Remediation*, *18*, 126-138.

Zheng, C. (1990), A modular three-dimensional transport model for simulation of advection, dispersion and chemical reactions of contaminants in groundwater systems, prepared for USEPA Kerr Environmental Research Laboratory, Ada, OK 7482.

Zheng, Z. P., P. Aagaard, and G. D. Breedveld (2002), Sorption and anaerobic biodegradation of soluble aromatic compounds during groundwater transport. 1. Laboratory column experiments, *Environmental Geology*, *41*, 922-932.

Zlotnik, V., and G. Ledder (1996), Theory of dipole flow in uniform anisotropic aquifers, *Water Resources Research*, *32*, 1119-1128.

Zlotnik, V. A., and B. R. Zurbuchen (1998), Dipole probe: Design and field applications of a single-borehole device for measurements of vertical variations of hydraulic conductivity, *Ground Water*, *36*, 884-893.

Zlotnik, V. A., B. R. Zurbuchen, and T. Ptak (2001), The steady-state dipole-flow test for characterization of hydraulic conductivity statistics in a highly permeable aquifer: Horkheimer Insel Site, Germany, *Ground Water*, *39*, 504-516.

Zlotnik, V. A., and B. R. Zurbuchen (2003), Field study of hydraulic conductivity in a heterogeneous aquifer: Comparison of single-borehole measurements using different instruments, *Water Resources Research*, *39*, 1101-1112.

9. Appendix A: Supplementary information for Chapters 2 and 3

9.1. Imaging box design

For the imaging experiments in Chapters 2 and 3 an acrylic box of internal dimensions 150 cm x 75 cm x 2.6 cm was especially constructed. This was of larger dimensions than previous designs to reduce boundary effects in tests. The lowest internal dimension was 2.6 cm to allow a well screen of 1 inch nominal diameter to closely fit in the box. The acrylic was 8 mm thick to provide extra strength to the box, reducing the effect of bulging and chance of damage when the box was full. The box was held together by epoxy cement and steel bolts. There are 16 bolts aligned vertically at either end at 5 cm intervals, see Figure 9-1, and 31 bolts spaced at 5 cm intervals along the bottom. The bolts at the end attached the box to painted steel stands. Stainless steel retraining blocks were placed at the top of the box 1/3 and 2/3 across the length, to prevent bulging and provide support when the box was full.

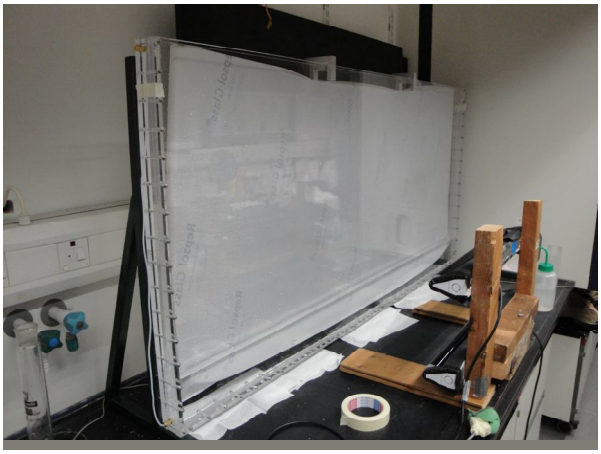

Figure 9-1: Imaging box before well screen insertion and bead packing

Ports were placed 1 cm down from the top and bottom of each end of the box to work as overflow and head regulation/ purging points respectively, see Figure 9-2. A Swagelock fitting was used connecting to 3 mm tubing. End chambers were originally constructed from 98 micron wire surrounding chicken mesh shaped to the box, see Figure 9-3. The 98 micron mesh size is smaller than the beads, while the chicken mesh provides rigidity. Upon filling beads managed to exploit small gaps around the sides to get into the end chambers. Therefore a 15 mm slotted rigid pipe was inserted into the meshed sections to

act as end chambers, see Figure 9-2. A small amount of mesh was glued to the end of the bottom Swagelock fittings to prevent clogging with beads

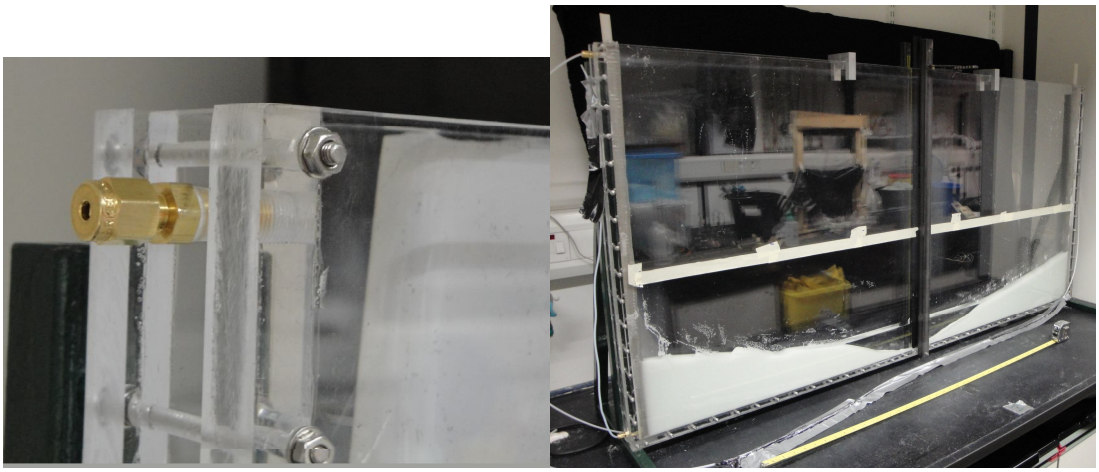

Figure 9-2: Left: Close up of top left overflow port, tubing unattached. Right: Imaging box with restraining bars and new end chambers being packed

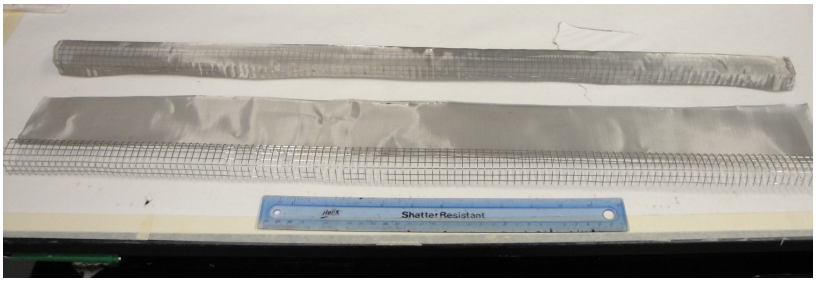

Figure 9-3: Original end chambers in construction

After initial experiments steel restraining bars were attached to the box, halfway along its length, see Figure 9-2. This reduced bulging of the box caused by the weight of beads and water when the box was filled. These was attached to the box at the bottom with a steel bolt and held together at the top with a clamp, see Figure 9-4. The bars are dark in colour and did not to significantly affect imaging.

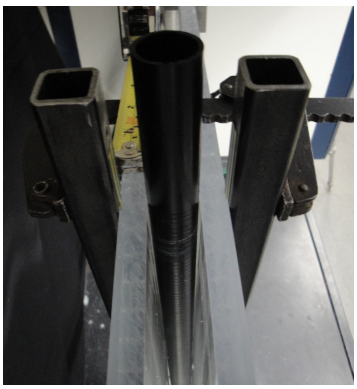

Figure 9-4: Close up of top of restraining bars, clamp and well screen

9.2. **Dipole/ Push-pull apparatus design**

The dipole flow and push-pull tracer test apparatus was constructed from silicon and uPVC disks on a threaded stainless steel rod. The uPVC disks were 10 mm radius and 7 mm thick and the silicon disks were 10 mm radius and 3 mm thick. Each had a central hole for the rod and extra holes for tubing if needing. These holes closely fitted the tubing, preventing leakage. When the silicon and uPVC disks were tightened together the silicon disks bulged outwards. The bulging provided a friction seal on the inside of the well screen. Groupings of the disks formed packers. It was found that using 2 silicon disks for every uPVC seal provided the best seal. This arrangement is useful as it allows different packer and chamber configurations to be made from the same parts. To tighten the packers 2 nuts were used to prevent slipping during apparatus insertion.

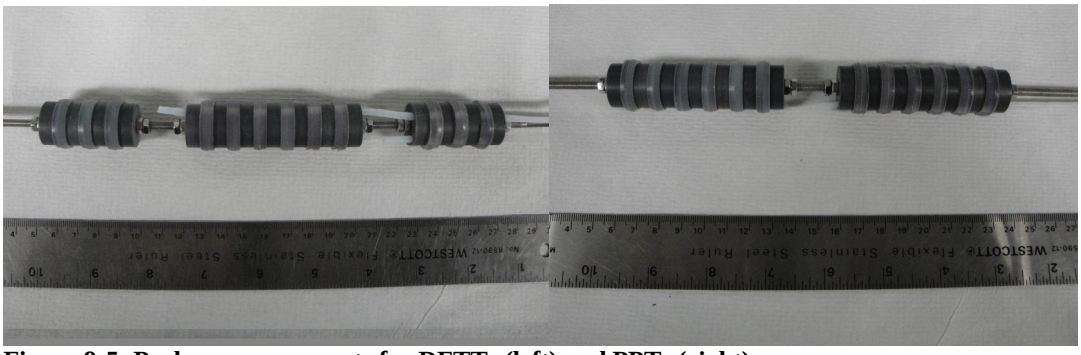

Figure 9-5: Packer arrangements for DFTTs (left) and PPTs (right)

9.3. **Well screen design**

The well screen was required to be small enough to fit in the box, have a similar open area to a field well screen, horizontal slots, regular slot spacing and a slot size smaller than the bead size used. Horizontal slots were important to help prevent short circuiting of flow up the well screen sides during tests.

A 1 inch nominal size well screen was required to fit the well. This was obtained from Boode UK, however it was not possible to obtain a 1 inch well screen with the correct slotting. Therefore slots were self cut. The bottom of the size range of the smallest beads used was 0.3 mm; therefore this was used as the top limit of slot size. A Citadel Razor (or Modelling) saw was obtained from Games Workshop. This produced slots of 0.27-0.28 mm. The open area of slotted segments of well screens commercially available with 0.2-

0.3 mm slots was measured at 6 to 7.8 %. It was calculated that if a slot was cut every 4 mm in the obtained well screen it would produce an open area of approximately 7.5 % in the slotted segments. A rig was made to insure that slots were made regularly and in line. Slots were cut manually and rough edges were filed down. The well screen's outer diameter was 27 mm and internal diameter 23 mm. The internal width of the tank was made to 26 mm, therefore two sides of the well screen were filed down after slotting to ensure a tight fit.

9.4. **Image calibration**

Initially 19 digital SLR camera set-ups were tested (see Table 9-1) to decide upon a preferential configuration. The lens was set to a wide angle (24 mm) to have a large field of view and a custom white balance was used. The initial configurations were based upon initial experimentation by North [2008] who used a thinner tank wall and different camera.

Calibration stocks were made up the same way as the stocks in experiments (see Chapter 2). Stocks were made to approximately 40, 20, 10, 5 and 2.5 mg/l. Imaging was performed in a small box 0.3 m wide and 0.3 m high with the same depth as the main imaging box. The camera lens was positioned 55 cm away from the box and focused on the bead surface. The 2 UV black lights were positioned above and below the lens 47 cm away from the box. Calibrations were performed in a dark room. UV lights were switched on for 10 minutes before imaging began. Bridge [2007] showed this was sufficient time for the UV intensity to stabilise. Green light intensity was measured in the centre of the calibration box. Initial calibrations were performed for both 0.3-0.355 mm and 1-1.4 mm bead sizes.

From the 19 different set-ups tested, configurations 11 and 14 were initially chosen as the best (see Figure 9-6). Better results were obtained with configuration 14 over 11 during a trial imaging experiment, therefore this configuration was chosen for all future tests. Calibrations were performed every time a new stock solution was made up. For later calibrations separate calibration curves were produced for separate parts of the calibration

box and a small piece of grey card was used as a constant reflector to normalise image intensity.

Table 9-9-1: Camera settings of configurations tested.

Configuration Number	Shutter Speed (sec)	F Stop	ISO
1	0.5	8	400
2	0.5	6.3	400
3	0.5	4.5	400
4	0.5	8	200
5	0.5	8	800
6	2.5	8	100
7	2.5	8	200
8	2.5	10	100
9	2.5	8	400
10	2.5	6.3	100
11	0.8	8	100
12	0.8	8	200
13	0.8	8	400
14	1.3	8	100
15	1.3	8	200
16	1.3	8	400
17	2	8	100
18	2	8	200
19	2	8	400

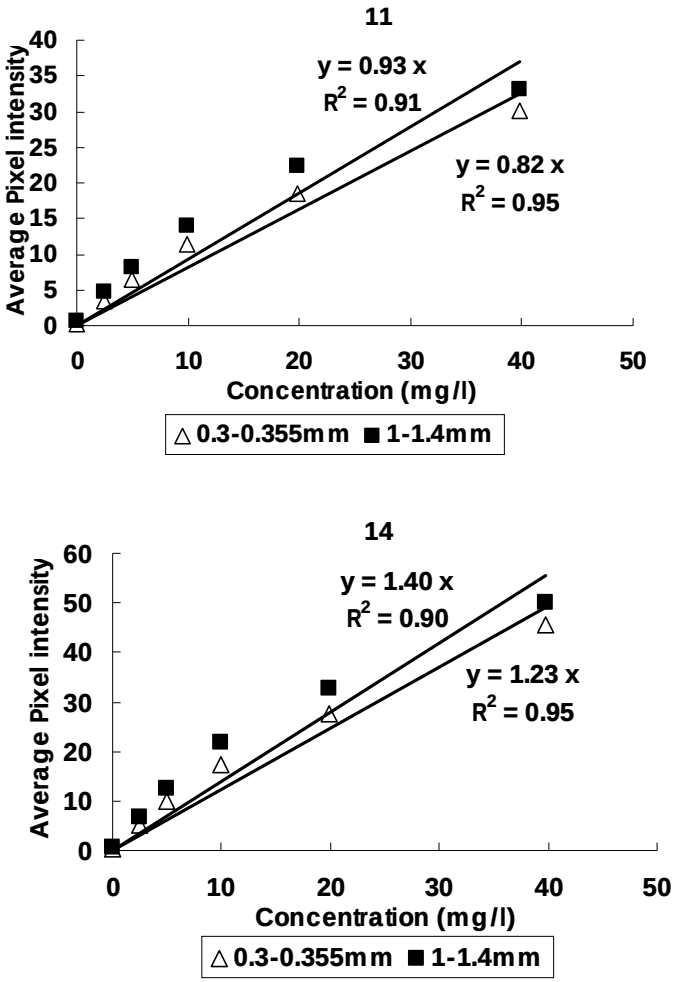

Figure 9-6: Initial calibrations for calibration configuration numbers 11 and 14 for 0.3-0.355 mm and 1-1.4 mm beads.

9.5. **Image penetration depth test**

A test was performed to estimate the effective imaging penetration depth. The calibration box was filled with the 300 to 355 µm beads saturated with deionised water. A small tube was positioned in the centre of the box and 40 mg/l fluorescein stock solution was pumped in at 1 ml/min. Images were taken every 10 to 15 seconds until the plume was deemed sufficiently large to be fully across the calibration box. Intensity was measured at the centre of the plume and concentration estimated from calibrations. For modelling it was assumed that the centre of the plume had a surface parallel with the sides of the

calibration box. Therefore estimated concentration should be directly related to the radius of the plume.

Initial modelling assumed that the tube was in the centre of the box, see Figure 9-7. Fluorescein image concentrations were detected later than expected; this suggested that effective image penetration did not reach all the way to the centre of the calibration box (1.3 cm in). Also concentrations increased faster than expected; this suggested that the small inflow tube was not directly in the centre. Radiuses above 1.3 cm in Figure 9-7 represent that the plume is spreading along the box side.

An improved fit to the measured concentrations was obtained when the inflow tube was assumed to be 0.2 cm off centre towards the front of the calibration box and the camera, see Figure 9-8. This suggested that effective image penetration was between 0.6 and 0.7 cm.

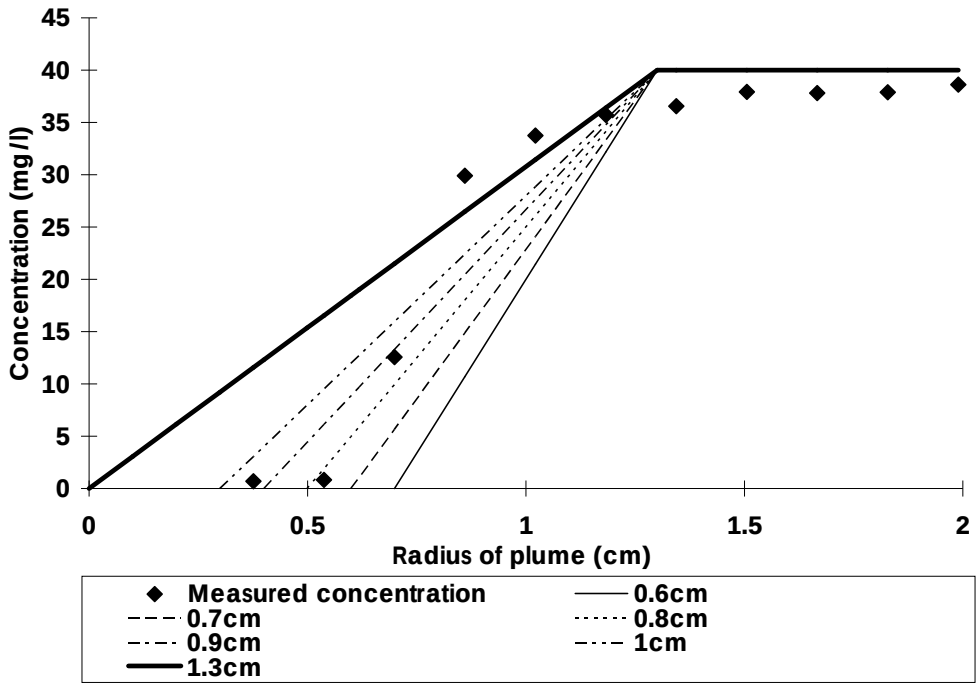

Figure 9-7: Results of plume growth test and modelling assuming the plume centre is 1.3 cm in. Modelled lines are the estimated measured concentration assuming image penetration to that depth.

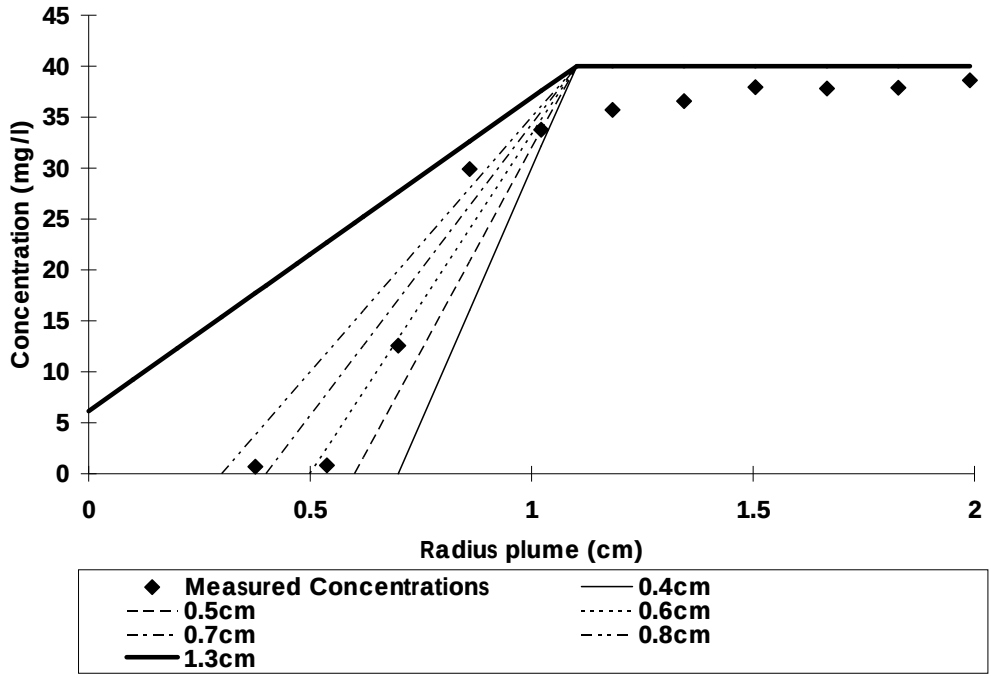

Figure 9-8: Results of plume growth test and modelling assuming the plume centre is 1.1 cm in. Modelled lines are the estimated measured concentration assuming image penetration to that depth.

Performing this test was crucial to allow effective modelling of imaging tests in HydroGeoSphere© and understanding total mass imaging data. Tests where mass in the box predicted by imaging was less than was expected from input concentrations and aqueous samples indicated that the majority of mass was focused in the centre of the box beyond the imaging penetration depth. When the mass from imaging was the same as that expected from input concentrations and aqueous samples it suggested that the mass was well mixed across the depth of the box.

9.6. **Beer Lambert law calculations**

The transmissivity (T) of electromagnetic radiation through a solution is related to the path length (L), concentration of the solution (C) and the molar absorbtivity (ε) of the solution [Bridge, 2007].

$$T = \frac{I}{I_0} = 10^{-AL} \tag{9.1}$$

$$A = \varepsilon LC \tag{9.2}$$

where A is the absorbance, I_o the original light intensity and I the intensity after passing through the substance. This formula can be used to estimate the proportion different depths into the bead pack contribute to imaging intensities. In this study it is used as a theoretical check to go with the practical test presented above. The A of the fluorescein calibration solutions was measured on a Biochrom S2100 diode array spectrophotometer for fluorescein adsorption and emission wavelengths, to allow calculation of ε. For the adsorption wavelength an average of ε of 42679.2 /M /cm was calculated. For the emission wavelength A was consistent with varying concentration hence ε was variable (Table 9-2).

Table 9-2: Table to show variation of molar absorbtivity with fluorescein concentration

Fluorescein Concentration (mg/l)	ε (/M /cm)
2.5	16216.53
5	7643.038
10	5084.282
20	3987.672
40	2741.525

The absorption ε was used to calculate transmissivity at a range of path lengths for light entering the box, while the emission ε was used to calculate transmissivity from the imaged point to the outside of the box. The total transmissivity is the multiplication of these two paths. Air and acrylic, representing the path between the camera and the bead pack, were assumed to have an absorbance of 0. It was attempted to measure A for calibration solution saturated beads. However the beads showed a low transmissivity on the spectrophotometer. This may be due to scattering of light away from the measuring device. Light could be seen through the box during the experiment and plume edges were reasonably sharp, suggesting any scattering affects largely cancelled out. The calculations are for a porosity of 1, giving conservative estimates especially if the beads have a negligible effect on absorbance.

The absorbance during the adsorption phase was seen to be more dominant than the emission phase on total transmissivity. Imaging were calculated to penetrate further into the box at lower concentrations. At a fluorescein concentration of 2.5 mg/l the mean

penetration depth of imaging was calculated to be approximately 0.7 cm (Table 9-3), similar to that estimated in the physical test. However at the test input concentration of 40 mg/l this was calculated to be less than 0.1 cm (Table 9-4). Modelling of the imaging point 2 cm out from the well screen parallel to the centre of the well chamber during the isotropic push-pull test (Chapter 2) gave best fits at a depths of approximately 0 cm and 0.4 cm, suggesting that the Beer Lambert calculations give a reasonable estimate of mean imaging depth.

Table 9-3: Transmissivities of light through 2.5 mg/l Fluorescein solution and contributions to light intensity seen in image taken for different depths into the box.

L (cm)	Adsorption (T)	Emission (T)	Total (T)	Segment Contribution (%)	Cumulative Contribution (%)
0.1	1	1	1	0	0
0.2	0.862548	0.945366	0.815424	18.457629	18.457629
0.3	0.801078	0.919179	0.736334	7.9089459	26.366575
0.4	0.743989	0.893717	0.664916	7.1418426	33.508418
0.5	0.690969	0.86896	0.600424	6.449142	39.95756
0.6	0.641727	0.84489	0.542188	5.8236278	45.781188
0.7	0.595994	0.821486	0.4896	5.2587833	51.039971
0.8	0.55352	0.79873	0.442113	4.7487241	55.788695
0.9	0.514073	0.776605	0.399232	4.2881366	60.076832
1	0.477438	0.755092	0.360509	3.8722222	63.949054
1.1	0.443413	0.734176	0.325543	3.4966482	67.445702
1.2	0.411813	0.713839	0.293968	3.1575018	70.603204
1.3	0.382465	0.694065	0.265455	2.8512498	73.454454
1.4	0.355208	0.674839	0.239708	2.5747018	76.029156
1.5	0.329894	0.656145	0.216459	2.3249767	78.354132
1.6	0.306384	0.63797	0.195464	2.0994729	80.453605
1.7	0.28455	0.620297	0.176506	1.8958411	82.349446
1.8	0.264271	0.603115	0.159386	1.71196	84.061406
1.9	0.245438	0.586408	0.143927	1.5459138	85.60732
2	0.227947	0.570164	0.129967	1.3959728	87.003293
2.1	0.211702	0.55437	0.117361	1.2605748	88.263868
2.2	0.196615	0.539014	0.105978	1.1383093	89.402177
2.3	0.182603	0.524083	0.095699	1.0279025	90.430079
2.4	0.16959	0.509565	0.086417	0.9282044	91.358284
2.5	0.157504	0.49545	0.078035	0.8381761	92.19646
2.6	0.146279	0.481726	0.070467	0.7568798	92.95334

Table 9-9-3: Calculated cumulative contributions to image intensity for different fluorescein concentrations at different depths into the box.

L	Concentration (mg/l)				
(cm)	2.5	5	10	20	50
0.1	9.699186	15.99922	28.17648	47.62388	71.60338
0.2	18.45763	29.43868	48.41382	72.56742	91.93632
0.3	26.36658	40.72794	62.94899	85.63188	97.71019
0.4	33.50842	50.21101	73.38866	92.47454	99.34977
0.5	39.95756	58.17686	80.8868	96.05845	99.81536
0.6	45.78119	64.86823	86.27223	97.93557	99.94757
0.7	51.03997	70.48904	90.14023	98.91873	99.98511
0.8	55.7887	75.21056	92.91837	99.43367	99.99577
0.9	60.07683	79.17668	94.91372	99.70338	99.9988
1	63.94905	82.50825	96.34686	99.84464	99.99966
1.1	67.4457	85.30679	97.37618	99.91863	99.9999
1.2	70.6032	87.65759	98.11548	99.95738	99.99997
1.3	73.45445	89.63228	98.64647	99.97768	99.99999
1.4	76.02916	91.29103	99.02785	99.98831	100
1.5	78.35413	92.6844	99.30177	99.99388	100
1.6	80.45361	93.85484	99.4985	99.99679	100
1.7	82.34945	94.83802	99.63981	99.99832	100
1.8	84.06141	95.66389	99.7413	99.99912	100
1.9	85.60732	96.35764	99.81419	99.99954	100
2	87.00329	96.94039	99.86655	99.99976	100
2.1	88.26387	97.4299	99.90415	99.99987	100
2.2	89.40218	97.8411	99.93116	99.99993	100
2.3	90.43008	98.1865	99.95055	99.99997	100
2.4	91.35828	98.47665	99.96449	99.99998	100
2.5	92.19646	98.72037	99.97449	99.99999	100
2.6	92.95334	98.9251	99.98168	100	100

.

9.7. **Photodegradation assessment**

A test was performed to assess potential decreases in fluorescein fluorescence intensity when left in front of UV lights for a period of time, which may lead to underestimation of imaged tracer concentrations in tests. This applied to tracer in the stock solution and tracer at the front of the imaging box. 20 mg/l fluorescein stock solution was left in the

calibration box in front of the UV lights for 6 hours, a similar time to which experiments were run over. Samples were taken and their fluorescence was measured on a Perkin Elmer LS30 luminescence spectrometer. No significant decrease in fluorescence was seen over the 6 hours, with values ranging from 96-106% of the starting value. This suggests that negligible photodegradation occurs over test timescales.

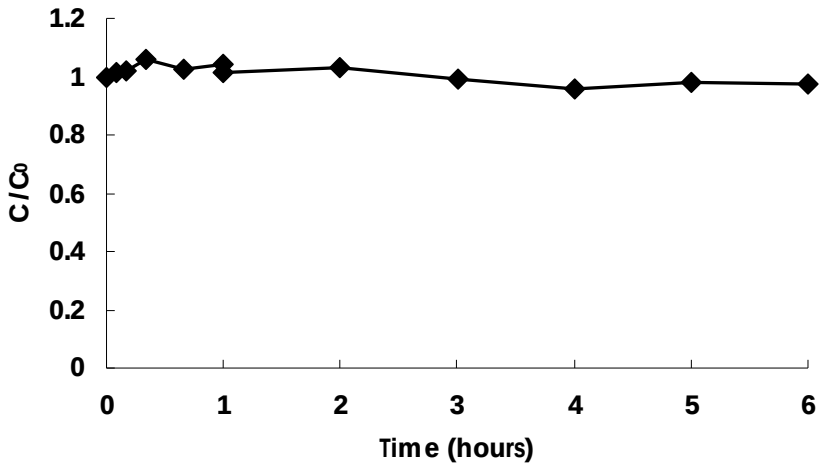

Figure 9-9: Variation of fluorescein fluorescence when left in front of UV lights. Normalised fluorescence is plotted against time.

9.8. Example HydroGeoSphere© input files

Presented are example input files used for modelling dipole flow and push-pull tracer tests in chapters 2 and 3. There is a brief explanation for each respective file. Repetition between files has been omitted. All the input files used are in the DVD-r (E1) provided, along with a copy of the program.

a. mprops file

```
!-----------------------------------------
porous medium

k isotropic
0.00715

specific storage
0.0

porosity
0.366
```

```
longitudinal dispersivity
0.001

transverse dispersivity
0.001

vertical transverse dispersivity
0.001

tortuosity
1.0

end material
!----------------------------------------

porous medium 2

k isotropic
0.0326

specific storage
0.0

porosity
0.366

longitudinal dispersivity
0.001

transverse dispersivity
0.001

vertical transverse dispersivity
0.001

tortuosity
1.0

end material
```

This is the material properties file that is referenced from the main input grok file. Porous medium represent in the low hydraulic conductivity zone and porous medium 2 the high hydraulic conductivity zone. Longitudinal, transverse and vertical transverse dispersivities are in the x,y,z direction respectively. As flow in the experiments is on a variety of vectors these values are set to be the same. All values are in SI units.

b. Dipole Flow Tracer Test grok file

PROBLEM DESCRIPTION

This is the input file from the experiment with a high hydraulic conductivity layer bisecting the centre of the central packer. Problem description generates a header to go on the top of files created and here refers to the imaging test experiment number.

GRID GENERATION

This section details the finite element matrix defined for the model. Greater resolution is desired for the centre of the box where the majority of tracer flow will occur. The first 2 numbers (A,B) on each line refer to the section on the axis that the last 3 (C,D,E) describe. C is the minimum grid spacing applying from A, E the maximum and D is the multiplier. All units are SI.

GENERAL SIMULATION

Units and the type of simulation are specified.

POROUS MEDIA PROPERTIES

The values from the mprops file are used to define properties to the entire grid and specific zones 3 cm thick in the z-axis either side of the well, representing the layer of different hydraulic conductivity. The blocks are defined by their first and last point in each axis the values being x_1, x_2 , y_1, y_2 , z_1, z_2.

POROUS MEDIA FLOW

The head and flow conditions are specified for the grid. Two planes either end of the x-axis are set to 0.73 m to represent constant head boundaries. A restart head file is used from a conditioning run, which is the same input file minus tracer flow and only lasting for 10 minutes, this allows equilibrisation of heads before tracer injection. Blocks are made inactive defining the packers in the well screen.

WELL PROPERTIES

Top and bottom of the well, pumping start and flow rate, centre of pumping and the radius of the well are defined for pumping wells which represent the injection and

extraction chambers. The best way to model open well segments was found to be to consider them as pumped wells with a negligible flow rate.

SOLUTE TRANSPORT

The solute properties are defined. A low diffusion coefficient was set as it was assumed dispersivity would be dominant at the flow rates used. No weighting was applied to velocities. The injection period of the tracer from the first defined well is set. Also the constant head boundaries are also assigned as 0 concentration boundaries. This section is not used in the model run to obtain the restart head file.

TIMSTEP CONTROLS

Definition of model run times and time steps, as well as output times at which contour plots can later be generated from.

OUTPUT

Position of observation points defined by their x,y and z co-ordinates. Observations points are defined for a number of different depths into the beads.

```
!------------------------- Problem description
Horizontal layer IT11
end title
!------------------------- Grid generation
generate blocks interactive
grade x
0.58  0.0    0.002  1.5  0.05

grade x
0.58  0.92  0.002  1  0.002

grade x
0.92  1.50   0.002  1.5  0.05

grade y
0.026 0.0     0.00325 1 0.00325

grade z
0.255  0.0    0.002  1.5  0.05

grade z
0.255  0.495  0.002  1  0.002

grade z
0.495  0.72   0.002  1.5  0.05

end generate block interactive
end grid generation
!------------------------- General simulation
parameters
units: kilogram-metre-second
finite difference mode
echo to output
transient flow
do transport
!------------------------- Porous media properties
use zone type
porous media

properties file
DFTT.mprops

clear chosen zones
choose zone number
1
read properties
porous medium

clear chosen elements
choose elements block
0.0, 0.737
0.0, 0.026
0.36, 0.39

choose elements block
0.763, 1.50
0.0, 0.026
0.36, 0.39

new zone
2

clear chosen zones
choose zone number
2
read properties
porous medium 2

!------------------------- Porous media flow
restart file for heads
DFTTco.hen

clear chosen nodes

choose nodes x plane
0.0
1e-5

choose nodes x plane
1.50
1e-5

specified head
1
0.0 0.73

clear chosen nodes
clear chosen elements

Choose elements block
0.737, 0.763
0.0, 0.026
0.4455, 0.4755

Choose elements block
0.737, 0.763
0.0, 0.026
0.3415, 0.4085

Choose elements block
0.737, 0.763
0.0, 0.026
0.2745, 0.3045

Make element inactive

echo flow boundary conditions

!------------------------- Well properties
make well
```

```
Injection
0.75, 0.013, 0.3045
0.75, 0.013, 0.3415
1
0,9.333e-8
0.75, 0.013, 0.3230
0.013
0.013

!5.6* ml/min equal to 9.333e-8 m3/sec

make well
Extraction
0.75, 0.013, 0.4085
0.75, 0.013, 0.4455
1
0,-9.333e-8
0.75, 0.013, 0.4270
0.013
0.013

make well
top
0.75, 0.013, 0.4755
0.75, 0.013, 0.72
1
0,-1e-20
0.75, 0.013, 0.50
0.013
0.013

make well
bottom
0.75, 0.013, 0.0
0.75, 0.013, 0.2745
1
0,-1e-20
0.75, 0.013, 0.4270
0.013
0.013

!-------------------------- Solute Transport

solute
name
Fluorescein
free-solution diffusion coefficient
1.0d-10
end solute

echo to output

control volume
Upstream weighting of velocities
1.0,1.0,1.0

specified well concentration
1
1
1,0,906.
!15.1 min injection starting

clear chosen nodes

choose nodes x plane
0.0
1e-5

choose nodes x plane
1.50
1e-5

specified concentration
1
0.0,18030,0.0

echo transport boundary conditions

!-------------------------- Timestep controls
generate target times
0.0          ! start time
10           ! initial timestep
1.05          ! timestep multiplier
120          ! maximum timestep
18030         ! end time

output times
1920.
18030.
end

!-------------------------- Output
make observation point
extraction
0.75, 0.013, 0.427

make observation point
injection
0.75, 0.013, 0.323

make observation point
injection side 1
0.783, 0.0, 0.3230

make observation point
injection side 2
0.783, 0.00325, 0.3230

make observation point
injection side 3
0.783, 0.0065, 0.3230
```

make observation point
injection side 4
0.783, 0.00975, 0.3230

make observation point
extraction side 1
0.783, 0.0, 0.4270

make observation point
extraction side 2
0.783, 0.00325, 0.4270

make observation point
extraction side 3
0.783, 0.0065, 0.4270

make observation point
extraction side 4
0.783, 0.00975, 0.4270

make observation point
Point A 1
0.773, 0.0, 0.3985

make observation point
Point A 2
0.773, 0.00325, 0.3985

make observation point
Point A 3
0.773, 0.0065, 0.3985

make observation point
Point A 4
0.773, 0.00975, 0.3985

make observation point
extraction bottom side 1
0.783, 0.0, 0.4085

make observation point
extraction bottom side 2
0.783, 0.00325, 0.4085

make observation point
extraction bottom side 3
0.783, 0.0065, 0.4085

make observation point
extraction bottom side 4
0.783, 0.00975, 0.4085

make observation point
extraction top side 1
0.783, 0.0, 0.4455

make observation point
extraction top side 2
0.783, 0.00325, 0.4455

make observation point
extraction top side 3
0.783, 0.0065, 0.4455

make observation point
extraction top side 4
0.783, 0.00975, 0.4455

c. Push-pull injection grok file

The set-up of the file is very similar to the DFTT grok file. The main differences are:

1. Horizontal layer at a slightly different depth

2.2 immobile blocks representing packers defined instead of 3

3. Different well set-up, with 1 injection well and 2 negligible flow rate wells representing open sections

4. Tracer injected for a longer period

5. Different time steps and test run times

6. Different position of observation points

d. Push-Pull extraction grok file

A large proportion of this file is similar to the injection phase grok file. Head and concentration data is carried forward from the injection phase with the grok file linking to the hen and cen files. The injection well is swapped for an extraction well and the timestep controls have been changed.

```
!------------------------- Problem description
Push Pull Test IT9
end title
!------------------------- Grid generation
As DFTT grok file
!------------------------- General simulation
 As DFTT grok file
!------------------------- Porous media properties
use zone type
porous media

properties file
PPI.mprops

clear chosen zones
choose zone number
1
read properties
porous medium

clear chosen elements
choose elements block
0.0, 0.737
0.0, 0.026
0.345, 0.375

choose elements block
0.763, 1.50
0.0, 0.026
0.345, 0.375

new zone
2

clear chosen zones
choose zone number
2
read properties
porous medium 2

!------------------------- Porous media flow
As DFTT grok file
clear chosen nodes
clear chosen elements

Choose elements block
0.737, 0.763
0.0, 0.026
0.3785, 0.4455

Choose elements block
0.737, 0.763
0.0, 0.026
0.2745, 0.3415

Make element inactive
echo flow boundary conditions

!------------------------- Well properties
make well
Injection
0.75, 0.013, 0.3785
0.75, 0.013, 0.3415
1
0,4.78825e-8
0.75, 0.013, 0.36
0.013
0.013

!2.87295 ml/min equal to 4.78825*e-8 m3/sec.

make well
top
0.75, 0.013, 0.72
0.75, 0.013, 0.4455
1
0,-1e-20
0.75, 0.013, 0.60
0.013
0.013

make well
bottom
0.75, 0.013, 0.2745
0.75, 0.013, 0.00
1
0,-1e-20
0.75, 0.013, 0.20
0.013
0.013

!------------------------- Solute Transport

As DFTT grok file

specified well concentration
1
1
1,0,4722.
!80 min injection

clear chosen nodes

choose nodes x plane
0.0
1e-5

choose nodes x plane
1.50
1e-5
```

```
specified concentration
1
0.0,7115,0.0

echo transport boundary conditions

!-------------------------- Timestep controls
generate target times
0.0          ! start time
10           ! initial timestep
1.05          ! timestep multiplier
30          ! maximum timestep
7115         ! end time

output times
7115
end

!-------------------------- Output
make observation point
well
0.75, 0.013, 0.36

make observation point
top well
0.75, 0.013, 0.50

make observation point
side 2cm 1
0.783, 0.0, 0.36

make observation point
side 2cm 2
0.783, 0.00325, 0.36

make observation point
side 2cm 3
0.783, 0.0065, 0.36

make observation point
side 2cm 4
0.783, 0.00975, 0.36

make observation point
side 4cm 1
0.803, 0.0, 0.36

make observation point
side 4cm 2
0.803, 0.00325, 0.36

make observation point
side 4cm 3
0.803, 0.0065, 0.36

make observation point
side 4cm 4
0.803, 0.00975, 0.36

make observation point
side 4cm U 1
0.803, 0.0, 0.39

make observation point
side 4cm U 2
0.803, 0.00325, 0.39

make observation point
side 4cm U 3
0.803, 0.0065, 0.39

make observation point
side 4cm U 4
0.803, 0.00975, 0.39

make observation point
side 4cm D 1
0.803, 0.0, 0.33

make observation point
side 4cm D 2
0.803, 0.00325, 0.33

make observation point
side 4cm D 3
0.803, 0.0065, 0.33

make observation point
side 4cm D 4
0.803, 0.00975, 0.33
```

!---------- Problem description
Push Pull Test PP9 E
end title
!---------- Grid generation
As Push-Pull Injection grok file
!---------- General simulation parameters
As Push-Pull Injection grok file
!---------- Porous media properties
As Push-Pull Injection grok file
!---------- Porous media flow
restart file for heads
PPIo.hen
As Push-Pull Injection grok file

!---------- Well properties
make well
Extraction
0.75, 0.013, 0.3785
0.75, 0.013, 0.3415
1
0,-4.7778e-8
0.75, 0.013, 0.36
0.013
0.013

!2.866 ml/min equal to 4.7777*e-8 m3/sec.

As Push-Pull Injection grok file
!---------- Solute Transport

As Push-Pull Injection grok file

restart file for concentrations
PPIo.cen

As Push-Pull Injection grok file

!---------- Timestep controls
generate target times
0.0 ! start time
10 ! initial timestep
1.05 ! timestep multiplier
30 ! maximum timestep
14410 ! end time

output times
7000
14410
end

!---------- Output
As Push-Pull Injection grok file

10. Appendix B: Supplementary information for Chapters 4-6

10.1. Fluorescence-pH relationship of fluorescein

Measured fluorescein fluorescence at a fixed concentration has been seen to vary in experiments. These include early column tests, where measured concentrations at the end of the column were greater than expected from the stock (Chapter 4), and also imaging experiments (Chapter 2 and 3), where fluorescein intensity is 3-4 times greater than expected in breakthrough curve aqueous samples. For both these situations the pH of the output solution was greater than the stock solution. For column experiments pH changed from approximately 6 to 10 and in the imaging tests from approximately 7 to 10. Variation in fluorescence with pH has been seen before [Smart and Laidlaw, 1977], but reduction of fluorescence was only seen to be significant below a pH of 7.

A test was performed titrating fluorescein to different pHs and measuring the fluorescence. One litre of 2×10^{-2} M fluorescein puriss aqueous solution was made up in a background of synthetic groundwater as used in the column experiments. It was required to add 0.8g of sodium hydroxide to the solution so that the fluorescein fully dissolved. The pH of the starting solution was 12.1. Hydrochloric acid (0.1 M) was used to titrate the solution to other values.

There was a large drop of fluorescence from pH 12.11 to 11.02, see Figure 10-1. Then at lower pHs the reduction of fluorescence was linearly related to the reduction of pH. This shows that in these conditions fluorescein fluorescence is pH dependant from pH 3 to 12. It is not understood why there is a large drop at first. The general trend probably relates to the mechanism of fluorescence. Fluorescence depends on free electrons on the molecule oxygens, these become more available at high pH when the molecule loses its hydrogens and becomes a -1 charge anion then a -2 charge dianion.

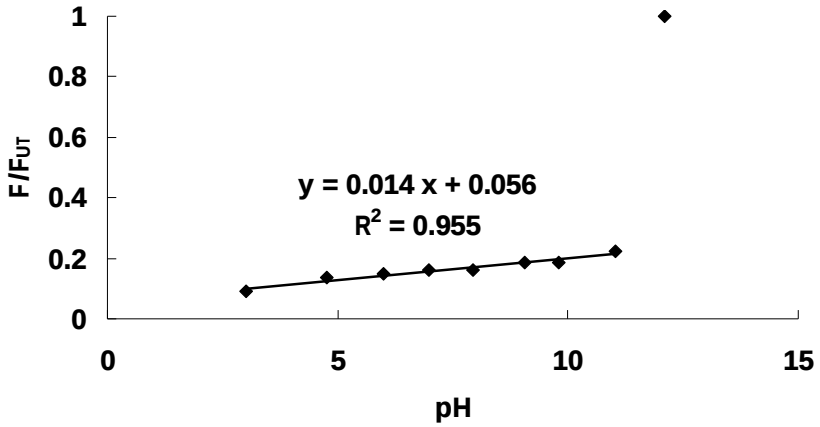

Figure 10-1: Graph of solution fluorescence over fluorescence of untitrated $2x10^{-2}$M fluorescein puriss solution vs. pH

10.2. **Ion chromatography detection limits**

Table 10-10-1: Lower limits of reliable detection in mg/l of ion chromatography analysis. Defined as 10 % of the lowest standard.

Acetate	Cl^-	NO_2^-	Br^-	NO_3^-	SO_4^-	PO_4^-	Na^+	K^+	Mg^{2+}	Ca^{2+}
0.25	0.4	0.25	0.6	0.5	1.13	0.79	0.125	0.25	0.2	0.388

10.3. **XRD analysis method**

X-ray diffraction analysis of the Permo-Triassic sand was performed at the Department of Materials Science and Engineering on a Philips PW1710/00 X-ray diffractometer using Cu K-alpha radiation. Aggregates in the sand were gently broken up by pestle and mortar prior to analysis. Samples were scanned over a 2θ angular range of 10-70˚, at a rate of 0.5˚ a minute and step size of 0.2˚.

10.4. **Example PHREEQC input file and explanation**

Fast Calibration Test for Column a

```
SOLUTION 1-18 Eq Effluent
    temp      25
    pH        7.55
    pe        4
    redox     pe
    units     mg/kgw
    density   1
    Cl        163.826
    S(6)      49.442
    Na        32.8
    Mg        16.9
    Ca        94.1
```

```
    K         19.1
    Alkalinity 32 mg/kgw as Ca0.5(CO3)0.5
    -water    1 # kg
EXCHANGE 1-18
    X       0.068236836
    -equilibrate with solution 1
EXCHANGE_SPECIES
Na+ + X- = NaX
    log_k     0
    -gamma    4 0.075
Ca+2 + 2X- = CaX2
    log_k     0.75
    delta_h   7.2 kJ
    -gamma    5 0.165
K+ + X- = KX
    log_k     0.7
    delta_h   -4.3 kJ
    -gamma    3.5 0.015
Mg+2 + 2X- = MgX2
    log_k     0.5
    delta_h   7.4 kJ
    -gamma    5.5 0.2
EQUILIBRIUM_PHASES 1
   Calcite   -0.6 0.1
   CO2(g)    -3.42 0.01
SOLUTION 0 NaBr
    temp      25
    pH        5.3
    pe        4
    redox     pe
    units     mg/kgw
    density   1
    Br        818.354
    Cl        164.29
    S(6)      49.691
    Na        277.3
    Ca        80.4
    Mg        14.4
    K         27.6
    Alkalinity 3 mg/kgw as Ca0.5(CO3)0.5
    -water    1 #
TRANSPORT
    -cells                 18
    -shifts                73
    -time_step             390.55555 # seconds
    -flow_direction        forward
    -boundary_conditions   flux flux
    -lengths               18*0.0416666666666667
    -dispersivities        18*0.00534
    -correct_disp          true
    -diffusion_coefficient 0
    -print_cells           18
    -punch_cells           18
    -warnings              true
USER_PUNCH
    -headings Pore_vol
    -start
```

```
    10 PUNCH (STEP_NO + .5) / 18.
SELECTED_OUTPUT
    -file                  9a.sel
    -reset                 false
    -time                  true
    -ph                    true
    -alkalinity            true
    -totals                Br  Na  Ca  Mg  K
END
```

```
SOLUTION 1-18 Eq Effluent
```

This is the composition of the time zero sample in the columns. It represents an equilibrium chemistry between the saturating solution and the column that occurs throughout all cells in the column before tracer flushing.

```
EXCHANGE 1-18
```

This sets up sorption equilibrium throughout the column. The number represents the amount of exchange sites in Mol/litre. Initial values are converted from the independently obtained sand CEC (Chapter 4) in meq/100g, using column properties.

```
EXCHANGE_SPECIES
```

This is a list of the cation exchange reactions that are in the experiment. The log Ks of reaction (Chapter 4) are varied from PHREEQC default. The new Ks for the experiment were obtained from trial and error curve fitting.

```
EQUILIBRIUM_PHASES 1
```

This is the list of the main mineral species that are in equilibrium with the column. The first numbers are target saturation indexes. The saturation indexes cannot go over these values. The second amount is the maximum amount of mineral allowed to dissolve to reach the saturation indexes. The mineral block is set to be in equilibrium with cell 1 at the start of the experiment. The equilibrium will migrate through the column with the tracer front. This setup is used to model reactions triggered by the tracer. The model does not allow for the mineral phases to be in equilibrium with cell 0 at the start of the experiment.

```
SOLUTION 0 NaBr
```

This is the composition of the tracer solution. It is said to be at cell 0 at the start of the experiment i.e. will be input only.

TRANSPORT

This summarises the column set up and hydraulic parameters. There are 18 cells in the column. 73 shifts will occur in the experiment. A shift is when the chemistry of 1 cell passes into the next. The time step is how long it takes for each shift. This was back calculated from the pore volume time achieved for bromide in STANMOD. Length is length of the cell. Dispersivities is the bromide dispersivity calculated by STANMOD for the BTC, applied to each cell.

USER_PUNCH

This is set up code for the calculation of dimensionless pore volume time, which will then be a column in the output file.

SELECTED_OUTPUT

This designates what will be produced in the output file and the file name. Here the totals of Br, Na, Ca, Mg and K at each time step are to be shown, as well as the pH, time and alkalinity.

10.5. **Sorption of trichlorofluoroethene to column material assessment**

It was desired to delineate the contribution to retardation of trichlorofluoroethene (TCFE) in column studies of sorption onto the uPVC column wall from sorption onto the sand. Rigid uPVC is considered to be reasonably unreactive and sorbing to hydrocarbons [Gillham and O'Hannesin, 1990]. Due to this and cost effectiveness over stainless steel it is often used as a well material. However as TCFE is a relatively unstudied compound it was considered important to quantify any sorption. Batch tests were not considered suitable as the total surface area added to a batch would be hard to quantify due to there being many small flakes of uPVC or serration along cut edges. A column test was decided to be the most appropriate method. The uPVC column was packed with 1-1.4 mm silicon beads. After packing the column was saturated with synthetic groundwater. Porosity was

measured at 0.357.

An estimate of the amount of sorption due to the beads was attempted through batch tests. In 70 ml hypovials approximately 48 ml of 1.12 mg/l TCFE was added to 60 g of beads sealed with no head space with crimp tops and left to equilibrate for a day. The concentrations left in the water averaged 1.132 ± 0.055 ppm; this was above the estimated concentration of 1.126 mg/l. Therefore it was assumed sorption to the beads was negligible.

The column experiments were performed in the same way as in those described in Chapter 6. A 10^{-2} M Br and 1 mg/l TCFE aqueous solution was pumped through the column at 2.32 ml / min. Samples were collected up to every 30 minutes and run on the Clarus GC ECD. Modelling of the data with STANMOD indicated a retardation of TCFE of 1.08 relative to Br. This correlates with a K_d of 0.016 cm^3/g for the entire column and, assuming sorption only onto the column surface, 0.209 mg of TCFE sorbing to each m^3 of uPVC surface. As the internal surface area of the column is 0.129 m^3 this suggests sorption onto uPVC is not too significant. This small amount of sorption onto the column was taken into account when calculating K_ds in later column experiments.

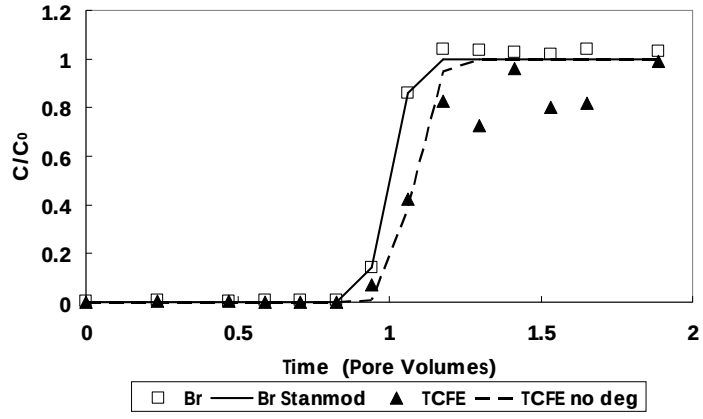

Figure 10-2: Graph of column test of Br and TCFE aqueous solution pumped through a silicon bead packed column.

11. Appendix C: Sandbox experiments

11.1. Introduction

The original project plan involved work in a man made aquifer known as the "sandbox". This was a 2 m x 2 m wide and 1m deep box. Chambers at opposite ends allowed the manipulation of head levels. There was a central 2 inch diameter well. Multilevel points allowed the sampling of aqueous samples in 10 cm depth and horizontal intervals, starting 15 cm out from the well along lines splitting the box into 4 even quadrants. Sand was packed to 5-10 cm below the top of the box. The sand is the same Permo-Triassic sand that was used in column experiments and grain size assessment (Chapter 4-6). A dipole apparatus was specially made with inflatable rubber packers.

Dipole flow tracer tests and push-pull tests were to be undertaken in the sandbox to investigate and compare the behaviour of tracer cocktails, in two single well forced gradient tests. This was to be a controlled 3-D environment, which could be modelled. This was to be the next step up from the column experiments. The effects of set-up parameters and background head gradient were also to be investigated.

Work was abandoned in the sandbox as results suggested tracer transport predominantly happened across the sides of the well screen. As the initial plan of tests focusing on tracer cocktails was never carried out, I have not considered it applicable to present the work in terms of methodology, results and conclusions. I have instead presented the tests that I performed in the sandbox in chronological order, the problems which they suggested and the actions undertaken to try to overcome these problems.

11.2. Initial dipole flow tracer test performed

A tracer test was performed with the dipole positioned centrally in the box. The middle packer end packers and chambers were all 10 cm long. Tracer was injected in the bottom chamber and extracted from the top chamber. Water was pumped round at a flow rate of 140 ml /min. NaBr aqueous tracer solution was injected into this background flow for 10 minutes at 5.6 ml /min, giving an end Br concentration of around 400 mg/l. The main

pump used was a Watson Marlow 503S, for tracer injection an Istmatec ISM832A was used.

Pressure transducers were located in the chambers and gave reliable readings and good calibrations. Readings were taken with a UNI-T UT70D professional multimeter. The readings taken during pressure field equilibration before the tracer test, see Figure 11-1, show a rapid change at the start when the pump is switched on. This is followed by a slow decrease in the pressure head in the injection and extraction chambers and lowering of the well water table. This suggests that the extraction chamber is hydraulically connected to the borehole, lowering its level. In turn this has reduced the total head in both dipole probe chambers. Readings suggest a bulk hydraulic conductivity of 1.53×10^{-5} m/s, using the analytical solution of Zlotnik and Ledder [1996].

Tracer concentrations injected into the well increased during the injection phase up from 400 mg/l to 575.72 mg/l Br. Also 24.09 mg/l of Br was measured in the borehole after 24 minutes. These observations suggest that water can travel easily between the chambers and borehole. It is unlikely that the packers were the problem as they were always inflated to high pressures. This suggests the presence of voids or mobile zones around the well. This theory is also supported by the breakthrough curve results, see Figure 11-2. They peak at a concentration of 0.810 C/C_0 at a t_d of 2.70, which quickly tales after the peak. The high concentration is not typical for aquifer peaks and the dimensionless time is similar to the short circuit peak that was seen in DFTT2 (Chapter 2). Quick tailing suggests mass is lost quickly to other parts of the box and not recovered. There is no sign of a peak representing transport through the aquifer.

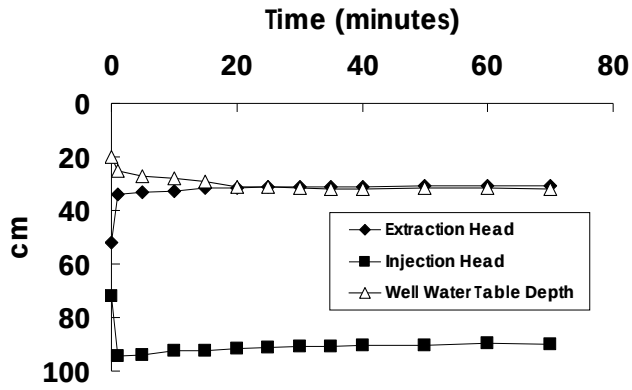

Figure 11-1: Chamber heads and well water table depth before tracer injection of initial dipole flow tracer test.

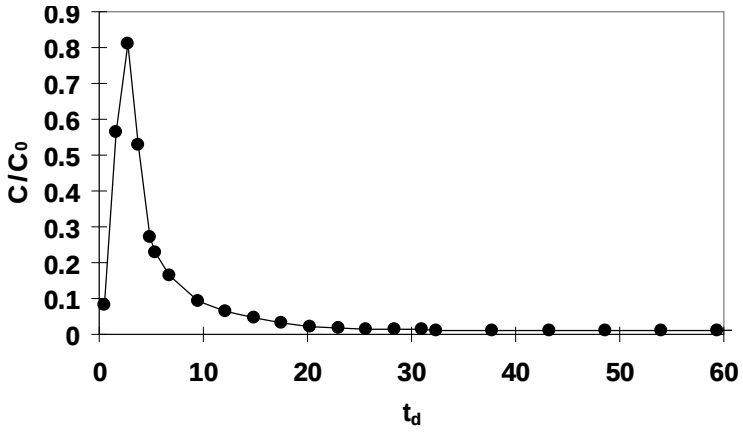

Figure 11-2: Breakthrough curve of Br during initial dipole flow tracer test. Notice the large early peak and quick tailing of concentrations.

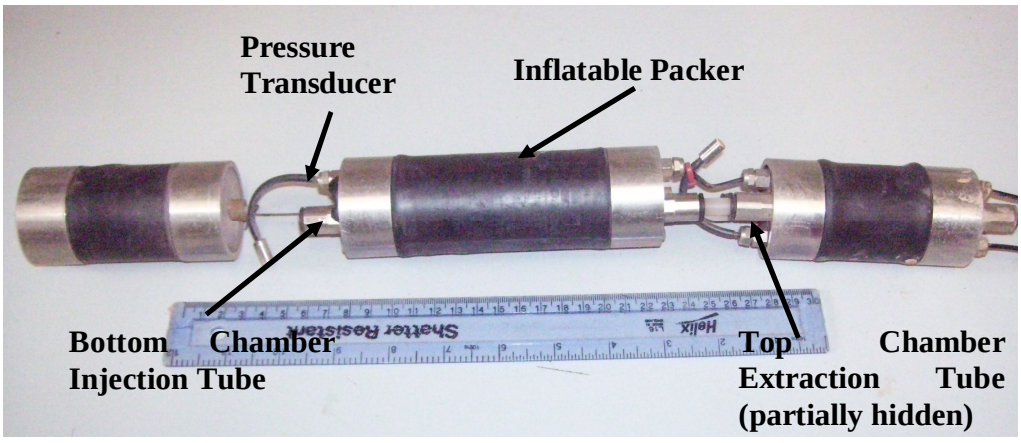

Figure 11-3: Dipole probe used in dipole flow tracer tests in the sandbox.

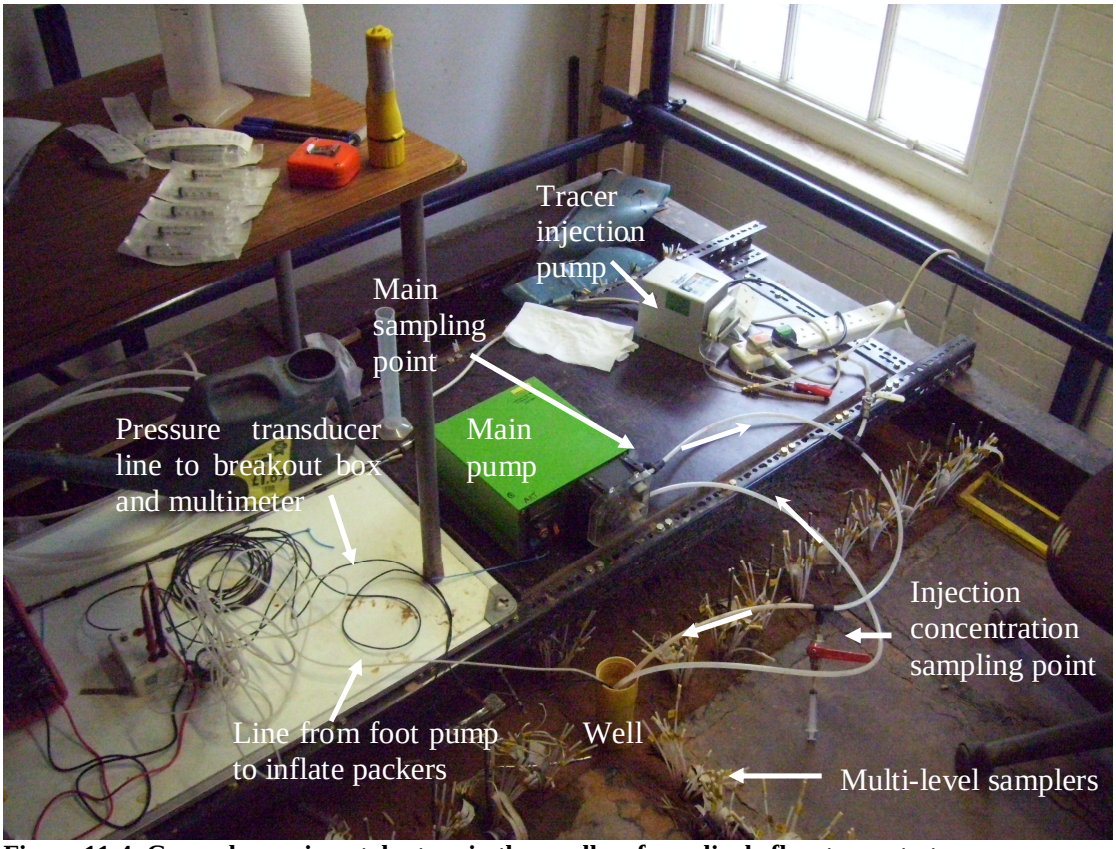

Figure 11-4: General experimental set-up in the sandbox for a dipole flow tracer test.

11.3. **Surge blocking and slug test**

The presence of voids and mobile zones was likely caused by the high proportion of find material in the sand. To remove the fine material and eliminate the potential voids a surge block was constructed. This was a silicon disk that could be squashed by two nuts, so that a seal could be formed in the well on the end of a pole. This was pushed up and down the well screen for 5 minutes. The well was then pumped out at 300 ml/min for 10 minutes removing the fines, the water level was then allowed to rise back. This process was repeated 20 times. The quantity of fines produced by the surge blocking did not decrease after 20 cycles. Considering that grain size analysis has shown that 30-45 % of sand was smaller than the slots in the well screen, this does not seem unlikely.

A slug test was performed in the central well to estimate the hydraulic conductivity after surge blocking, independently from the dipole flow test. 1.29 litres of water was quickly removed and the rebound of well head level was measured over time. Considering well levels for the first 5 minutes estimates gave an estimate of hydraulic conductivity of 4.59

x 10^{-6} m/s using the Bouwer-Rice method [Fetter, 1994], while considering all data gave an estimate of 3.72 x 10^{-6} m/s. These hydraulic conductivities are very low, suggesting a dominance of the silt sized grain sizes shown in the grain size analysis. This suggested that despite surge blocking a large portion of fine material remained around the well.

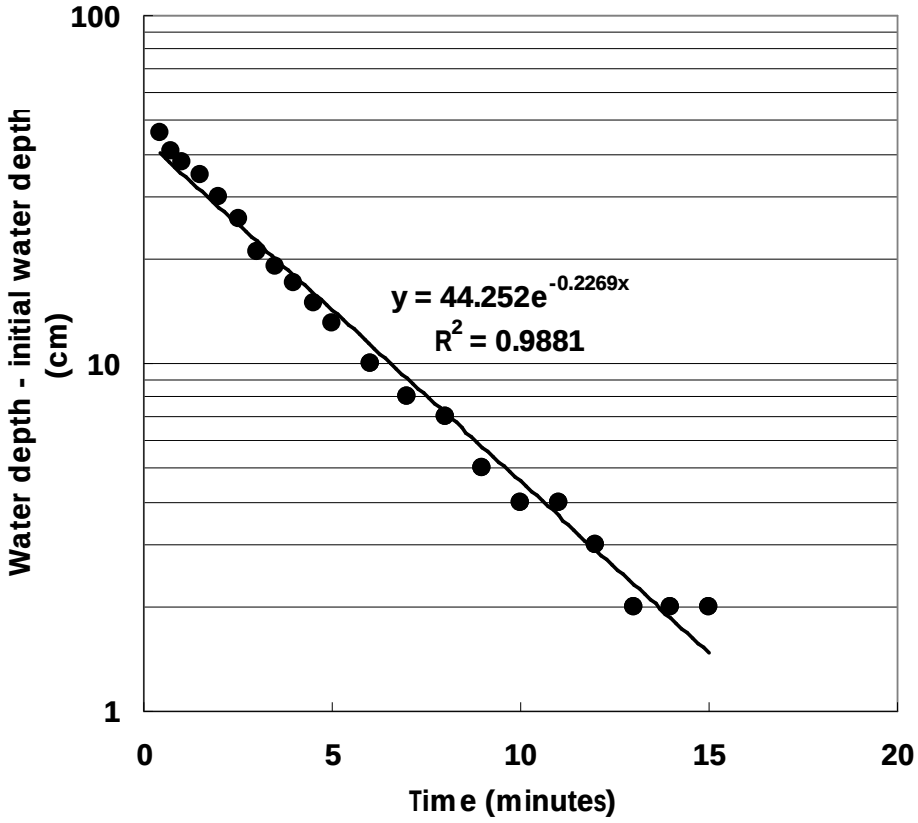

Figure 11-5: Test data from slug test performed in the central sandbox well.

11.4. **Second dipole flow tracer test**

A dipole flow tracer test was performed to test if the surge blocking had improved conditions around the well. The test was performed similarly to before with a lower Br stock concentration to give input concentrations averaged at 259.98 mg/l. Peak height and timing were similar to before, see Figure 11-6, and the tailing of concentrations was slower. This suggests tracer is kept in a loop around the injection and extraction chamber for longer before being lost to the aquifer. Again there was no sign of an aquifer peak.

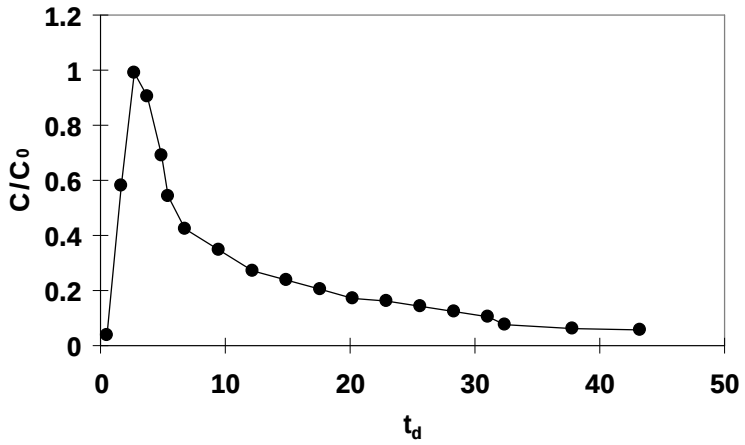

Figure 11-6: Breakthrough curve of Br during the second dipole flow tracer test.

It was considered that the sand around the central well may have been overdeveloped from tests performed by me and other PhD students. Also it was considered that the current slot size of 0.3 mm of the well screen was probably not suitable considering the amount of fine material in the sand.

11.5. **New well installation and last dipole flow tracer test**

A 1 m long, 52 mm internal diameter uPVC well screen with 0.3 mm horizontal slots was obtained from Boode UK. This was the smallest slot 2 inch well screen that could be purchased. To reduce the amount of sand that could pass through the slots a 98 micron mesh was obtained from Rigby Wire Works, Sheffield and attached to the well screen with stainless steel wire wrapped in a spiral with cable the top and bottom. A 60 mm internal diameter aluminium tube with a bevelled bottom end and 5 mm walls was hammered in at the centre of the chosen quadrant (0.5 m from the left and front walls and the central well). The sand inside the tube was then slurried out. The well screen and attached mesh was then put in the aquifer. A rubbed bung was used to seal the bottom of the well screen. The interstitial space between the well screen and the aluminium tube was filled with dry sand and the aluminium tube was removed. Any sand at the bottom of the well was removed and the well was pumped for 3 days to help clean it and aid the collapse of sand into any voids.

A dipole flow tracer test was performed to assess the suitability of the new well. As the ion chromatograph was not functional at this time it was decided to use fluorescein as a conservative tracer for this test. This was considered suitable as only qualitative measurements were required from the test. The rest of the test-set up was the same as previous experiments. The early large peak and long tail (see Figure 11-7) suggest short circuiting around the well between the chambers with little loss to the aquifer.

At a flow rate of 120 ml/min the pump had problems pumping water into the sandbox, but not extracting. This suggests something blocking water flow into the sandbox. It is possible the fine sand was coating the stainless steel mesh effectively forming a seal. At higher flow rates parts of the seal were broken through and sand was likely mobilised.

The large amount of fines present in the sand seemed to be a crucial factor in the failure to undertake a successful dipole flow tracer test in the sandbox. If the sand was replaced by a more regular and coarser grained choice, then it may be possible to successfully perform tests. This option was considered overly time consuming, due to the size of the box. Therefore dipole flow tracer tests ceased in the sandbox.

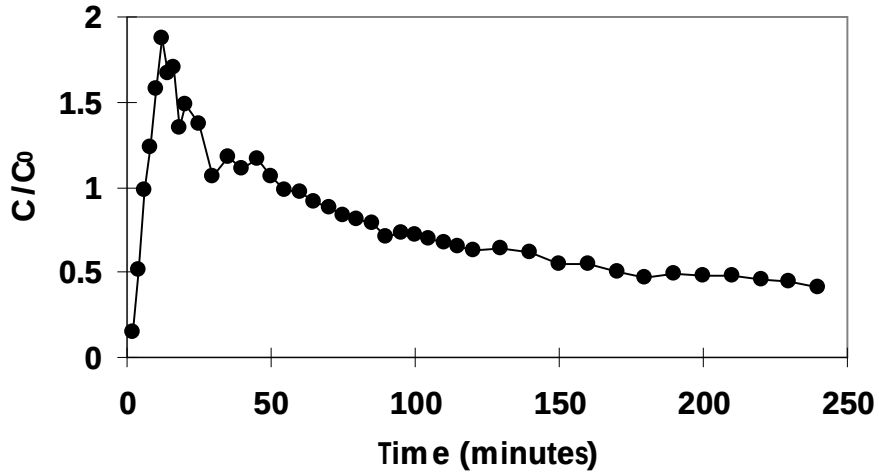

Figure 11-7: Breakthrough curve of fluorescein for dipole flow tracer test undertaken in newly installed well.

Figure 11-8: Pictures left to right of: New well screen with stainless steel mesh attached, aluminium tube being inserted, sand being slurried out from centre of tube.

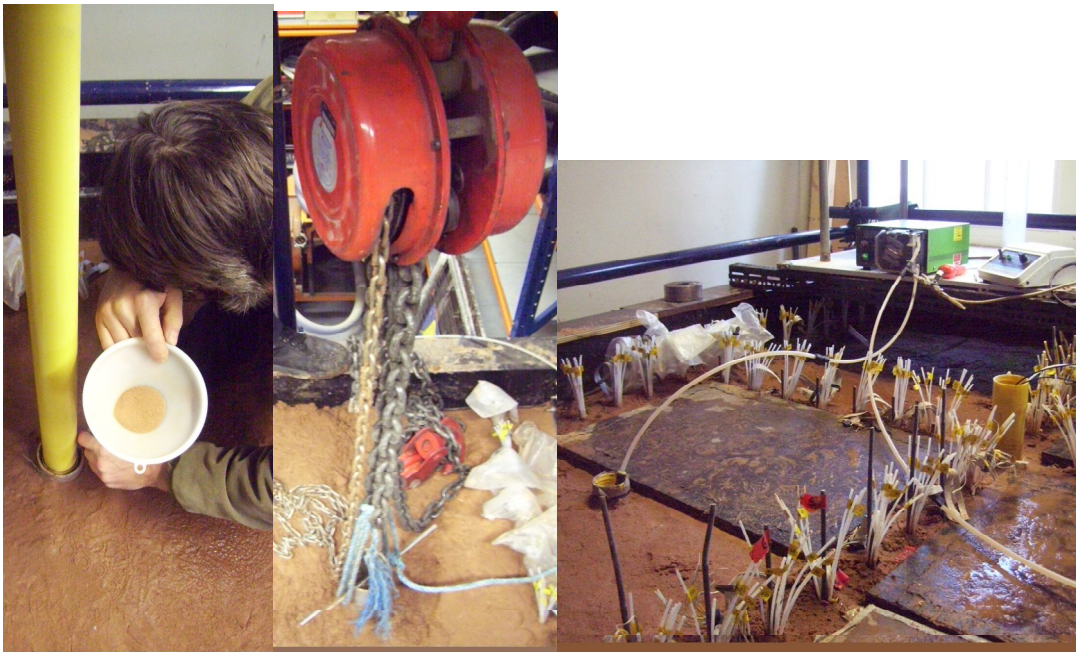

Figure 11-9: Pictures left to right of: Gap in between well screen and aluminium tube being filled with sand, aluminium tube being removed with aid of winch, new well being pumped clean.

11.6. **Push-Pull tests performed**

At a similar time to the new well installation, push-pull tests were being trialled in the central well. Although dipole flow tracer tests performed suggested that a direct comparison with push-pull tests for reactive tracers was not viable, it was considered that using the reactive tracers and cocktails in a pseudo field environment in push-pull tests alone was worthwhile. Tests were performed with the assistance of Tom Haighton who was undertaking an undergraduate project.

Tests were run with the dipole flow apparatus. The top chamber was used during the test for injection and extraction of tracer and the bottom chamber was removed from the plumbing. The top chamber was positioned centrally in the well. Two problems with running these tests were initially indicated:

(1) Pump rate was related differently to flow rate during the injection and extraction phases. During injection siphoning effects significantly contributed to the flow rate, leading to injection of tracer taking far less time than predicted.

(2) There was also significant short circuiting from the injection chamber to the top well and the water table typically rose over the surface during the injection phase.

Three push-pull tests were performed, the first two extraction breakthroughs were not successfully obtained. In the third test push-pull test conducted 1 x 10^{-5} M fluorescein was used as the conservative tracer (1 L of 1x10^{-4} M aqueous solution was made and this was diluted to make 10 L). Br would have been preferred however the ion chromatograph was not functional at this moment of time and there were time restraints on Tom Haighton's project. Stock was injected at 98.25 ml/min and extracted at 63.39 ml/min. There was no flush phase like the imaging tests. Multilevel samples were taken 15 cm out from the well at 60 cm depth parallel to the chamber and 45 cm depth. Results were modelled in PHREEQC [USGS, 2008] considering outwards flow into the aquifer to be similar to a horizontal column. This was considered suitable as Schroth and Istok [2005]

have shown that spherical flow and radial flow solutions are very similar for push–pull tests. Therefore this was further collapsed down into a 1 dimensional radial model. It was also considered that there was not sufficient time for Tom Haighton to learn and run MODFLOW (a 3-D finite difference groundwater flow model developed by the USGS) models. At this time a copy of HydroGeoSphere© had not been obtained. The length of the columns was estimated from the volume of injected tracer assuming it travelled along a set thickness of aquifer.

The acquired breakthrough curve was compared to the expected breakthrough if the tracer had travelled through a 10 cm thick zone. An estimate of dispersivity was obtained from initial column tests presented in Chapter 4 and was set to 0.0067 ± 0.0025 m. Tracer concentrations observed were less than that expected from the model. This may be partly due to a decrease in pH reducing observed fluorescence; however tracer which flowed out of the top of the well during the test suggests that a significant portion of mass was also lost. Over the time period with available data 31.0% of mass is lost. The data fits best to a model assuming 30% consistent mass loss, see Figure 11-10.

It was clear from the multilevel samplers that mass had not travelled out as far as expected. Also concentrations at 45 cm depth were higher than those at 65 cm depth suggesting that in this zone of the aquifer tracer preferentially travelled up and across rather than radially as would be expected (see Figure 11-11). PHREEQC modelling was used to predict the position of the breakthrough front on the level of the multilevel sampler assuming radial flow outwards. The multilevel sampler at 60 cm depth was best modelled assuming the middle of the breakthrough front reached 9.5 cm at the end of the injection phase and the sampler at 45 cm was best modelled assuming the middle of the breakthrough front reached 15 cm. The breakthrough front would be expected to be further out at 60 cm as it parallel to the chamber. Also a full breakthrough with a peak at 1 C/C_0 is expected at both points. The greatly reduced horizontal migration of tracer may be partially caused by the short circuiting round the well, also fine material may be causing preferential zones of flow. The short circuiting may be caused by voids around the well or an insufficient seal around the packers. However these were always inflated to

20 psi or above, therefore this seems unlikely. The repeatability was good between the second and third test performed. This may suggest preferential flow paths have been set up permanently in the aquifer.

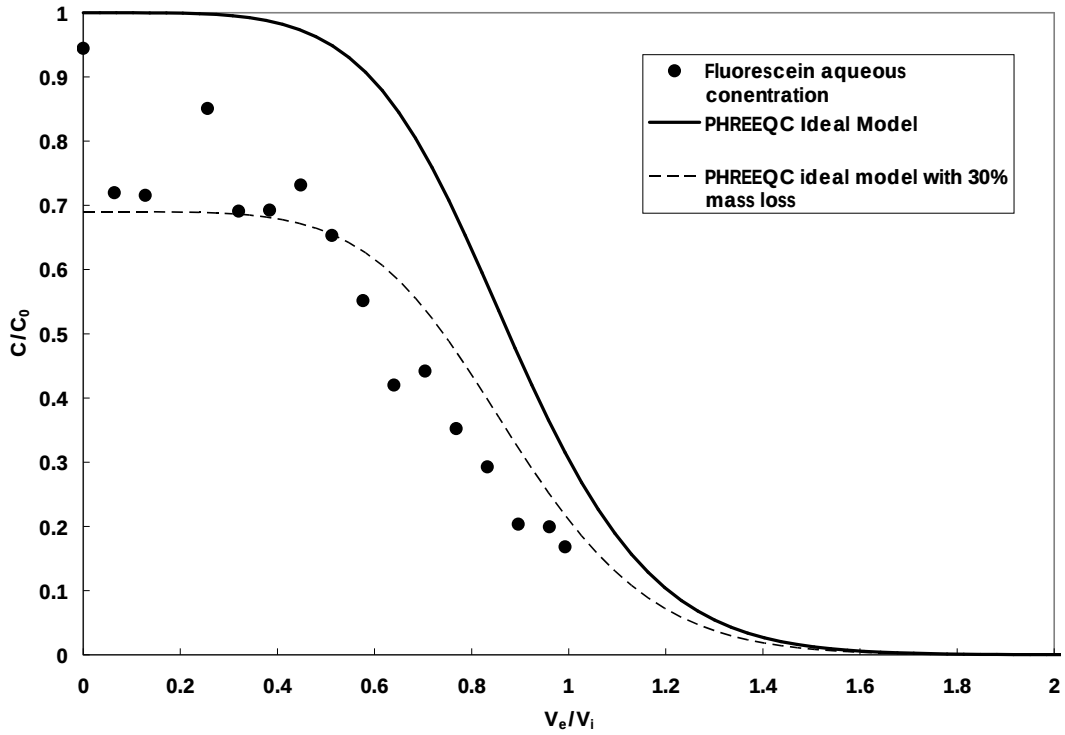

Figure 11-10: Extraction phase breakthrough curve from third push-pull test and PHREEQC modelled curves. Modified from Haighton (2009) .

The high mass loss and irregular flow present during the tests, suggested that it would not be possible to perform an accurate push-pull test in the sandbox. Results from all sandbox tests have shown that accurate experiments cannot be performed. The likely cause of the problems is the high proportion of fine material in the sand. This can prevent flow at low flow rates, mobilise sand at high flow rates, cause sand flow through well screen gaps and create voids and sand bridges around the well. These problems may have been amplified over time with repeated experimentation. The multilevel samplers and end chambers still make the sandbox a worthwhile experimental tool, however it is highly recommended that a well sorted medium to coarse grained sand is used for future experimentation. Care should be made to insure that the well screen chosen is compatible with the sand and flow rates used in the experiment will not cause any mobilisation. It was not considered in the

best interests of the project to refill the sandbox at the time and focus was put on the imaging tests which were showing good results.

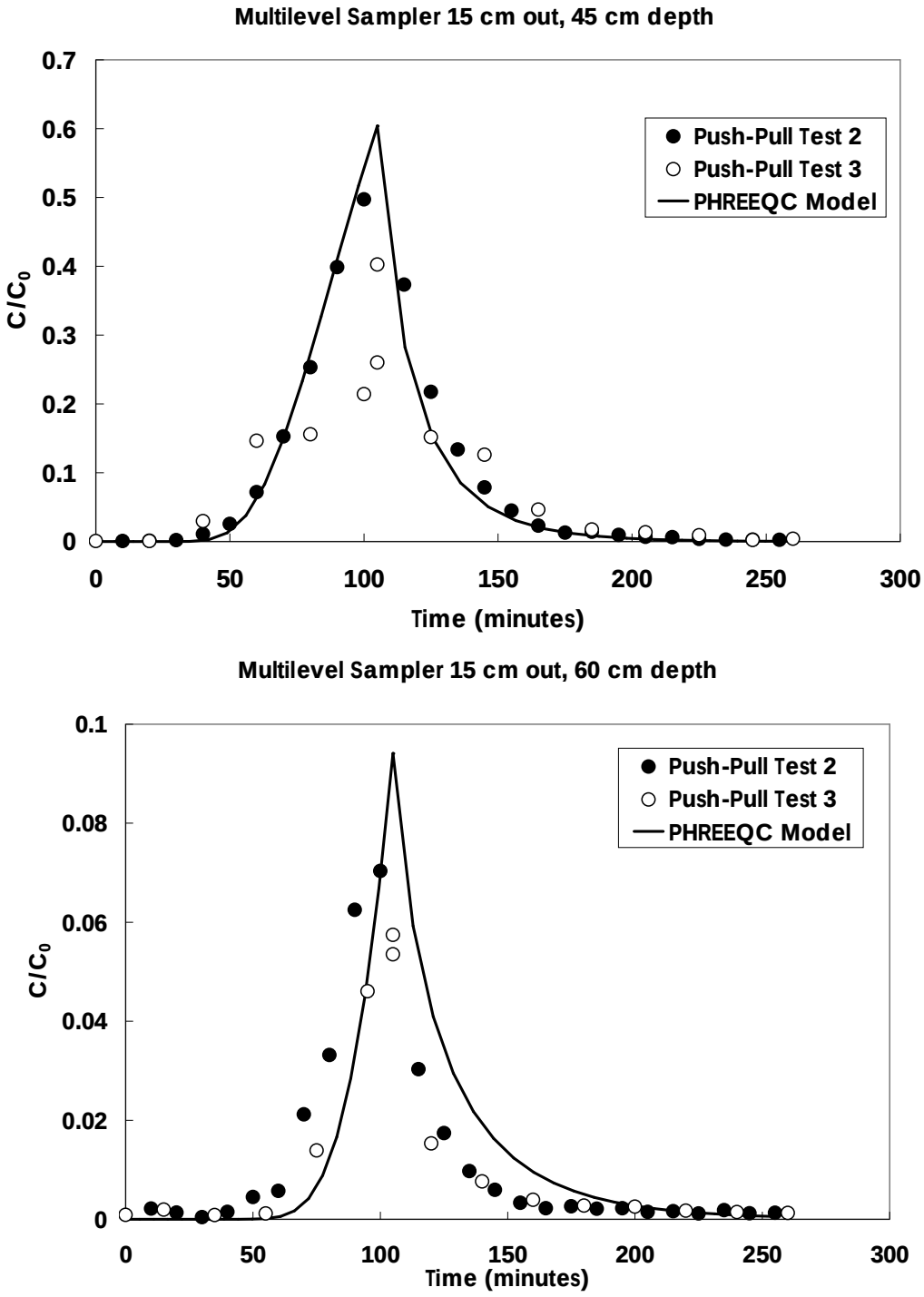

Figure 11-11: Multilevel sampler fluorescein aqueous concentrations from push-pull tests 2 and 3. Notice the larger scale of the 45 cm depth data and the good repeatability between tests.

12. **Appendix D: Paper Accepted For Publication in Groundwater Quality 2010 (International Association of Hydrological Sciences Publication 342)**

Barns, G..L., Wilson R.D. and Thornton, S.F. (2011). Assessing of the effect of physical heterogeneity on single well tracer tests using imaging experiments, *in* GQ10: Groundwater Quality Management in a Rapidly Changing World (IAHS Publ. 342), M.Schrimer, E. Hoeh and T Vogt (Ed), IAHS Press, ISBN 978-1-907161-16-2, p275-278

Assessing of the effect of physical heterogeneity on single well tracer tests using imaging experiments

G. L. BARNS, R. D. WILSON & S. F. THORNTON
Groundwater Protection and Restoration Group, University of Sheffield, Kroto Research Institute, Broad Lane, Sheffield S3 7HQ, UK
g.barns@sheffield.ac.uk

Abstract Single well forced gradient tracer tests can be used to assess aquifer properties for natural attenuation and remediation design. Measurements of aquifer properties monitored in the well are depth-averaged and therefore may misrepresent or fail to identify important flow and mass flux paths. Such spatial information is critical for remedial system design. UV imaging tests were undertaken in a pseudo 2D tank filled with glass beads, with a centrally positioned slotted well screen. Fluorescent tracer migration during dipole flow tracer tests (DFTTs) and push–pull tests (PPTs) were examined under isotropic and simple layered conditions. Results show that small variations in hydraulic conductivity significantly affect tracer flow. For DFTTs these produce discernable differences in breakthrough curves, which can be used to help identify important hydrogeological features.
Key words imaging; heterogeneity; tracer tests; natural attenuation; remediation

INTRODUCTION

Single well forced gradient tracer tests are able to quantify the hydraulic properties and potential sorption or biodegradation of a contaminant in an aquifer [Istok et al., 1997; Sutton et al., 2000]. The volume of aquifer sampled in tests is often considered homogenous in nature, even though flow heterogeneity is common in sand aquifers [Korte et al., 2000]. Even small scale physical heterogeneity has been shown to significantly affect tracer transport at the field scale [Welty and Gelhar, 1994]. Failing to account for the real effects of heterogeneities can contribute considerable error in the parameterisation of aquifer properties. This could lead to poorly designed remediational schemes or misjudgements on the natural attenuation of a pollutant.

IMAGING OF TRACER TESTS

UV fluorescent imaging has been shown to be less sensitive to background noise than visible light imaging [Huang et al., 2002]. Fluorescein was used as a tracer because it exhibits negligible hydrophobic sorption to silica beads [Kasnavia et al., 1999]. UV imaging has previously been used to study dispersion [Gaganis et al., 2005], pore-scale heterogeneity [Corapcioglu and Fedirchuk, 1999] and biodegradation [Huang et al., 2003; Rees et al., 2007]. The experiments in this study are at a larger scale of observation that allows the effect of significant heterogeneity on tracer response to be assessed.

Imaging technique

An acrylic box with internal dimension of 1500 mm × 750 mm × 26 mm and a wall thickness of 8 mm was constructed to contain the porous media. A 1-inch well screen was

placed centrally. This was slotted manually to give 0.2 mm wide slots with an open area of around 7%. The box was filled with either 300–355 μm, silica glass beads, or a combination of these and 600–800 μm beads, to evaluate the effect of layers with different hydraulic conductivity (K).

UV light was supplied by two horizontally mounted 350 nm black light bars. A digital SLR camera was positioned between the light bars, 0.5 m from the front of the box, to capture the images. Image green light intensity was calibrated for fluorescein concentration in a separate smaller box. Images were analysed with Image J software.

Test set-up

The well apparatus was made from alternating uPVC and silica disks mounted on a threaded stainless steel rod. Segments were tightened so that the silica disks formed a friction seal against the well screen, forming packers. Chambers between the packers were 37 mm long and the central packer for dipole tests was 65 mm. A flow rate of approx. 3 ml min^{-1}, an 80-min injection period and a 45-min flush period was used for PPTs. A flow rate of 5–6 ml min^{-1} with a 15 min injection period was used for DFTTs. For DFTTs water was injected from the bottom chamber and extracted from the top. Br or Cl was used to determine breakthrough curve concentrations, which were measured on a Dionex DX-120 Ion Chromatograph.

Isotropic conditions

The breakthrough curves from DFTTs and PPTs were modelled with Hydrogeosphere [Thierren et al., 2005], see Fig. 1(a),(b). Imaging analysis suggested that effective image penetration is 4–7 mm into the beads, which was taken into account for in the modelling. Image intensity from specific points correlated well with model predictions for PPTs, while tracer breakthroughs measured by imaging around the extraction well for DFTTs were slightly delayed relative to model predictions.

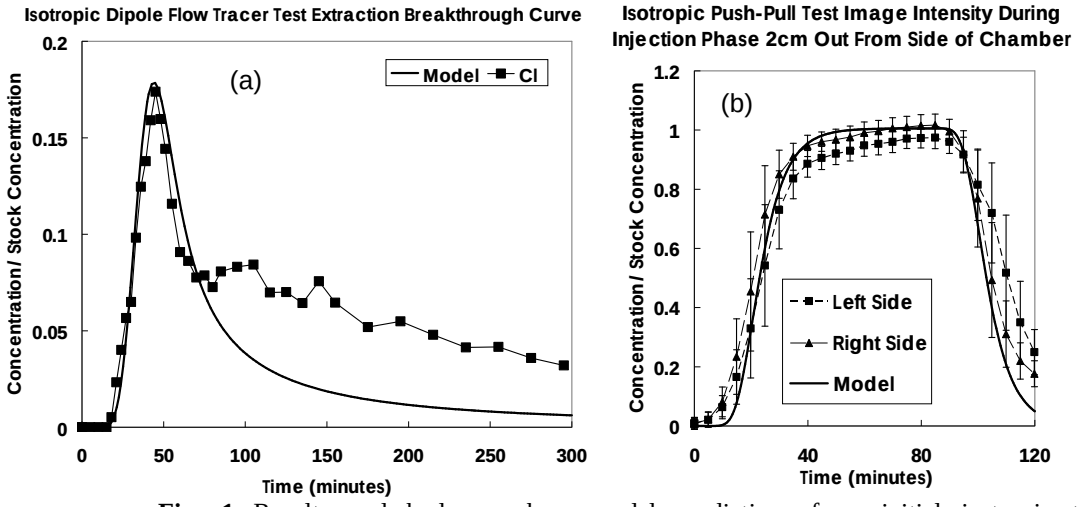

Fig. 1 Results and hydrogeosphere model predictions from initial isotropic tests. Hydrogeosphere cannot model tracer that is recirculated through the system. The model is therefore fitted to the initial breakthrough of a dipole flow tracer test.

HETEROGENEOUS CONDITIONS

Dipole flow tracer tests

A 3 cm thick horizontal layer of the larger beads was placed mid-depth across the box. The K, estimated from porosity and median bead size, was 4.55 times greater in the larger beads [Bear, 1972; Corapcioglu and Fedirchuk 1999].

By moving the well packer assembly, tests were performed with the higher K layer intersecting (a) the middle packer, (b) the injection chamber, or (c) the extraction chamber. Tracer moves out as a halo from the injection chamber, and is pulled towards the extraction chamber due to the pressure differential. A fainter halo inside the larger halo represents the recirculated tracer (see Fig. 2). When the layer was over the packer tracer breakthrough occurred quicker than under isotropic conditions, suggesting the tracer is moving faster over the higher K zone. When the higher K layer intersected either the injection or extraction chamber a slight delay of tracer breakthrough relative to isotropic conditions is seen. This is likely due to an increase in the flow path length and dilution when the layer is over the injection and extraction chamber, respectively.

Push-pull tests

Tests were performed with the higher K bead layer (a) bisecting the chamber and (b) positioned 3 cm below the middle of the chamber. As predicted in modelling the layer had little effect on the extraction phase breakthrough. In the isotropic test the tracer radiated away from the chamber during injection, near equally in all directions. When the large bead layer was present the tracer migrated preferentially in that layer (see Fig. 3) rather than radially. In another test a weak background head gradient caused

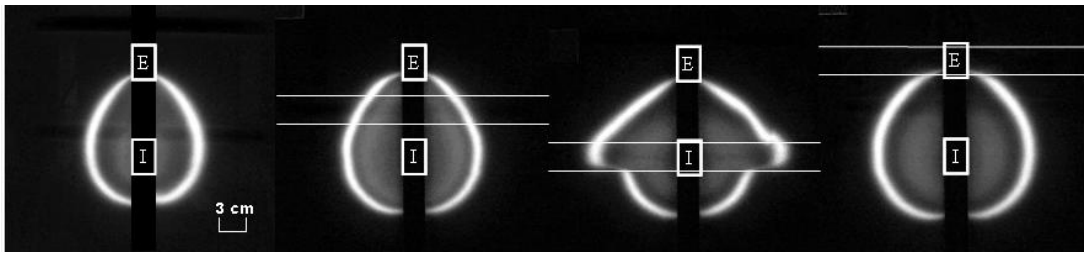

Fig. 2 Green light intensity of images taken at 60 min from DFTTs from left to right: isotropic, layer central, layer over injection and layer over extraction. I = injection chamber, E = extraction chamber.

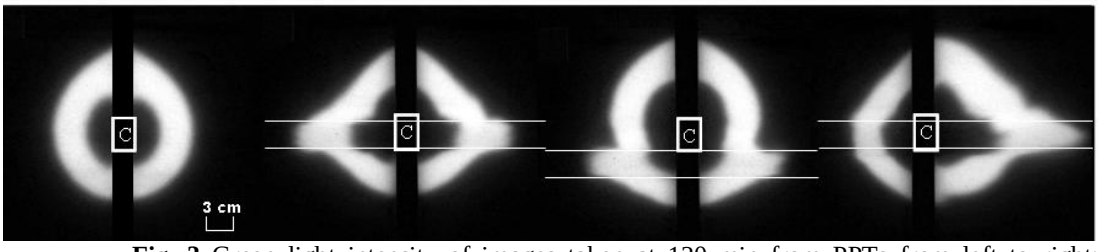

Fig. 3 Green light intensity of images taken at 120 min from PPTs from left to right: isotropic, layer over chamber, layer below chamber, layer over chamber with background hydraulic gradient. C = chamber.

high background flow velocities in the layer, leading to high asymmetry and a loss of mass.

IMPLICATIONS AND FUTURE WORK

Results show that tracer flow in tests is significantly affected by the presence of even small zones of differing K. Although there was no significant variation in tracer breakthrough for the PPTs evaluated, the pathway of the tracer was greatly affected by the higher conductivity layer. If there was a long rest period between injection and extraction or a significant natural head gradient, the presence of different hydraulic conductivity zones may lead to a loss of mass. DFTTs have the potential to identify layers with different K in tests, however this high sensitivity to discrete K variations may lead to breakthrough curves being difficult to recover in the field. If not accounted for, physical heterogeneity may lead to misinterpretation of reactive tracer signals and therefore errors in the estimation of fate and transport parameters. The consequence of this is poor remediation system design or prediction of natural attenuation.

Future work will examine the effect on tracer behaviour and recovery of a low hydraulic conductivity layer in a higher conductivity bead pack, using DFTTs and PTTs. Hydrogeosphere will be used to further analyse these results and investigate other scenarios.

Acknowledgements We would like to thank the UK EPRSC for funding G. Barns with an Industrial Case Studentship. This DFTT research is undertaken in conjunction with Prof. Neil Thomson, University of Waterloo, Canada

REFERENCES

Bear, J. (1972) *Dynamics of Fluids in Porous Media. Elsevier*, New York, USA.

Corapcioglu, M. Y. & Fedirchuk, P. (1999) Glass bead micromodel study of solute transport. *J. Contam. Hydrol.* **36**(3–4), 209-230.

Freyburg, D. L. (1986) A natural gradient experiment on solute transport in a sand aquifer. 2 Spatial moments and the advection and dispersion of non-reactive tracers. *Water Res.* **22**(13), 2031–2046.

Gaganis, P., Skouras, E. D., Theodoropoulou, M. A., Tsakiroglou, C. D. & Burganos. V. N. (2005) On the evaluation of dispersion coefficients from visualization experiments in artificial porous media. *J. Hydrol.* **307**(1–4), 79-91.

Huang, W. E., Oswald, S. E. Lerner, D. N. Smith, C. C. & Zheng. C. (2003) Dissolved oxygen imaging in a porous medium to investigate biodegradation in a plume with limited electron acceptor supply. *Environ. Sci. Technol.* **37**(9), 1905–1911.

Huang, W. E., Smith, C. C. Lerner, D. N. Thornton, S. F. & Oram, A. (2002) Physical modelling of solute transport in porous media: evaluation of an imaging technique using UV excited fluorescent dye. *Water Res.* **36**(7), 1843-1853.

Istok, J. D., Humphrey, M. D., Schroth, M. H., Hyman, M. R. & Oreilly. K. T. (1997) Single-well, "push-pull" test for in situ determination of microbial activities. *Ground Water* **35**(4), 619–631.

Kasnavia, T., V. De & David, A. S. (1999) Fluorescent dye and media properties affecting sorption and tracer selection. *Ground Water* **37**(3), 376–381.

Korte, N., Kearl, P. M., Siegrist, R. L., Muck, M. T. & Schlosser, R. M. (2000) An evaluation of horizontal recirculation using single-well tests, pumping tests, tracer tests, and the colloidal borescope.*Ground Water Mon. Rem.* **20**(1),78-85.

Rees, H. C., Oswald, S. E. Banwart, S. A. Pickup, R. W. & Lerner. D. N. (2007) Biodegradation processes in a laboratory-scale groundwater contaminant plume assessed by fluorescence imaging and microbial analysis. *Appl. Environ. Microbiol.* **73**(12), 3865–3876.

Sutton, D. J., Kabala, Z. J. Schaad, D. E. & Ruud, N. C. (2000) The dipole-flow test with a tracer: a new single-borehole tracer test for aquifer characterization. *J. Contam. Hydrol.* **44**(1), 71–101.

Therrien, R., Mclaren, R. G. Sudicky, E. A. & Panday, R. M. (2005) Hydrogeosphere: a three-dimensional numerical model describing fully-integrated subsurface and surface flow and solute transport. Model and Manual, Groundwater Simulations Group, University of Waterloo and Université Laval, Canada.

Welty, C. & Gelhar, L. W. (1994) Evaluation of longitudinal dispersivity from nonuniform flow tracer tests. *J. Hydrol.* **153**(1–4), 71-102.

13. Appendix E: DVD-Rs

5.1 Contents

E1: HydroGeoSphere© input files, installation file and manual
Inorganic column test data and spreadsheets
Ni-EDTA column test data and spreadsheets
Acetate column test data and spreadsheets
TCFE test data and spreadsheets
PHREEQC input and output files
STANMOD output files
XRD images
Imaging test data and spreadsheets relating to Chapter 2
Image calibrations and image penetration test raw data and spreadsheets
Copy of this thesis

E2: Imaging test raw data and spreadsheets relating to dipole flow tracer tests in Chapter 3

E3: Imaging test raw data and spreadsheets relating to push-pull tests in Chapter 3

Appendix references

Bridge, J. (2007), High-Resolution Measurement of Colloid Transport in Variably Saturated Quartz Sand Using Time Lapse Fluorescence Imaging, D.Phil thesis, University of Sheffield.

Fetter, C. W. (1994), Applied hydrogeology, 3rd ed., Maxwell Macmillan International.

Gillham, R. W., and S. F. O'Hannesin (1990), Sorption of Aromatic Hydrocarbons by Materials in Construction of Ground-Water Sampling Wells, in Ground Water and Vadose Zone Monitoring, edited by D. M. Nielsen and A. I. Johnson, pp. 108-122, American Society for Testing and Materials, Philadelphia.

Haighton, T. (2009), Suitability of Push-Pull Tests for use in a Model Aquifer in Relation to Groundwater Remediation Engineering, Undergraduate Project, University of Sheffield.

North, J. (2008), Capturing and quantifying a dipole flow tracer test using a novel imaging technique, MSc thesis, University of Sheffield.

Schroth, M. H., and J. D. Istok (2005), Approximate solution for solute transport during spherical-flow push-pull tests, Ground Water, 43, 280-284.

Smart, P. L., and I. M. S. Laidlaw (1977), An Evaluation of Some Fluorescent Dyes for Water-Tracing, Water Resources Research, 13, 15-33.Fetter, C. W. (1994), Applied hydrogeology, 3rd ed., Maxwell Macmillan International.

USGS (2008), PHREEQC (Version 2)--A Computer Program for Speciation, Batch-Reaction, One-Dimensional Transport, and Inverse Geochemical Calculations. http://wwwbrr.cr.usgs.gov/projects/GWC_coupled/phreeqc/,.

Zlotnik, V., and G. Ledder (1996), Theory of dipole flow in uniform anisotropic aquifers, *Water Resources Research*, *32*, 1119-1128.